GRAVITATIONAL LENS B0957+561: A STUDY AT RADIO WAVELENGTHS

by

Deborah Joy Becker Haarsma

Bachelor of Science in Physics
Bachelor of Music in Piano
Bethel College, 1991

Submitted to the Department of Physics
in partial fullfillment of the requirements for the degree of

DOCTOR OF PHILOSOPHY

at the

MASSACHUSETTS INSTITUTE OF TECHNOLOGY

June 1997

Author_____
Department of Physics
May 16, 1997

Certified by_____
Bernard F. Burke
Professor of Physics
Thesis Supervisor

Accepted by_____
George F. Koster
Professor of Physics
Chairman, Physics Graduate Committee

Gravitational Lens B0957+561:
A Study at Radio Wavelengths

by

Deborah Joy Becker Haarsma

Submitted to the Department of Physics
on May 16, 1997, in partial fulfillment of the
requirements for the degree of
Doctor of Philosophy

Abstract

The gravitational lens B0957+561 has been observed monthly at 6 cm with the VLA radio telescope since its discovery in 1979. Since 1990, the monitoring included 4 cm observations as well. The VLA data were analyzed using the same techniques that were applied to earlier observations in the light curve by Lehár *et al.* (1992). Three different statistical techniques have been used to determine the time delay between the images: χ^2 structure function analysis (Press, Rybicki, & Hewitt 1992b, 1992c), dispersion analysis (Pelt *et al.* 1994, 1996), and discrete correlation function analysis (Lehár *et al.* 1992). A comparative discussion of these techniques is given. Joint analysis of the 6 cm and 4 cm light curves using the χ^2 structure function technique yields a time delay of 420 ± 13 days (1.15 ± 0.04 years), with events occurring first in the A image. This result is consistent with the time delay found from optical monitoring (Kundić *et al.* 1997). The flux ratio between the images (B/A) at 6 cm is $0.6996^{+0.0021}_{-0.0024}$ and at 4 cm is 0.6968 ± 0.0036. When the delay is combined with a model of the mass distribution (Grogin & Narayan 1996a, 1996b) and the lensing galaxy velocity dispersion (Falco *et al.* 1997), the angular diameter distance to the lens is calculated to be $D_{OL} = 1032^{+119}_{-122}$ Mpc. For a variety of cosmological models, this distance implies that the Hubble parameter H_0 is between 60 and 75 $\mathrm{km\,s^{-1}Mpc^{-1}}$, with about 12% error on H_0 for a given cosmology. A review of the 0957+561 lens mass models and of other distance measurement techniques is included. Besides the cosmological results, the combined light curves give information about the physical properties of the source and the light propagation paths. At 4 cm, intrinsic source variations occur earlier and are twice as variable as at 6 cm, consistent with the shock front model of active galactic nuclei variability. One significant difference between the two light curves is a fluctuation in the B image at 6 cm in Spring 1990. This event could be either microlensing by a star in the lensing galaxy, or scattering by a plasma cloud in the Galaxy (an extreme scattering event).

Thesis Supervisor: Bernard F. Burke
Title: Professor of Physics

Solo Deo Gloria

Acknowledgments

There are many people who assisted me in this thesis work. First, I'd like to thank Bernie Burke for his support and for providing the opportunity to do this project. Bernie, Jackie Hewitt, and Ed Bertschinger served as my thesis committee, provided valuable feedback, and wrote many recommendation letters for my job applications. In addition, Jackie helped tremendously as I worked on the time delay statistics, provided computer code for the PRH method, and wrote an early version of §4.2 on the PRH statistical technique. Joseph Lehár helped me understand many details about his work on the 0957+561 light curves, gave lots of helpful advice and encouragement, and provided the AIPS Run files for the 6 cm VLA data reduction (Appendix C) and the computer code for the discrete correlation statistic. The monitoring of 0957+561 began long before I joined the group, and thanks are due to Dave Roberts and others in the MIT radio astronomy group who worked on this project in the 1980s. Tomislav Kundić gave permission for the optical light curves to be used in this thesis.

I would like to thank all the members of MIT radio astronomy group from 1992-1997 for their friendship and for providing a helpful and pleasant working environment. In particular, I am grateful to Chris Moore, Cathy Trotter, Charlie Katz, and Max Avruch for valuable discussions regarding this thesis work. Sam Conner, Grace Chen, and John Ellithorpe helped me learn VLA data reduction techniques and the UNIX environment. André Fletcher taught me the basics of optical observing. Katherine Blundell gave comments on a few of the thesis chapters and encouragement during the final months of the thesis.

Finally, a big "thank you" to all of my family and friends, both near and far, for their tremendous support throughout my time at MIT and especially during the last six months of job searching and thesis writing. I truly could not have done it without you. In particular, I want to thank my parents for their undying confidence in me – their teaching, guidance, and love gave me the strength and confidence to attempt and complete this Ph.D. And Loren, your encouragement and help strengthened me more times than I can count – you fill the present with joy and the future with hope.

Foreword for the Non-Scientist

The bulk of this thesis will be difficult to understand by anyone except a research scientist in astronomy or physics. This *Foreword* is intended for everyone else – a brief statement in everyday language of the topic, purpose, and results of this thesis. The non-scientist may also find "Afterword: Astrophysics in Context" interesting.

The observations for this thesis were done at the Very Large Array (VLA) radio telescope, located near Socorro, New Mexico. This telescope detects light coming from stars and galaxies, but it is sensitive to radio wavelength light (radio waves a few centimeters long) instead of the usual "optical" wavelength light (seen with your eyes or the Hubble Space Telescope). The VLA is made up of 27 individual antennas (the antennas are similar to satellite TV dishes, except they are 82 feet in diameter), arranged in a Y shape with three arms, each about 12 miles long. This telescope is located on the Plains of San Augustin in the mountains of western New Mexico. The location is at high altitude (so that the telescope looks through less atmosphere) and is far from human radio sources. The information detected by the 27 antennas is combined together to create the resolving power (ability to distinguish objects close together on the sky) of a telescope several miles in diameter. The antennas can be moved on railroad tracks up and down the arms of the Y to create different resolutions. The observations in this thesis have a resolution of about 1 arc-second, which is the apparent size of a penny located 2.5 miles away.

Galaxies look very different at radio wavelengths than at optical wavelengths. A radio galaxy has a small, bright core and two jets of hot gas shooting out thousands of light years to form large lobes and bright spots. The observations in this thesis are of a radio galaxy called 0957+561 (it is named after its coordinates on the sky) located several billion light years away from us. There is a cluster of galaxies about halfway between us and this radio galaxy, and the cluster acts as a "gravitational lens."

Gravitational lensing is a result of Einstein's theory of general relativity. Usually, we think of light (including radio waves) as traveling in a straight line. But light from a distance source can be bent by a small angle if it passes near a massive object, such as a galaxy, called the *lens* (see Figure 2-1 for a diagram of a gravitational lens). A gravitational lens is

different than most everyday glass lenses. It doesn't focus light to a particular point, but it does distort, magnify, slow, and bend light. The effect is similar to the mirage seen above a hot road. In the 0957+561 system, the lens is a cluster of galaxies with a large galaxy at the center. This lens causes light from the bright core of the radio galaxy to appear at two different positions, one on either side of the lens. These are the two *images* of the source. The top left panel of Figure 3-1 shows the double-lobed radio galaxy with its bright core (the "A" image), the second image of the core 6 arc-seconds south (the "B" image), and some emission from the lensing galaxy just north of the B image.

Light in the images takes longer to travel to us than the light from the source would take if there were no lens. This is due to two effects: the path of the light through the universe is longer (which can be seen from the lensing diagram, Figure 2-1), and the light travels more slowly when it passes very close to the massive lensing galaxy. The two effects are both stronger for the B image, so light from the B image arrives here later than light from the A image. It is impossible to measure exactly how long it takes for light from one image to get to us, but the difference in the arrival times for the two images is measurable, by watching a flare or variation of the source happen first in one image and then the other.

The 0957+561 system was monitored at the VLA to measure this difference in the arrival time of the two images – the "time delay." Observations have been made about once a month from 1979 to the present. Figures 3-5 and 3-6 show how the A and B images have varied in brightness over 17 years, at two slightly different observing wavelengths. You can see from these "light curves" that the light in the B image arrives about 1 year after the A image. Chapters 4 and 5 contain a long discussion of the statistics to determine the time delay precisely and accurately; my result for the delay is 420 ± 13 days, or 1.15 ± 0.04 years.

What can this measurement be used for? Why was it worth all the effort to make it? It turns out that if the shape of the lens mass distribution is well known, a measurement of the time delay gives you a measurement of the distance to the lens. I found that the lens is 3.4 ± 0.4 billion light years away from us. Gravitational lensing is one of the few ways to measure the distance to an object this far away. Such measurements must be made in order to measure the expansion rate of the universe and its decrease in time; the expansion is a result of the Big Bang, and causes all of the galaxies in the universe to move away

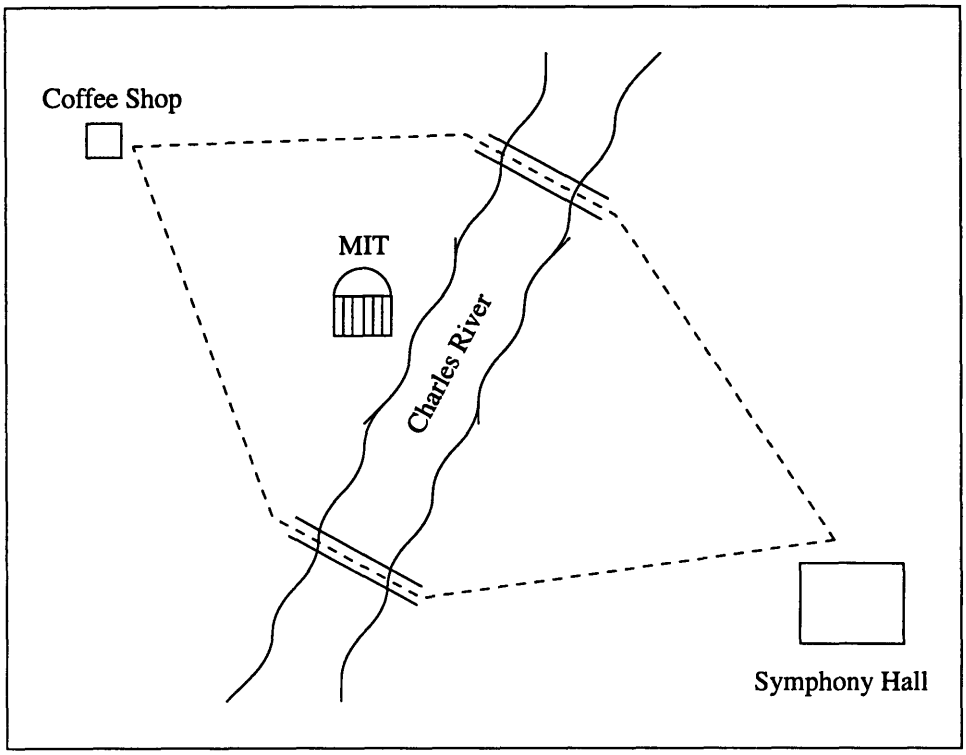

from each other, with more distant galaxies moving faster. The expansion rate is sort of a "yardstick" for cosmology, and must be measured in order to estimate the size and age of the universe.

The figure above illustrates how measuring the time delay of a gravitational lens gives an estimate of the size of the universe. The figure is a sketchy map of Boston. Note that there is no scale, so that if you've never been to Boston you don't know if an inch is a few blocks or a few miles. Imagine that a group of your friends went to a concert at Symphony Hall, and afterwards joined you at a coffee shop on the other side of the river. Some of your friends went over one bridge, some went over the other bridge. You have a good idea of how fast they are walking, and from the map you know all the angles and *relative* sizes in the problem. So if you measure the difference in arrival time of the two groups of friends, and use all of that information, you can estimate the size scale of the map. In the same way, measuring the difference in arrival time of two images of a gravitational lens gives the size scale of the whole universe.

From the distance to the lens in the 0957+561 system, I found that the universe is expanding at a rate of 60 to 80 kilometers/second per Megaparsec, or (in terms you may be more familiar with) 45 miles/hour per thousand light years. That means that a galaxy one thousand light years away is moving away from us at a speed of 45 miles/hour, and a galaxy one million light years away is receding at 45,000 miles/hour. The age of the universe corresponding to these expansion rates is between 10 and 17 billion years. This result is similar to what has been found using other techniques besides gravitational lensing. Lensing is a novel technique and has only been feasible for a few sources, but the advantage of this technique is that it is completely independent of other techniques, and can be used to study much more distant sources. When more gravitational lens time delays have been measured, the result will be more precise.

The light curves from the A and B images can be used to study things besides the gravitational lens time delay. One interesting topic is why the source gets brighter and dimmer at different times and at different observing wavelengths. The radio wavelength light comes from hot, ionized gas in the source which spirals rapidly in a magnetic field. As the cloud of gas gets larger and smaller, the brightness increases and decreases. Another topic is differences between the light curves for the two images. The source emission is the same for both, but the light has traveled two different paths through space; thus, any differences between the curves tell about different physical processes along the two paths. I found that the light from the B image might be affected by a star crossing the ray path (gravitational micro-lensing), or by a cloud of hot gas crossing the path and scattering the light. I estimate that the size of the variable emission region is roughly one light year.

Contents

List of Figures

List of Tables

Chapter 1

Introduction

1.1 History of the Gravitational Lens 0957+561

The gravitational lensing phenomenon is an observable result of general relativity (Einstein 1915). The topic became an area of observational research in 1979, with the discovery of the lens called "the double quasar" (Walsh *et al.* 1979), and now referred to by its B1950 coordinate name "0957+561." The object is composed of two images of a compact radio source separated by about $6''$. The source is the core of a double-lobed radio galaxy (see Figures 3-1 and 3-3) at a redshift of $z_s = 1.4$. The lens creating the double image is a cluster of galaxies at a redshift of $z_l = 0.36$. The brightest member of the cluster, a large cD elliptical, is just $1''$ from the B image.

With the discovery of this object, observational cosmology using gravitational lenses began. The light from the two images is expected to arrive at different times, with a "time delay" between them of about a year. A measurement of this delay, when combined with a complete understanding of the lens gravitational potential, determines the distance to the lens. This in turn can be used to set limits on the Hubble parameter H_0, the scaled mass density of the universe Ω_0, and the cosmological constant Λ_0.

Motivated by the possibility of a unique cosmographic measurement, several groups have monitored 0957+561 in order to measure the time delay. Table 1.1 is a summary of the results, showing the literature reference, the light curves and statistical method used, and the estimate of the delay in days and in years. Before 1989, the results were scattered in

Table 1.1: History of the Time Delay.

Reference	Data Set	Statistic†	Delay‡(days)	Delay (years)
Lloyd 1981	28 optical obs over 2 years	1	> 730	> 2
Keel 1982	17 optical obs over 2 years	1	> 990	> 2.7
Florentin-Nielsen 1984	54 optical obs over 5 years	1	566 ± 40	1.55 ± 0.1
Bonometti 1985	3 VLBI obs over 4 years	1	470 ± 260	1.3 ± 0.7
Gondhalekar *et al.* 1986	11 UV obs over 4 years	1	660 ± 70	1.8 ± 0.2
Schild & Cholfin 1986	28 optical obs over 4 years	2	376 ± 40	1.03 ± 0.1
Lehár *et al.* 1988	40 radio obs over 8 years	3	500 ± 100	1.4 ± 0.3
Vanderriest *et al.* 1989 (V89)	131 optical obs over 8 years	2, 4	415 ± 20	1.14 ± 0.05
Schild 1990 (S90)	329 optical obs over 10 years	2	404	1.11
Falco *et al.* 1991b	V89	5	430 ± 17	1.18 ± 0.047
	S90	5	490 ± 34	1.34 ± 0.093
Lehár *et al.* 1992 (L92), Roberts *et al.* 1991	80 radio obs over 11 years	6	513 ± 40	1.40 ± 0.10
Press *et al.* 1992b	V89	7	536^{+14}_{-12}	$1.47^{+0.038}_{-0.033}$
Press *et al.* 1992c	L92	7	548^{+19}_{-16}	$1.50^{+0.052}_{-0.044}$
	V89, L92	7	540 ± 12	1.48 ± 0.033
Oknyanskij & Beskin 1993	L92	8	540 ± 30	1.48 ± 0.082
Pelt *et al.* 1994	V89, S90	9	415 ± 32	1.14 ± 0.088
	L92*	9	409 ± 23	1.12 ± 0.063
Beskin & Oknyanskij 1995	V89, S90	8	530 ± 15	1.45 ± 0.04
Schild & Thomson 1995 (ST95)	835 optical obs over 16 years	...	...	...
Campbell *et al.* 1995	4 VLBI obs over 6 years	1	~ 365	~ 1
Pelt *et al.* 1996	ST95	10	423 ± 6	1.16 ± 0.016
	L92*	10	421 ± 25	1.15 ± 0.068
Haarsma *et al.* 1997	112 radio obs over 15 years	6, 7, 10	398 to 461	1.09 to 1.26
Kundić *et al.* 1995, 1997	97 optical obs over 2 years	2, 6, 7, 10	417 ± 3	1.142 ± 0.008

History of Time Delay *continued.*

Reference	Data Set	Statistic†	Delay‡(days)	Delay (years)
Oscoz *et al.* 1996, 1997, Kundić *et al.* 1995	40 optical obs over 1 year	6, 10	424 ± 3	1.161 ± 0.008
Schild & Thomson 1997	368 optical obs over 3 years	11	404 ± 26	1.11 ± 0.071
Pijpers 1997	ST95	12	425 ± 17	1.16 ± 0.057

†Statistical techniques are: 1) Inspection, 2) Interpolation and Cross Correlation,
3) Polynomial Fitting, 4) Discrete Fourier Analysis, 5) Dispersion (all pairs),
6) Discrete Correlation Function, 7) χ^2 Structure Function Analysis,
8) Flux Ratio Dispersion, 9) Dispersion (near-neighbors), 10) Weighted Dispersion (near-neighbors),
11) Interpolation, Smoothing, and Cross Correlation,
12) Subtractive Optimally Localized Averages
‡Time delays were converted from number given in reference using 1 year = 365.25 days.
* 1990 April 10 and 1990 May 7 removed.

delay, with large errors, and few sophisticated statistical techniques were used. Around 1990, Vanderriest *et al.* (1989) and Schild (1990) published improved optical monitoring data, and both estimated the time delay to be about 410 days. At radio wavelengths, the source had a strong increase in 1990, and Lehár *et al.* (1992) estimated a delay of about 540 days. Gravitational lens theory predicts that the delay will be independent of wavelength for a particular source, so this discrepancy was a source of concern. Press, Rybicki, and Hewitt (1992b, 1992c) resolved the discrepancy between the radio and optical values through a χ^2 structure function analysis of the curves, and found the data of both Vanderriest *et al.* (1989) and Lehár *et al.* (1992) to have a delay around 540 days. Pelt and collaborators (1994, 1996) also worked to resolve the discrepancy, applying a dispersion statistic to the same two data sets, and estimated a delay for both of around 410 days. So although more sophisticated statistics resolved the discrepancy between the radio and optical data, the statistics did not agree with each other, even when applied to the same observations. Many workers in the field began to call for new and better observations as a way to resolve the issue. Early results of this thesis (Haarsma *et al.* 1997) used several statistical techniques with lengthened 6 cm radio light curves to show that the delay was definitely less than 500 days (in the range 400 to 460 days), but without a conclusive estimate. While this thesis work was being done, a sharp decrease occurred in the optical light curves, and Kundić *et al.* (1997) made a precise measurement of 417 ± 3 days. Given the many years of controversy, it is essential that this recent optical result be confirmed at

radio wavelengths.

1.2 Scientific Goals

The main scientific goal of this thesis is to set useful limits on cosmological parameters using the time delay of the 0957+561 lens system. Given the redshift of the lens, the strongest limits will be on the Hubble parameter, H_0. In order to estimate H_0 to within 10%, the time delay of the system must be measured accurately, with a precision of 5% or less. Much of the thesis work is centered around making the time delay measurement. An important part of this goal is confirmation of the optical time delay (Kundić *et al.* 1997), and resolution of the discrepancy between the radio and optical observations. Another part of the goal is to clarify the statistical analysis issues, necessary to make an accurate measurement and understand any systematic effects in the results. In order to make the cosmological measurement, the time delay must be combined with a good model of the lens mass distribution, and thus the thesis includes a comparative evaluation of current models in the literature.

A secondary goal of this thesis is to use the large and unique data set produced by the monitoring to determine other scientific information besides the time delay. This includes information about the size of the emission region, the cause of the variability, and the path traversed by the light from the two images between the source and observer.

1.3 Radio Interferometry

This section is a basic introduction to radio interferometry, intended to provide background for Chapter 3. For more information, consult "Synthesis Imaging in Radio Astronomy," eds. R.A. Perley, F.R. Schwab, & A.H. Bridle (1989), and "Interferometry and Synthesis in Radio Astronomy" by A.R. Thompson, J.M. Moran, G.W. Swenson, Jr. (1994). All of the radio interferometric data in this thesis were reduced using the Astronomical Image Processing System (AIPS), distributed by the National Radio Astronomy Observatory.

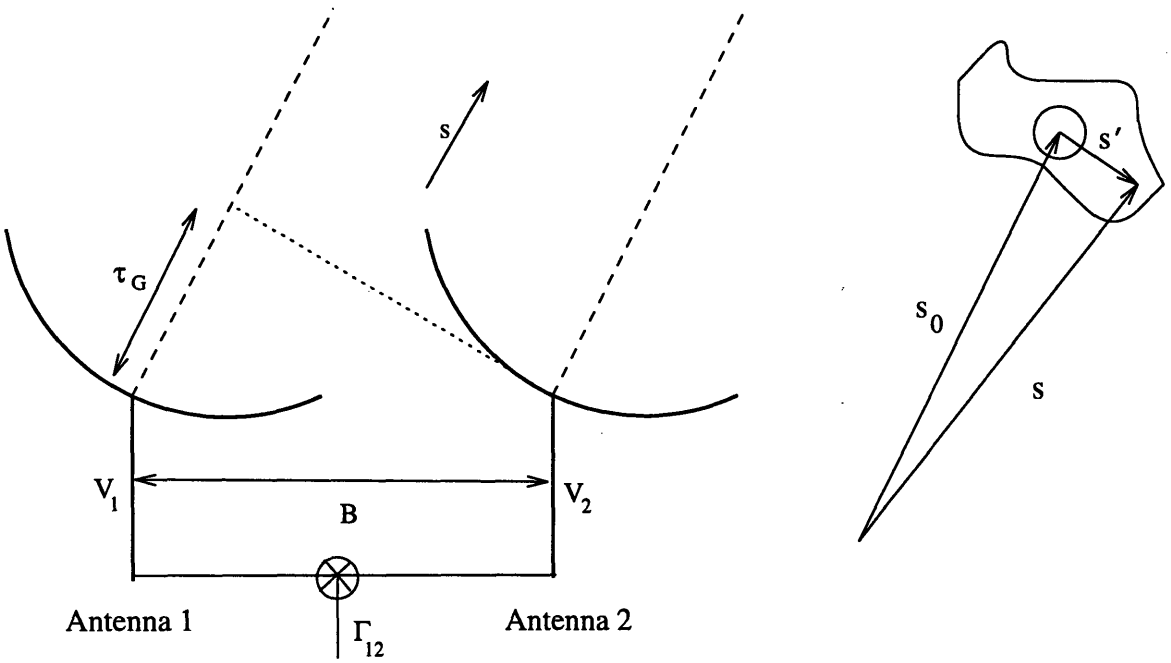

Figure 1-1: The two-element interferometer.

1.3.1 The Two-Element Interferometer

To understand the synthesis of an image from a large array of antennas, it is helpful to first consider a two-element interferometer.

Assume that a coherent monochromatic plane wave travels from the source to the two antennas. Referring to Figure 1-1, the position of the source is $\vec{s}$, while the position of the phase tracking center is $\vec{s}_0$. We define $\vec{s}'$ as the two-dimensional vector on the sky between the tracking center and the source, such that

$$\vec{s} = \vec{s}_0 + \vec{s}'. \tag{1.1}$$

We will use the coordinates (l, m, n) for the sky and (u, v, w) for the ground. In this coordinate system, these quantities can be written as $\vec{s}' = (l, m, 0)$ and $\vec{s}_0 = (0, 0, 1)$, and thus, $\vec{s} = (l, m, 1)$.

The distance between the two antenna elements is called the baseline $\vec{B}$, and is written in (u, v, w) coordinates. The baseline is usually measured in units of the wavelength. As

can be seen in the figure, there is a delay between the arrival of the plane wave at Antenna 1 and Antenna 2. This is the geometric delay t_G, which is simply equal to the extra light travel path divided by c,

$$t_G = \frac{\vec{B} \cdot \vec{s}}{c}. \tag{1.2}$$

The voltage measured at Antenna 2 is simply the sinusoid of the incoming plane wave,

$$V_2 = Ae^{i2\pi\nu t}, \tag{1.3}$$

where ν is the observing frequency. The voltage at Antenna 1 is similar, but includes the geometric delay, thus

$$V_1 = Ae^{i2\pi\nu(t-t_G)}. \tag{1.4}$$

Note that the geometric delay causes only a phase shift, and the amplitude of the signal is the same for both antennas.

The signals are multiplied together at the correlator and time averaged, producing the "visibility" for the baseline:

$$\Gamma_{12} = V_1 V_2^* = A^2 e^{i2\pi\nu[(t-t_G)-t]} = A^2 e^{-i2\pi\nu t_G}. \tag{1.5}$$

Thus, the geometrical delay causes a sinusoidal pattern, or fringes, in the observed visibility. The source moves through the fringes as it moves across the sky. The width of these fringes is much narrower than the beam of one of the antennas alone, and the resolution improves as the baseline increases.

For a point source, the visibilities are constant in amplitude and phase once the geometrical delay is removed. For an extended source, the visibility is an integral over the source,

$$\Gamma(u,v) = \int I_\nu(\vec{s}) e^{-i\frac{2\pi\nu}{c}\vec{B}\cdot\vec{s}} dldm, \tag{1.6}$$

where $I_\nu(\vec{s})$ is the intensity of emission from the source at observing frequency ν and position $\vec{s}$.

If we write $\vec{b} \cdot \vec{s} = ul + vm + w$, and write (u,v,w) in units of the observing wavelength,

then

$$\Gamma(u,v) = e^{-i2\pi w} \int I_\nu(l,m) e^{-i2\pi(ul+vm)} dl dm. \tag{1.7}$$

The exponential term in front of the integral is the fringe pattern of the phase tracking center $\vec{s}_0$. This is removed online at the VLA, "stopping" the fringes. Thus, the measured visibility Γ is related to the two-dimensional Fourier transform of the sky emission $I_\nu(l,m)$, and vice versa

$$I_\nu(l,m) = \int \Gamma(u,v) e^{+i2\pi(ul+vm)} du dv. \tag{1.8}$$

The above discussion is somewhat idealized. The visibility actually measured is Γ multiplied by the sampling function, $\mathcal{S}$, in the (u,v) plane. $\mathcal{S}$ is equal to 1 where a measurement of Γ is made, and 0 everywhere else. Its Fourier transform is the synthesized beam for the array, or the "dirty beam":

$$D(l,m) = \int \mathcal{S}(u,v) e^{+i2\pi(ul+vm)} du dv. \tag{1.9}$$

The dirty beam is related to the dirty image by a convolution $(*)$ with the true emission:

$$I_\nu^{dirty} = I_\nu * D. \tag{1.10}$$

Finally we have

$$\mathcal{S}(u,v)\Gamma(u,v) = \int I_\nu^{dirty}(l,m) e^{-2\pi i(ul+vm)} dl dm. \tag{1.11}$$

and

$$I_\nu^{dirty}(l,m) = \int \mathcal{S}(u,v)\Gamma(u,v) e^{+2\pi i(ul+vm)} du dv. \tag{1.12}$$

Thus the image obtained from the Fourier transform of the visibilities is the "dirty" image, which must be deconvolved from the dirty beam D to obtain the true image $I_\nu(l,m)$ (see §1.3.4).

The whole line of reasoning can be generalized from a two-antenna system to an array of N_a antennas. There are $N_a(N_a-1)/2$ pairs of antennas, or baselines, in such an array, covering many values of (u,v) in the sampling function $\mathcal{S}(u,v)$. This gives much more information to the two-dimensional Fourier transform and a better image of the true emission

$I_\nu(l,m)$.

1.3.2 Calibration of the Antenna Gains

The dominant source of error in the measured visibilities is due to the antenna-based gains in both amplitude and phase. These gains need to be found and removed from the data, using observations of a phase calibrator source and a flux calibrator source.

The flux calibrator is used to set the overall flux level of the observation. It must be non-varying and of well-known flux density, and bright enough to detect in a short observation (a few minutes). Ideally, the flux calibrator will also be point-like, so that the Fourier transform of the source emission is simply a constant across the array. If it is not point-like, however, it is still possible to use it for flux calibration, as long as a model of the structure is included in the calibration, or the calibration is limited to an appropriate range of baseline lengths (such that the source emission is constant in that range).

The phase calibrator is used to set the phase gains of the antennas, particularly as they change in time due to atmospheric and instrumental effects. The phase calibrator must be point like, so that the astronomical emission is constant in amplitude and phase for all antennas. Also, the phase calibrator should be near the program source on the sky and bright enough to detect in a short scan. The flux density of the phase calibrator may vary, as long as it does not vary more quickly than observations of the flux calibrator.

To make use of these calibrator observations, we assume that the observed visibility is simply the antenna-dependent gains multiplied by the true visibility. This ignores baseline-dependent gains, and gains independent of the true visibility (such as offsets and noise in the instruments). These are reasonable assumptions for initial VLA calibration. The observed visibility is then

$$\tilde{\Gamma}_{ij} = g_i g_j^* \Gamma_{ij} \tag{1.13}$$

where $\tilde{\Gamma}_{ij}$ is the measured complex visibility, Γ_{ij} is the true complex visibility, and g_i is the complex gain for antenna i (for convenience, the time dependence of each of the terms is not shown in the notation).

Writing the complex numbers in terms of amplitudes and phases, we have

$$\tilde{A}_{ij}e^{i\tilde{\vartheta}_{ij}} = a_i e^{i\phi_i} a_j e^{-i\phi_j} A_{ij} e^{i\vartheta_{ij}}, \tag{1.14}$$

where $\tilde{A}_{ij}$ and $\tilde{\vartheta}_{ij}$ are the amplitude and phase of the observed visibility, A_{ij} and ϑ_{ij} are the amplitude and phase of the true visibility, and a_i and ϕ_i are the amplitude and phase of the gain for antenna i. For a point source, the true phase, ϑ_{ij}, is the same for all baselines and can be set to zero. If the point source is of known amplitude S, the true amplitude can be set $A_{ij} = S$. Then we have

$$\begin{aligned} \tilde{A}_{ij} &= a_i a_j S \\ \tilde{\vartheta}_{ij} &= \phi_i - \phi_j \end{aligned} \tag{1.15}$$

For N_a antennas, these are $N_a(N_a - 1)$ equations, which can be solved for the $2N_a$ unknown values of a_i and ϕ_i. The AIPS task CALIB solves these equations to find a_i and ϕ_i for each antenna.

1.3.3 Mapping

After calibration of the antenna gains, a map of the source can be made. This is done by applying the Fourier transform described in §1.3.1. The AIPS routines that produce the map offer two options for performing the transform. The first is the Direct Fourier Transform (DFT), which performs the FT directly on each visibility measurement. The second option is to grid the data first, then perform a Fast Fourier Transform. The DFT is more accurate, but can be much slower than the gridding method, especially for large data sets.

Another choice to be made when mapping is how to weight the data in the (u, v) plane (hereafter referred to as UV data). "Natural" weighting simply assigns each visibility the same weight; all are included equally. This gives the best sensitivity in the final map. "Uniform" weighting reduces the sensitivity but improves the resolution of the beam by giving each *section* of the UV plane a similar weight. This means that in regions where the sampling is more dense, particularly the central part of the UV plane, the individual visi-

bilities will be down-weighted. This improves the resolution by giving the longer baselines in the outer portion of the UV plane more weight. There are many more ways to customize the beam pattern besides natural and uniform weighting, such as tapering the weights on the outer UV plane, and by not including portions of the UV plane. Briggs (1995) has characterized and improved these options with the "robust" parameter in the AIPS task IMAGR, allowing beam shapes nearly as narrow as uniform weighting but without the deep sidelobes that usually accompany it.

1.3.4 Deconvolution

The initial "dirty" map of the source is corrupted by the sparse sampling of the UV plane. Since each source is effectively multiplied by the dirty beam pattern, the map is confused and faint source emission is obscured. These effects can be removed through deconvolution of the beam pattern and the image. There are several deconvolution algorithms available, including CLEAN, Maximum Entropy Methods, and Non-Linear Least Squares. The VLA data in this thesis were deconvolved with the CLEAN algorithm.

The basic CLEAN algorithm was created by Högbom (1974). The central concept is to select a bright point in the map, then subtract a fraction of its flux density multiplied by the dirty beam. Iteration of this procedure gradually subtracts all the emission out of the map. The location and flux density of each bright point (called a "clean component") is recorded, and the set of these becomes a point source model of the emission. To create the CLEANed map, each clean component is multiplied by a "clean beam" (a Gaussian fit to the center of the dirty beam) and added to the residuals of the dirty map.

A more sophisticated version of CLEAN was developed by Clark (1980), Cotton, and Schwab (1984). Steps 2 through 5 below are the minor cycle, and Steps 2 through 8 are the major cycle.

1. Perform a Fourier transform on the visibility data to create the dirty map.
2. (Minor cycle) Select the brightest point in specified regions (clean boxes) of the dirty map.
3. (Minor cycle) Multiply together: the flux density of the selected point, the loop gain

(a fraction between zero and one), and the inner portion of the dirty beam (out to its first sidelobe).

4. (Minor cycle) Subtract this from the dirty map.

5. (Minor cycle) If there are still pixels in the clean boxes with flux density above a specified limit, return to step 2. If not, continue to step 6.

6. Fourier transform the point source model (the CLEAN components) to the UV plane, and subtract it from the UV data.

7. Use the result of step 6 to create an updated version of the dirty map.

8. If the iteration limit has been reached, continue to step 9. If not, return to step 2.

9. Convolve the final point source (clean component) model with the clean beam. Add this to the residuals left from step 7 to make the clean map.

There are many parameters that affect CLEAN's performance, including the clean boxes, the loop gain, the iteration limits for the minor and major cycles, and the weighting of the UV data in the Fourier transform. CLEAN generally converges, but the resulting map is non-unique (different parameters can give different results for the same data). Cleaning with small loop gain, tight clean boxes, and many iterations avoids creating artifacts in the map but also requires more processing time.

1.3.5 Self-Calibration

After the map has been cleaned, it will generally be far from the thermal noise limit of the observation (see §1.3.6). The map can be improved through self-calibration. This is used to remove antenna-based gain errors that change more rapidly than the time between phase calibration. It is very similar to the antenna gain calibration (§1.3.2), and CALIB is used to solve the antenna gain equations (eq. 1.15). The differences are that in this case, instead of using a point source of known flux density, the self-calibration algorithm compares the observed visibilities to a model of the source emission. This model is often found from the clean components obtained during deconvolution. Another important difference is that the

gain errors are assumed to be just in phase, not amplitude, since the rapid changes due to the atmosphere are primarily in the phase information. When self-calibration is performed on the visibilities, the absolute position information for the source is lost, since a position shift (change in $\vec{s}'$ above) corresponds to a simple phase shift.

1.3.6 Error Estimation

Once the data have been self-calibrated and deconvolved, astronomical information about the map can be determined. For this thesis, an accurate measurement of the flux density of the point images is desired, along with an estimate of its uncertainty.

Unless the CLEAN deconvolution is unconstrained, the RMS noise in the map cannot be smaller than the thermal noise due the system temperature. The system temperature refers to white Gaussian noise added to the signal from various sources. This is primarily thermal noise in the receiver, but also includes emission from the cosmic microwave background, the Galaxy background, and thermal noise from the ground, attenuators, and feeds (Crane & Napier 1989).

For an array of N_a identical antennas, each with system temperature T_{sys} and effective antenna area A_e, the RMS noise in a natural-weighted image of a point source at the center of the map is

$$\Delta I_m = \frac{2k_B T_{sys}}{\eta_c A_e \sqrt{N_a(N_a-1)t_{obs}\Delta\nu}}, \tag{1.16}$$

where k_B is the Boltzmann constant, η_c is the correlator efficiency, $\Delta\nu$ is the total bandwidth, and t_{obs} is the total observing time (Crane & Napier 1989).

The expression can also be written in terms of the System Equivalent Flux Density (SEFD), which is a measurement of overall sensitivity in units of Janskys:

$$\text{SEFD} = \frac{2k_B T_{sys}}{A_e}. \tag{1.17}$$

Then the thermal noise can be written (Walker 1995)

$$\Delta I_m = \frac{\text{SEFD}}{\eta_c \sqrt{N_a(N_a-1)t_{obs}\Delta\nu}}. \tag{1.18}$$

These expressions assume that the map has been made using natural weighting (§1.3.3). The thermal noise will be larger when using other weighting schemes. Note that the Gaussian noise is inversely proportional to the square root of observing time, and the square root of bandwidth. Reducing the thermal noise requires increasing the bandwidth, observing time, or both.

There are several types of noise and error that are not Gaussian, and thus not included in T_{sys} or the SEFD. These include radio frequency interference and gain calibration errors (*e.g.* gains that don not fit the assumptions of §1.3.2). In addition, the self-calibration and deconvolution algorithms give non-unique solutions and are non-linear, so it is impossible to track uncertainties from the raw visibility data to the final image. The results of the deconvolution routine are also heavily dependent on the sampling $\mathcal{S}$ of the UV plane and the structure of the source emission.

Although there is no way to determine analytically the errors in the final image, besides the lower limit of the thermal RMS, there are several ways to estimate it. The RMS noise in the background of the image, far from any true emission, is one indicator. This number can be compared with the theoretical sensitivity to determine whether more self-calibration and deconvolution would improve the map. The error reported by the AIPS task JMFIT when fitting a Gaussian to a feature and determining its flux density is another indicator. Experience shows that both of these indicators significantly underestimate the error in the measured flux density of a feature. Another technique is to break the data set into segments in time, and repeat the analysis on each segment individually. The scatter in the values found from the segments is then an indicator of uncertainty. Finally, Moore (1996) determined the systematic errors due to deconvolution and self-calibration by running Monte Carlo simulations of the visibility data. A model of the source and measurement noise was created in the UV plane, using the same sampling $\mathcal{S}$ of the real observations, and the data sent through the same reduction program. Moore found a systematic offset of the final image flux density that significantly exceeded the error estimated using other methods. This technique is computationally intensive, so it was not attempted on the light curves for this thesis. See §3.4 for determination of errors in the thesis data.

Chapter 2

Gravitational Lenses and Cosmology

2.1 Gravitational Lensing

In 1915, Einstein suggested that the deflection of light by a massive body would be an observable effect of his theory of general relativity (1915). Later, Einstein calculated the deflection of light from one star by another and noted that the separation of the images would make them nearly impossible to resolve (1936). Zwicky (1937) pointed out, however, that if the lens is much more massive, such as a *nebulae* or galaxy, the multiple images could have observable separations. A few decades later, the subject was reopened with papers further developing the theory (Liebes 1964; Refsdal 1964a). Refsdal (1964b, 1966) discussed potential applications of lenses, including the use of the time delay to probe cosmological quantities. Bourassa & Kantowski (1973, 1975) were the first to explore lens mass distributions that are not spherically symmetric. Press & Gunn (1973) discussed the possibility of identifying lenses by the similar, but delayed, variations in the multiple images of a varying source. A few years later, Cooke & Kantowski (1975) gave a general expression for the time delay between multiple images, showing the geometrical and gravitational contributions to the delay. For a more detailed account of the history of gravitational lensing, see Schneider, Ehlers, & Falco (1992).

This chapter reviews the basic features of gravitational lensing, with an emphasis on

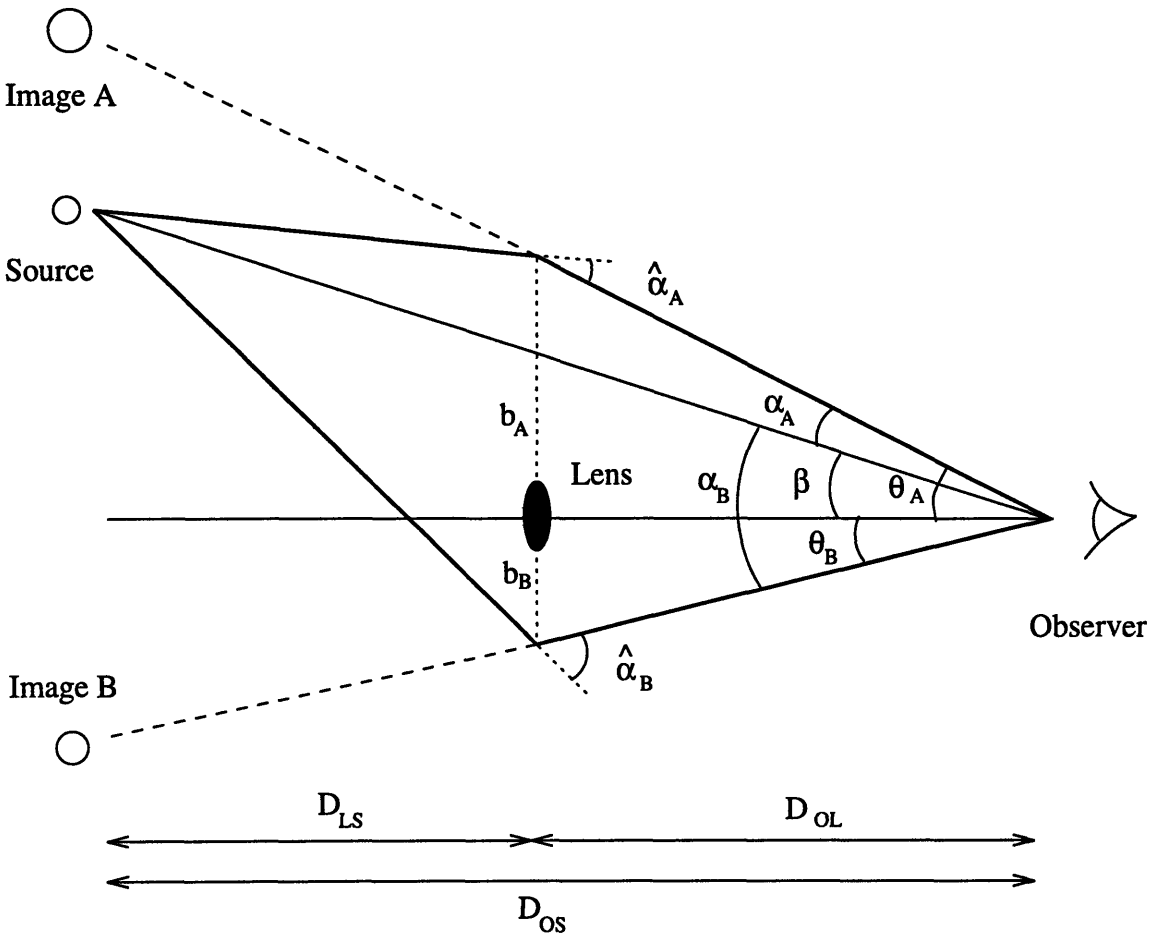

Figure 2-1: Gravitational lens geometry.

time delays and their use in cosmology. The notation is based primarily on the lectures by Narayan & Bartelmann (1996). For further information on lensing theory and observations, see the book by Schneider, Ehlers, & Falco (1992), the proceedings of IAU Conference 173 (1996) and the review articles by Blandford & Narayan (1992), Blandford & Kundić (1996), and Schneider (1996).

2.1.1 Geometry

Figure 2-1 shows the basic geometry of gravitational lensing. Light from a source at position $\vec{\beta}$ is bent as it passes near a massive object, the lens, with an impact parameter $\vec{b}_i$. The light is bent by an angle $\vec{\hat{\alpha}}_i$, and the observer sees the image i at position $\vec{\theta}_i$, an

angular distance $\vec{\alpha}_i$ from the source position $\vec{\beta}$. The angles $\vec{\beta}$, $\vec{\theta}_i$, and $\vec{\alpha}_i$ are two-dimensional positions on the sky, where $\vec{\beta}$ and $\vec{\theta}_i$ are defined with respect to the position of the lens, and $\vec{\alpha}_i$ is defined with respect to the position of the source. The distance $\vec{b}_i$ is a two-dimensional linear distance from the lens in the lens plane. (The radial three-dimensional distance from the lens will be written as $\vec{r}$.) When the directional information is not important, the scalar length of these vectors will be written as $\beta, \theta_i, \alpha_i, \hat{\alpha}_i, b, r$, etc.

The distance from the observer to the lens is D_{OL}, from the lens to the source is D_{LS}, and from the observer to the source is D_{OS}. These distances and angles can be related by the *lens equation*,

$$D_{OS}\vec{\theta}_i = D_{OS}\vec{\beta} + D_{LS}\vec{\hat{\alpha}}_i, \tag{2.1}$$

which can also be written

$$\vec{\theta}_i = \vec{\beta} + \vec{\alpha}_i. \tag{2.2}$$

These expressions follow simply from the geometry of the angles and distances in Figure 2-1 (using the small angle approximation and assuming that the distances are angular diameter distances, see §2.2). Note that the bending angle $\vec{\hat{\alpha}}$ and the effective bending angle $\vec{\alpha}$ are related by

$$\vec{\alpha}_i \equiv \frac{D_{LS}}{D_{OS}}\vec{\hat{\alpha}}_i. \tag{2.3}$$

It is also useful to define the effective distance of the lens,

$$D_{\rm eff} \equiv \frac{D_{OL}D_{OS}}{D_{LS}}. \tag{2.4}$$

The bending angle $\vec{\hat{\alpha}}$ is the integral of the gradient of the gravitational potential of the lens

$$\vec{\hat{\alpha}}(\vec{b}) = \frac{2}{c^2}\int \vec{\nabla}\Phi(\vec{b}, s)ds, \tag{2.5}$$

where the integral is taken along the ray path s, and $\Phi(\vec{b}, s)$ is the 3-dimensional Newtonian gravitational potential, defined to be zero at infinite distance from the lens. The effective bending angle $\vec{\alpha}$ can be written as

$$\vec{\alpha}(\vec{b}) = \vec{\nabla}\psi(\vec{b}), \tag{2.6}$$

where $\psi(\vec{b})$ is the 2-dimensional scaled surface potential, defined as

$$\psi(\vec{b}) \equiv \frac{2}{c^2 D_{\rm eff}} \int \Phi(\vec{b}, s) ds, \tag{2.7}$$

where the integral is again along the line of sight. ψ is also called the effective potential.

The lens equation (eqs. 2.1 and 2.2) has multiple solutions which correspond to the multiple images of the source. Multiple images are formed when the surface mass density $\Sigma(\vec{b})$ of the lens exceeds the critical surface mass density,

$$\Sigma_{cr} \equiv \frac{c^2}{4\pi G} \frac{D_{OS}}{D_{LS} D_{OL}}. \tag{2.8}$$

The surface potential ψ is related to the surface mass density by

$$\nabla^2 \psi(\vec{b}) = 2 \frac{\Sigma(\vec{b})}{\Sigma_{cr}}. \tag{2.9}$$

If the observer, lens, and source are co-linear (*i.e.* the source is directly behind the lens), then the source position $\vec{\beta}$ is zero, and the solution to the lens equation is simply $\vec{\theta}_i = \vec{\alpha}_i$ for all images i. This solution is defined as the Einstein radius $\vec{\theta}_E$, so named because all images appear at the same angular distance from the lens, in an "Einstein ring." Even if the source and lens are not aligned, the Einstein radius is a useful quantity for parameterizing the strength and geometry of the lens.

Comparison to optical lensing

This gravitational phenomenon is called "lensing" because of its similarities with an ordinary optical lens. In both cases, images can be magnified or inverted, and the thin lens approximation is used. In the gravitational case, the effect on the light (in the limit of a weak gravitational field) can be described in terms of an index of refraction n_r, where

$$n_r = 1 - \frac{2\Phi}{c^2}. \tag{2.10}$$

Since Φ is negative, n_r is greater than 1. Just as in an optical lens, this means that light will bend toward the potential well, and will travel more slowly in the potential than in

free space. An important difference is that optical lenses are usually carefully shaped to focus an image at the observer, whereas the potential of a gravitational lens is due to the astronomical system and in general creates multiple distorted images. Gravitational lensing is actually more analogous to a mirage on the horizon, where the distortions and multiple imaging are due to the changing index of refraction in the atmosphere. In fact, the French refer to the phenomena as "gravitational mirages."

2.1.2 Magnification

An important aspect of gravitational lensing is the magnification of the images. As the ray from the source is bent by the lens, its angular size is magnified or demagnified. Since surface brightness of the ray is conserved (this is true whenever there is no absorption or emission), this causes a brightening or dimming of an unresolved source. Although the flux density in the direction of the observer might increase, it will decrease in other directions, so that the total luminosity of the source is always conserved when the emission is integrated over all directions.

The magnification of an image i compared to the unlensed case is defined to be the derivative of the image position with respect to the source position,

$$\mathsf{M}_i \equiv \frac{\partial \vec{\theta}_i}{\partial \vec{\beta}}. \tag{2.11}$$

M is a two-dimensional matrix, because $\vec{\theta}_i$ and $\vec{\beta}$ each have two dimensions on the sky. The matrix is symmetric. For an image i of a point source, the increase in flux density is the absolute value of the determinant of M_i. If the absolute value of $|\mathsf{M}_i|$ is less than 1 (where vertical bars indicate the determinant), the image is demagnified; if it is greater than 1, the image is magnified. If $|\mathsf{M}_i|$ is positive, the image is upright; if it is negative, the image is inverted.

Since we do not see the unlensed source, the magnification matrix can not be measured. We can only measure the relative magnification matrix between images i and j,

$$\mathsf{M}_{ij} = \mathsf{M}_i \mathsf{M}_j^{-1} = \frac{\partial \vec{\theta}_i}{\partial \vec{\theta}_j}. \tag{2.12}$$

This matrix is generally non-symmetric, so it includes four unique observables. All four can be determined from a good observation of an extended source. For a point source, only the relative magnification, the determinant $|\mathsf{M}_{ij}|$, can be measured.

2.1.3 Lens Potentials

The lensing mass may take on a variety of geometries. This section describes a few basic lens potentials; lens potentials used for 0957+561 are discussed in §6.2.

Point Mass

The point mass distribution is simply a mass M confined to a point. The effective lensing potential can be written

$$\psi(\theta) = \frac{D_{LS}}{D_{OL}} \frac{4GM}{c^2} \frac{\ln\theta}{D_{OL}}. \tag{2.13}$$

The effective bending angle of the point mass is then

$$\alpha(b) = \frac{D_{LS}}{D_{OS}} \frac{4GM}{c^2 b} \tag{2.14}$$

and the Einstein radius is

$$\theta_E = \sqrt{\frac{4GM}{c^2 D_{\rm eff}}}. \tag{2.15}$$

Note that the bending angle increases with the mass of the lens, and is inversely proportional to the impact parameter b. This is typically the case for all lens mass distributions.

For a source inside the Einstein radius ($\beta < \theta_E$), one inverted demagnified image will be seen inside the Einstein radius, and one upright magnified image outside,

$$\vec{\theta}_{\pm} = \frac{1}{2}\left(\vec{\beta} \pm \sqrt{\beta^2 + 4\theta_E^2}\right). \tag{2.16}$$

The magnification of each image relative to the unlensed source is

$$|\mathsf{M}|_{\pm} = \frac{q^2+2}{2q\sqrt{q^2+4}} \pm \frac{1}{2} \tag{2.17}$$

where $q = \beta/\theta_E$. As a source moves further from the lens, the inner image becomes fainter

and the magnification of the outer image goes to unity.

Singular Isothermal Sphere (SIS)

The singular isothermal sphere is described by one parameter, the line of sight velocity dispersion σ (different from the 3-dimensional velocity dispersion σ_{3D}.) In this potential, the velocity dispersion is a constant, independent of the distance from the center of the potential. The SIS is typically used to describe a galaxy, where the velocity dispersion is of the stars in the galaxy. The mass distribution of the SIS is

$$\rho(r) = \frac{\sigma^2}{2\pi G r^2}, \tag{2.18}$$

where $\rho(r)$ is the three-dimensional mass density as a function of radius r. The mass density is infinite at the center of the lens, hence the name "singular." The effective potential of the lens is

$$\psi(\theta) = \frac{D_{LS}}{D_{OS}} \frac{4\pi\sigma^2}{c^2} \theta, \tag{2.19}$$

and the effective bending angle is

$$\alpha = \frac{D_{LS}}{D_{OS}} \frac{4\pi\sigma^2}{c^2}. \tag{2.20}$$

Note that both the potential and the bending angle are independent of the impact parameter b, and are described by a single parameter σ. The Einstein radius for the SIS is just

$$\theta_E = \alpha. \tag{2.21}$$

If the source is inside the Einstein radius ($\beta < \theta_E$), two images appear at

$$\vec{\theta}_{\pm} = \vec{\beta} \pm \vec{\theta}_E \tag{2.22}$$

(with the "-" image inside the Einstein radius, inverted and demagnified). If the source is outside the Einstein radius ($\beta > \theta_E$) then one image will be present at $\vec{\theta} = \vec{\beta} + \vec{\theta}_E$. The

magnifications of the two images is

$$|\mathsf{M}|_{\pm} = \frac{\theta_{\pm}}{\beta} = \left(1 \mp \frac{\theta_E}{\theta_{\pm}}\right)^{-1}. \tag{2.23}$$

Isothermal Sphere with Core Radius

In this potential, the isothermal sphere is "softened" so that the mass density is not infinite at the center. The core radius is defined such that interior to that radius the surface mass density $\Sigma(\theta)$ is constant. The core radius is written as $\vec{\theta_c}$ in angular units, and $r_c = \theta_c D_{OL}$ in linear units. The effective potential is then

$$\psi(\theta) = \frac{D_{LS}}{D_{OS}} \frac{4\pi\sigma^2}{c^2} \sqrt{\theta_c^2 + \theta^2}, \tag{2.24}$$

and the effective bending angle is

$$\alpha(\theta) = \frac{D_{LS}}{D_{OS}} \frac{4\pi\sigma^2}{c^2} \frac{\theta}{\sqrt{\theta_c^2 + \theta^2}}. \tag{2.25}$$

The addition of a core radius to an isothermal sphere decreases the bending angle when the impact parameter is less than the core radius ($\theta < \theta_c$). The multiple imaging is similar to that of the singular isothermal sphere, except that there is a strongly demagnified image near the lens position. This third image does not appear in SIS because the singularity of the mass causes it to be infinitely demagnified.

Constant Density Sheet

Often a lens galaxy is part of a cluster of galaxies, and the cluster contributes to the lensing potential. If the cluster mass density is constant in the region of multiple imaging, it can be modeled as a sheet of constant surface density Σ. The sheet is characterized by its convergence, κ, defined as

$$\kappa = \frac{\Sigma}{\Sigma_{cr}}. \tag{2.26}$$

Since the surface density Σ cannot be negative, we know that κ is always > 0. The mass distribution is then $\Sigma(\theta) = \kappa\Sigma_{cr}$, the effective potential is

$$\psi(\theta) = \frac{\kappa}{2}\theta^2, \tag{2.27}$$

and the effective bending angle is

$$\alpha(\theta) = \kappa\theta. \tag{2.28}$$

The convergence causes an isotropic focusing of the images and an increase in the time delay for each (see §2.3.1).

Shear

If a cluster is not a constant density, it can often be characterized by two parameters, the convergence κ and the shear γ. The shear describes a change in surface density in a particular direction. Adding shear to a lens model is a way of breaking the circular symmetry and creating an elliptical potential. The effective potential could be written

$$\psi(\vec{\theta}) = \frac{\kappa}{2}(\theta_{xcl}^2 + \theta_{ycl}^2) + \frac{\gamma}{2}(\theta_{xcl}^2 - \theta_{ycl}^2) \tag{2.29}$$

where the vector $\vec{\theta}$ has components θ_{xcl} and θ_{ycl} along the major and minor axes of the cluster.

Ellipse

The above lens potentials (with the exception of shear) are all circularly symmetric, a case which is easy to study analytically but not typically true of astronomical lenses. Smooth lenses with circular symmetry are capable of producing at most three images of a source, and the lens, source, and images appear along a straight line in the sky. To study realistic astronomical lensing (asymmetric, with more than three images) we need to consider elliptical lenses.

There are several ways to create a lens with elliptical, rather than circular, symmetry. One is to add a sheet of matter with shear, as shown above. Another is to model the lens

with elliptical isodensity contours. In this case, the surface mass density is

$$\Sigma(\vec{\theta}) = \frac{\Sigma_0}{\sqrt{\theta_c^2 + (1-\epsilon)\theta_x^2 + (1+\epsilon)\theta_y^2}} \tag{2.30}$$

where ϵ is the ellipticity, and $\vec{\theta}$ has components θ_x, θ_y along the major and minor axis of the lens. Unfortunately the corresponding expressions for the potential and the bending angle are complicated, especially if the core radius θ_c is non-zero. A third alternative is to model the lens with elliptical contours in the effective potential. One way to write the elliptical potential is

$$\psi(\vec{\theta}) = \frac{D_{LS}}{D_{OS}} \frac{4\pi\sigma^2}{c^2} \sqrt{\theta_c^2 + (1-\epsilon)\theta_x^2 + (1+\epsilon)\theta_y^2}. \tag{2.31}$$

Section §6.2.3 gives another expression for an elliptical potential. Unfortunately, for large ellipticities, an elliptical potential corresponds to "peanut" shaped mass density contours, but for small ϵ it is a reasonable mass model and has a simple expression for the bending angle.

2.2 Cosmological Distances

The distance to an object at high redshift is dependent on cosmological parameters (H_0, Ω_0, and Λ_0), and on how the distance is measured. Two main types of distances, "angular diameter" and "luminosity," are defined below. The distances in Figure 2-1 and eqs. 2.1 and 2.2 are angular diameter distances. Note that for a lens and source at high redshift, D_{OS} is not in general equal to $D_{OL} + D_{LS}$, despite the appearance of Figure 2-1.

We define $\lambda_0 \equiv \Lambda_0/3H_0^2$ as a dimensionless expression for the cosmological constant Λ_0, comparable to Ω_0. A flat universe corresponds to $\Omega_0 + \lambda_0 = 1$. Inflationary theory predicts a flat universe, but observations indicate that Ω_0 (the ratio of the universe mass density to the critical mass density) is a few tenths, thus non-zero values of cosmological constant are being considered.

2.2.1 Angular Diameter Distance, Filled-Beam

The angular diameter distance D^A is found by comparing the linear size of an object to its apparent angular size. D^A depends not only on the mass density of the universe as a whole, but on whether the universe is homogeneous or clustered, which determines how much mass lies along the ray path. In this section we consider the standard "filled-beam" distance. This expression for the distance makes the assumption that matter is smoothly distributed in the universe, rather than clumped.

If $\Omega_0 > 0$ and $\lambda_0 = 0$ the filled-beam angular diameter distance between objects at redshifts z_1 and z_2 is

$$D^A(z_1, z_2) = \frac{2c}{H_0} \frac{(1 - \Omega_0 - \sqrt{1+\Omega_0 z_1}\sqrt{1+\Omega_0 z_2})(\sqrt{1+\Omega_0 z_1} - \sqrt{1+\Omega_0 z_2})}{\Omega_0^2(1+z_1)(1+z_2)^2}. \quad (2.32)$$

This equation can be simplified by assuming object 1 is the observer, at redshift $z_1 = 0$, giving

$$D^A(0, z) = \frac{2c}{H_0} \frac{(1 - \Omega_0 - \sqrt{1+\Omega_0 z})(1 - \sqrt{1+\Omega_0 z})}{\Omega_0^2(1+z)^2}. \quad (2.33)$$

If $\Omega_0 = 0$ and $\lambda_0 = 0$, the filled-beam angular diameter distance is (Fukugita *et al.* 1992)

$$D^A(z_1, z_2) = \frac{c}{H_0(1+z_2)} \sinh\left[\ln\left(\frac{1+z_2}{1+z_1}\right)\right] \quad (2.34)$$

If $\lambda_0 + \Omega_0 = 1$ (a flat universe), the filled-beam angular diameter distance is (Fukugita *et al.* 1992):

$$D^A(z_1, z_2) = \frac{c}{H_0(1+z_2)} \int_{z_1}^{z_2} \frac{dz}{\sqrt{\Omega_0(1+z)^3 + \lambda_0}} \quad (2.35)$$

2.2.2 Angular Diameter Distance, Empty-Beam

The assumption that matter is smoothly distributed along the line of sight is not always a good one. Matter in the universe is clumped, so that the mass occurs mostly in galaxies and large scale structure that are not along the line of sight to the source. The angular diameter distance can be found assuming an "empty-beam," *i.e.* that no matter lies along the line of sight, as proposed by Dyer & Roeder (1972). For the same value of Ω_0, the empty-beam distance is larger than the filled-beam distance.

For all values of λ_0 and Ω_0, the empty-beam angular diameter distance is (Fukugita *et al.* 1992):

$$D^A(z_1, z_2) = \frac{c(1+z_1)}{H_0} \int_{z_1}^{z_2} \frac{(1+z)^{-2}\, dz}{\sqrt{\Omega_0(1+z)^3 + (1-\Omega_0-\lambda_0)(1+z)^2 + \lambda_0}} \tag{2.36}$$

2.2.3 Luminosity Distance

The luminosity distance D^L is found by comparing the intrinsic luminosity of an object to its apparent luminosity. The filled-beam luminosity distance for $\Omega_0 > 0$, $\lambda_0 = 0$, and $z_1 = 0$ is

$$D^L(0, z) = \frac{2c}{H_0} \frac{(1 - \Omega_0 - \sqrt{1+\Omega_0 z})(1 - \sqrt{1+\Omega_0 z})}{\Omega_0^2}. \tag{2.37}$$

Note that under these conditions, the luminosity and angular diameter distances can be related by

$$D^L = D^A(1+z)^2. \tag{2.38}$$

2.3 Time Delays and Cosmology

Gravitational lenses can be used to make several types of cosmological measurements. In this thesis, the time delay of a particular lens is used to determine H_0 for several possible cosmologies. For further information on time delays and cosmology, see Refsdal 1964b, Refsdal 1966, Blandford & Narayan 1986, Narayan 1991, and Blandford & Kundić 1996.

2.3.1 Time Delay Equation

Light in each image of a gravitational lens is delayed in its arrival time compared to its arrival time in the absence of the lens. This delay is due to two effects. The first is the increased path length of the ray, as can be seen in Figure 2-1. This geometrical delay can be written

$$\tau_{\rm geom}(\theta_i) = \frac{D_{\rm eff}(1+z_l)}{2c} \alpha_i^2. \tag{2.39}$$

The second effect is the "slowing" of the light as it passes through the gravitational potential, which is simply the Shapiro delay multiplied by $1 + z_l$ due to the redshifting of distant

sources,

$$\tau_{\rm grav}(\theta_i) = -\frac{2(1+z_L)}{c^3}\int \Phi(\theta_i, s)ds = -\frac{D_{\rm eff}(1+z_l)}{c}\psi(\theta_i). \tag{2.40}$$

Combining these together, we have the total delay for one image relative to the no-lens case

$$\tau_i(\theta_i) = \frac{D_{\rm eff}(1+z_l)}{c}\left[\frac{1}{2}\alpha_i^2 - \psi(\theta_i)\right]. \tag{2.41}$$

The time delay between two images is simply $\tau_i(\theta_i) - \tau_j(\theta_j) = \tau_{ij}$.

The time delay equation is surprisingly simple for a singular isothermal sphere lens. Using equations 2.19 and 2.20, and assuming $\kappa = 0$, we have

$$\tau_i^{SIS}(\theta_i) = \frac{D_{OL}(1+z_l)}{c}\frac{4\pi\sigma^2}{c^2}\left(\frac{1}{2}\left[\frac{D_{LS}}{D_{OS}}\frac{4\pi\sigma^2}{c^2}\right] - \theta_i\right), \tag{2.42}$$

so that the time delay between two images is

$$\tau_{ij}^{SIS} = \frac{D_{OL}(1+z_l)}{c}\frac{4\pi\sigma^2}{c^2}(\vec{\theta}_j - \vec{\theta}_i). \tag{2.43}$$

If the time delay has not been measured for a lens, it can be estimated with this equation by assuming the lens is SIS, plugging in the measured image positions, velocity dispersion, and lens redshift, and assuming a cosmology to find D_{OL} from z_l. This estimate is probably correct to within a factor of two. If the velocity dispersion has not been measured, the equation can be modified by using the fact that the image separation $\theta_i + \theta_j$ is twice the Einstein radius for SIS, and using equations 2.20 and 2.21 to obtain

$$\tau_{ij}^{SIS} = \frac{(1+z_l)}{c}\frac{D_{\rm eff}(\theta_j+\theta_i)}{2}(\theta_j - \theta_i) = \frac{D_{\rm eff}(1+z_l)}{2c}(\theta_j^2 - \theta_i^2) \tag{2.44}$$

An estimate of the time delay using this equation requires knowledge of the source redshift z_s to estimate the distances D_{OS} and D_{LS} in $D_{\rm eff}$.

Gorenstein *et al.* (1988b) showed that for lenses that include a cluster or other sheets of constant density matter, there is a fundamental degeneracy in the time delay between the convergence due to the cluster and the convergence due to the primary lens. The degeneracy is related to the fact that gravitational delay of a constant density sheet contributes to the

time delay with the same dependence on θ as the geometrical delay. If the mass of the primary lens is reduced by $(1-\kappa)$, and a constant density sheet with convergence κ is placed in front of it, the image positions $\vec{\theta}_i$, $\vec{\theta}_j$ and the relative magnification M_{ij} do not change, but the time delay does. The dependence of the time delay on the convergence can be expressed explicitly by writing

$$\tau_i(\theta_i) = \frac{D_{\rm eff}(1+z_l)}{c}(1-\kappa)\left[\frac{1}{2}\alpha_i^2 - \psi(\theta_i)\right], \tag{2.45}$$

where α and ψ are now the effective bending angle and potential found by modeling the system under the assumption that $\kappa = 0$.

The example of an SIS lens is again instructive. If a constant density sheet with convergence $\kappa = 0$ is placed in front of the lens, the time delay between two images becomes

$$\tau_{ij}^{SIS,CL} = \frac{D_{\rm eff}(1+z_l)}{2c}(1-\kappa)(\theta_j^2 - \theta_i^2), \tag{2.46}$$

or

$$\tau_{ij}^{SIS,CL} = \frac{D_{OL}(1+z_l)}{c}\frac{4\pi\sigma^2}{c^2}(\vec{\theta}_j - \vec{\theta}_i), \tag{2.47}$$

where σ is still the velocity dispersion of the lensing galaxy. Thus, if the velocity dispersion of the galaxy is not measured, the time delay is a function of $D_{\rm eff}$ and κ. If, however, the velocity dispersion of the galaxy is known, the degeneracy between the convergence of the galaxy and the cluster is broken, and the time delay is a direct measure of D_{OL} (see §2.3.3 for further discussion of what can be learned from a measurement of the time delay).

2.3.2 Time Delay Surface

It is useful to describe the multiple imaging and magnification properties of lensing in terms of the *time delay surface* (Blandford & Narayan 1986). The surface $\tau(\theta)$ is given by eq. 2.41. Note that the gradient of the term in brackets (*i.e.* $\nabla[\frac{1}{2}(\vec{\theta}-\vec{\beta})^2 - \psi(\vec{\theta})]$) is equivalent to the lens equation (eq. 2.2). This means that the gradient of the time delay at the location of an image (a solution to the lens equation) will be zero. Thus, the images occur at extrema or saddle points in the time delay surface.

Consider the two contributions to the delay (eqs. 2.39 and 2.40) separately. Without the lens, the gravitational delay is zero everywhere on the surface, and the geometric delay is at a minimum in the direction to the source. With the lens, the gravitational delay is a maximum at the position of the lens, and the minimum of the geometric delay has shifted away from the direction of the source. For a source nearly aligned with an elliptical lens, this results in a surface with two minima, a relative maximum, and two saddle points, which corresponds to five images.

The time delay surface can be used to determine the relative delay(s) between the images. The deepest minimum in the time delay surface corresponds to the image with the smallest travel time, thus intrinsic variations of the source will occur in this image first, followed by the image with the second deepest minimum in the surface, etc.

The curvature of the time delay surface determines the magnification of the image. If the curvature is small along a coordinate direction, the image is strongly magnified in that direction; if the curvature of the surface is large in another direction, the image magnification is small in that direction. The images at minima and maxima of the surface are upright, while the images at saddle points are inverted.

As the source is moved with respect to the lens, new extrema are formed or removed. As each extrema is formed, a new saddle point is also made, so two images are formed. When the source position is aligned such that an extrema has just been formed, the curvature of the surface is small, so the magnification is large and the two images are bright.

2.3.3 Cosmological Tests Using Time Delays

The time delay between two images of a gravitational lens gives important information about the angular diameter distances of the lens and the source. There is often a variety of other information available for a lens system, including the lens model, the velocity dispersion of the lens σ, the redshifts z_l and z_s, and assumptions about Ω_0, Λ_0, and H_0. Narayan (1991) outlines what results can be derived for various combinations of this information. Here we outline the results most interesting for the 0957+561 system.

A constant density sheet of matter gives ambiguity to a lens system. Narayan (1991) defines $\zeta(\sigma, \kappa)$ to be that function of the cluster convergence κ and the galaxy velocity

dispersion σ which is determined from modeling the lens system. A measurement of the velocity dispersion of the galaxy or the cluster is necessary to break the ambiguity within ζ, and thus within the time delay. The constant density sheet causes only an increase in time delay between images, but no other observable change.

In each of the following cases, it is assumed that the lens redshift and image positions have been measured, and that the lens potential, source position, and ζ have been modeled using the available constraints.

Measure z_s, τ_{ij}, assume no cluster. If there is no cluster of galaxies present, and no other sheets of dark matter along the line of sight, the convergence and shear are zero. Then the modeled value of ζ, combined with an estimate of D_{OS}/D_{LS} (made from the measured redshifts and assumptions about Ω_0 and λ_0), gives the velocity dispersion σ. This can be used in the time delay equation to measure the distance to the lens D_{OL}. This measurement of D_{OL} is dependent on the assumed values of Ω_0 and λ_0.

Measure z_s, τ_{ij}, with cluster. In the case of 0957+561, where a cluster of galaxies is part of the lens, the convergence and shear are non-zero and there is an ambiguity in the time delay. We know, however, that the cluster mass is positive, thus the convergence must be greater than zero. Thus a measurement of the source redshift and the time delay ultimately gives an upper limit on the velocity dispersion of the galaxy, which gives a lower limit on D_{OL}, again dependent on Ω_0 and λ_0.

Measure σ and τ_{ij}, with cluster. If there is a cluster and the galaxy velocity dispersion and time delay are both measured, then we have all of the necessary information to make a direct measurement of D_{OL}, rather than just set a limit. This value of D_{OL} is independent of the cluster convergence, the source redshift, and any assumptions about cosmology.

Measure z_s and σ, with cluster. If the velocity dispersion of the galaxy is measured and we assume a cluster of positive mass is present, then a lower limit can be placed on the ratio D_{OS}/D_{LS}. This limit is independent of cosmological parameters and the value of the time delay. If in addition the convergence of the cluster can be estimated independently (from the velocity dispersion of the galaxies for instance), then D_{OS}/D_{LS} can be measured.

Measure z_s, σ, and τ_{ij}, with cluster. Combining the last two options, if the velocity

dispersion, time delay, and source redshift are measured, and the cluster mass is assumed to be positive, then we have a measurement of D_{OL} as well as a lower limit on D_{OS}/D_{LS}, all independent of cosmological parameters.

The above scenarios indicate which distances or limits on distances can be found for a lens system. When the distance and redshift are known for an object, the expressions for angular diameter distance in §2.2 can be used to determine the values of H_0, Ω_0, and λ_0. This is illustrated in Figure 2-2, where angular diameter distance is plotted against redshift for a variety of cosmologies, assuming a filled-beam. The vertical dashed lines indicate z_l for the known lenses where a time delay might be measured. If the distance to the lens D_{OL} were measured for all of these lenses, good constraints could be set on H_0, Ω_0, and Λ_0.

Large scale structure along the line of sight can cause uncertainties in the determination of D_{OL}. The structure is effectively many sheets of matter that each contribute to the delay of the light from the source. The total delay added to both images is large, but the important quantity is the difference in the delay for the two images. Bar-Kana (1996) showed that these differences combine to cause a 5 to 10% uncertainty in the determination of H_0.

The determination of cosmological parameters from time delays will improve significantly as more lens time delays are known. For any particular lens, inhomogeneities along the line of sight will affect the measurement of a parameter, and make it differ from the global average. If several lens time delays are measured in different parts of the sky, differences due to local inhomogeneities will average to a robust global measurement. Also, if several lens delays are found at a variety of redshifts, more information can be learned: low redshift lenses set strong limits on H_0 but only weak limits on Ω_0 and Λ_0, while high redshift lenses can set limits on Ω_0 and Λ_0 once H_0 is determined.

See §6.3.3 for a discussion of the advantages, disadvantages, and results of this distance measurement technique in comparison with other techniques.

Dark matter and σ

The velocity dispersion of the lens is essential for determining D_{OL}, entering the equation as a square. The measured velocity dispersion σ is a line-of-sight dispersion of the visible

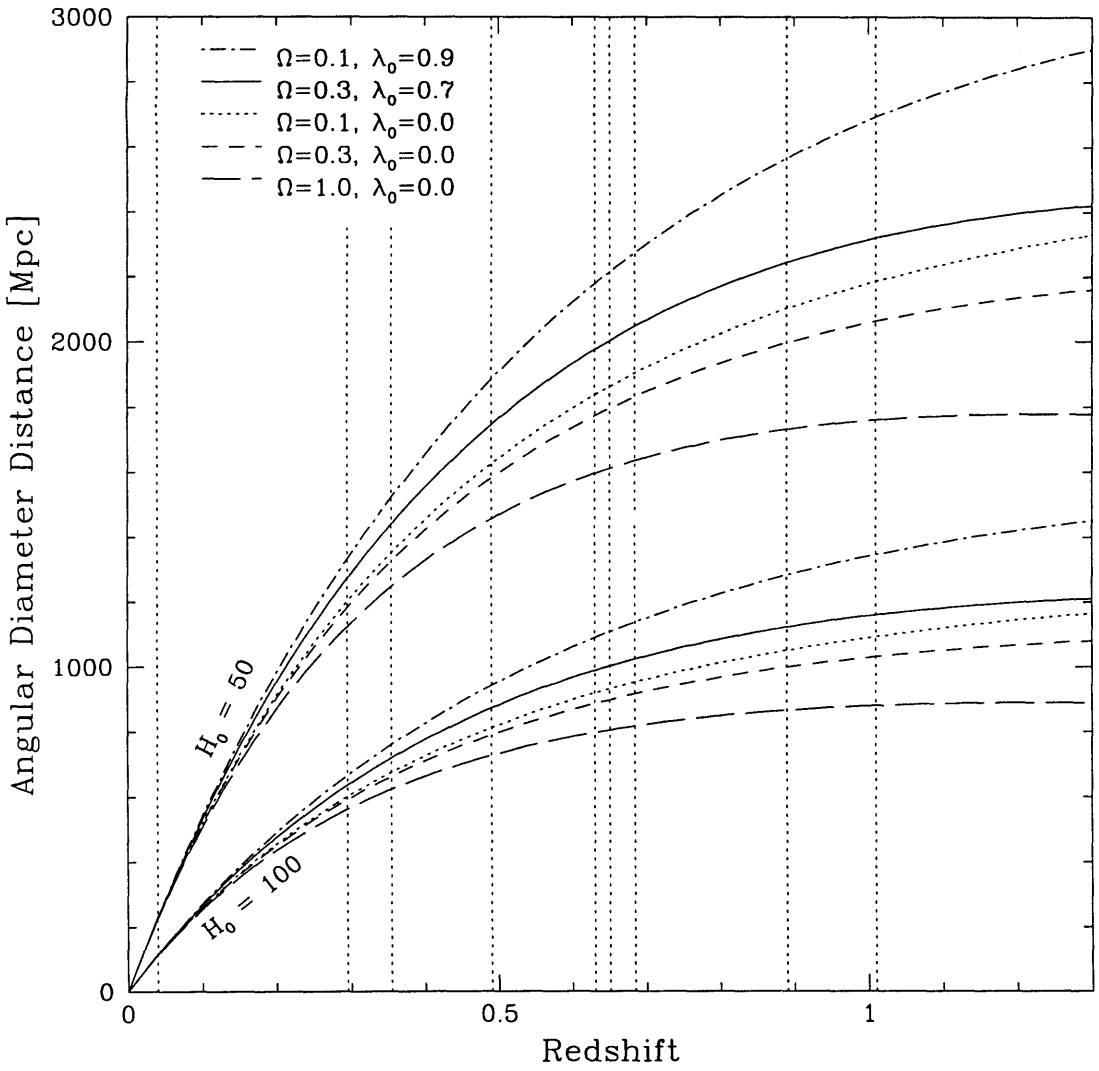

Figure 2-2: Filled-beam angular diameter distance as a function of redshift for several cosmologies.

stars in the lensing galaxy. The velocity dispersion of the dark matter σ_{dark} may, however, be up to $\sqrt{3/2}$ larger than σ. For a large mass-to-light ratio, the dark matter dominates the mass distribution, and σ_{dark} should be used to measure D_{OL}, which would result in a 50% increase in the value of H_0 (Roberts *et al.* 1991).

The origin of the $\sqrt{3/2}$ term is explained by Gott (1977). Observations of galaxies motivate a two-component mass distribution, where the visible component has a mass profile of $\rho \propto 1/r^3$ (assuming mass traces light), and the dark matter in the halo has a mass profile of $\rho \propto 1/r^2$ (giving a flat rotation curve). For an isothermal, isotropic distribution, the Boltzmann equation relates the velocity dispersion to the total gravitational potential and the mass profile,

$$\frac{d\Phi}{dr} = -\frac{\langle\sigma^2\rangle}{r}\frac{d\ln\rho}{d\ln r}. \tag{2.48}$$

Applying this to each of the mass profiles, we find $d\Phi/dr = 3\langle\sigma^2\rangle/r$ for the visible matter, and $d\Phi/dr = 2\langle\sigma^2_{\rm dark}\rangle/r$ for the dark matter. Thus, $\langle\sigma^2_{\rm dark}\rangle = 3\langle\sigma^2\rangle/2$.

The above analysis is somewhat naive. Kochanek (1993) and Grogin & Narayan (1996a, see §6.2.4) use modeling and observations to set the mass profile of both components (the luminous and dark matter), rather than assuming the $1/r^3$ or $1/r^2$ distributions. They also carefully include observational effects such as finite slit width and anisotropy in the galaxy.

Chapter 3

The Data Set

3.1 Observational Program

The MIT radio astronomy group has monitored the gravitational lens 0957+561 at 6 cm since shortly after its discovery in 1979. Since 1990 October the monitoring has included 4 cm observations as well. Earlier versions of the 6 cm light curves have been presented by Lehár *et al.* (1988), Lehár *et al.* (1992), and Haarsma *et al.* (1997); the 4 cm data is presented here for the first time. The monitoring observations are about 1-2 hours duration each and occur about once per month at the National Radio Astronomy Observatory (NRAO) Very Large Array radio telescope (VLA)[1].

The 6 cm observations are made at two frequency bands, 4.885 and 4.835 GHz with 50 MHz bandwidth each. Only the 4.885 GHz observations are used in the time delay analysis, since the other band was not in use in the early 1980s at the VLA. The 4 cm observations were made at 8.415 and 8.465 GHz (50 MHz bandwidth each) up to and including the 96Feb05 observation. In 1996 February the VLA changed the frequency defaults, so observations from 96Feb26 to the present have been at 8.435 and 8.485 GHz (50 MHz bandwidth each). This frequency change caused a flux density change of 0.4% in the flux calibrator 3C286, well below the error in the light curves (§3.4).

The VLA cycles through four configurations (A, B, C, and D) about once every 480 days.

[1]The National Radio Astronomy Observatory is operated by Associated Universities, Inc., under cooperative agreement with the National Science Foundation.

At 6 cm, the beam full-width half-maximum in the reference maps is approximately 0″.34, 1″.0, 2″.9, and 10″, at A, B, C, and D arrays, respectively. At 4 cm, the beamwidth of the reference maps for the four arrays is approximately 0″.21, 0″.7, 2″.2, and 5″.8 (where the 4 cm D-array data was mapped using robust uniform weighting of the UV data to create a narrower beam). Since the separation of the A and B images in 0957+561 is 6″, it is impossible in D-array to resolve the images at 6 cm and difficult at 4 cm. With careful weighting of the UV data (see §1.3.3) it may be possible to resolve the images at 4 cm and subtract the extended structure for at least some of the data sets, but this has not been done. Gaps in the monitoring due to D-array are approximately 120 days in every 480 day period, and were longer in the mid-1990s due to the D-array survey at the VLA. Fortunately, the source variability occurs at different times in the light curves for the two wavelengths, so the effect of the gaps is reduced.

Appendix B contains a list of all observations of 0957+561 made with the VLA at all frequencies. There are several observations listed that are not included in the time delay analysis. Only observations originally made under proposals by the MIT Radio Astronomy Group and collaborators are included. D-array observations are not included, since, as stated above, the images could not be easily resolved at either wavelength. There were several short observations taken in 1995 August (to catch the rise in the B image at 6 cm), and at other times. Observations of 30 minutes or less in length were not included, since the poor UV coverage and shorter integration time increased the systematic and random error in the flux density measurements. The one exception to the 30-minute rule is the 91Jul10 observation, which reduced well and is included to break up a large gap in the monitoring (this gap is crucial at 6 cm). In some of the 4 cm maps, the extended structure subtracted poorly from the map (see §3.2), leaving behind artifacts or excess noise that corrupted the flux density measurements, so these data were not included. This was less of a problem at 6 cm because the models used in the subtraction at 6 cm were based on observations with superior UV coverage. There are a few pre-1990 observations not included by Lehár *et al.* (1992), which have also been excluded from this analysis, most notably four observations from 80Jul26 to 80Oct03 which were of poorer quality. Finally, there were a few data sets with serious weather or equipment problems that are not included.

Thus, from 79Jun23 to 97Feb26 there are a total of 140 observations in the 6 cm light curves, with 65 from A-array, 38 from B-array, and 37 from C-array. From 90Oct04 to 97Feb26 there are a total of 52 observations in the 4 cm light curves, with 20 from A-array, 17 from B-array, and 15 from C-array.

3.2 Data Reduction

This section contains an overview of the VLA data reduction. See Appendix C for listings of the automated AIPS code ("run" files) used for data reduction and the details of parameter settings. See §1.3 for more information on radio interferometric techniques. First the reduction of the 4 cm data is described, then differences between the 4 cm and 6 cm reductions are explained.

Each raw UV data set was edited manually to remove obviously corrupted data, using the AIPS task TVFLG (AIPS tasks will be indicated in capital letters). Editing occurred again after the antenna gain calibration to remove more subtle problems in the data.

The antenna gains were then found using the tasks GETJY, SETJY, and CALIB. Initially the VLA flux standard source 3C286 was used to set the amplitude gains. This source, however, is resolved in the larger arrays, especially at 4 cm. The extended structure meant that the calibration (which assumed a point source) was limited to a range of baseline lengths and/or a subset of antennas. The calibration with these limits failed obviously in some cases (the calibrated data was much brighter on some antennas than others), and was dubious in others (caused unusually large changes from month to month in the flux density of 1031+567). A good model of the 3C286 structure would allow use of all the baselines and antennas in the calibration, but such a model requires a several-hour observation of the source, which was unavailable.

In lieu of 3C286, the phase calibrator point source 1031+567 was assumed to have a constant flux density over the 17 years of observations. Lehár *et al.* (1992) determined that 1031+567 did not typically vary in flux density by more than 2%, which is at the level of the error in the light curves. Thus the antenna phase and amplitude gains were found from 1031+567, and interpolated through the scans of 0957+561 using the task CLCAL.

At 4.885 GHz, the flux density of 1031+567 was assumed to be 1.241 Jy, and at 8.415 and 8.465 GHz it was assumed to be 776 and 771 mJy, respectively. These values are based on observations for which the flux gain calibration using 3C286 seemed to work well.

The 0957+561 data then underwent two iterations of mapping, deconvolution, and phase self-calibration using the task SCMAP. Experimentation with a few data sets found that there was little improvement after two iterations of self-calibration.

Phase cross-calibration was then performed with the Reference model of the source (see below for how the Reference map was made) using the task CALIB. The purpose of this was to remove position shifts that may have occurred during self-calibration, so that the map would be properly aligned for subtraction of the Jet model (see below). The cross-calibration also helped to remove any spurious structure or ambiguities that may arise during self-calibration of poor data by calibrating it to the better quality Reference data. Tests were done on the cross-calibration process using model UV data (the same flux, structure, and UV coverage as the real data, but without noise), which found that cross-calibration corrected position shifts up to at least 1″.

Even though only phase gains were allowed to change during cross-calibration, tests showed that the flux density of the point images made a significant shift towards the values in the Reference map. The tests also showed that two additional iterations of phase self-calibration after cross-calibration created a map with the correct position, but with the flux densities of the point images shifted back to the values before cross-calibration. Thus two additional iterations of mapping, deconvolution, and self-calibration were performed again on each data set, using the task SCMAP.

A model of the extended structure in the image was then subtracted from the data using the task UVSUB. This model is the Jet map, containing the jets, lobes, and the lensing galaxy G, but not the point images A and B. By subtracting this model from the data set, the point images are left behind in the map for accurate measurement of the flux. This subtraction is necessary for observations in the compact arrays, where the determination of the point source flux density is confused by the surrounding structure.

The resulting data was then mapped and deconvolved using the task IMAGR, and flux densities of the point images were measured using the task JMFIT. JMFIT fits a Gaussian

separately to each image, and returns the total flux density in that Gaussian. In the case of C-array observations at 6 cm, two Gaussians were fit at once to the two images.

Following the automated reduction, the maps made at each stage were examined manually to check for any problems, particularly with the subtraction of the extended structure. Often the subtraction left behind low levels of noise (a few times the RMS) in the regions of extended structure, which did not significantly affect the flux density measurement of A and B. Occasionally, however, the subtraction left behind significant holes (> 1 mJy) or ripples across the map. These data sets were excluded from the analysis.

The bulk of the data reduction was automated using AIPS Run Files, which are listed in Appendix C. A description of the manual aspects of data reduction and the necessary set up for the Run files is also included in Appendix C.

The Reference and Jet maps were made from the best data sets available in each array at both wavelengths. These were chosen to have good UV coverage, lasting several hours in order to sample as much of the UV plane as possible, and occurring at transit rather than low in the sky to avoid a distorted beam. At 6 cm the reference observations chosen were 82May08, 85Jun02, 83Apr09, and 82Dec19 for the A, B, C, and D arrays, respectively. At 4 cm, the observations 92Dec10, 93Apr09, 94Nov07, and 93Nov12 were chosen. The reference maps were made with two iterations of mapping, deconvolution, and self-calibration. While working on the reference maps, parameters such as the image and pixel sizes, clean boxes, and shifts (to center the point images on the pixels for better deconvolution) were determined; these parameters were later used for all the data sets. The Jet maps were then made from the Reference data by subtraction of the point image fluxes. For A-array observations, the A and B flux densities and positions were determined using JMFIT. For the more compact arrays, the Jet model from the next larger array was subtracted to obtain the first approximation of the A and B flux densities and positions. The 4 cm Reference maps are shown in Figure 3-1, and the 4 cm Jet maps are shown in Figure 3-2. The 6 cm Reference and Jet maps are shown in Figures 3-3 and 3-4. Note that the lowest contours are different in the 4 cm and 6 cm maps.

In order to keep the analysis of the 6 cm data as uniform as possible throughout the 17 years, all of the post-1990 6 cm data were analyzed using exactly the procedure of

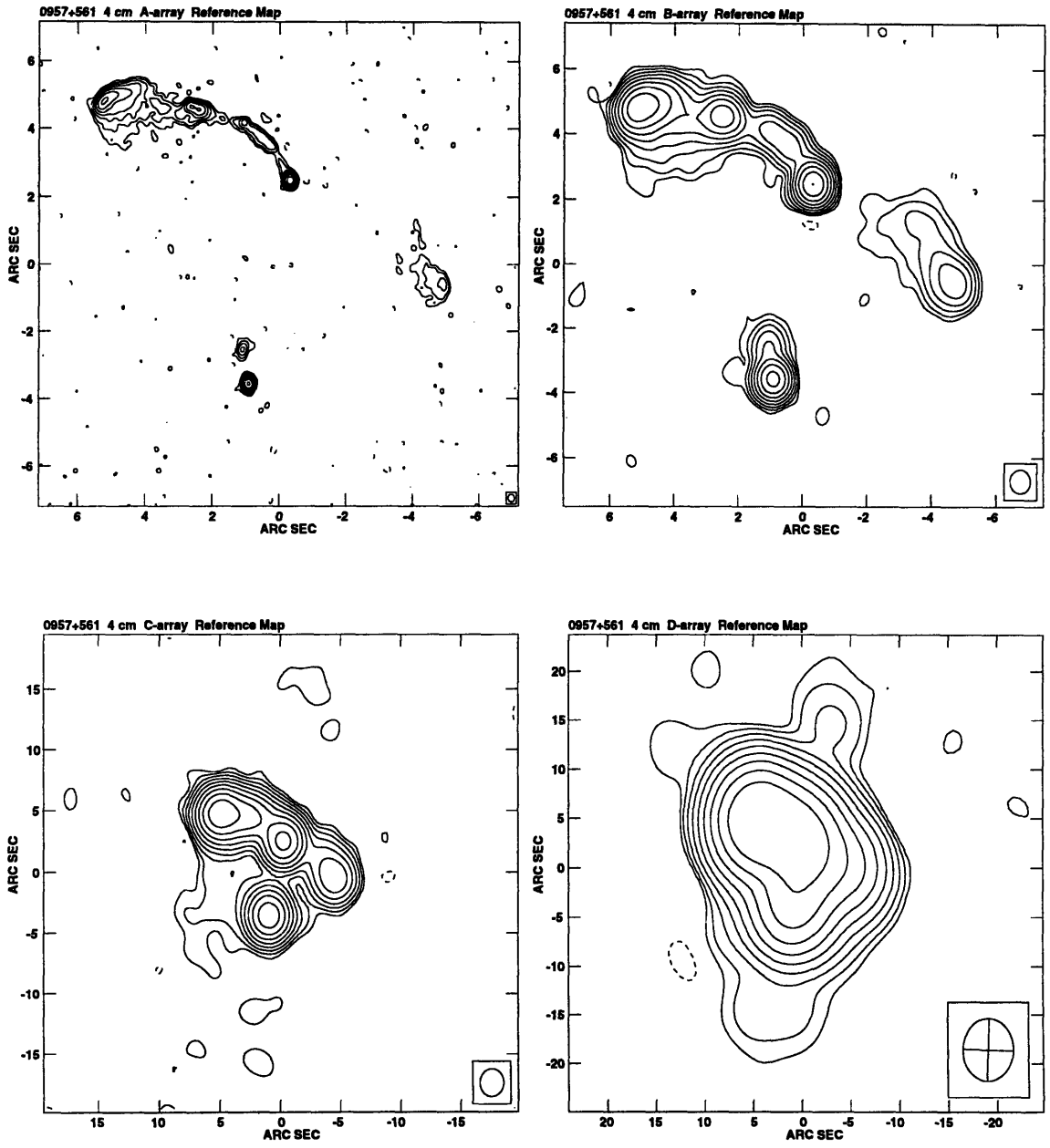

Figure 3-1: 4 cm reference maps, in A, B, C, and D arrays. The center of the maps is the J2000 position RA 10 01 20.728 Dec 55 53 53.12. The contours are -0.1, 0.1, 0.2, 0.4, 0.8, 1.6, 3.2, 6.4, 12.8, 25.6 mJy.

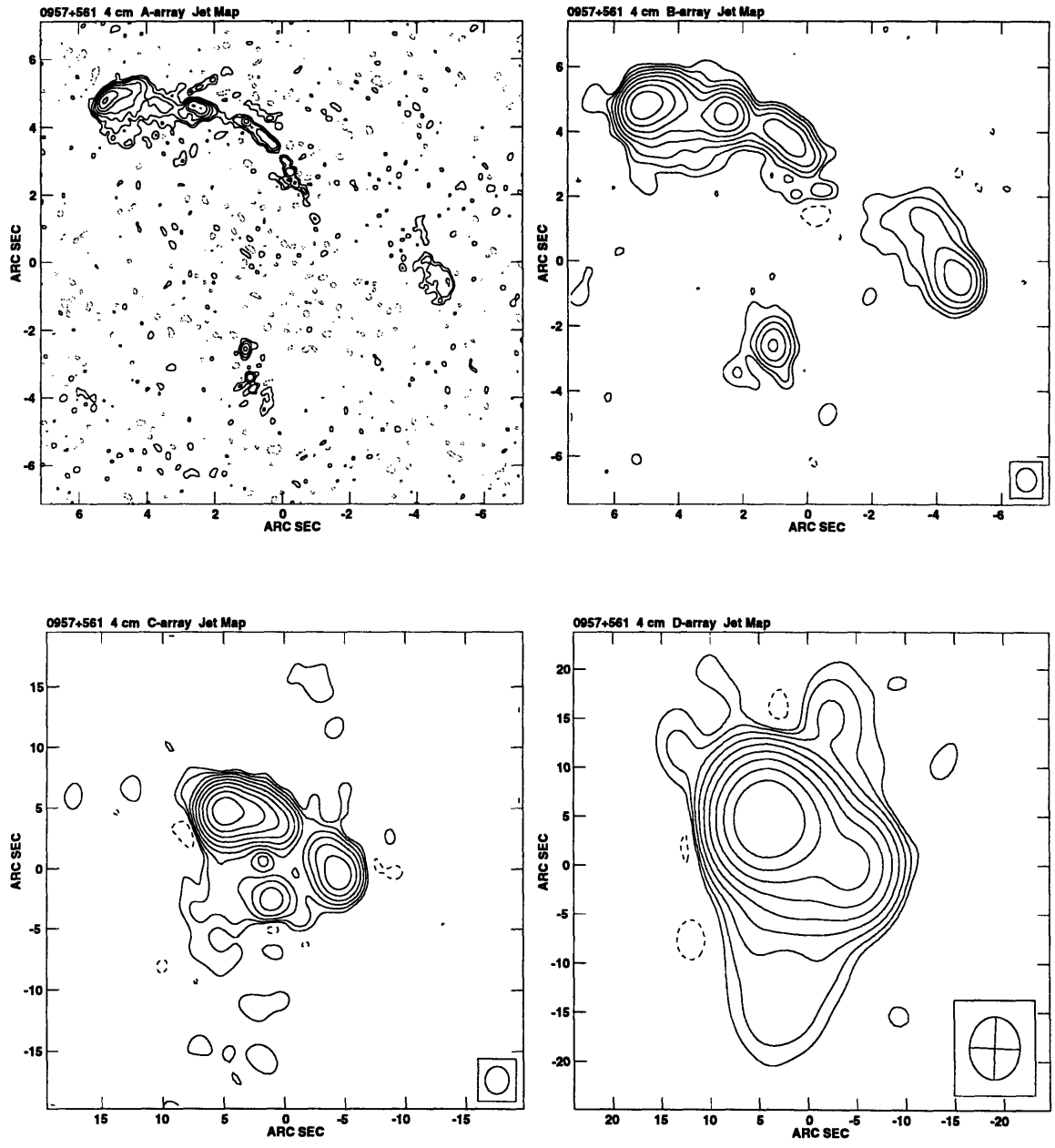

Figure 3-2: 4 cm jet maps, in A, B, C, and D arrays. The center and contours are the same as Figure 3-1.

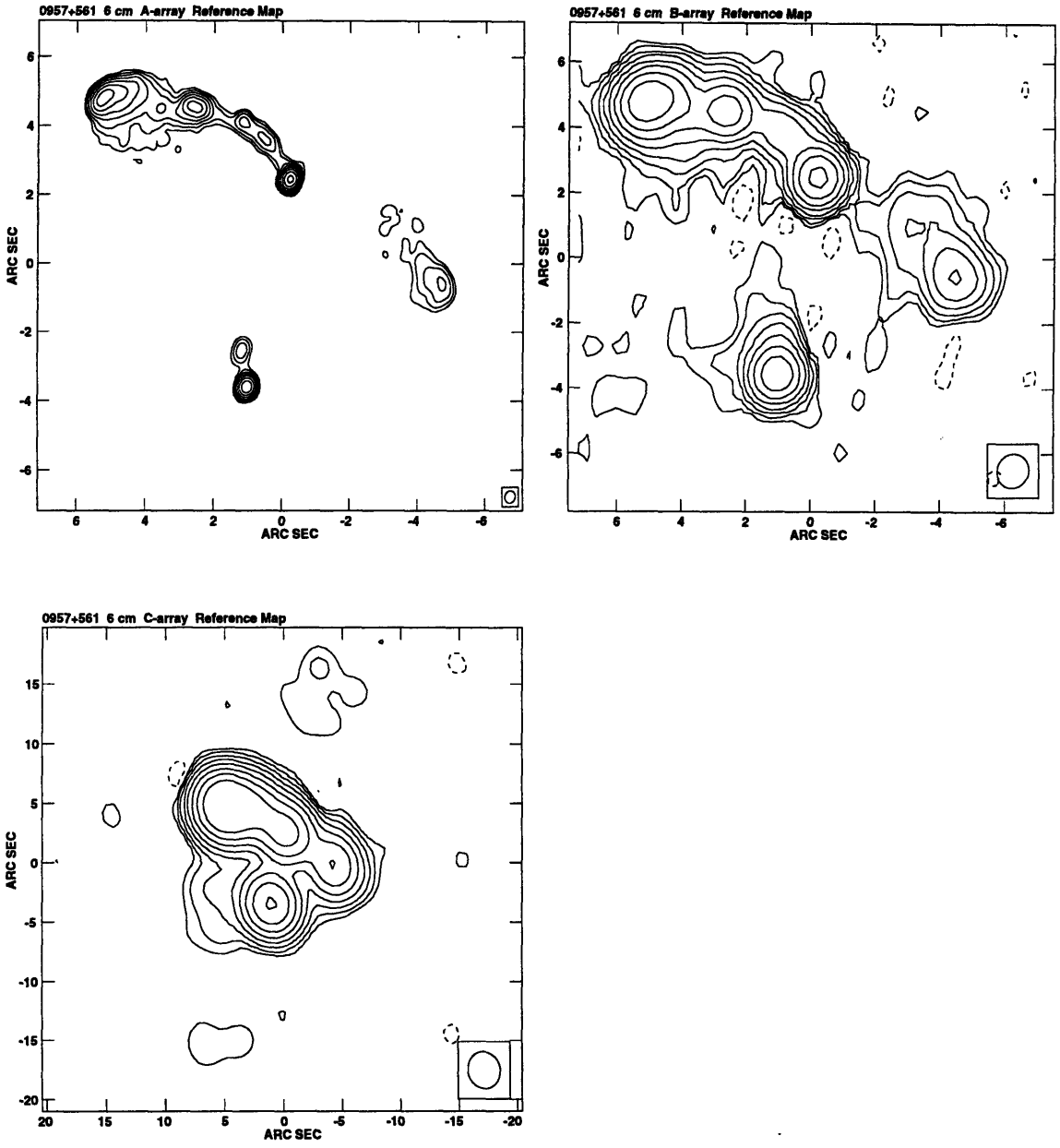

Figure 3-3: 6 cm reference maps, in A, B, and C arrays. The center of the maps is the B1950 position RA 09 57 57.300, Dec 56 08 20.00. The contours are -0.2, 0.2, 0.4, 0.8, 1.6, 3.2, 6.4, 12.8, 25.6 mJy.

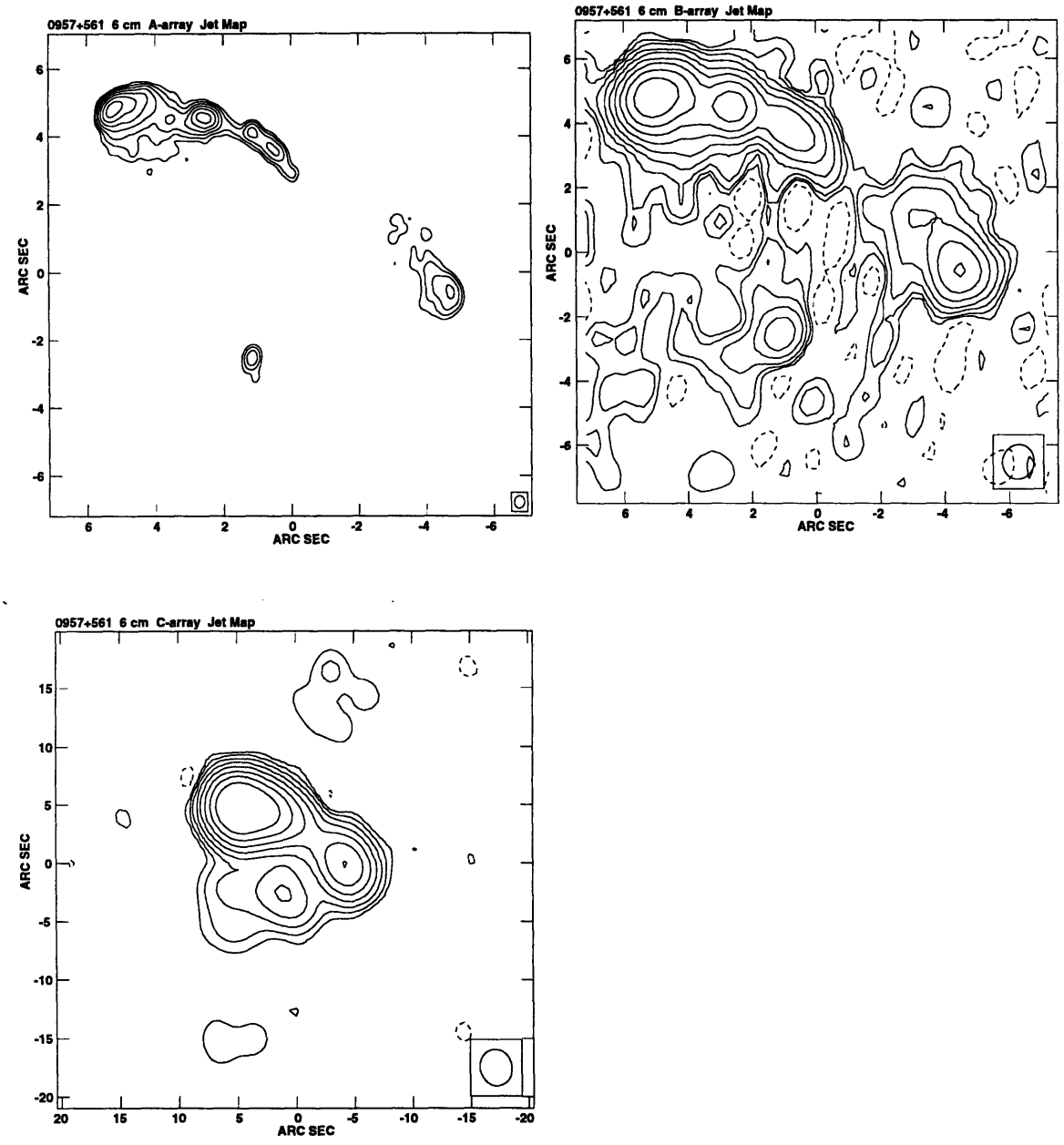

Figure 3-4: 6 cm Jet Maps, in A, B, and C arrays. The map center and contours are the same as in Figure 3-3.

Lehár *et al.* (1992), including the Reference and Jet maps and the AIPS Run files. The 6 cm reduction was thus somewhat different than the 4 cm reduction described above. The run files used the task APCLN for mapping and deconvolution, and ASCAL for self- and cross-calibration, which are older and less flexible than the current tasks SCMAP, IMAGR, and CALIB. Deconvolution was done with one large clean box around the structure, rather than several boxes closely surrounding the emission. Most importantly, there was no self-calibration done after the cross-calibration, putting a bias in the 6 cm A and B flux densities towards the image fluxes in the reference maps. The reference map values were set at the average of the light curve, so this bias has the effect of reducing the range of the variability by perhaps a few percent. Ideally, all of the 6 cm data back to 1979 should be reanalyzed to fix these problems.

In spite of these imperfections, the resulting light curves at both wavelengths have obvious flux density variations, with good signal to noise. Reanalyzing all of the data to eliminate the problems mentioned above would probably reduce the overall error in the flux density measurements from about 2% (see §3.4) to about 1%. Since this would not cause a significant improvement in the estimate of the time delay, reanalysis of the old data has not been done. A reduction in error to 1% may, however, improve the understanding of the physical source of the variability and differences in the propagation path of the two images (see Chapter 7).

3.3 The Light Curves

Table 3.1 contains the A and B image flux densities for the monitoring data. The first column gives the calendar date of the observation, and the fourth column gives the corresponding Julian Day number. The second column gives the array of the observation, which in the later years was often a combination array or an array between configurations. The "P" array for the earliest observations indicates "partial," these observations occurred while the VLA was still being built. For each observation with a non-standard array, a standard array was assumed for the reduction of the data, and this is shown in the third column. The flux density measurements are reported in the remaining columns. See §3.4 for a discussion

Table 3.1: 6 cm and 4 cm Light Curve Data.

				6 cm		4 cm	
Calendar Date	Observation Array	Reduction Array	Julian Day minus 2440000.0	A flux density (mJy)	B flux density (mJy)	A flux density (mJy)	B flux density (mJy)
79Jun23	P	A	4047.5	39.47	31.71	...	...
79Oct13	P	A	4160.16	39.26	29.67	...	...
80Feb23	P	A	4292.79	37.37	29.69	...	...
80Jun20	P	A	4411.30	35.90	29.01	...	...
80Nov24	A	A	4567.93	36.04	27.76	...	...
80Dec16	A	A	4589.5	35.90	27.50	...	...
81Jan06	A	A	4610.99	35.79	27.95	...	...
81Jan23	A	A	4628.25	35.64	27.34	...	...
81Jan24	A	A	4628.75	35.70	27.09	...	...
81Jan26	A	A	4631.47	34.99	27.68	...	...
81Mar03	A	A	4666.71	35.10	25.87	...	...
81Mar27	A	A	4690.71	35.02	26.65	...	...
81May14	B	B	4738.61	34.85	26.59	...	...
81May28	B	B	4752.68	35.08	26.89	...	...
81Jun14	B	B	4769.55	35.32	26.58	...	...
81Jul16	B	B	4802.41	33.86	26.24	...	...
81Aug15	B	B	4832.30	34.23	26.34	...	...
81Oct20	C	C	4898.16	32.64	26.71	...	...
81Nov21	C	C	4930.08	32.22	25.60	...	...
81Nov25	C	C	4934.00	32.22	25.10	...	...
81Dec05	C	C	4944.06	31.94	24.83	...	...
82Jan09	C	C	4978.97	32.36	25.58	...	...
82Feb09	A	A	5009.81	33.15	24.73	...	...
82Mar03	A	A	5031.75	32.67	25.11	...	...
82Mar27	A	A	5055.64	32.40	25.19	...	...
82May08	A	A	5097.61	33.48	24.91	...	...
82Jun03	A	A	5123.52	32.87	24.68	...	...
82Jun27	A	A	5148.41	32.57	24.98	...	...
82Jul16	B	B	5167.32	31.81	24.83	...	...
82Aug21	B	B	5203.30	31.81	24.48	...	...
82Sep23	B	B	5236.13	31.91	23.95	...	...
82Oct25	B→D	B	5268.14	32.73	24.17	...	...
83Jan20	C	C	5354.89	31.12	23.18	...	...
83Feb16	C	C	5381.81	30.77	23.85	...	...
83Mar15	C	C	5408.82	30.61	23.48	...	...
83Apr03	C	C	5427.67	32.10	23.76	...	...
83May05	C	C	5459.62	31.20	23.08	...	...
83Aug04	A	A	5551.41	31.20	23.07	...	...
83Sep06	A	A	5584.30	30.52	22.30	...	...
83Oct08	A	A	5616.19	30.55	22.75	...	...
83Nov26	A	A	5665.06	31.03	22.67	...	...
84Feb11	B	B	5741.85	30.94	22.62	...	...
84Apr22	C	C	5812.69	30.15	21.51	...	...
84Jun22	C	C	5874.43	30.73	22.26	...	...
84Dec12	A	A	6046.95	31.82	21.15	...	...
85Feb12	A	A	6108.86	32.62	20.64	...	...
85Apr20	B	B	6175.72	32.40	21.29	...	...

6 cm and 4 cm Light Curve Data. *continued*

Calendar Date	Observation Array	Reduction Array	Julian Day minus 2440000.0	6 cm		4 cm	
				A flux density (mJy)	B flux density (mJy)	A flux density (mJy)	B flux density (mJy)
85Jun03	B	B	6219.55	31.16	21.07	...	...
85Aug17	C	C	6295.25	30.78	21.11	...	...
86Feb19	A	A	6480.80	31.29	22.28	...	...
86Apr03	A	A	6523.66	31.40	21.51	...	...
86May21	A	A	6571.59	31.98	21.55	...	...
86Jul20	B	B	6632.28	30.63	21.53	...	...
86Sep11	B	B	6685.12	31.85	22.26	...	...
86Nov12	C	C	6747.11	31.44	21.62	...	...
87Jan11	C	C	6806.89	31.00	21.62	...	...
87Jul20	A	A	6997.35	30.49	20.46	...	...
87Sep27	A	A	7066.27	30.99	20.94	...	...
87Dec09	B	B	7138.99	31.46	21.79	...	...
88Jan26	B	B	7186.83	31.05	21.65	...	...
88Mar17	C&D	C	7237.71	30.53	21.77	...	...
88May08	C&D	C	7289.59	32.68	22.06	...	...
88Oct27	A	A	7462.12	33.26	21.85	...	...
88Nov18	A	A	7484.03	35.52	22.35	...	...
88Dec21	A	A	7516.98	35.14	21.55	...	...
89Jan24	A	A	7550.94	35.12	21.51	...	...
89Feb24	AnB	A	7581.75	37.24	22.19	...	...
89Mar25	B	B	7610.71	36.47	21.38	...	...
89Apr26	B	B	7642.65	37.04	21.11	...	...
89May19	BnC	B	7665.56	36.60	21.94	...	...
89Jun20	C	C	7697.59	35.52	21.59	...	...
89Jul16	C	C	7724.40	38.03	22.51	...	...
89Sep27	C	C	7797.28	35.84	21.87	...	...
90Feb19	A	A	7941.84	36.49	24.56	...	...
90Mar15	A	A	7965.82	36.73*	26.14*	...	...
90Apr10	A	A	7991.65	36.38*	22.30*	...	...
90May07	A→AnB	A	8018.72	37.09*	23.65*	...	...
90May23	A→AnB	A	8034.53	34.84*	26.63*	...	...
90Jun07	A→AnB	A	8049.57	35.35	25.46	...	...
90Jul15	AnB	A	8088.36	34.69	25.33	...	...
90Aug21	B	B	8125.32	34.75	26.39	...	...
90Sep06	B	B	8141.21	35.68	24.75	...	...
90Oct04	BnC	B	8169.22	34.04	24.18	23.87	21.96
90Nov01	C	C	8197.06	32.70	25.35	23.71	22.57
90Dec13	C	C	8238.89	32.74	25.57	22.75	22.49
91Jan17	C	C	8273.79	32.40	25.36	bad subtraction	
91Jul10	A	A	8448.40	31.15	24.81	22.28	17.98
91Aug18	A	A	8487.31	32.44	25.09	...	...
92Jan06	B	B	8627.97	31.32	21.94	23.33	15.12
92Feb04	BnC	B	8656.80	30.58	23.26	22.93	15.54
92Feb29	C	C	8681.74	31.13	22.41	24.08	15.72
92Mar07	C	C	8688.67	31.70	22.57	23.96	15.55
92Apr18	C	C	8730.60	31.31	22.80	24.30	15.85
92May03	C	C	8745.60	31.74	22.76	24.98	15.88

6 cm and 4 cm Light Curve Data. *continued*

Calendar Date	Observation Array	Reduction Array	Julian Day minus 2440000.0	6 cm		4 cm	
				A flux density (mJy)	B flux density (mJy)	A flux density (mJy)	B flux density (mJy)
92Oct23	A	A	8919.08	31.15	21.26	bad self-cal	
92Nov11	A	A	8938.09	31.18	21.92	25.57	15.61
92Dec10	A	A	8966.97	31.69	21.90	25.19	15.34
93Feb05	AnB	A	9023.78	30.56	22.73	25.22	15.68
93Mar21	B	B	9067.64	31.69	22.23	25.58	16.21
93Apr09	B	B	9086.67	31.40	22.73	25.98	16.98
93May18	B→BnC	C	9126.48	30.62	22.00	25.55	16.54
93Jul25	C	C	9194.21	30.70	22.58	27.82	17.13
93Aug26	C	C	9226.26	31.26	22.21	28.02	16.65
94Mar04	A	A	9415.73	34.50	21.55	31.34	17.71
94Apr11	A	A	9453.68	34.53	21.03	31.14	17.17
94May07	A→AnB	A	9479.63	34.87	21.39	31.31	17.80
94Jun25	B	B	9528.52	35.58	22.07	31.15	18.58
94Jul06	B	B	9540.42	34.75	22.56	30.83	18.56
94Aug18	B	B	9583.28	34.67	22.23	31.78	18.62
94Sep08	B	B	9604.27	35.42	23.62	31.65	19.42
94Oct10	BnC	B	9636.18	34.96	21.96	31.04	18.97
94Nov07	C	C	9664.08	35.37	22.86	31.75	20.29
94Dec08	C	C	9694.92	34.86	21.58	31.32	20.51
95Jun18	D→A	A	9886.57	35.13	22.89	bad subtraction	
95Jun23	A	A	9892.50	36.82	23.67	30.19	20.99
95Jun28	A	A	9896.53	37.02	22.75	bad subtraction	
95Jul08	A	A	9907.23	35.97	25.32	30.49	22.18
95Jul21	A	A	9919.51	36.13	24.92	30.05	21.80
95Aug07	A	A	9937.34	36.02	24.69	30.48	21.72
95Sep01	A	A	9962.33	35.41	24.75	29.94	22.05
95Sep09	A→AnB	A	9970.14	37.12	24.04	29.91	21.02
95Sep15	AnB	A	9976.10	38.31	24.65	30.76	21.78
95Sep23	AnB	A	9984.17	35.99	24.48	29.45	21.73
95Sep30	AnB	A	9991.17	36.36	25.90	29.19	22.54
95Oct10	B	B	10001.17	36.68	26.13	29.41	22.88
95Oct27	B	B	10018.20	36.50	25.36	29.95	22.51
95Nov09	B	B	10031.06	35.39	24.08	28.55	21.81
95Dec26	B	B	10077.95	35.66	24.65	28.34	21.56
96Jan26	BnC	B	10108.83	33.99	25.12	27.02	22.52
96Feb05	BnC	B	10118.77	35.18	24.57	27.19	21.96
96Feb26	C	C	10139.67	35.48	24.07	27.95	23.03
96Mar04	C	C	10146.68	36.55	24.18	28.11	22.79
96Apr05	C	C	10178.56	34.31	25.06	27.52	22.89
96Apr25	C	C	10198.66	35.09	25.07	27.84	23.15
96Jun11	CnD	C	10246.48	34.00	25.14	bad subtraction	
96Oct19	A	A	10376.05	35.30	25.20	25.49	20.67
96Nov10	A	A	10397.95	34.62	25.36	24.66	20.68
96Dec26	A	A	10443.98	35.17	24.74	24.73	20.05
97Jan10	A	A	10458.89	34.81	24.86	25.32	20.13
97Feb26	B	B	10505.82	33.62	24.38	24.53	19.44

of the error on the measurement. The dots (· · ·) indicate that the observation did not include that frequency. Asterisks (*) on four observations in Spring 1990 indicate data later removed in the time delay analysis (see §5.1.1).

The 6 cm light curves are plotted in Figure 3-5. The error bars in the figure are derived using structure function analysis in §5.1.2. The flux density of the source was initially large, then declined for several years. In the mid-1980s the light curves were relatively quiescent. Around 1990 there was a large, symmetric event in both images that lasted for about two years before returning to the quiescent level previous to the event. In the mid-1990s another event began in both images which has already lasted longer than the event around 1990. The variability of the 6 cm light curve as a percentage of the average is about 20%.

The 4 cm light curves are plotted in Figure 3-6. The error bars in the figure are derived using structure function analysis in §5.2.1. The 4 cm monitoring began just at the end of an event, with a sharp decline in the B image. Then both images increased over several years, peaked, and began to decrease. The variability of the 4 cm light curve as a percentage of the average is about 40%.

The features at the two wavelengths are definitely correlated. The features start earlier at 4 cm than 6 cm, and have a longer rise time. The variability at 4 cm is twice as much as at 6 cm. This continued variation of the source at both wavelengths is fortunate; without it the estimate of the time delay could not be improved.

Consideration of these light curves raises several questions. Is this variability typical of radio galaxies? Is there a physical reason for the 4 cm features to be larger and earlier than those at 6 cm? Is the low-level variability measurement error, or some physical process? These questions will be addressed in Chapter 7.

In particular, there is a sharp feature in Spring 1990 at 6 cm in the B image, where the flux density changes by nearly 4 mJy in a few months. These data points have already been the subject of considerable discussion (Kayser 1993; Pelt *et al.* 1994, 1996), which prompted a reconsideration of the raw 6 cm data for that epoch. No abnormalities were found in these observations: there were no weather problems, no bad antennas, and the self-calibration, mapping, and subtraction of extended emission all proceeded smoothly. The final maps had no artifacts from the reduction and were of low noise. The flux densities of A and B

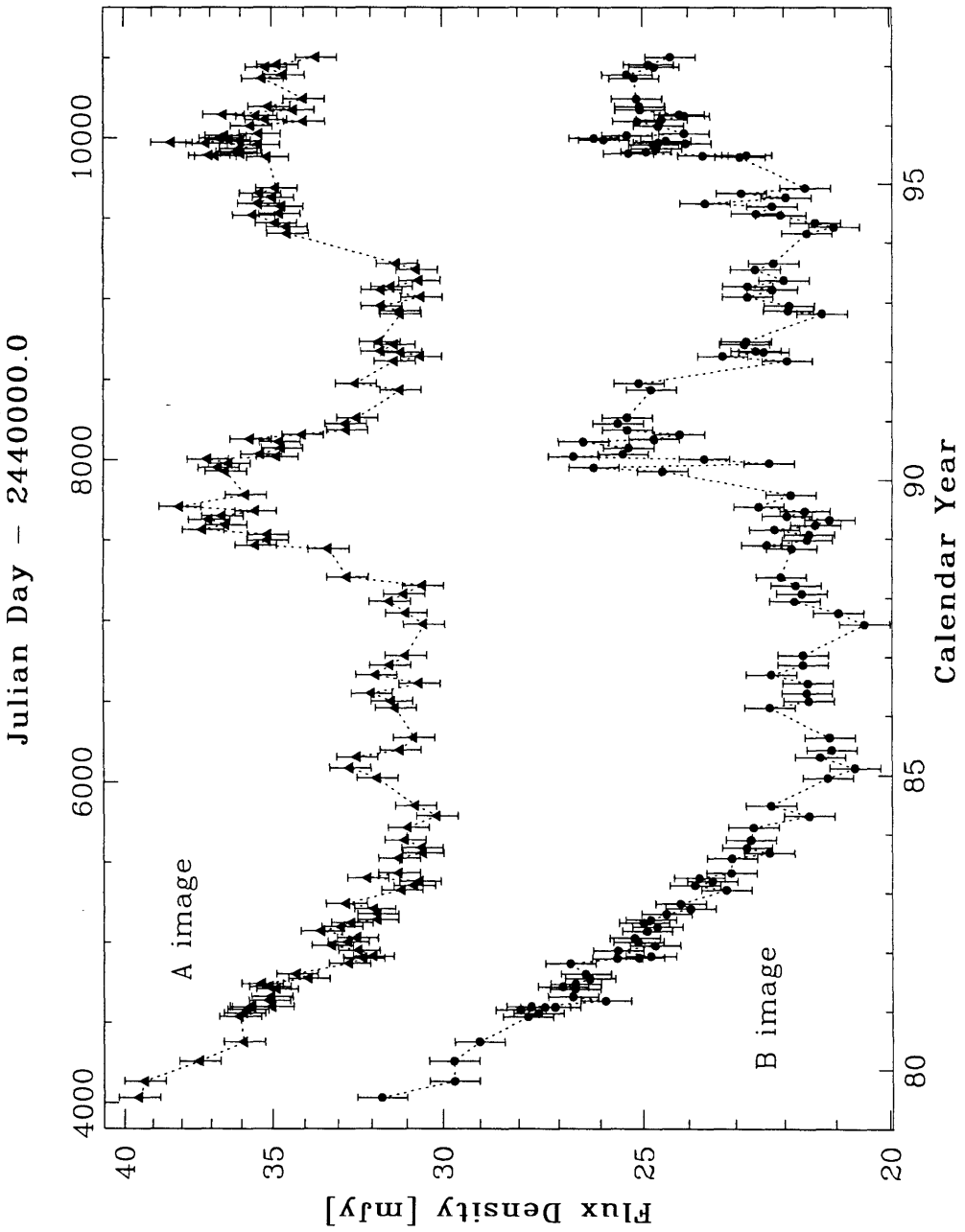

Figure 3-5: 6 cm light curves.

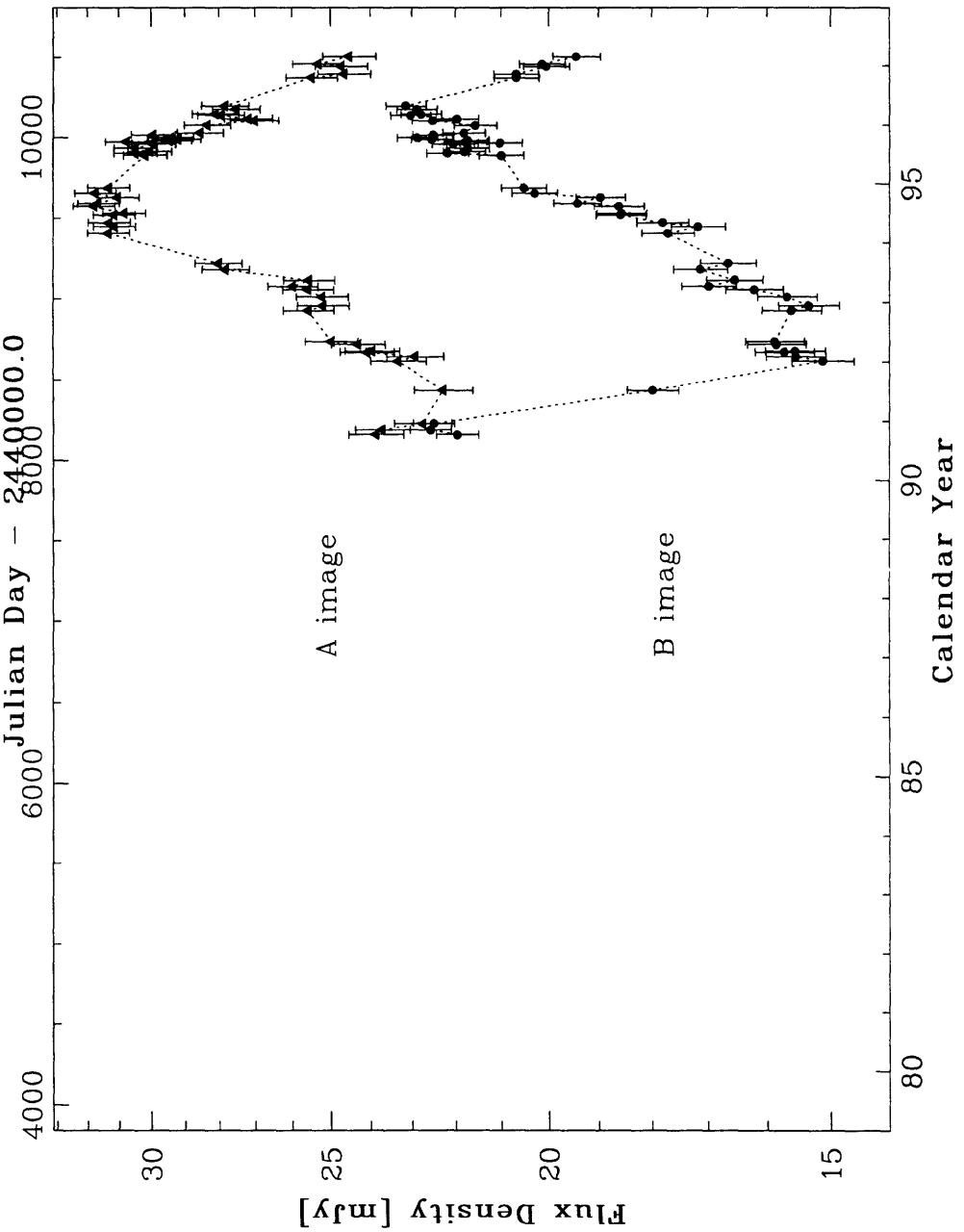

Figure 3-6: 4 cm light curves.

observed with the second VLA band (4.835 GHz) were slightly different than the reported data (about 0.15 mJy for these data sets), a difference which is typical for data sets at other times in the light curve (Sopata 1996). This implies that there were no frequency-dependent measurement errors or corruption of the data. Thus, the fluctuation of Spring 1990 is of physical origin and the points cannot be excluded as poor quality data. The statistical properties of these data are discussed in §5.1.1, and possible physical origins for the event are discussed in §7.3, §7.4, and §7.5.

Inspection of the light curves shows that there is obviously a delay of one to two years between the images. Although a formal statistical analysis is necessary for a robust determination of the delay (Chapters 4 and 5), one can gain insights into the problem by sliding the curves across one another until they agree by eye. Playing with the curves in this way reveals the give-and-take between the features, the particular epochs that determine the delay most strongly, the interaction between delay and flux ratio, etc.

Figures 3-7 to 3-10 show the light curves combined at various delays: $\tau_{AB} = 540$ days (Lehár *et al.* 1992; Press *et al.* 1992c), $\tau_{AB} = 460$ days (Haarsma *et al.* 1997), $\tau_{AB} = 420$ days (Kundić *et al.* 1997), and $\tau_{AB} = 400$ days (Schild 1990). In these figures the error bars have been omitted for clarity. At 6 cm the 1990 Spring feature gives the B image two possible rises, either in 1990 February-March or in 1990 May, depending on which points you choose to ignore. At a delay of 540 days, the second rise fits well, as does the long decline in the early 1980s, but the decline in 1991 is significantly different for the A and B images. At the other extreme, a delay of 400 days, the first B rise in 1989 first well, as does the 1991 decline, but the long decline in the early 1980s is not as neat and, more importantly, the rise in 1994 happens in the A image before the B image. A delay of 460 days seems to be a good compromise for the 6 cm light curves.

At 4 cm, a delay of 540 days is very inconsistent with the data, and there is no flux ratio that makes the both the rise and decline agree for the two images. At 460 days, the situation is somewhat better, however there is a "knee" in the long rise (around 1993) in both images that does not line up. At 400 days, the "knee" and all other features are aligned well. A delay of about 420 days may be a good compromise between the 4 cm and 6 cm data.

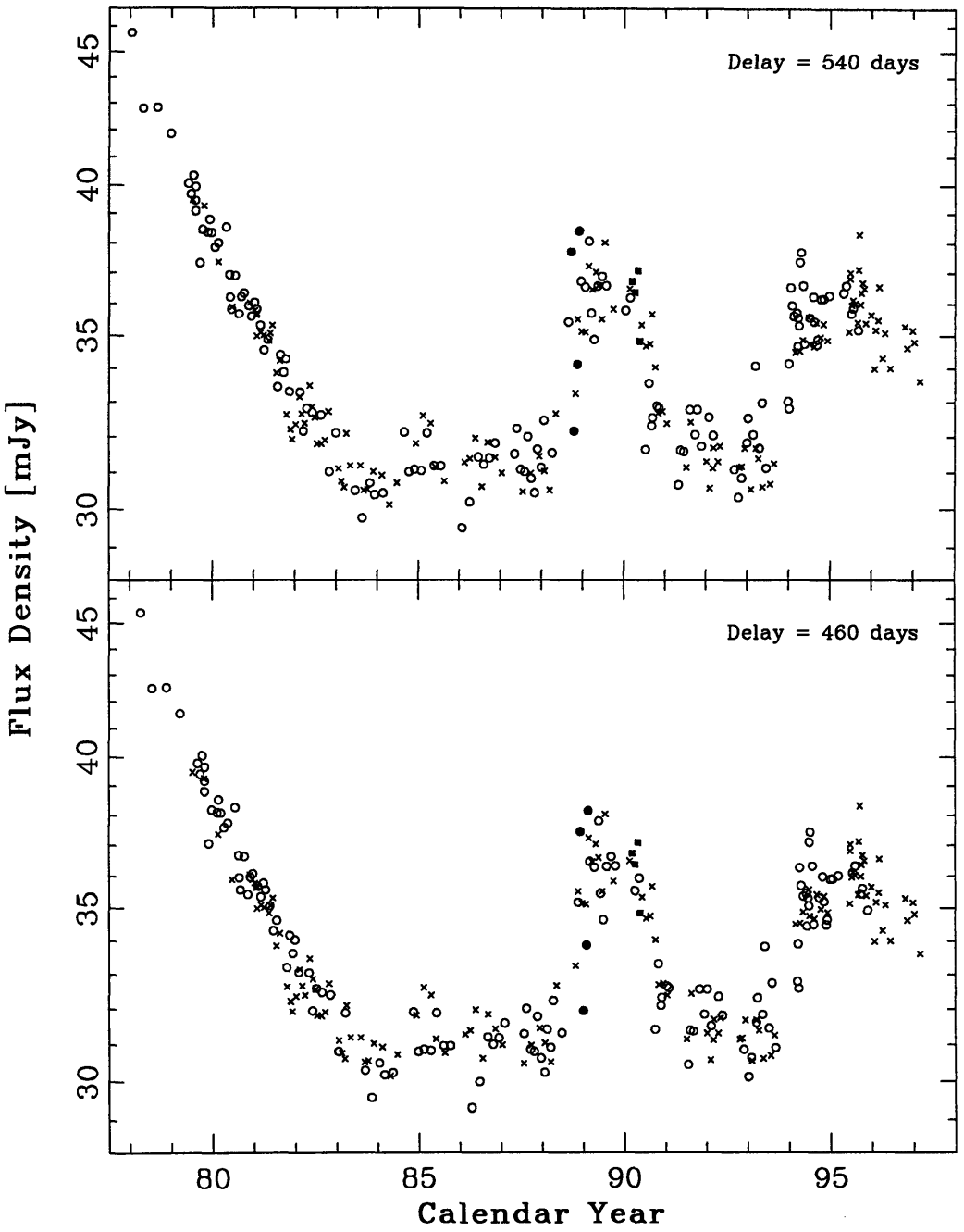

Figure 3-7: Combined 6 cm Light Curves. The upper curve is combined at $\tau_{AB} = 540$ days, R =0.693. The lower curve is combined at τ_{AB} =460 days, R =0.698. Crosses indicate the A image, circles indicate the B image, and the four points removed are indicated by filled symbols.

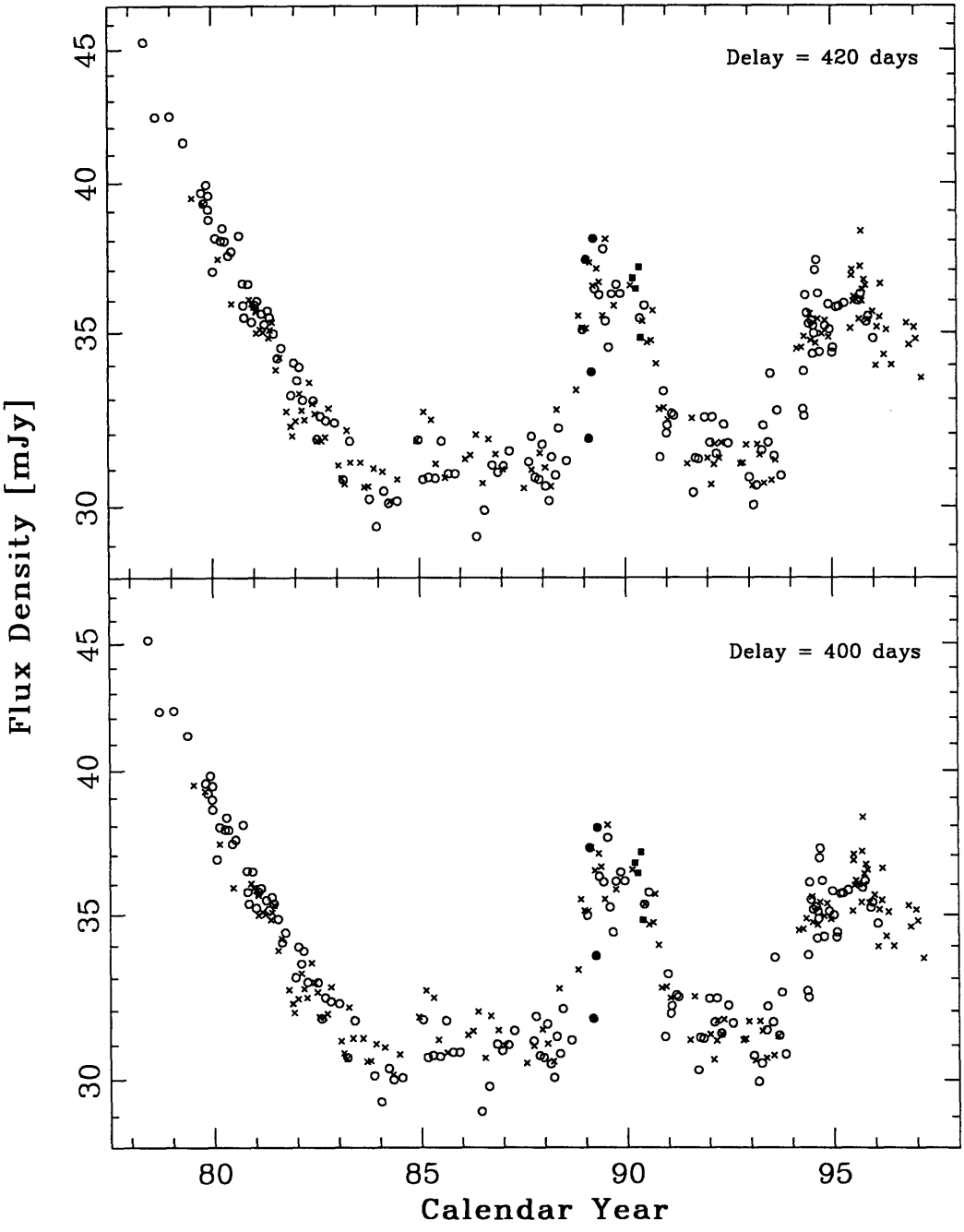

Figure 3-8: Combined 6 cm light curves. The upper curve is combined at τ_{AB} =420 days, R =0.700. The lower curve is combined at τ_{AB} =400 days, R =0.702. Symbols are the same as in the previous plot.

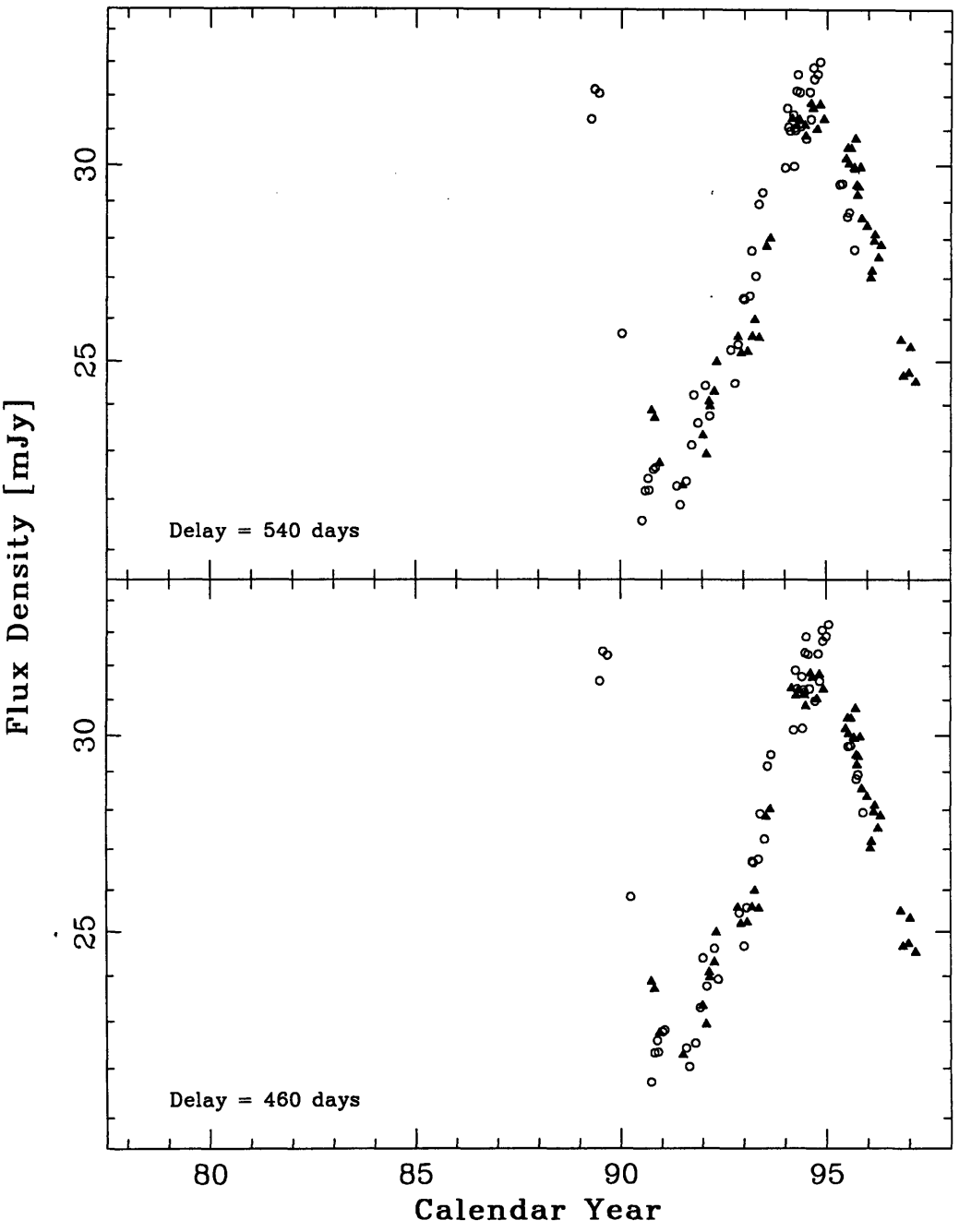

Figure 3-9: Combined 4 cm Light Curves. The upper curve is combined at τ_{AB} =540 days, R =0.701. The lower curve is combined at τ_{AB} =460 days, R =0.696. Filled triangles indicate the A image, and open circles indicate the B image.

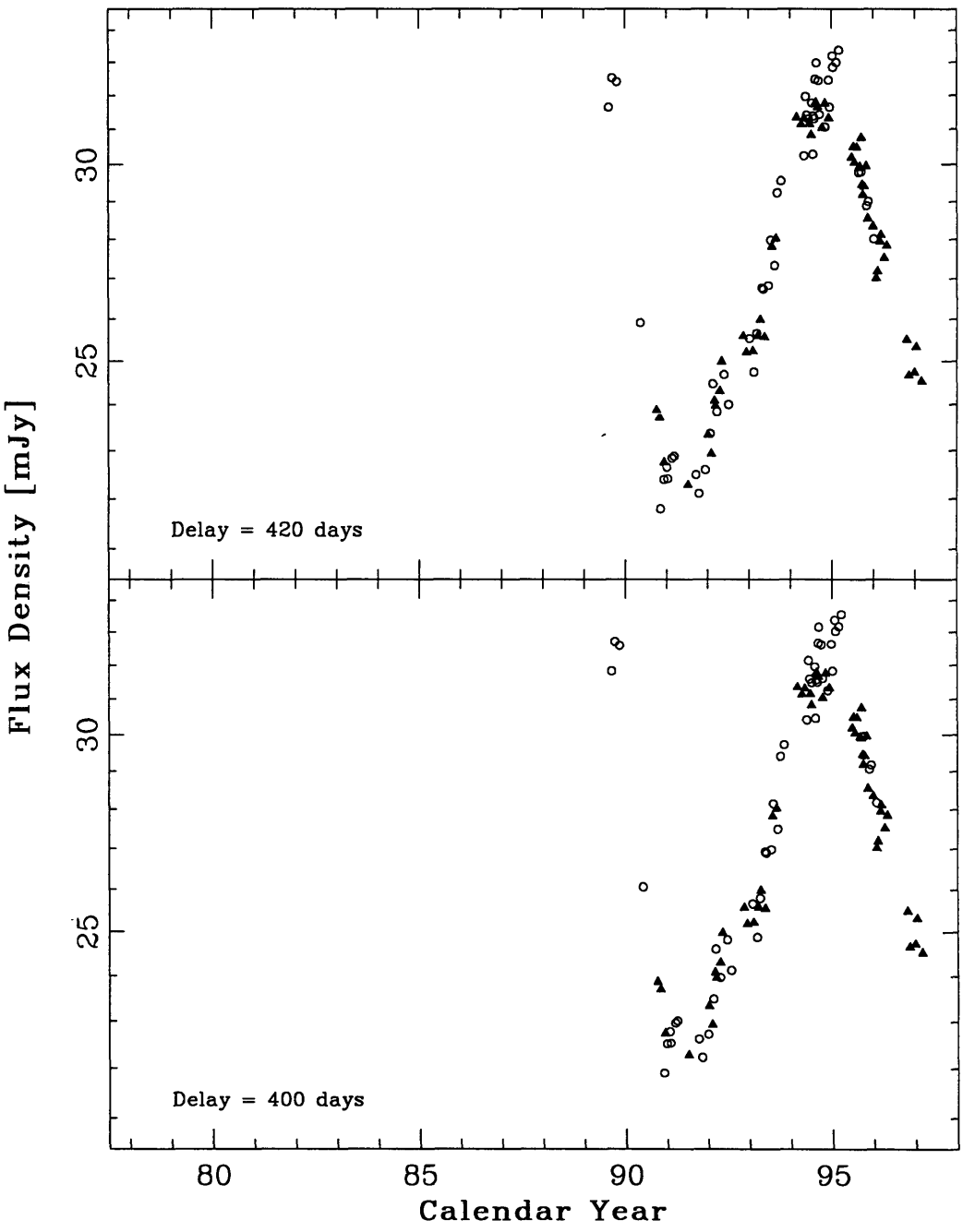

Figure 3-10: Combined 4 cm Light Curves. The upper curve is combined at τ_{AB} =420 days, $R = 0.694$. The lower curve is combined at τ_{AB} =400 days, $R = 0.690$. Symbols are the same as in the previous plot.

3.4 Error Estimation

As stated in §1.3.6, VLA data reduction involves non-linear techniques (i.e. deconvolution and self-calibration), so the accuracy of the flux densities listed in Table 3.1 cannot be determined analytically.

Lehár *et al.* (1992) estimated the errors on the 6 cm measurements in three ways: as the RMS during the quiescent period (1983.3 to 1988.0 for A and 1984.5 to 1989.5 for B), as the RMS of the residuals about a 2nd-order polynomial fit to the long decline (1980.5 to 1984.0), and by splitting a single observation into subsections in time. L92 concluded that the errors are approximately 2% of the flux density, which is about 0.6 mJy for the A image, and about 0.4 mJy for the B image. The errors on the 4 cm measurements are probably comparable. This is similar to the error found from structure function analysis (§5.1.2 and §5.2.1).

Due to the different synthesized beams in the three VLA arrays used, it is possible that the errors are significantly different for these arrays. Differences in UV coverage due to the length and hour angle of the observation, weather problems, or missing antennas may also cause the uncertainty to vary from observation to observation. For simplicity, a homogeneous error model has been used for the time delay analysis, in which every data point has the same fractional error. An inhomogeneous error model that takes into account the differences between data sets would be more true to the data, but would also introduce more variables into the analysis, and has not been attempted here.

Chapter 4

Time Delay Analysis Techniques

Over the last several years, several statistical techniques have been presented in the literature for measuring the time delay between two gravitational lens light curves. Three of these methods were selected for analysis of the 0957+561 radio light curves in this thesis, and are described below. The units used for the analysis, and the synthetic data used to estimate the uncertainty in the time delay measurement, are also described. This chapter ends with a discussion comparing the advantages and disadvantages of the three techniques. Chapter 5 reports the results of applying these techniques to the light curves.

Most of this chapter is based on the paper by Haarsma, Hewitt, Lehár, & Burke (1997, *ApJ* **479**, 102). The code implementing the PRH and dispersion methods (§4.2, 4.3) included several routines from *Numerical Recipes* (Press *et al.* 1992a).

4.1 Types of Analysis Available

Many types of statistical analysis have been used to determine the time delay between gravitational lens light curves. Table 1.1 lists *twelve* different analyzes that have been used on the 0957+561 curves. There are even a few interesting methods which are not included in Table 1.1. One is a wavelet analysis by Hjorth *et al.* (1992), which did not find a conclusive value for the 0957+561 delay. Another is the recent analysis by Bar-Kana (1997) of the light curves of gravitational lens PG 1115+080. Like the PRH technique, it is a χ^2 analysis, but it makes different assumptions about the statistical properties of the curve (it does

not assume the curves are stationary or have a particular structure function, but that the variation can be modeled by an interpolated curve), and allows for correlated measurement errors. Unfortunately, the method appeared in the literature too recently for inclusion in this thesis.

Of the methods listed in Table 1.1, three were chosen for analysis of the light curves in this thesis: PRHχ^2 structure function analysis, weighted dispersion, and the discrete correlation function (numbers 7, 10, and 6 in Table 1.1). These were chosen because they have been applied previously to the 0957+561 radio curves, they are clearly documented in the literature, and they avoid interpolation of the light curves.

4.2 PRH χ^2 Analysis

Press, Rybicki, and Hewitt (1992b, 1992c, hereafter PRH1, PRH2) found time delays for the published optical and radio light curves (Vanderriest *et al.* 1989; Lehár *et al.* 1992) using structure function analysis and a chi-squared fitting technique. Rybicki & Press (1992) and Rybicki & Kleyna (1994) further describe the technique and present some modifications. This discussion follows PRH1.

The measured light curve $y(t)$ can be written as the sum of the signal $s(t)$ from the source and the noise signal $e(t)$ representing the measurement error,

$$y(t) = s(t) + e(t). \tag{4.1}$$

The covariance matrix associated with $s(t)$ is $\mathsf{C}_{ij} = \langle s(t_i)s(t_j)\rangle$, where the angled brackets indicate an expectation value. Similarly, the covariance model B associated with $y(t)$ has the elements

$$\mathsf{B}_{ij} = \mathsf{C}_{ij} + \langle e_i^2\rangle\delta_{ij}, \tag{4.2}$$

where δ_{ij} is the usual delta function. The inverse of the covariance model is $\mathsf{A} = \mathsf{B}^{-1}$. The joint probability distribution of the data vector $y(t)$, assuming it is a Gaussian process, is

$$P(y) = \left[(2\pi)^N|\mathsf{B}|\right]^{-1/2} e^{-\chi^2/2}, \tag{4.3}$$

where the vertical bars indicate the determinant of the matrix. The PRH technique is to minimize χ^2,

$$\chi^2 = \sum_{ij}(y_i - \bar{y})\mathsf{A}_{ij}(y_j - \bar{y}), \tag{4.4}$$

where

$$\bar{y} = \frac{\sum_{ij} y_i \mathsf{A}_{ij}}{\sum_{ij} \mathsf{A}_{ij}} \tag{4.5}$$

is the estimate of the mean of y_i obtained by minimizing χ^2 with respect to the unknown value of $\bar{y}$ (one degree of freedom is lost in this estimate).

The PRHχ^2 statistic is a measure of the goodness-of-fit of a light curve to a model of its temporal correlations, which are described by the covariance model B_{ij}. The statistic was shown by PRH1 to be independent of the underlying mean and variance of the time series. PRH1,2 estimated the time delay by adopting trial delays τ_{AB} and trial flux ratios R, combining the light curves according to these trial values, and computing the PRHχ^2 statistic of the combined light curve for each (τ_{AB}, R) pair using the covariance model that describes a single light curve. Note that the PRHχ^2 sum includes contributions from all pairs of points y_i, y_j in the light curve under consideration ($4N^2$ pairs for the combined curve). Each point is compared to every other point to test how well that pair fits the model, and thus all information available in the light curve is used.

Rybicki & Kleyna (1994) point out that *both* the PRHχ^2 statistic and the normalization factor in the joint probability distribution (eq. 4.3) are functions of the correlation model. Therefore, minimizing only the PRHχ^2 statistic does not give a true measure of the most likely data set. Rather, a maximum likelihood estimate is found by minimizing the following quantity:

$$Q = \log|\mathsf{B}| + \sum_{ij}(y_i - \bar{y})\mathsf{A}_{ij}(y_j - \bar{y}). \tag{4.6}$$

Since the time delay is a parameter of the covariance model that applies to the combined light curves, the neglect of $\log|\mathsf{B}|$ in the PRHχ^2 minimization procedure is a concern. The effect of neglecting the $\log|\mathsf{B}|$ term is to favor samplings of the combined light curve that discriminate less among different time delays. In other words, time delays are favored in which the overlap is small when the light curves are combined. Thus, the use of Q rather

than PRHχ^2 will, in part, alleviate the impact of sampling on the time delay result. For this data set, however, the value of $\log|\mathsf{B}|$ does not change by more than a few (in units of χ^2) for delays in the range 200–800 days. Also, the location of the minimum in delay-ratio space for the Q and PRHχ^2 surfaces differs by no more than a few days in delay. For "window function" data (light curves of constant flux density but the same sampling as the real light curves), Q was not immune to the sampling and varied over the range of delays in a way similar to PRHχ^2 (see §5.1.2 and Figure 5-9). Since Q is the correct maximum likelihood estimator in this problem, the time delay that minimizes the Q statistic will be reported, although it differs only slightly from the time delay that minimizes PRHχ^2.

In order to use Q or PRHχ^2, the covariance model B_{ij} for the data must be determined. The variability properties of the light curves can be described by a first-order structure function (Simonetti *et al.* 1985),

$$V(T) = \frac{1}{2}\langle[s(t) - s(t-T)]^2\rangle, \tag{4.7}$$

where $T = t_i - t_j$ is the lag between two points on the light curve. Figure 4-1 shows an idealized structure function. For most lags, the structure function can be modeled as a power law,

$$V(T) = V_0 T^{\alpha}. \tag{4.8}$$

The exponent α indicates the dependence of the variability on time scale. Hughes *et al.* (1992) discuss the physical types of variability corresponding to different values of α, and find that extragalactic radio sources typically have an exponent of $\alpha = 1.09 \pm 0.34$. They also note that long linear trends in the light curve tend to steepen the structure function to $\alpha = 2$. At long lags, the structure function deviates from the power law, and asymptotes to a value of twice the variance of the signal, $V(\log T) \rightarrow 2\langle s^2\rangle$. The lag at this turnover indicates the time scale for uncorrelated variability in the light curve. The behavior of the structure function for real data can be erratic for lags greater than about half the length of the light curve, due to the dominance of individual features in the curve at long lags, so the structure function features beyond a lag of half the time series length are typically ignored. If measurement error were included in the time series, the structure function at short lags

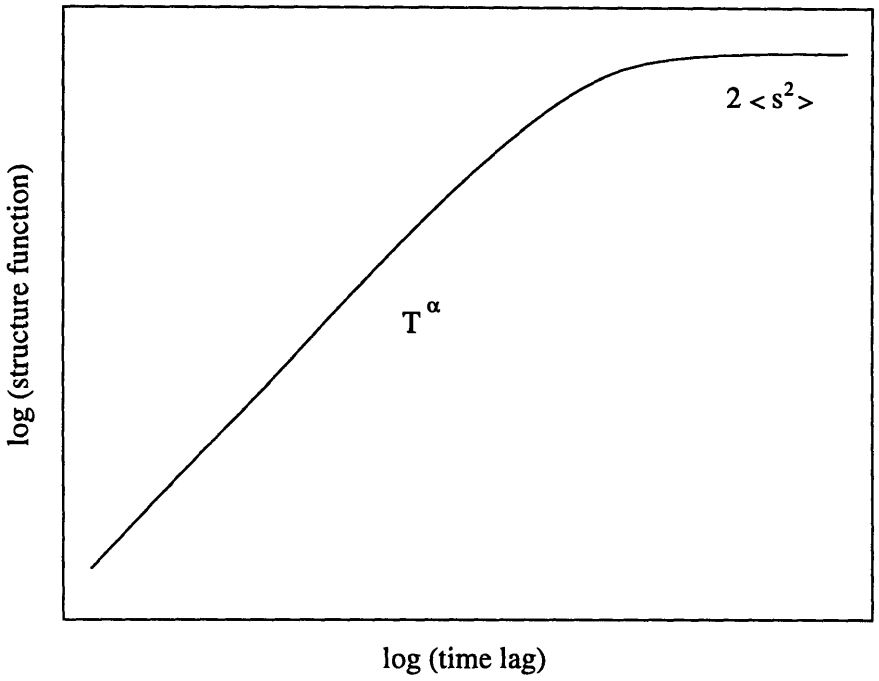

Figure 4-1: Idealized structure function for the signal $s(t)$.

would asymptote to twice the variance of the measurement error, $V(\text{short}T) \rightarrow 2\langle e^2 \rangle$ (note that eq. 4.7 is for the signal $s(t)$ which does not include measurement error $e(t)$). The coefficient and exponent of the structure function (eq. 4.8) can be fit by using point estimates found directly from the data,

$$v_{ij} = \frac{1}{2}\left[(y_i - y_j)^2 - e_i^2 - e_j^2\right]. \tag{4.9}$$

If the light curves are assumed to be stationary, then the covariance matrix elements become $\mathsf{C}_{ij} = \mathsf{C}(t_i - t_j) = C(T)$. The autocorrelation function $C(T)$ is related to the structure function by

$$C(T) = \langle s^2 \rangle - V(T). \tag{4.10}$$

Thus, from an expression for $V(T)$, elements of the covariance model are computed by

$$\mathsf{B}_{ij} = \mathsf{B}(t_i - t_j) = \langle s^2 \rangle - V(t_i - t_j) + e_i^2 \delta_{ij}. \tag{4.11}$$

The term "covariance model" will be used in Chapter 5 to refer to the combined effect of the structure function $V(T)$ and the measurement errors e_i. As shown by PRH1, the PRHχ^2 and Q statistics are independent of the assumed value of the variance $\langle s^2 \rangle$.

An optimal reconstruction $\hat{s}(t)$ of the underlying signal $s(t)$ can be found by minimizing the squared difference $\langle [\hat{s}(t) - s(t)]^2 \rangle$ between them for each time. PRH1 show that

$$\hat{s}(t) = \sum_{ij} \langle s(t_j) s(t) \rangle \mathsf{A}_{ij} (y_i - \bar{y}). \tag{4.12}$$

Thus the optimal reconstruction $\hat{s}(t)$ can be found from $y(t)$ once A_{ij} is known.

4.3 Dispersion Analysis

The dispersion analysis technique was developed by Pelt *et al.* (1994) and Pelt *et al.* (1996), hereafter P94, P96.

The dispersion method compares the flux densities of nearby points in the light curve, and sums their squared differences over the whole curve. To measure the dispersion, the light curves from the A and B images are first combined at a trial time delay τ_{AB} and trial flux ratio R. For this combined set of points, the dispersion is

$$\mathcal{D}(\tau_{AB}, R) = \frac{\sum_{ij} W_{ij} Z_{ij} (a_i - b_j)^2}{2 \sum_{ij} W_{ij} Z_{ij}}, \tag{4.13}$$

with weighting terms

$$Z_{ij} = \begin{cases} 1 - \frac{|t_i - t_i|}{\Delta} & \text{if } |t_i - t_j| \leq \Delta \\ 0 & \text{if } |t_i - t_j| > \Delta \end{cases} \tag{4.14}$$

and

$$W_{ij} = \frac{W_i W_j}{W_i + W_j}, \tag{4.15}$$

where $W_i = 1/e_i^2$ is the statistical weight for each observation. The pairs included in this sum are all AB pairs in the combined curve with separation less than Δ, which is of order 2N pairs. The Z_{ij} term, a modification to P94 added by P96, decreases the weight on pairs with larger separations, and is essential for making the dispersion a smooth function of time

delay. For the analysis in Chapter 5, the value of Δ was assumed to be 60 days for the radio light curves, and 7 days for the optical light curves. This weighting is in effect a type of covariance model, where points less than Δ days apart are expected to have identical flux densities, and points more than Δ days apart can have any flux density difference. The minimum of $\mathcal{D}$ with respect to trial values of τ_{AB} and R gives the estimate of the time delay and flux ratio.

P94 also define a statistic $\mathcal{I}$ to show the effects of the removal of points,

$$\mathcal{I}(l, m, \tau_1, \tau_2) = \mathcal{D}(l, m, \tau_1) - \mathcal{D}(l, m, \tau_2), \tag{4.16}$$

where l is the location in the list of observations where m points are removed. The statistic compares the dispersion at two different delays (τ_1 and τ_2) when certain points are removed, indicating whether those points favor one particular delay or another. P94 discussed mainly the case of $m = 2$ points, $\tau_1 = 536$ days, and $\tau_2 = 415$ days. They found that $|\mathcal{I}|$ was large when 1990 April 10 and 1990 May 7 were removed, and on this basis removed these observations.

The P94 $\mathcal{I}$ statistic is different from the pseudo-jackknife test (described in §4.6.3). When using $\mathcal{I}$, two neighboring points are removed, instead of just one point at a time. More importantly, $\mathcal{I}$ only checks whether $\tau_{AB} = 415$ days or $\tau_{AB} = 536$ days is a better fit, while the pseudo-jackknife test determines the *best* delay for each data set. Finally, even if two points are found to strongly affect the value of the time delay, that does not mean the points should be excluded from the analysis. It may just mean that the points are very influential to the final result (for instance, if they occur during a rise or fall in the light curve).

4.4 Discrete Correlation Function Analysis

The discrete correlation function was developed by Edelson & Krolik (1988), and modified by Lehár *et al.* (1992, hereafter L92). See White & Peterson (1994) and Litchfield, Robson, & Hughes (1995) for a current discussion of the discrete correlation function in comparison with the interpolated cross correlation function of Gaskell & Sparke (1986, method 2 in

Table 1.1).

A cross-correlation function was one of the first statistical techniques used to find the time delay. The peak in the correlation between two signals in time should be a reasonable estimate of the delay between them. However, serious errors can result if the signal is irregularly sampled or if interpolation is used (Falco *et al.* 1991b; PRH1; L92), so the correlation function needs to be modified to handle a discrete set of points rather than a continuously measured function. In this method, the correlations are found directly from discrete pairs of points in the A and B light curves, then binned according to the time separation between the A and B points. The binned correlations are normalized according to the contents of the bin. Thus the locally normalized discrete correlation function is

$$\mathcal{L}(\tau_{AB}) = \frac{1}{n_*} \sum_{ij} \frac{(a_i - \bar{a}_*)(b_j - \bar{b}_*)}{[(\sigma_{a*}^2 - e_a^2)(\sigma_{b*}^2 - e_b^2)]^{1/2}}, \tag{4.17}$$

where n_* is the number of pairs in the bin, $\bar{x}_*$ and σ_{x*} are the mean and standard deviation of the x_i in the bin, and e_x are the measurement errors. The sum is over all AB pairs such that

$$\tau_{AB} - \frac{\Delta\tau_{AB}}{2} \leq |t_i - t_j| \leq \tau_{AB} + \frac{\Delta\tau_{AB}}{2}. \tag{4.18}$$

where $\Delta\tau_{AB}$ is the size of the delay bin around τ_{AB}. The number of pairs in this calculation is of order $N/2$. Since the mean and variance may not be constant for the entire light curve (*i.e.* the curve may not be stationary), they are calculated separately for each delay bin. Since the correlation is binned by definition, it cannot be determined independently for all values of the delay. Decreasing the bin size improves the resolution with respect to τ_{AB}, but also increases the error for each bin. In Chapter 5 a bin size of 30 days is used for the radio light curves. To find the time delay more precisely than the bin size, a cubic polynomial is fitted to the peak of $\mathcal{L}(\tau_{AB})$. Unfortunately, the fitted peak is very sensitive to the delay range used for the fit, see §5.1.5.

An advantage of the discrete correlation function is that it is independent of the flux ratio and is only a function of time delay. To obtain the flux ratio, the two curves are combined at the fitted delay, then the flux ratio is adjusted to minimize the summed dispersion between the curves (where the dispersion at each observed time is computed using a linear

interpolation of the adjacent points from the other curve).

4.5 Units

Although the light curve measurements in Table 3.1 are reported in mJy, all of the real and synthetic light curve data were converted to logarithmic units for time delay analysis. This has been done in order to be consistent with PRH2, who chose a logarithmic scale for analysis of the 6 cm light curves so that it would be similar to the optical magnitude scale. Thus, the 6 cm and 4 cm data are analyzed in units of decibels relative to 1 Jy, or "dBJ" units. For a flux density y measured in Jy, written $y_{\rm Jy}$, the flux density in dBJ is

$$y_{\rm dBJ} = 10 \log_{10} \left(\frac{y_{\rm Jy}}{1\,{\rm Jy}} \right). \tag{4.19}$$

The error on $y_{\rm dBJ}$ in dBJ is found by considering the change in $y_{\rm dBJ}$ for a fractional change of $y_{\rm mJy}$. The conversion between the fractional linear error $e_{\rm lin}$ (*i.e.* the change in $y_{\rm mJy}$ divided by $y_{\rm mJy}$) and the logarithmic error $e_{\rm dBJ}$ is then

$$\begin{aligned} e_{\rm dBJ} &= -10 \log_{10}(1 - e_{\rm lin}) \\ e_{\rm lin} &= 1 - 10^{-(e_{\rm dBJ}/10)}. \end{aligned} \tag{4.20}$$

For example, a fractional change of $e_{\rm lin} = 0.02$ (*i.e.* 2%) is equivalent to a logarithmic error of $e_{\rm dBJ} = 0.088\,{\rm dBJ}$.

In these logarithmic units, the effect of the flux ratio between the A and B images becomes an additive factor, rather than the multiplicative factor used for linear units. For the linear flux ratio

$$R = \frac{b_{\rm mJy}}{a_{\rm mJy}}, \tag{4.21}$$

the B image flux density b is shifted to b' at the level of the A image flux density by dividing by R,

$$b'_{\rm mJy} = \frac{b_{\rm mJy}}{R}. \tag{4.22}$$

For logarithmic dBJ units, the B image flux density is shifted to

$$b'_{\rm dBJ} = b_{\rm dBJ} - 10\log_{10}(R), \tag{4.23}$$

and for optical magnitude units, it is shifted to

$$b'_{\rm mag} = b_{\rm mag} + 2.5\log_{10}(R). \tag{4.24}$$

4.6 Synthetic Data

In order to determine the uncertainty in the time delay estimates found by various techniques, several batches of synthetic light curves were made. These are defined and discussed here, then used in Chapter 5. The way in which the synthetic data are made and how they interact with the time delay analysis method may affect the uncertainty estimate, see §4.7.

4.6.1 Gaussian Process Monte Carlo Data

For each of the light curves ($\mathcal{Y}_6$, $\mathcal{Y}'_6$, $\mathcal{Y}_4$, see Chapter 5), a set of 500 Gaussian Monte Carlo light curve pairs were made. Each Monte Carlo light curve pair was given the same observation times as the corresponding real light curve pair. The Monte Carlo curves were made to be a stationary Gaussian process with the same mean as the real light curves, and are characterized by the same structure function as that assumed for the real light curves in Chapter 5. The measurement errors were modeled as Gaussian random variables with zero mean and the same RMS as the measurement errors found for the real data. The data were then given a randomly chosen time delay and flux ratio, uniformly distributed in the ranges 300 to 600 days in delay and 0.68 to 0.72 in ratio. The same list of 500 τ_{AB}, R pairs was used for the $\mathcal{Y}'_6$ and $\mathcal{Y}_4$ Monte Carlo data, to allow uncertainty analysis for the joint radio light curves.

In Chapter 5, these 500 Gaussian Monte Carlo data sets are used to determine the uncertainty in the time delay and flux ratio values found for the real light curves. This is done by determining the fitted delay and ratio for each of the 500 data sets, and then finding the differences between the fitted and true delays (and the fitted and true flux ratios). The

median of the fitted-minus-true values measures the bias in the result, and this value is subtracted from the fitted delay and ratio of the real data. The 68% confidence interval is found by counting out 170 data sets on both sides of the median (enclosing 68% of the points), then adjusting the interval for the bias by subtracting the median.

Ideally, Monte Carlo data should be made to have *all* of the statistical properties of the real light curves. The real light curves are probably not a stationary Gaussian process with Gaussian random errors. The only way to create synthetic data with all the properties of the real data is to derive the synthetic light curves directly from the real ones. The next section discusses ways to do this.

4.6.2 Bootstrap and Jackknife Techniques

For a non-ordered data set, *i.e.* a set of measurements that is not ordered in time or any other variable, synthetic data can be made by using *jackknife* or *bootstrap* techniques. To jackknife a data set of N measurements, each individual measurement is removed one by one from the data set, creating N synthetic data sets of $N-1$ measurements each. To bootstrap the same data, N measurements are randomly chosen from the data set with replacement (an individual measurement can be chosen more than once), creating an arbitrary number of synthetic data sets of N measurements each. These synthetic data have many of the same statistical properties as the original data set. Statisticians have shown that if the original measurements are independent and identically distributed (*i.i.d.*), the synthetic data made by jackknife or bootstrap techniques can be used to estimate the uncertainty in the analysis of the original data (see Efron & Tibshirani 1986, 1993).

Unfortunately, a time series is ordered by definition, and in general is correlated in time. This means that the measurements are *not* independent and identically distributed. The idea of using bootstrap or jackknife techniques on a stationary time series has been discussed in the statistics literature (Carlstein 1986; Kunsch 1989; Liu & Singh 1992; Lahiri 1992; and Politis & Romano 1992), in an attempt to find a property of the time series which is *i.i.d.*. There are two main ways of doing this. One is to create a model of the variation in time (such as a polynomial fit), then assume that the errors between the model and the data are *i.i.d.* and apply the bootstrap to the errors. The result can be dependent on the

model chosen, and the assumption that such errors are *i.i.d.* should be checked carefully. P94, P96, and Bar-Kana (1997) used this method to create synthetic light curves.

The second way is to break the time series into blocks of data, assume that the blocks are *i.i.d.*, then remove, resample, or shuffle the blocks (rather than the individual data points). The method requires that the blocks be long enough so that two observations separated by the block size are independent. The result can be dependent on the block size used. Experimentation with block shuffling on the 6 cm light curves showed that it did not work well for this time series, due to the highly correlated measurements. The resulting synthetic light curves had sharp changes in flux density at the edges between blocks which were uncharacteristic of the real curves.

Both of these time series bootstrapping techniques have an additional problem when applying them to gravitational lens light curves. When assuming a model light curve shape before bootstrapping the residuals, the time delay and ratio are also assumed (so that the same shape applies to both curves). When shuffling blocks, the delay must be removed before shuffling and reinserted afterwards in order for the curves to be copies of each other. Thus, neither technique is independent of time delay.

Because of the dependence on the delay and modeled light curve shape, a formal bootstrap or jackknife analysis was not done.

4.6.3 Pseudo-Jackknife Data

A set of *pseudo-jackknife* synthetic data was also made for each light curve pair. For a light curve of N points, each individual observation was removed from the curve one by one, creating N jackknife light curves of $N-1$ points each. Since the jackknifed points are correlated and not *i.i.d.*, the pseudo-jackknife does not allow the application of the results statisticians have found for the jackknife and bootstrap statistics. Despite this, the pseudo-jackknife light curves are useful in two important ways. First, it is a way of making synthetic light curves that include all the statistical properties of the real data, without assuming the curves are stationary or a Gaussian process. In this sense, it can be used as a check on the error estimate found from the Gaussian Monte Carlo data. Second, it is a response to Pelt *et al.* (1994), who removed the two points from the 6 cm curve that

had the most influence on the time delay. The pseudo-jackknife data allow a more formal analysis of the effect of leaving out points, and can be used to determine the dependence of a statistic on individual points.

4.7 Comparative Discussion of Techniques

The statistical techniques described in this chapter each have different advantages and disadvantages. Ideally, all the techniques would agree on the time delay between a particular pair of light curves, but this is often not the case (see Table 1.1 and Haarsma *et al.* 1997). In such situations, one is forced to choose between the results based on the merits of the methods themselves.

The PRHQ statistic has the advantage of using all of the data in the light curves ($4N^2$ pairs). Each point is compared to every other point, and the difference is checked for consistency with the covariance model, rather than just comparing every point to its nearest neighbors and checking if the difference is zero. The method is less dependent on the exact features of the light curve than the other methods, and instead relies on the statistical properties of the underlying quasar emission and the measurement error. The formalism and rigor underlying the method and the goodness-of-fit measures that accompany the result are also advantages. The use of PRHQ reduces the impact of sampling on the result (but the method still has a slight tendency to anti-align gaps in the curves, see §5.1.2, Figure 5-9). However, PRHQ, as applied here, requires two important assumptions about the data: that the light curve is statistically stationary (assumed when one covariance model was fit for the whole light curve), and that the covariance model correctly describes the variations in the light curve. The choice of covariance model for the PRHχ^2 or Q analysis has little effect on the fitted delay, but it can have a significant effect on the smoothness of the the function PRH$\chi^2(\tau_{AB}, R)$ and on the confidence interval found from Monte Carlo analysis (see §5.1.3).

The dispersion method does not assume that the light curves are stationary. It does assume that nearby points will have identical flux densities if their separation is less than Δ (60 days for the radio curves), which corresponds to assuming the structure function in the

PRH method. The dispersion only uses about $2N$ pairs of points in the calculation. While the original version of the dispersion given in P94 produced a very rough function $\mathcal{D}(\tau_{AB}, R)$, the weighting modifications of P96 have made the dispersion function much smoother so that there is a convincing, but broader, global minimum.

The discrete correlation function has the advantage of being completely independent of the flux ratio, since it fits only in delay. It assumes that the light curves are stationary within each delay bin, and assumes that nearby points will have similar flux densities. The number of pairs going into a calculation is on the order of $N/2$. The correlation is dominated by the non-performing parts of the signal, such as linear ramps and flat sections, rather than the sharper features (thus, non-linear variability is more important for this method than the others). This method may tend to favor delays that align gaps in the light curves. Because of the bin size, the correlation has poor resolution in delay, and a function must be fit to the binned correlations to determine the peak. For the light curves analyzed in Chapter 5, the correlation is broad for delays of interest, thus the fitted peak is highly dependent on the range used for the fit (see §5.1.5). This is a major disadvantage of the discrete correlation method.

Given these arguments, none of the methods is obviously superior to the others. If forced to choose, however, the rigor and goodness-of-fit measures of the PRH method are strong advantages, while the fitting range problem in the discrete correlation function is a significant disadvantage. It seems important to try both the PRH and dispersion methods on each light curve, since these two methods have a very different set of assumptions and can be a good check on each other. If forced to choose between the PRH and dispersion methods, the advantages of the PRH method seem greater, yet this is a matter of opinion. The discrete correlation function would also be an interesting check, since it has yet a different set of assumptions, but it does not have a clear peak for the light curves studied so it is less useful. Obviously, the problem disappears if all of the statistical methods agree on the same result. This has happened for light curves with a sharp event (Kundić *et al.* 1997), and for Gaussian Monte Carlo data (see below). But for light curves with slowly changing features or non-Gaussian properties, the methods often produce different results and a choice between them must be made.

Finally, the methods interact with the Gaussian Monte Carlo data in different ways. As described in §4.6.1, the Monte Carlo light curves are made to be a Gaussian process with a particular covariance model. Since the PRH method compares these light curves to precisely that covariance model, the method is well able to recover the delay and ratio inserted in the Monte Carlo data. The dispersion and discrete correlation methods, however, do not use the covariance model, but rely more on the specific features of a given light curve pair to determine the delay. Inspection of the Gaussian Monte Carlo light curves revealed some of them to be composed of long, slow changes over the whole curve, or to have an ambiguity between similar features in two parts of the curve. This can create a dispersion minimum up to 250 days from the true delay (§5.2.2). The discrete correlation function also does a poor job of recovering the delay in such light curves. Although all three methods agree, on average, about the time delays inserted in stationary, Gaussian Monte Carlo light curves (with $\sim$5% uncertainty), they can disagree by $\sim$15% on the time delay for the real light curves (Haarsma *et al.* 1997). This indicates that the real light curves may have non-Gaussian properties. To improve the statistical analysis of the light curves beyond what is described in this Chapter, the non-Gaussian characteristics of the time series need to be incorporated into the analysis. Note, however, that the arrival of more clear features in the light curves can be enough to determine the time delay clearly, in spite of non-Gaussian properties.

Chapter 5

Time Delay Results

In this chapter, the three types of time delay analysis defined in Chapter 4 are applied to the light curves. Section 5.1 describes the results for the 6 cm light curves, §5.2 gives the results for the 4 cm light curves, and §5.3 gives the results for the 6 and 4 cm light curves together. In §5.4, the optical light curves of Kundić *et al.* (1997) are presented, and the time delay is found from the 6 cm, 4 cm, and optical curves together. The results of all the analysis are summarized in §5.5 and Table 5.1.

As explained in §4.5, the radio light curves are converted to dBJ units for time delay analysis, a logarithmic scale similar to the magnitude units used for the optical light curves. The full 6 cm light curves will be referred to as the data vector $\mathcal{Y}_6$. The same data set with four points from Spring 1990 removed (see §5.1.1, 5.1.2) is referred to as $\mathcal{Y}_6'$. Other lengths of the 6 cm light curves will be referred to by the number of points, N. The 4 cm light curves are denoted $\mathcal{Y}_4$, and the optical light curves observed with a g band filter are denoted $\mathcal{Y}_g$.

5.1 6 cm Light Curves

This section is based on the time delay analysis of an earlier version of the 6 cm light curves presented in Haarsma, Hewitt, Lehár, and Burke (1997, *ApJ* **479**, 102).

5.1.1 PRHχ^2 Analysis of 6 cm Light Curves, Old Covariance Model

The PRHχ^2 and PRHQ statistics are defined in §4.2.

Initially, the full 6 cm light curves $\mathcal{Y}_6$ were analyzed using exactly the same technique that Press, Rybicki, & Hewitt (1992c, hereafter PRH2) applied to the 6 cm light curves with N=80 points. The same structure function was assumed,

$$V(T) = 8.28 \times 10^{-5}\,\mathrm{dBJ}^2 \left(\frac{T}{1\,\mathrm{day}}\right)^{1.06}, \tag{5.1}$$

and the same error estimate,

$$e_A = 0.047\,\mathrm{dBJ} = 1.08\%, \quad e_B = 0.088\,\mathrm{dBJ} = 2.01\%. \tag{5.2}$$

The fit of this structure function to the point estimates v_{ij} (found directly from $\mathcal{Y}_6$) is shown in Figure 5-1.

Applying this covariance model to $\mathcal{Y}_6$ and using a downhill simplex search, or "amoeba" (Press *et al.* 1992a), the delay and ratio minimizing PRHχ^2 was found. The PRHχ^2 surface is plotted in Figure 5-2. For 277 degrees of freedom (2N minus three for τ_{AB}, R, and $\bar{y}$), the global minimum is PRHχ^2 = 391 at τ_{AB} = 453 days and R = 0.6987. This time delay is much shorter than the delay PRH2 found from the first 80 data points ($\tau_{AB} = 548^{+19}_{-16}$ days, 95% confidence interval). The estimate of the delay has changed significantly with the addition of new features to the light curves.

There are, however, several reasons to be suspicious of this result for $\mathcal{Y}_6$. First, the structure function shown in Figure 5-1 is a poor fit for lags of 100-1000 days, the expected range of the delay where it must fit well. Also, the point estimates are larger than the power law at the shortest lags, indicating the values of e_A and e_B are too small (see eq. 4.9). (Recall that the fit is expected to be poor at long lags due to uncorrelated parts of the signal and to individual features in the curves, see §4.2).

Second, for 277 degrees of freedom and Gaussian light curves, $\chi^2 \geq 391$ is a poor fit, with a probability of 0.0007%. If the real light curves are indeed a Gaussian process with Gaussian noise, then PRHχ^2 can be used in this way as a measure of goodness-of-fit. Even

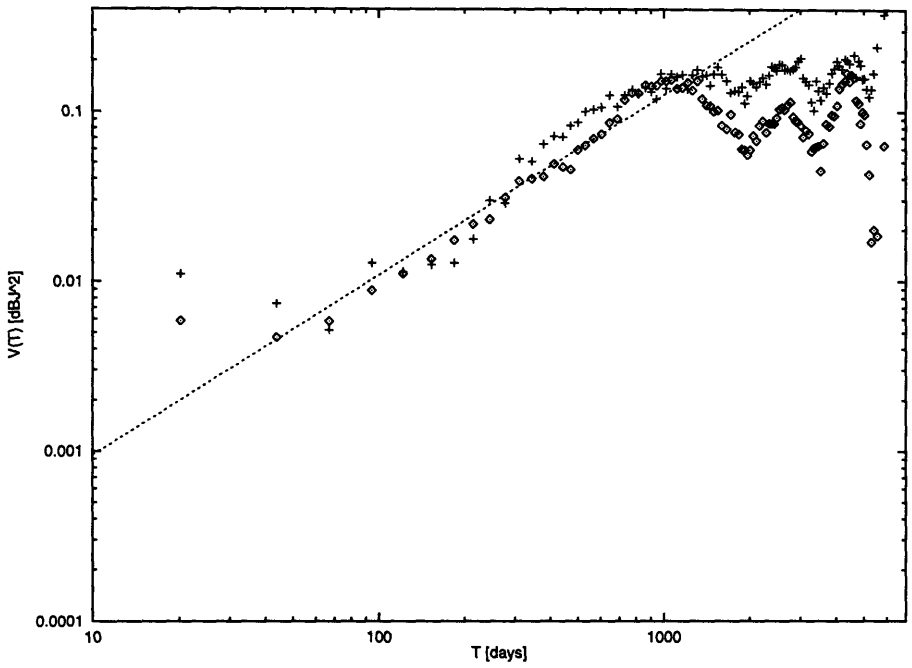

Figure 5-1: Point estimates of the structure function for $\mathcal{Y}_6$. The diamonds are from the A light curve, and the crosses are from the B light curve. The dotted line is the structure function found by PRH2.

if not, PRHχ^2 of the A light curve alone plus PRHχ^2 of the B light curve alone should be similar to PRHχ^2 of the combined curve, if the covariance model, delay, and ratio are correct. Here, PRHχ^2=171 (for A) plus PRHχ^2=152 (for B) equals 323. If 323 degrees of freedom are assumed, the probability of $\chi^2 \geq 391$ is still only 0.56%. For the N=80 6 cm light curves, PRHχ^2 was also larger than the degrees of freedom, but the probability (8%) was more acceptable (PRH2).

Third, the PRHχ^2 surface has several secondary minima, including one at $\tau_{AB} \simeq 530$ days with PRH$\chi^2 \simeq 415$, and another at $\tau_{AB} \simeq 400$ days with PRH$\chi^2 \simeq 400$. While the minimum at$\tau_{AB} = 455$ days is formally more significant than the other minima, it still raises some doubt about which is the best delay for the data set.

Finally, the optimal reconstructions of the individual A and B light curves of $\mathcal{Y}_6$, shown in Figure 5-3 indicate problems. The reconstruction of the A image light curve has a lot of short time scale variation. By eye, one would guess that many of the small fluctuations in the

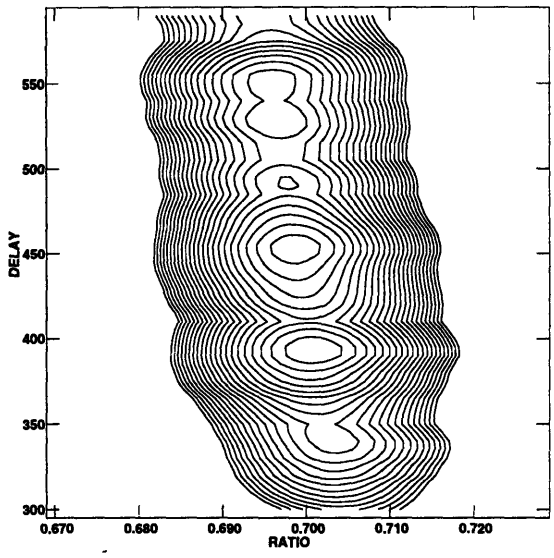

Figure 5-2: The PRHχ^2 surface for $\mathcal{Y}_6$ using the PRH2 covariance model. The global minimum is PRH$\chi^2 = 391$ at $\tau_{AB} = 453$ days and $R = 0.6987$, for 277 degrees of freedom. Contours start at PRHχ^2=395 and increase by 5 to 505.

real data are measurement error, but the PRH2 covariance model causes the reconstruction to interpret them as signal. Figure 5-4 shows the differences between the real data and the optimal reconstruction. For both light curves, the one σ error bars of the reconstruction have been scaled to equal unity, and this scale has been applied to the flux densities and errors of the corresponding real observations. There are two epochs where the observations and the reconstruction disagree significantly. Around Julian Day 2450000, both images have several σ differences between the data and the reconstruction. Higher deviations in both images also occur elsewhere in the curve (such as around Julian Day 2445000), whenever observations are also more frequent than once per month. This is an indication that the reconstruction is less able to follow the variations (due primarily to measurement error) that occur on time scales of less than a few weeks. The largest deviation in the A image in Figure 5-4 is 1995 September 15, which had neighboring observations 6 days before and 8 days after, rather than the typical one month between observations. An increase in the

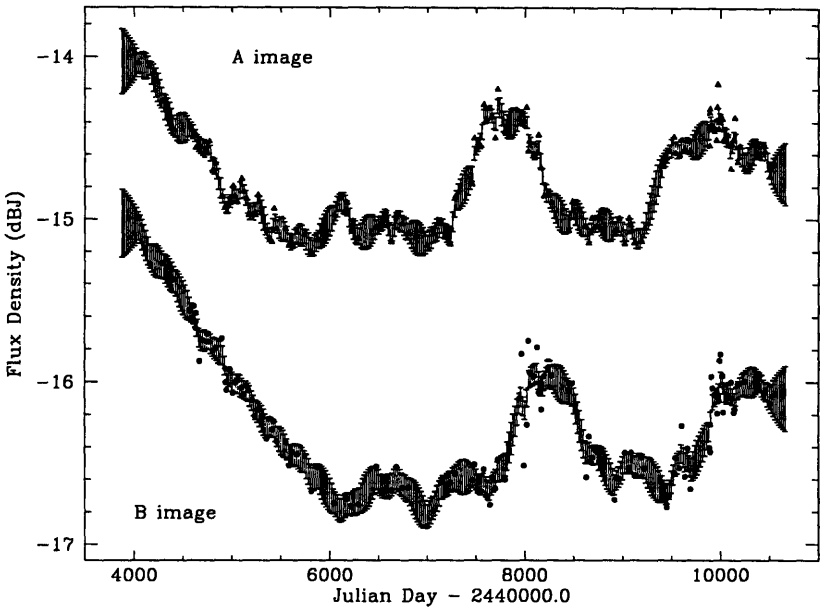

Figure 5-3: Optimal reconstruction of the $\mathcal{Y}_6$ light curves, using the PRH2 covariance model. The gray region is the one σ error about the reconstruction.

sampling rate such as this does not seem a good argument for exclusion of the observation, so the data around Julian Day 2450000 were not removed from the analysis.

The other epoch where the observations and reconstruction disagree is around Julian Day 2448000 (in Spring 1990), only in the B image. The observations in this epoch occurred about once a month, not significantly more often than usual, and the deviation only occurs in the B image. In §3.3, these points were noted as unusual just by inspection of the light curves, and the raw data reduction was shown to be free of problems. When attempting to fit a structure function to the individual light curves, none could be found that provide a fit good for both the Spring 1990 points and the rest of the B light curve. These points definitely have *different* statistical properties than the rest of the B light curve. Since the difference is not due to data problems or frequent sampling, this is evidence that a different (or additional) physical process is at work during this epoch than during the rest of the B image light curve.

The above concerns are indications that the assumed structure function and measure-

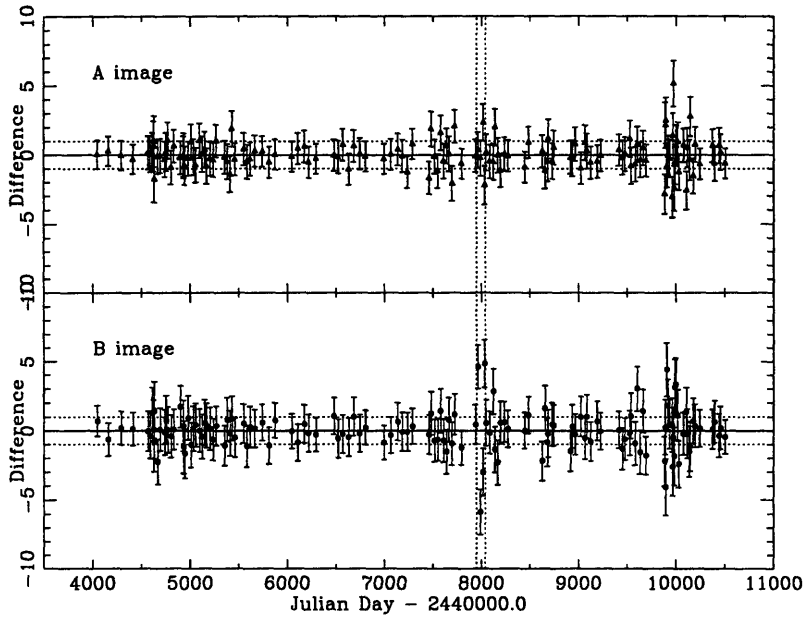

Figure 5-4: Differences between the real data and the optimal reconstruction for the $\mathcal{Y}_6$ light curves, using the PRH2 covariance model. The observed data points and their errors were normalized so that the one σ band about the optimal reconstruction was unity, marked by the dashed lines. The epoch later removed is marked with dashed lines.

ment error (Eqs. 5.1 and 5.2), found by PRH2 for the N=80 light curves, are not a good covariance model for $\mathcal{Y}_6$; the additional observations since 1990 give more information about the variability, allowing an improved covariance model to be made.

Since the optimal reconstructions of the B image data points from Spring 1990 shows that these data are modeled incorrectly even in the individual curve, they are removed to avoid confusing the analysis of the combined curve. Thus, the entire analysis is done both for the complete light curves ($\mathcal{Y}_6$) and the light curves with four consecutive observations from Spring 1990 removed: 1990 March 15, 1990 April 10, 1990 May 7, and 1990 May 23 (this data set will be denoted $\mathcal{Y}_6'$). In Haarsma *et al.* (1997), the 1990 February 19 observation was also removed (even though it has a small difference with the reconstruction), to avoid selecting the first rise rather than the second rise of the B image in Spring 1990 (see §3.3). Since then, analysis of the 4 cm curves (§5.2) and the optical curves (Kundić *et al.* 1997)

has shown conclusively that the delay is consistent with the first rise, not the second. Thus the 90Feb19 observation is now included in the time delay analysis. Both the A and B measurements are removed at each of these times, since the software has not been adapted to handle A and B light curves of differing lengths; these A image points do not occur during a crucial feature in the light curve, so their removal will probably not affect the result. All of the following analysis has been done with two versions of the 6 cm light curve, $\mathcal{Y}_6$ and $\mathcal{Y}_6'$.

5.1.2 PRHQ Analysis of 6 cm Light Curves, New Covariance Model

With the removal of the Spring 1990 points from the B image light curve, the $\mathcal{Y}_6'$ light curves are a more homogeneous data set for which a single covariance model can accurately describe the underlying physical process for both light curves. For correctness, the PRHQ statistic is used rather than PRHχ^2 (see §4.2).

The new covariance model was made using an iterative process. Initially, the measurement errors for the A and B light curves were assumed to be 0.088 (or 2%), based on §3.4. The point estimates v_{ij} were then found for both light curves. The estimates were fit to a power law in the range 100 to 700 days, giving an estimate of V_0 and α. This structure function was then used to adjust the measurement errors, so that the PRHχ^2 fit of the individual curves to the structure function was equal to the degrees of freedom. This entire process was repeated until the errors and structure function stopped changing. The process converged more smoothly when only half the correction was made at each step. The resulting structure function for $\mathcal{Y}_6'$ is

$$V(T) = 1.985 \times 10^{-6}\,\mathrm{dBJ}^2 \left(\frac{T}{1\,\mathrm{day}}\right)^{1.665}, \tag{5.3}$$

with measurement errors

$$e_A = 0.082\,\mathrm{dBJ} = 1.87\%, \quad e_B = 0.100\,\mathrm{dBJ} = 2.28\%. \tag{5.4}$$

The fit of this structure function to the point estimates v_{ij} is shown in Figure 5-5. This covariance model has larger measurement errors and a larger exponent when compared with

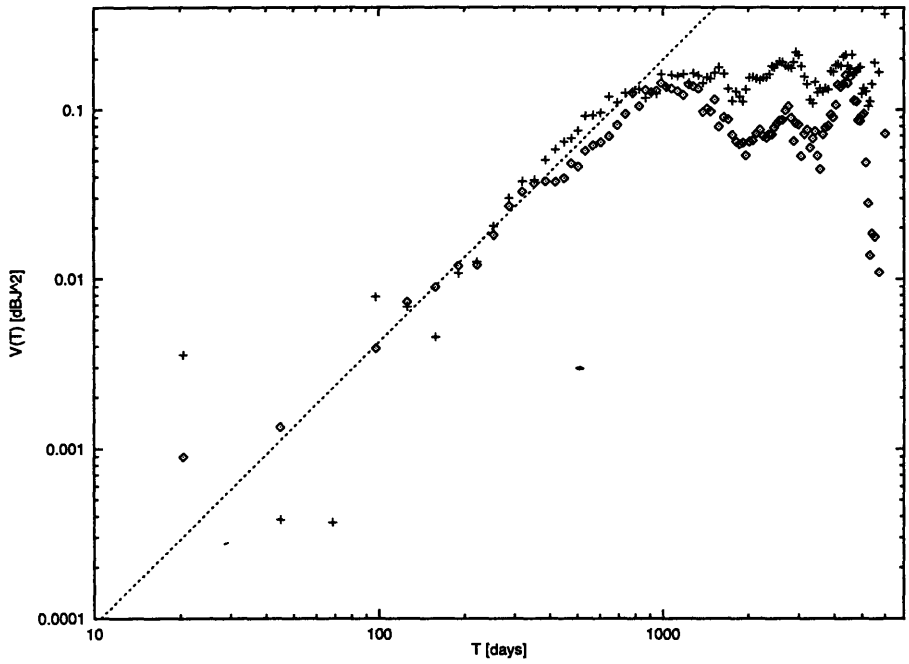

Figure 5-5: Point estimates of the structure function for $\mathcal{Y}_6'$. The diamonds are from the A light curve, and the crosses are from the B light curve. The dotted line is the new fit for the structure function.

both the PRH2 model (eqs. 5.1, 5.2), and the model for the 6 cm N=107 light curves in Haarsma *et al.* (1997). The larger error estimates are probably a result of later points in the curve having larger errors than earlier points (the increased scatter at later times can be seen in the light curves themselves, Figure 3-5). This increased error could be due to the later observations being split between time at 4 cm and time at 6 cm. The increase in α is also a result of the larger errors: if larger errors are subtracted off in the point estimates, the slope of the fitted structure function becomes steeper (see Figure 5-1), explaining the increase in α for later structure function fits.

Using the new covariance model, the delay and ratio minimizing PRHQ were found for $\mathcal{Y}_6'$. The Q surface in delay and ratio is shown in Figure 5-6. The minimum of the surface was found using a downhill simplex search to be $Q = -905$, at $\tau_{AB} = 448$ days, $R = 0.6988$, and $\chi^2 = 280$. (The PRHχ^2 surface is very similar, with the values of χ^2, τ_{AB}, and R at the minimum all having the same values within the significant digits.) When the bias and 68%

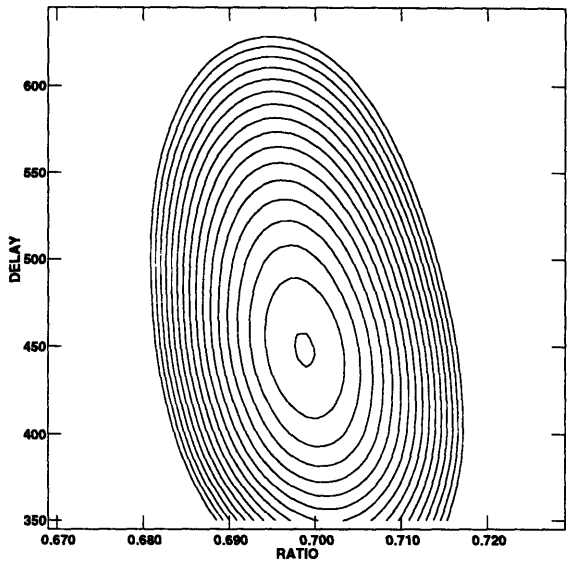

Figure 5-6: The PRHQ surface for the $\mathcal{Y}_6'$ light curves, using the new covariance model. The global minimum is $Q = -905$ at $\tau_{AB} = 448$ days and $R = 0.6988$. Contours start at -905 and increase by 5 to -825.

confidence intervals are found using the 500 $\mathcal{Y}_6'$ Gaussian process Monte Carlo data sets, the delay and ratio are

$$\tau_{AB} = 449^{+19}_{-18} \text{ days}, \quad R = 0.6990^{+0.0025}_{-0.0025} \quad (\mathcal{Y}_6', \text{PRH}Q). \tag{5.5}$$

The value of the delay for $\mathcal{Y}_6'$ found with PRHQ is very similar to that obtained for $\mathcal{Y}_6$ with PRHχ^2. This time, however, the result is more reliable for several reasons. First, the structure function fit shown in Figure 5-5 is better in the lag range 100 to 700 days, and the point estimates follow the power law a bit better at short lags.

Second, the value of PRHχ^2 at the Q minimum is 280, with a probability of 30.7% that $\chi^2 \geq 280$ for 269 degrees of freedom (272 minus 3 for τ_{AB}, R, and $\bar{y}$). If the curves are consistent with a Gaussian process, then PRHχ^2 can be used as a measure of goodness of the Q fit, because the $\log|\mathsf{B}|$ term is a constant for a given covariance model and sampling, and thus Q will have the same distribution as PRHχ^2. (The PRHχ^2 of the individual curves

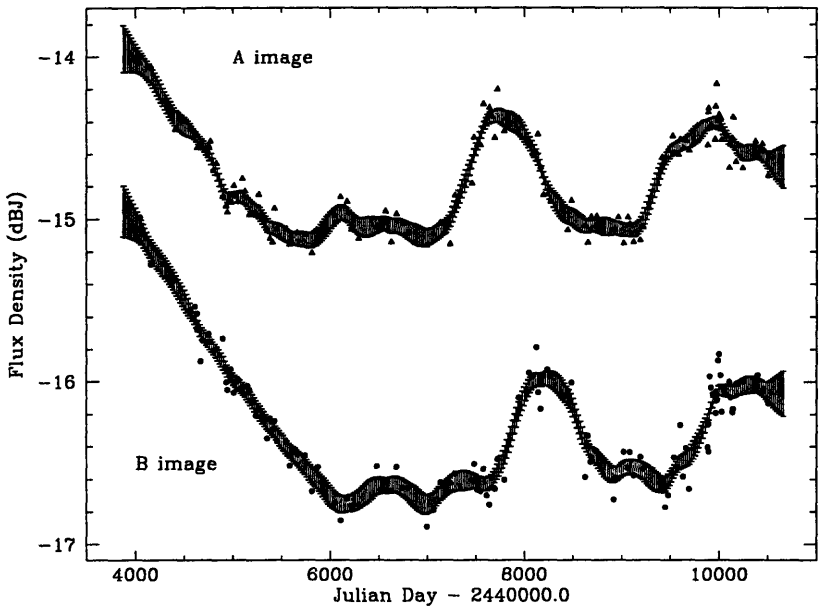

Figure 5-7: Optimal reconstruction of $\mathcal{Y}_6'$ light curves, using the new covariance model. The gray region is the one σ error about the reconstruction.

was already used to determine e_A and e_B, so it can no longer be used as a check on the goodness of fit.)

Third, both the Q and PRHχ^2 surfaces for $\mathcal{Y}_6'$ with the new covariance model are smooth and have a single minimum, without the secondary minima that characterized the analysis of $\mathcal{Y}_6$ using the old covariance model. Note that the width of the global minimum has also increased in delay space.

Finally, the optimal reconstructions of the individual $\mathcal{Y}_6'$ curves are shown in Figure 5-7. The reconstruction of the $\mathcal{Y}_6'$ A light curve has less short time scale power than the corresponding $\mathcal{Y}_6$ curve, agreeing with the guess by eye that most of the short time scale activity is measurement error rather than signal. The differences between the reconstruction and the original data are shown in Figure 5-8; the differences are similar to Figure 5-4, except all of the data now fall further from the reconstruction and the Spring 1990 points have been removed.

To test the impact of sampling on the time delay, an "ersatz" or "window function"

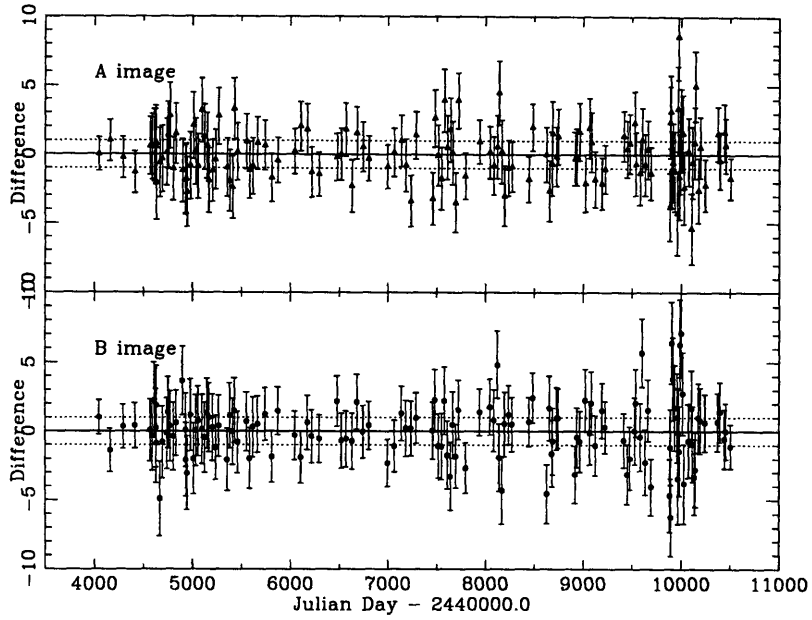

Figure 5-8: Differences between the real data and the optimal reconstruction for $\mathcal{Y}_6'$ light curves, using the new covariance model. The observed data points and their errors were normalized so that the one σ band about the optimal reconstruction was unity, marked by the dashed lines.

data set was made, in which the light curves have the same sampling as the real data but constant flux density. The Q statistic for the ersatz data is plotted in Figure 5-9, along with the Q statistic for the real data (where the flux ratio has been set to $R = 0.6988$). The ersatz data show a mild peak at about 480 days, corresponding to the VLA configuration cycle. Delays of 480 days are excluded most strongly because at that delay there is the most overlap between the A and B light curves. Thus, the real data show a minimum at a time delay of ~450 days *in spite of* the sampling effects.

With the covariance model derived from the $\mathcal{Y}_6'$ data in hand, the $\mathcal{Y}_6$ light curves can be analyzed. The Q surface for $\mathcal{Y}_6$ is shown in Figure 5-10. Notice that the surface is much smoother than in Figure 5-2. Thus, the change between Figures 5-2 and 5-6 was due to the new covariance model, *not* to the removal of points (or to the use of Q instead of PRHχ^2,

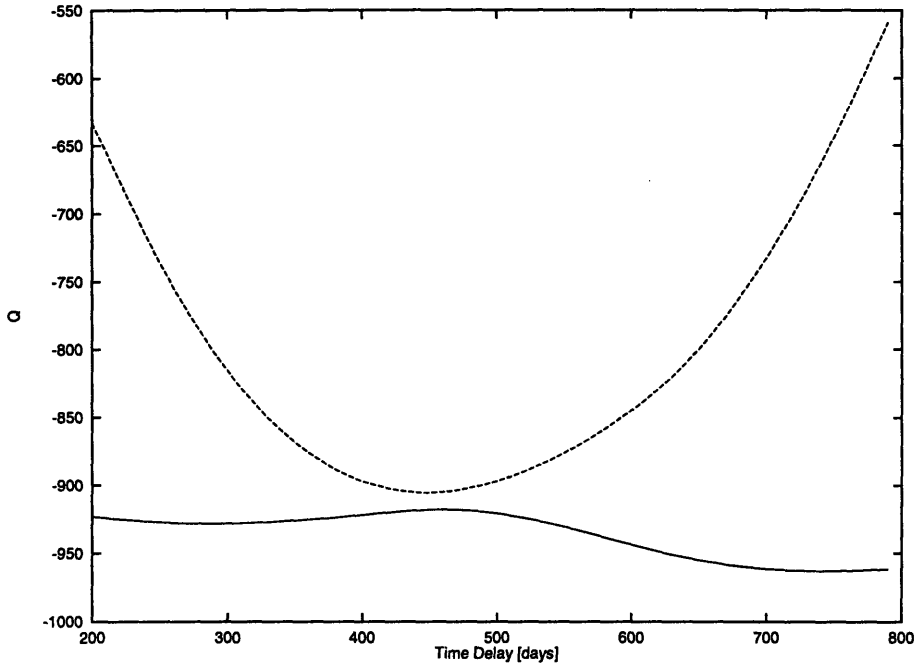

Figure 5-9: PRHQ for $\mathcal{Y}_6'$ ersatz data (solid line) and real data (dotted line, flux ratio set to $R = 0.6988$.)

since $\log|\mathrm{B}|$ is nearly flat over the surface). The minimum of the $\mathcal{Y}_6$ surface is $Q = -896$ at $\tau_{AB} = 454$, $R = 0.6982$, and PRH$\chi^2 = 326$. When the 500 $\mathcal{Y}_6$ Gaussian process Monte Carlo data sets are analyzed with the same procedure, the bias and confidence intervals are found and the delay and ratio are

$$\tau_{AB} = 451^{+16}_{-18}\,\mathrm{days}, \quad R = 0.6981^{+0.0019}_{-0.0026} \quad (\mathcal{Y}_6, \mathrm{PRH}Q). \tag{5.6}$$

For 277 degrees of freedom (2N minus three for τ_{AB}, R, and $\bar{y}$), the probability of $\chi^2 \geq 326$ is 2.3%, a significant improvement over the fit with the PRH2 covariance model. The $\mathcal{Y}_6$ A image light curve with the new covariance model has PRH$\chi^2 = 142$, and the B light curve has PRH$\chi^2 = 175$; thus the B image is the cause of the bad fit, as expected since the Spring 1990 points are included. The optimal reconstructions of the $\mathcal{Y}_6$ A and B curves, using the new covariance model, are comparable to Figures 5-7 and 5-8, except the Spring 1990 points are more than five σ away from the reconstruction.

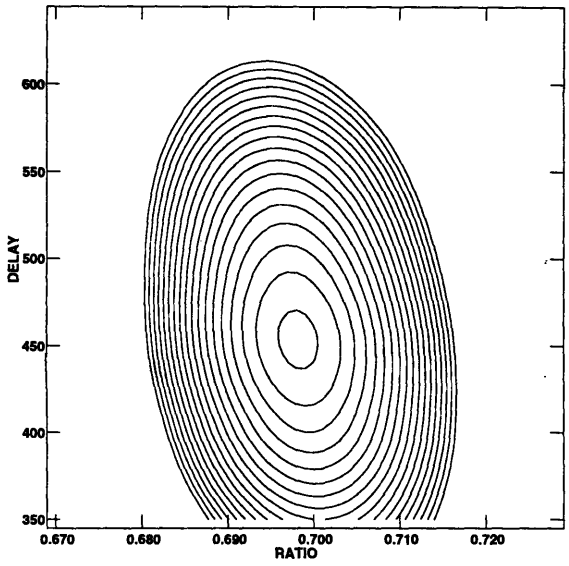

Figure 5-10: The PRHQ surface for the $\mathcal{Y}_6$ light curves, using the new covariance model. The global minimum is $Q = -896$ at $\tau_{AB} = 454$, and $R = 0.6982$. Contours start at $Q = -895$ and increase by five to -810.

Finally, the pseudo-jackknife data for the $\mathcal{Y}_6$ and $\mathcal{Y}_6'$ light curves were analyzed using PRHQ. Delays for the $\mathcal{Y}_6$ pseudo-jackknife sets were scattered between 449 and 463 days (-5 and $+9$ days from the delay found above for the real data), except for the four Spring 1990 data sets which shifted the delay by as much as -13 to $+7$ days. This scatter is less than the confidence interval from the Gaussian Monte Carlo data. For the $\mathcal{Y}_6'$ pseudo-jackknife data, where the four points of Spring 1990 were already removed, the delays were scattered between 443 and 455 days (-5 and $+7$ days from the real data), except removal of 1992 January 6 shifted the delay estimate by $+13$ days to 461 days. This is not surprising, since 1992 January 6 is the first point after the flux density decrease in the B image in 1991, and the alignment of this feature with the A image decrease in 1990 is essential to the calculation of the delay. The removal of no single point caused the time delay estimate to shift by as much as the confidence interval which was obtained from the Gaussian Monte Carlo data. The scatter in time delays obtained from the pseudo-jackknife data, which has all

the properties of the real data (including any non-Gaussian characteristics), is confirmation that the confidence intervals determined from the Gaussian Monte Carlo data are roughly correct.

5.1.3 Discussion of PRH Technique

The time delay estimate found using PRHχ^2 has changed significantly since Press, Rybicki, & Hewitt (PRH2) applied their analysis to the first 80 data points in the VLA light curves (N=80). The change is due to the new features that have entered the light curves, particularly the flux density decrease in both images in 1990-91 and the increase in both images in 1994-95. For comparison, the 6 cm N=80 light curves, and the N=80 light curves with five Spring 1990 points removed (N=75), were reanalyzed with both the old and new covariance models. With the old model, the N=80 and N=75 PRHχ^2 surfaces have local minima (around 455 and 600 days), and the global minimum in both cases is around 550 days. With the new covariance model, the N=80 and N=75 PRHχ^2 surfaces are smooth, with a single minimum at about 540 days. The minimum is also much broader with the new covariance model, corresponding to the larger confidence interval. *Since removing points and changing the covariance model has little effect on the best-fit delay in any version of the light curves, the change in the delay estimate since 1992 is not due to the new covariance model or to the removal of certain points, but to the additional features.* Also, the choice of covariance model was found to have little effect on the value of the best fit time delay (confirming the finding of PRH1), but it does have a significant effect on the smoothness of the PRHχ^2 surface and the confidence interval.

5.1.4 Dispersion Analysis of 6 cm Light Curves

The time delay of the $\mathcal{Y}_6$ light curves was also found using the dispersion method, defined in §4.3. Figures 5-11 and 5-12 show the dispersion surface in delay and ratio for $\mathcal{Y}_6$ and $\mathcal{Y}_6'$, respectively. In order to find the global minima of the surfaces, a downhill simplex search was used. To avoid local minima, ten "amoeba" searches were started at various locations in the surface, and the deepest point found was taken as the global minimum. The global minimum for the $\mathcal{Y}_6$ light curves was $\mathcal{D} = 0.01120\,\mathrm{dBJ}^2$ at $\tau_{AB} = 429$ days and $R = 0.6999$.

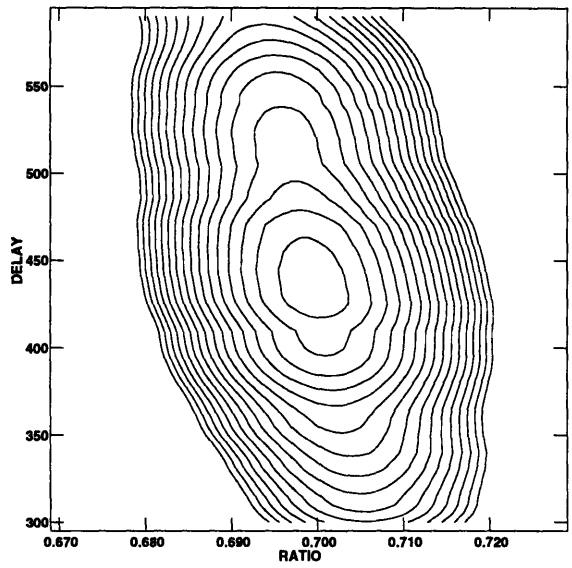

Figure 5-11: The dispersion surface for $\mathcal{Y}_6$ light curves. The global minimum is $\mathcal{D} = 0.01120\,\mathrm{dBJ}^2$ at $\tau_{AB} = 429$ days and $R = 0.6999$. Contours start at 0.0115 and increase by 0.0005 to 0.0190.

The number of AB pairs used in the calculation of the dispersion at the minimum was 388. The bias and the 68% confidence intervals were found from the 500 $\mathcal{Y}_6$ Gaussian Monte Carlo data sets, giving

$$\tau_{AB} = 428^{+26}_{-30}\,\mathrm{days}, \quad R = 0.7000^{+0.0029}_{-0.0030} \quad (\mathcal{Y}_6, \mathrm{Dispersion}). \tag{5.7}$$

The global minimum for $\mathcal{Y}'_6$ was $\mathcal{D} = 0.00894\,\mathrm{dBJ}^2$ at $\tau_{AB} = 424$ days and $R = 0.7012$. The number of pairs used in the calculation at the minimum was 372. The bias and the 68% confidence intervals were determined from the 500 $\mathcal{Y}'_6$ Gaussian Monte Carlo data sets. When the bias is taken into account, the result and its error is

$$\tau_{AB} = 425^{+27}_{-28}\,\mathrm{days}, \quad R = 0.7013^{+0.0031}_{-0.0030} \quad (\mathcal{Y}'_6, \mathrm{Dispersion}). \tag{5.8}$$

The results can be compared to the dispersion analysis of earlier versions of the light

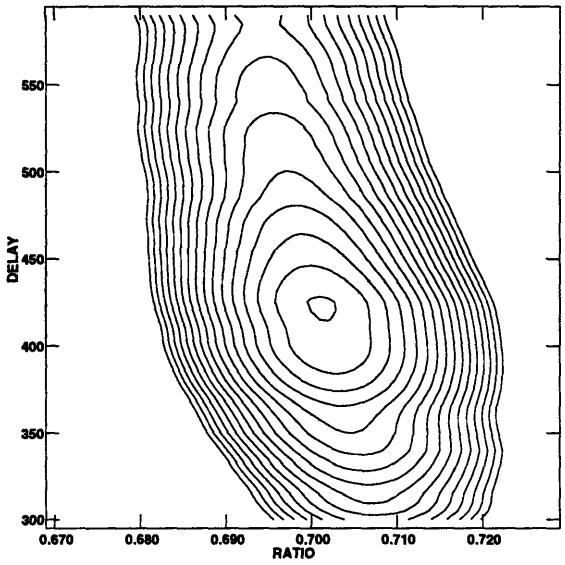

Figure 5-12: The dispersion surface for the $\mathcal{Y}_6'$ light curves. The global minimum is $\mathcal{D} = 0.00894\,\mathrm{dBJ}^2$ at $\tau_{AB} = 424$ days and $R = 0.7012$. Contours start at 0.0090 and increase by 0.0005 to 0.0165.

curves. The minimum dispersion for the N=80 6 cm light curves, with no points removed, is at 616 days. Pelt *et al.* (1994) found that this minimum shifts to 421 days when the 1990 April 10 and 1990 May 7 observations were removed. When all five Spring 1990 points are removed from the N=80 data set, the minimum shifts to 555 days. In Haarsma *et al.* (1997), the removal of 5 points from the N=112 light curves shifted the minimum from about 440 to about 400 days. Thus, removal of these key points from shorter versions of the 6 cm curves changed the delay significantly. With the current light curves, the value of the delay is about 425 days for both the full light curves $\mathcal{Y}_6$ and for the curves with four points removed $\mathcal{Y}_6'$, although the results of pseudo-jackknife analysis show that removal of these points still has an effect.

The dispersion analysis of the $\mathcal{Y}_6$ pseudo-jackknife data found minima at a few particular delay values, rather than a random scatter over a range of delays. About half of the data sets had a minimum dispersion close to 442 days, and about half were close to 428 days. The

result for $\mathcal{Y}_6$ was about 428 days, but this jackknife test indicates it is very unstable and that a delay of 442 days would be almost as consistent with the data. The $\mathcal{Y}_6'$ pseudo-jackknife data also had delays at a few particular values, but most were close to 424 days, the delay for the real data. There were 18 data sets with minima close to 427 days (+3 days from the minimum for the real data), three sets close to 420 days (−4 days from the real data), and five sets scattered to as short as 398 days. The results of the dispersion pseudo-jackknife test have significantly less scatter than the results of the Gaussian Monte Carlo analysis, and are useful here mainly for detecting instabilities in the data.

Using the $\mathcal{I}$ statistic, P94 and P96 found that the removal of the 1990 April 10 and 1990 May 7 observations from the N=80 data set shifted the delay to a shorter value. This is no longer the case for the $\mathcal{Y}_6$ data set with these two points removed (the delay estimate stays at 424 days). So the delay estimate is less dependent on these two points now than it was for the shorter light curve.

5.1.5 Discrete Correlation Analysis of 6 cm Light Curves

The locally normalized discrete correlation function $\mathcal{L}$, or correlation, is defined §4.4. The values of $\mathcal{L}$ for the $\mathcal{Y}_6$ light curves are plotted in Figure 5-13, with the correlation and its error shown for each delay bin, along with the cubic fit to the peak in the range 180-720 days. The maximum correlation of 0.979 is at $\tau_{AB} = 447$ days, where about 100 pairs were used in the calculation. The fitted flux ratio for this delay is $R = 0.6976$. The discrete correlation for $\mathcal{Y}_6'$ is shown in Figure 5-14, with a cubic fit again in the range 180-720 days. The maximum correlation of 1.008 is at $\tau_{AB} = 437$ days, where about 90 pairs were used in the calculation. For this delay, the fitted flux ratio is $R = 0.6987$. Note that the removal of the Spring 1990 points causes a larger correlation at lags around 600 days, and shifts the fitted peak to a shorter value.

Unfortunately, there is reason to doubt these delay estimates. In Figures 5-13 and 5-14, the discrete correlation is broad in the range 300-600 days, without a clearly defined peak. The values of $\mathcal{L}$ itself do not clearly discriminate between delays of interest. Thus the result for the time delay depends strongly on the cubic fit to the peak, in particular on the range of delays over which the fit is made. For example, the correlation analysis of the 6 cm light

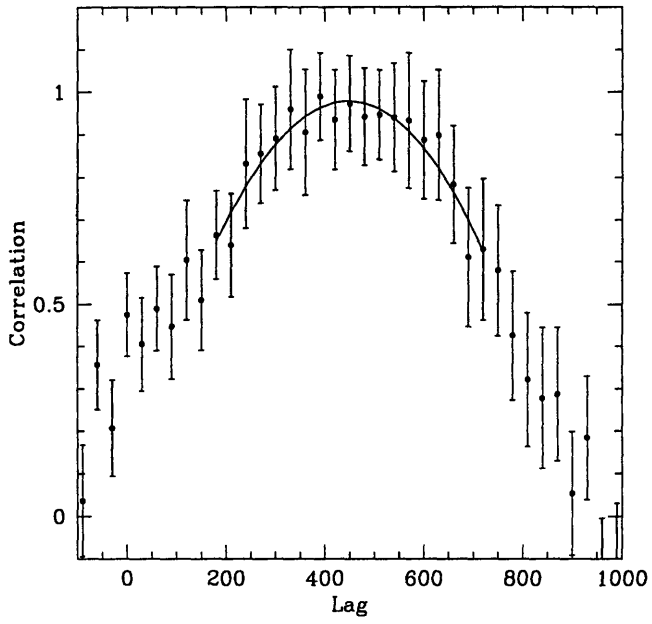

Figure 5-13: Discrete correlation for the $\mathcal{Y}_6$ light curves, and the cubic polynomial fit in the range 180 to 720 days. The peak correlation was 0.979 is at $\tau_{AB} = 447$ days.

curves in Haarsma *et al.* (1997) depended on the range of the fit in this way: for a fitting range of 180-660 days, the fitted peak to $\mathcal{L}$ for the N=112 light curves is 436 days, and for the N=107 curves is 405 days. For a range of 240-720 days, the peak for N=112 is 463 days and for N=107 is 412 days. Thus changing the range shifted the delay estimate by up to 27 days.

Given the dependence of τ_{AB} on fitting range, how should the range be chosen? In Haarsma *et al.* (1997), the range was chosen for the real and Monte Carlo data by first smoothing the values of $\mathcal{L}$ (with a boxcar of 100 days), finding the peak of the smoothed values, and selecting a range ±250 days around that peak. Thus, the values published in Haarsma *et al.* were the 240-720 fit of the N=112 data, and the 180-660 fit of the N=107 data. There are, however, other ranges that could be used for the fit that look just as reasonable to the eye, or even better, than these fits. In general, smaller fitting ranges give a fit that follows the detailed structure at the peak, whereas larger ranges give a fit that follows the larger trends. The center of the range also affects which features are best fit.

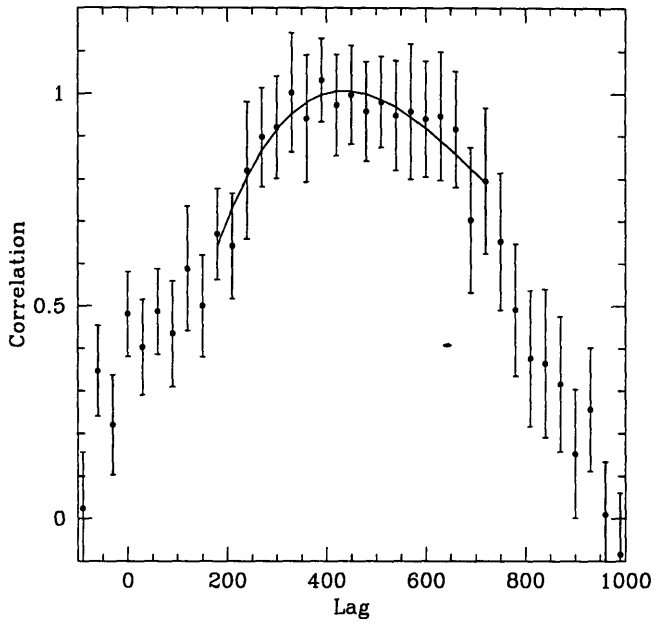

Figure 5-14: Discrete correlation for the $\mathcal{Y}_6'$ light curves, and the cubic polynomial fit in the range 180 to 720 days. The peak correlation was 1.008 at $\tau_{AB} = 437$ days.

Thus, the choice of fitting range is somewhat subjective.

Since the error bars on $\mathcal{L}$ indicate that the detailed features are less significant than the larger trends, a larger fitting range of 180-720 days was selected for the fit reported above and shown in Figures 5-13 and 5-14. For comparison, the fitted peak for a range of 180-660 days was 438 days for $\mathcal{Y}_6$, and 417 days for $\mathcal{Y}_6'$ (this range follows closely the details of the peak for $\mathcal{Y}_6'$). For a range of 240-720 days, the fitted peak of the $\mathcal{Y}_6$ correlation was 462 days, and of the $\mathcal{Y}_6'$ correlation was 441 days. For all of these ranges, the peak is at a shorter delay for $\mathcal{Y}_6'$ than for $\mathcal{Y}_6$, so the removal of the Spring 1990 feature definitely has an effect.

The dependence on the choice of fitting range causes two problems. First, it introduces a subjective element into the analysis, decreasing the reliability of the result. Second, the time needed to check the fitting range for each of the 500 Monte Carlo data sets and the jackknife data becomes prohibitive, so the confidence interval on the result cannot be estimated. Given these difficulties, discrete correlation analysis of the Gaussian Monte Carlo

and jackknife light curves was not done. Since the Monte Carlo analysis in Haarsma *et al.* (1997) found larger errors for the discrete correlation method than for the PRH or dispersion methods, neglecting this method will not significantly affect the conclusions for the time delay.

5.2 4 cm Light Curves

5.2.1 PRHQ Analysis of 4 cm Light Curves

In order to analyze the 4 cm light curves, denoted $\mathcal{Y}_4$, with PRHQ, a covariance model for the 4 cm curves must be found. A similar iterative process was used as for the $\mathcal{Y}_6'$ light curves above (§5.1.2). In the $\mathcal{Y}_4$ case, the structure function was significantly different for the A and B light curves, due to the difference in the features in the two light curves: the first three points in the B image curve define the initial fall, a feature not seen in the A image. The difference in the structure functions made it difficult for the iterative process to converge. Since these three B image points do not constrain the delay, the $\mathcal{Y}_4$ structure function was obtained with these points removed. The structure function converged to

$$V(T) = 4.884 \times 10^{-6}\,\mathrm{dBJ}^2 \left(\frac{T}{1\,\mathrm{day}}\right)^{1.702}, \tag{5.9}$$

with measurement errors,

$$e_A = 0.068\,\mathrm{dBJ} = 1.55\%, \quad e_B = 0.105\,\mathrm{dBJ} = 2.39\%. \tag{5.10}$$

The structure function and the point estimates are plotted in Figure 5-15. The fit is good in the lag range 100 to 700 days, and the point estimates follow the power law well at short lags, especially for the A image.

An attempt was made to refine this fit by iterating with the complete light curves (including the first three points in the B image), starting from the above solution, but the iterations were driven towards $e_B > 3\%$, with no indication that the fit was improving. Using the above covariance model with the full B image light curve gives $\chi^2 = 59$ for 51 degrees of freedom. Thus, the above covariance model is a reasonable fit to the full light

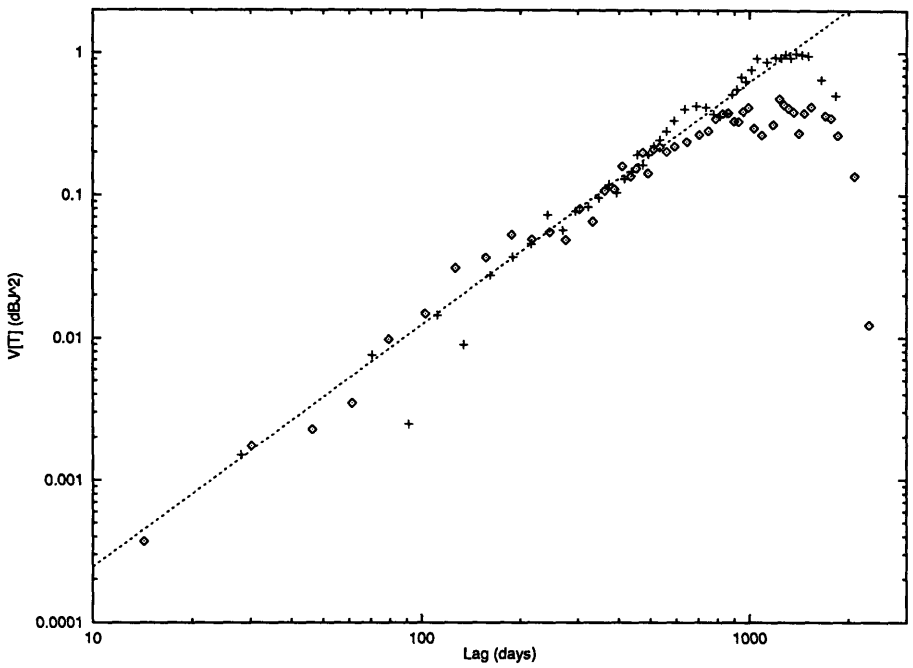

Figure 5-15: Point estimates of the structure function for $\mathcal{Y}_4$ with the first three points in the B image removed. The diamonds are from the A light curve, and the crosses are from the B light curve. The dotted line is the structure function fit.

curves.

The optimal reconstructions of the individual $\mathcal{Y}_4$ curves are shown in Figure 5-16, and look reasonable (there is no excess short time scale power, unlike the A image in Figure 5-3). The differences between the data and the reconstruction are shown in Figure 5-17. Again, during the epoch of most frequent observations the differences go up, but otherwise there is nothing unusual here. Even the first three points in the B light curve are well fit.

Using this covariance model, the delay and ratio minimizing PRHQ was found for the $\mathcal{Y}_4$ light curves using a downhill simplex search. The Q surface in delay and ratio is shown in Figure 5-18. The minimum of the surface is $Q = -332$ at $\chi^2 = 106$, $\tau_{AB} = 407$ days, and $R = 0.6959$. (The PRHχ^2 surface is very similar, with a minimum of $\chi^2 = 106$ at $\tau_{AB} = 406$ days, and $R = 0.6959$.) When the bias and 68% confidence intervals are found

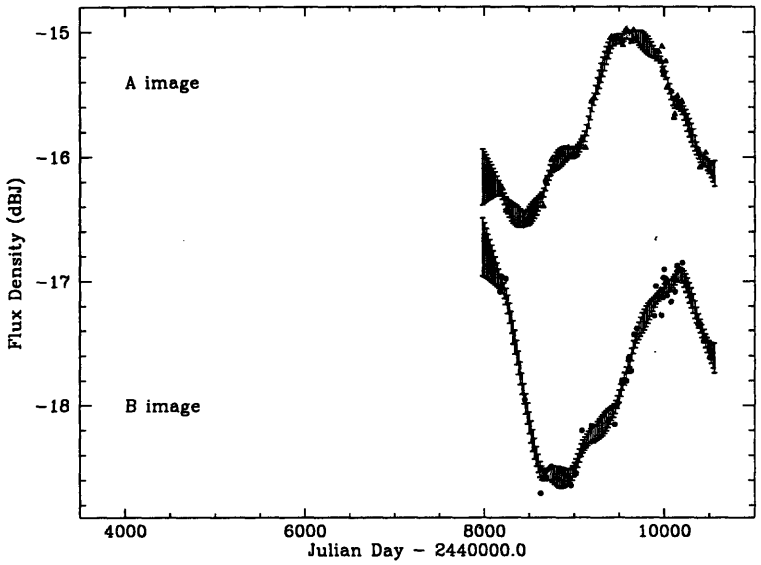

Figure 5-16: Optimal reconstruction of the $\mathcal{Y}_4$ light curves. The B image data and reconstruction have been shifted down by 0.5 dBJ to prevent overlap.

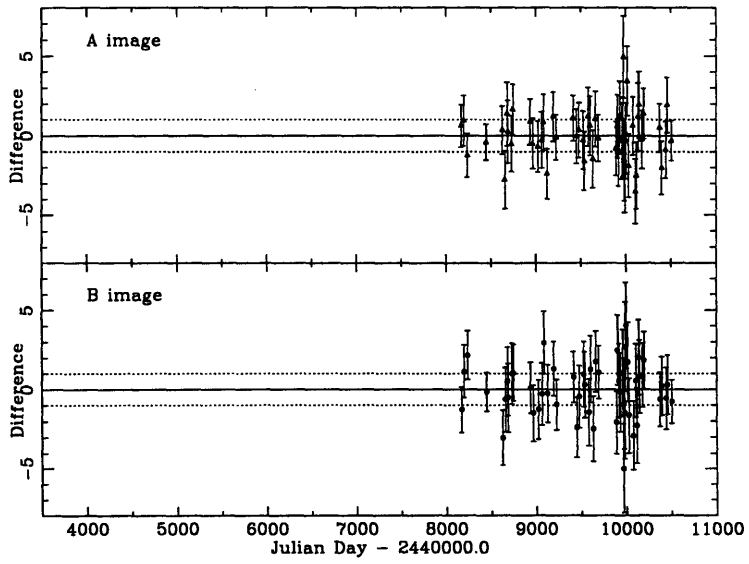

Figure 5-17: Differences between the real data and the optimal reconstruction for the $\mathcal{Y}_4$ light curves. The observed data points and their errors were normalized so that the one σ band about the optimal reconstruction was unity, marked by the dashed lines.

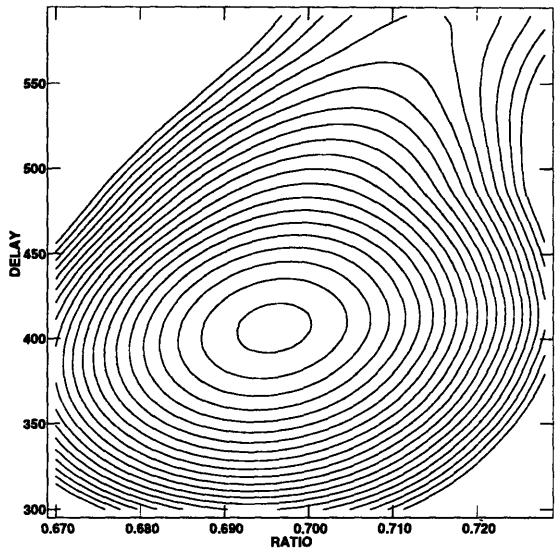

Figure 5-18: The PRHQ surface for $\mathcal{Y}_4$. The global minimum is $Q = -332$, at $\tau_{AB} = 407$ days, $R = 0.6959$. Contours start at $Q = -330$ and increase by 5 to -230.

using the 500 $\mathcal{Y}_4$ Gaussian process Monte Carlo data sets, the result is

$$\tau_{AB} = 407^{+21}_{-21} \text{ days}, \quad R = 0.6959^{+0.0045}_{-0.0041} \quad (\mathcal{Y}_4, \text{PRH}Q). \tag{5.11}$$

The value of PRHχ^2 at the Q minimum is reasonable, with a probability of 34.7% that $\chi^2 \geq 106$ for 101 degrees of freedom (104 minus 3 for $\tau_{AB}, R, \bar{y}$).

Both the Q and PRHχ^2 surfaces for $\mathcal{Y}_4$ are smooth and have a single minimum, although there is a small plateau at about 600 days. The minimum around 400 days is broader in delay than in ratio, in contrast with both $\mathcal{Y}_6$ and $\mathcal{Y}_6'$. The minimum is slanted so that larger delays correspond to larger ratios, which is an indication of the degeneracy between delay and ratio due to the long increase in the 4 cm light curves.

The 52 $\mathcal{Y}_4$ pseudo-jackknife data sets were analyzed with PRHQ, and had minima scattered from 404 to 412 days (or -3 to $+5$ days from the real delay). The scatter of the jackknife results is less than the confidence interval found from the Monte Carlo data sets.

5.2.2 Dispersion Analysis of 4 cm Light Curves

Figure 5-19 shows the dispersion surface in delay and ratio for $\mathcal{Y}_4$. The global minimum of the surface was found with a downhill simplex search. To avoid local minima, ten "amoeba" searches were started at various locations in the surface, using the deepest point found as the global minimum. The global minimum for $\mathcal{Y}_4$ was $\mathcal{D} = 0.00687\,\mathrm{dBJ}^2$ at $\tau_{AB} = 401$ days and $R = 0.6955$. The number of AB pairs used in the calculation of the dispersion at the minimum was 139. The bias and the 68% confidence intervals were found from the 500 $\mathcal{Y}_4$ Gaussian Monte Carlo data sets, giving

$$\tau_{AB} = 399^{+32}_{-30}\,\mathrm{days}, \quad R = 0.6957^{+0.0056}_{-0.0051} \quad (\mathcal{Y}_4, \mathrm{Dispersion}). \tag{5.12}$$

Of the 500 data sets, eighteen had dispersion minima over 150 days from the delay inserted in the data, which is the largest number of outliers of all the Gaussian Monte Carlo tests done. Inspection of these eighteen light curves showed that they tended to be one long increase or decrease, had a repeating feature in the emission that caused ambiguity about the delay, or had gaps in the curve that missed key features. The real $\mathcal{Y}_4$ data had none of these problems. Inspection of light curves for which the true delay was recovered showed them to more similar to the real light curves, with multiple unambiguous features. Thus the confidence interval found using the middle 68% of the 500 data sets is reasonably accurate for the real data. See §4.7 for further discussion on the interaction between Monte Carlo data and statistical methods.

When the dispersion is applied to the 52 $\mathcal{Y}_4$ pseudo-jackknife light curves, delays are mostly in the range of 399 to 402 days (or -2 to $+1$ days from the delay found for the real data). Removal of three data points shifts the delay up to as much as 409 days (or $+8$ from the delay for the real data). This spread is much less than the range found from dispersion analysis of the Gaussian Monte Carlo data.

5.2.3 Discrete Correlation Analysis of 4 cm Light Curves

The discrete correlation for the 4 cm light curves $\mathcal{Y}_4$ is plotted in Figure 5-20. The correlation and its errors are plotted for each delay bin, along with the cubic fit to the peak of the

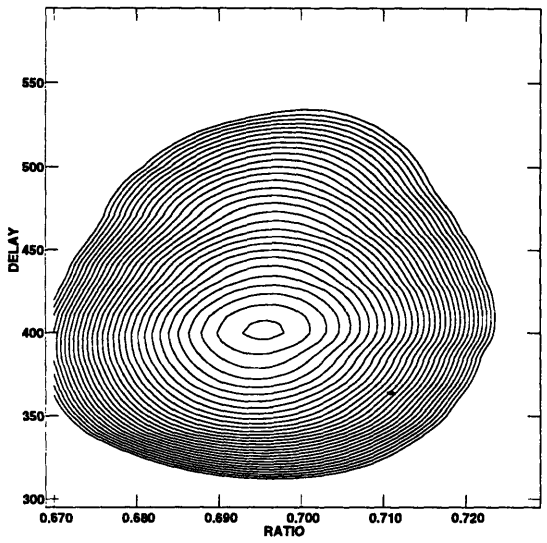

Figure 5-19: Dispersion surface for the $\mathcal{Y}_4$ light curves. The global minimum is $\mathcal{D} = 0.00687\,\mathrm{dBJ}^2$ at $\tau_{AB} = 401$ days and $R = 0.6955$. Contours start at 0.0070 and increase by 0.0005 to 0.0220.

discrete correlation in the range 210-600 days. This fitting range was chosen to follow the clear peak in $\mathcal{L}$ around 400 days, but ignore the peak around 600 days, based on the results of the PRHQ and dispersion analysis of $\mathcal{Y}_4$. The maximum correlation of 1.005 is at $\tau_{AB} = 411$ days, where about 35 pairs were used in the calculation. The fitted flux ratio for this delay is $R = 0.6945$. Analysis of the Gaussian Monte Carlo and jackknife data with the discrete correlation function was not done for reasons discussed in §5.1.5.

5.3 Joint Analysis of 6 cm and 4 cm Light Curves

In this section, the information in both the 6 cm and 4 cm radio light curves is brought together to determine the delay. The delay is assumed the same for both wavelengths, while the flux ratios (*i.e.* magnification) are allowed to be different for the two wavelengths (due to possible differences in the location and structure of the emission region). The discrete correlation analysis is not included, due to the problems discussed in §5.1.5. The

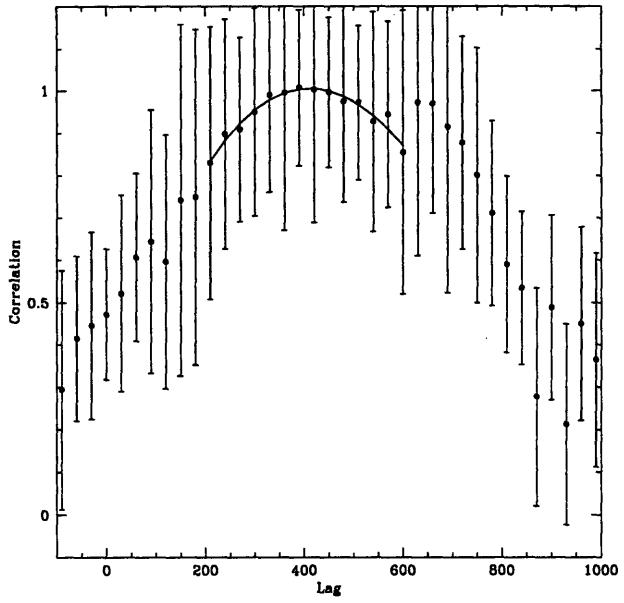

Figure 5-20: Discrete correlation for $\mathcal{Y}_4$ and the cubic polynomial fit in the range 210 to 600 days. The peak is 1.005 is at $\tau_{AB} = 411$ days.

Monte Carlo analysis was only done for $\mathcal{Y}_6'$ and $\mathcal{Y}_4$, not for $\mathcal{Y}_6$ and $\mathcal{Y}_4$, because it was too computationally intensive to be done for both versions, because the delay estimates from the corresponding real data did not change much between $\mathcal{Y}_6'$ and $\mathcal{Y}_6$, and because the confidence intervals for $\mathcal{Y}_6$ and $\mathcal{Y}_6'$ alone (without $\mathcal{Y}_4$) were similar for a given statistic. The $\mathcal{Y}_6'$ data was chosen over $\mathcal{Y}_6$ because for both the PRHQ and dispersion statistics, the analysis was less ambiguous for $\mathcal{Y}_6'$ ($\mathcal{Y}_6$ had poor PRHχ^2 values and large outliers in the optimal reconstruction, and the dispersion minimum was unstable as shown in the jackknife analysis). The pseudo-jackknife analysis was also not done here, since its benefits were mainly in detecting instabilities or understanding the impact of key features on the light curves for a given wavelength. Once these qualities are known for an individual wavelength, problematic areas (such as dispersion analysis of $\mathcal{Y}_6$, and the Spring 1990 points at 6 cm) can be avoided in the joint analysis of the two wavelengths together.

5.3.1 PRHQ Analysis of 6 cm and 4 cm Light Curves

The PRHQ method can be used in the following way to find the delay from both light curves at once. Both curves are compared to their respective covariance models (§5.1.2 and 5.2.1), and Q is found for each wavelength. The sum of Q for the two wavelengths, $Q_6 + Q_4$, is now the maximum likelihood estimator, and its minimum indicates the best fit. The search is made in three parameters: the time delay τ_{AB} (same for both wavelengths), and the two flux ratios R_6 and R_4 (assumed different for the two wavelengths).

The result of the PRH analysis of the $\mathcal{Y}_6'$ and $\mathcal{Y}_4$ data is a minimum of $Q_6+Q_4 = -1233$ at $\tau_{AB} = 419$, $R_6 = 0.6996$, $R_4 = 0.6966$, $\chi_6^2 = 283$, and $\chi_4^2 = 107$. The 500 Monte Carlo $\mathcal{Y}_6'$ and $\mathcal{Y}_6$ data sets were used to determine the bias and uncertainty, giving

$$\tau_{AB} = 420^{+13}_{-13}\,\text{days}, \quad R_6 = 0.6996^{+0.0021}_{-0.0024}, \quad R_4 = 0.6968^{+0.0036}_{-0.0036}$$
$$(\mathcal{Y}_6' \text{and} \mathcal{Y}_4, \text{PRH}Q). \tag{5.13}$$

Figure 5-21 shows $Q_6 + Q_4$ as a function of time delay, with the flux ratios set to the values at the minimum. The curve is very smooth, as is expected from the surfaces for the individual curves. The confidence interval on the delay is less than it was for either $\mathcal{Y}_6'$ or $\mathcal{Y}_4$, so combining the information from the two wavelengths refined the estimate.

Compared to the analysis of the curves individually, the minimum has shifted down 30 days from the $\mathcal{Y}_6'$ value, and up 12 days from the $\mathcal{Y}_4$ value. Note that the delay for the joint curves is closer to the 4 cm value than the 6 cm value; this can be seen in the PRHQ surfaces for the wavelengths individually (Figures 5-6 and 5-18), where the $\mathcal{Y}_4$ surface is less extended in delay than the $\mathcal{Y}_6'$ surface. The χ^2 values for each wavelength did not change much between the fit for the individual wavelengths and the fit for the wavelengths together: χ_6^2 increased by 3, χ_4^2 increased by 1.5. Thus, the goodness-of-fit for a delay of 419 days is of similar probability to the fit of $\mathcal{Y}_6'$ to 449 days or the fit of $\mathcal{Y}_4$ to 407 days. A delay of 419 days is well fit by both light curves.

When the same analysis is repeated for $\mathcal{Y}_6$ and $\mathcal{Y}_4$, the minimum is $Q_6+Q_4 = -1222$ at $\tau_{AB} = 423$, $R_6 = 0.6989$, $R_4 = 0.6966$, $\chi_6^2 = 331$, $\chi_4^2 = 108$. As in the individual curves, the inclusion of four points from Spring 1990 did not change the delay estimate significantly,

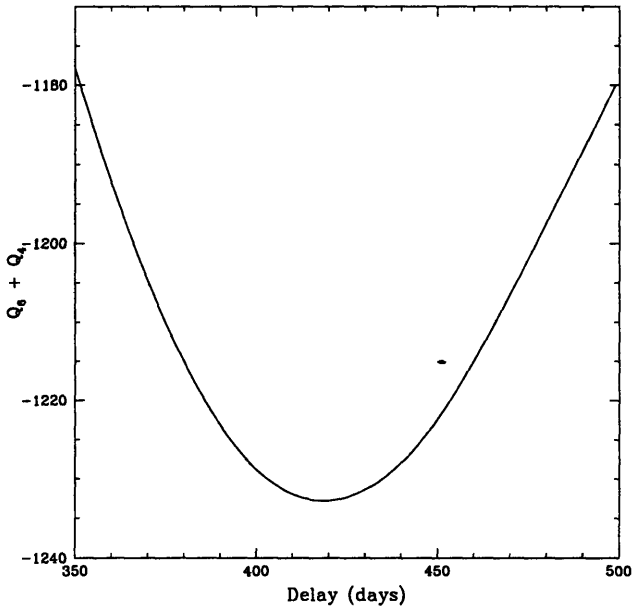

Figure 5-21: PRHQ as a function of τ_{AB} for $\mathcal{Y}_6'$ and $\mathcal{Y}_4$ light curves. The flux ratios are set at $R_6 = 0.6996$, $R_4 = 0.6966$. The minimum is $Q_6 + Q_4 = -1233$ at $\tau_{AB} = 419$.

but did increase χ_6^2.

5.3.2 Dispersion Analysis of 6 cm and 4 cm Light Curves

It is also possible to use the dispersion technique to study multiple light curves from different wavelengths. The sum of the dispersion for the individual curves, $\mathcal{D}_6 + \mathcal{D}_4$, is now the parameter to minimize. When applying the dispersion to the $\mathcal{Y}_6'$ and $\mathcal{Y}_4$ data, the minimum is $\mathcal{D}_6 + \mathcal{D}_4 = 0.01594$ at $\tau_{AB} = 401$, $R_6 = 0.7022$, and $R_4 = 0.6955$. When the same analysis is applied to the 500 $\mathcal{Y}_6'$ and $\mathcal{Y}_4$ Monte Carlo light curves, the bias and uncertainty are found, giving the result

$$\tau_{AB} = 401^{+23}_{-21}\,\text{days}, \qquad R_6 = 0.7024^{+0.0028}_{-0.0029}, \qquad R_4 = 0.6958^{+0.0048}_{-0.0046}$$
$$(\mathcal{Y}_6' \text{and} \mathcal{Y}_4, \text{Dispersion}). \tag{5.14}$$

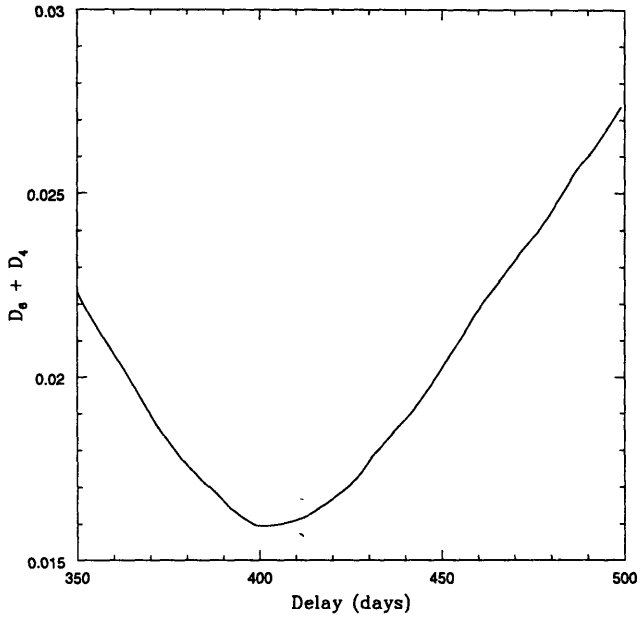

Figure 5-22: Dispersion as a function of τ_{AB} for $\mathcal{Y}_6'$ and $\mathcal{Y}_4$. The flux ratios are set at $R_6 = 0.7022$, $R_4 = 0.6955$. The minimum is $\mathcal{D}_6 + \mathcal{D}_4 = 0.01594$ at $\tau_{AB} = 401$.

Figure 5-22 shows $\mathcal{D}_6 + \mathcal{D}_4$ as a function of delay when the flux ratios are set at the fitted values. The line is impressively smooth.

Compared to the dispersion analysis of the curves individually, the delay estimate has stayed within 0.1 days of the delay found for $\mathcal{Y}_4$, rather than shifting to a compromise between the $\mathcal{Y}_6'$ and $\mathcal{Y}_4$ values. This can be seen from the dispersion surfaces for the two wavelengths (Figures 5-12 and 5-19, which are plotted with the same contour intervals). The surface for the 4 cm data is much steeper around the minimum than the 6 cm surface, so it will dominate the result for the surfaces added together.

When the dispersion is used to analyze the $\mathcal{Y}_6$ and $\mathcal{Y}_4$ data, the minimum is $\mathcal{D}_6 + \mathcal{D}_4 = 0.01875$ at $\tau_{AB} = 402$, $R_6 = 0.7008$, $R_4 = 0.6955$. This result is also dominated by the 4 cm curves, so the removal of the Spring 1990 points from the 6 cm curves does not have much of an effect.

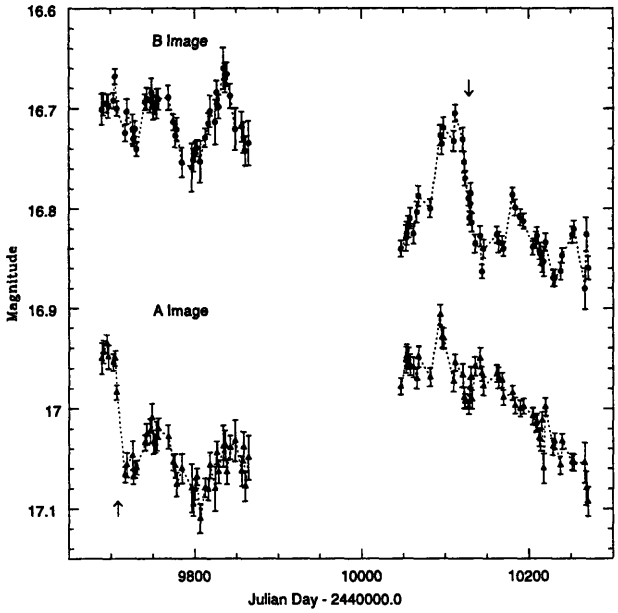

Figure 5-23: Optical light curves $\mathcal{Y}_g$, from Kundić *et al.* (1997). An offset of -0.1 mag has been applied to the B image to prevent overlap. Arrows indicate the sharp event in each image.

5.4 Joint analysis of Radio and Optical Light Curves

5.4.1 The Optical Data

In December 1994, the optical magnitude of the A image decreased sharply (by 0.1 mag over 10 days). A similar event occurred in the B image in February 1996, clearly indicating a short delay (less than 500 days between the A and B images). This event was recorded by three different groups monitoring 0957+561 at optical wavelengths: Kundić *et al.* (1995, 1997), Oscoz *et al.* (1996), and Schild & Thomson (1997). Kundić *et al.* have made their data set available electronically[1], so it was used in the analysis here. The monitoring occurred at two wavelengths (g and r bands), but the event was much more prominent in the g band so only that data is discussed in this thesis. The 97 observations in the g light curve, $\mathcal{Y}_g$, are shown in Figure 5-23.

[1]By anonymous ftp to `astro.princeton.edu`, in directory `elt/:0957`.

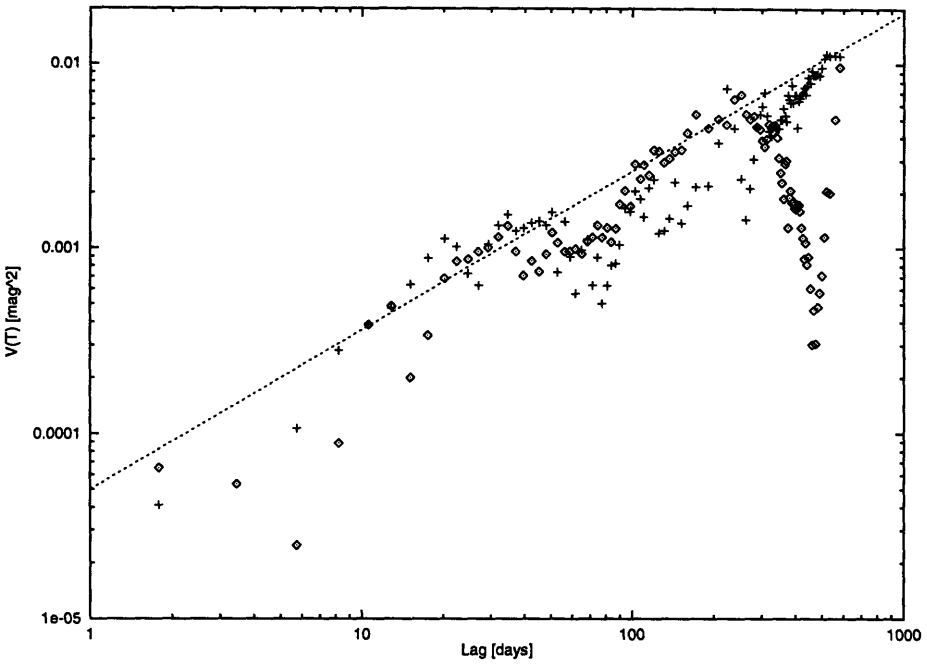

Figure 5-24: Point estimates of the structure function for $\mathcal{Y}_g$. The diamonds are from the A light curve, and the crosses are from the B light curve. The dotted line is the structure function found by Kundić *et al.* (1997).

5.4.2 PRHQ Analysis of Radio and Optical Light Curves

For the PRHQ analysis, the structure function found by Kundić *et al.* (1997) was used,

$$V(T) = 5.01 \times 10^{-5}\,\mathrm{mag}^2 \left(\frac{T}{1\,\mathrm{day}}\right)^{0.86}. \tag{5.15}$$

Figure 5-24 shows the fit of this structure function to the point estimates found from $\mathcal{Y}_g$. When this structure function is used with the individual $\mathcal{Y}_g$ light curves, PRHχ^2 for the A image curve is 73, and for the B image curve is 72, for 97 degrees of freedom. This is a reasonable fit, considering that the actual measurement errors were used (rather than adjusting the errors to make χ^2 equal the degrees of freedom, as was done above for the radio curves). Given these values for the individual curves, the value for PRHχ^2 for the combined curves will be ≥ 145.

When analyzing $\mathcal{Y}_g$ with PRHQ and the above structure function, the minimum is

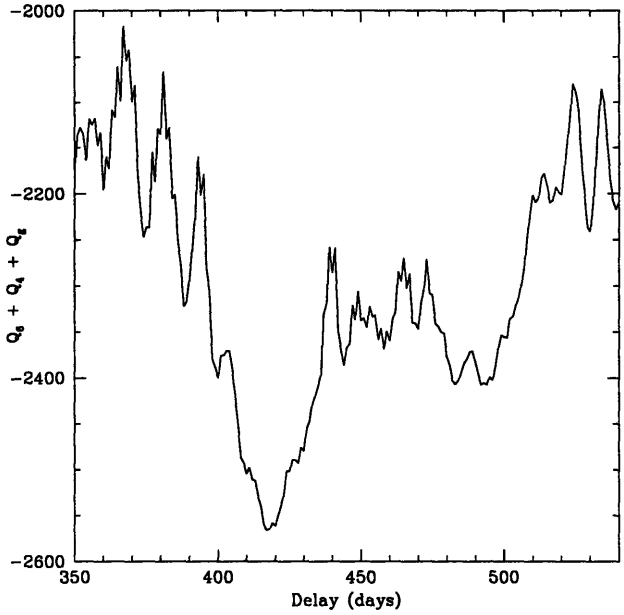

Figure 5-25: $(Q_g + Q_6 + Q_4)$ as a function of time delay for $\mathcal{Y}_6'$, $\mathcal{Y}_4$, and $\mathcal{Y}_g$. The flux ratios were set at $R_6 = 0.7007$, $R_4 = 0.6975$, and $R_g = 1.112$. The minimum is $Q_g + Q_6 + Q_4 = -2568$ at $\tau_{AB} = 417$.

$Q = -1335$ at $\tau_{AB} = 417$, $R = 1.114$, and $\chi^2_g = 157$. This flux ratio corresponds to a shift of -0.117 mag (see eq. 4.24). This reproduces the result of Kundić *et al.* (1997).

When the light curves from the three wavelengths, $\mathcal{Y}_6'$, $\mathcal{Y}_4$, and $\mathcal{Y}_g$, are analyzed together with PRHQ, the minimum is $Q_6+Q_4+Q_g = -2568$ at $\tau_{AB} = 417$, $R_6 = 0.7007$, $R_4 = 0.6975$, $R_g = 1.112$, $\chi^2_6 = 284$, $\chi^2_4 = 107$, and $\chi^2_g = 157$. Figure 5-25 shows the dependence of $Q_6 + Q_4 + Q_g$ on time delay, with the flux ratios set at their values at the minimum. The function is not smooth, and since the radio light curves have smooth surfaces (Figures 5-6 and 5-18), the jaggedness must be due to Q_g. This is probably due to a poor covariance model for $\mathcal{Y}_g$. Despite the roughness, however, the global minimum is clear.

5.4.3 Dispersion Analysis of Radio and Optical Light Curves

First, the optical curves $\mathcal{Y}_g$ were analyzed with the dispersion alone, before combination with the radio curves. The dispersion minimum is $\mathcal{D} = 0.000302\,\mathrm{mag}^2$ at $\tau_{AB} = 417$ days,

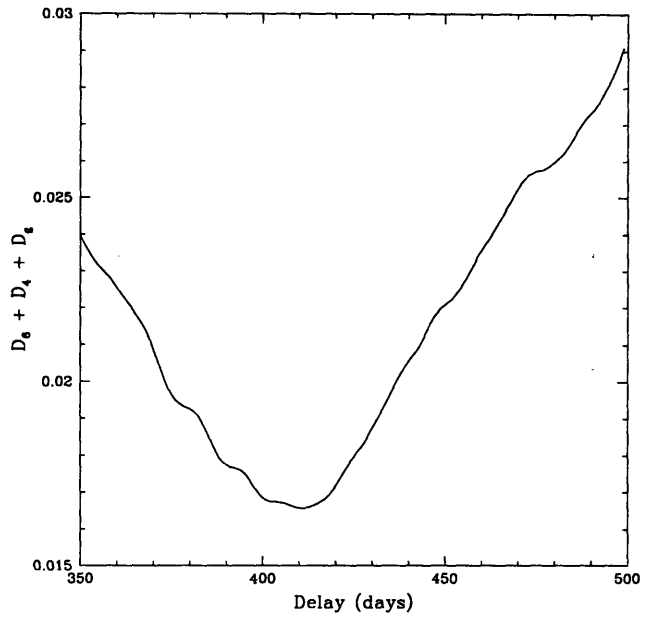

Figure 5-26: Dispersion as a function of τ_{AB} for $\mathcal{Y}_6'$, $\mathcal{Y}_4$, and $\mathcal{Y}_g$. The flux ratios are set at $R_6 = 0.7022$, $R_4 = 0.6955$, and $R_g = 1.130$. The minimum is $\mathcal{D}_6 + \mathcal{D}_4 + \mathcal{D}_g = 0.01655$ at $\tau_{AB} = 410$.

$R_g = 1.114$. This confirms the result of Kundić *et al.* (1997).

To estimate the delay for $\mathcal{Y}_6'$, $\mathcal{Y}_4$, and $\mathcal{Y}_g$ together, the sum of the three dispersions, $\mathcal{D}_6 + \mathcal{D}_4 + \mathcal{D}_g$, is minimized. For the $\mathcal{Y}_6'$, $\mathcal{Y}_4$, and $\mathcal{Y}_g$ light curves, the minimum is $\mathcal{D}_6 + \mathcal{D}_4 + \mathcal{D}_g = 0.01655$ at $\tau_{AB} = 410$, $R_6 = 0.7019$, $R_4 = 0.6957$, and $R_g = 1.130$. The fitted delay is no longer at the minimum from the $\mathcal{Y}_4$ data, but has shifted to a compromise between the minimum from $\mathcal{Y}_4$ alone and from $\mathcal{Y}_g$ alone.

Figure 5-26 shows $\mathcal{D}_6 + \mathcal{D}_4 + \mathcal{D}_g$ as a function of delay, when the flux ratios are set at the fitted values. The curve is a bit less smooth than the curve without $\mathcal{Y}_g$ (see Figure 5-22).

5.5 Summary of Time Delay Results

In the preceding sections, results have been presented for three types of statistical analysis of light curves observed at three different wavelengths, as well as various combinations of these light curves. Confidence intervals have been found for several of the time delay estimates

Light Curve	Statistic	Time Delay (days)	Flux Ratio 6 cm	4 cm	Green
$\mathcal{Y}_6$	PRHQ	451^{+16}_{-18}	$0.6981^{+0.0019}_{-0.0026}$	...	...
	Dispersion	428 or 442	$0.7000^{+0.0029}_{-0.0030}$	...	...
	Correlation	447	0.6976	...	...
$\mathcal{Y}'_6$	PRHQ	449^{+19}_{-18}	$0.6990^{+0.0025}_{-0.0025}$	...	...
	Dispersion	425^{+27}_{-28}	$0.7013^{+0.0031}_{-0.0030}$	...	...
	Correlation	437	0.6987	...	...
$\mathcal{Y}_4$	PRHQ	407^{+21}_{-21}	...	$0.6959^{+0.0045}_{-0.0041}$	...
	Dispersion	399^{+32}_{-30}	...	$0.6957^{+0.0056}_{-0.0051}$	...
	Correlation	411	...	0.6945	...
$\mathcal{Y}_6$ & $\mathcal{Y}_4$	PRHQ	423	0.6989	0.6966	...
	Dispersion	402	0.7008	0.6955	...
$\mathcal{Y}'_6$ & $\mathcal{Y}_4$	PRHQ	420^{+13}_{-13}	$0.6996^{+0.0021}_{-0.0024}$	$0.6968^{+0.0036}_{-0.0036}$	...
	Dispersion	401^{+23}_{-21}	$0.7024^{+0.0028}_{-0.0029}$	$0.6958^{+0.0048}_{-0.0046}$	...
$\mathcal{Y}'_6$, $\mathcal{Y}_4$, & $\mathcal{Y}_g$	PRHQ	417	0.7007	0.6975	1.112
	Dispersion	410	0.7019	0.6957	1.130

Table 5.1: Time Delay Results

using Gaussian process Monte Carlo data with the same sampling and structure function as the real light curves. Table 5.1 lists all of these results.

Which of these time delay estimates should be used to find cosmological results? The analysis of the 6 cm and 4 cm light curves together contains all of the radio monitoring information, so that time delay estimate should be better than the estimates for each wavelength individually. The result for $\mathcal{Y}'_6$ & $\mathcal{Y}_4$ is judged to be more reliable than $\mathcal{Y}_6$ & $\mathcal{Y}_4$ due to some problems with $\mathcal{Y}_6$ in both the PRH and dispersion methods (this choice does not change the delay estimate by much). The discrete correlation method was not even attempted on the 6 cm and 4 cm curves together, given the peak fitting problems when analyzing them individually. Thus, the choice of the best delay estimate is between the

results of the PRH and dispersion analyses of $\mathcal{Y}_6'$ & $\mathcal{Y}_4$: $\tau_{AB} = 420^{+13}_{-13}$ and $\tau_{AB} = 401^{+23}_{-21}$, respectively. *Both of these delay estimates are completely consistent with the delay estimate of* 417 ± 3 *days from the* $\mathcal{Y}_g$ *optical light curves* (Kundić *et al.* 1997). This is one of the most important results of this thesis. Because the result of the PRH method has a smaller confidence interval, and because it is closer to the precise optical result, a delay of 420±13 days will be used for determining the cosmological results in Chapter 6. Figure 5-27 shows the $\mathcal{Y}_6'$ and $\mathcal{Y}_4$ light curves aligned at $\tau_{AB} = 420$ days, $R_6 = 0.6996$, and $R_4 = 0.6968$ along with the optimal reconstruction for each wavelength.

The flux ratios calculated here also need some comment. Recall that the flux ratio is due to the relative magnification of the two images (§2.1.2). In 0957+561 the magnification changes rapidly from the B image core along the milli-arcsec (mas) scale B jet towards the lensing galaxy. The VLA flux ratios reported here ($R_{6,4}$) include both the core and the mas jet, and thus average the core and jet flux ratios. The core and jet flux ratios are discussed further in §6.1. The optical flux ratio (R_g) given here is very different than the radio wavelength values, because the emission from the lensing galaxy was not removed from the optical light curves (making the B image appear much brighter). Schild & Smith (1991) measured the ratio of emission lines at times separated by roughly the delay and found an optical flux ratio of 0.75 ± 0.02.

The time delay has a dependence on which light curve is being studied, regardless of the statistical method. All methods find a shorter delay for the 4 cm curves than the 6 cm curves, and the difference for the PRH method is at the two σ level. In §7.6, this dependence on wavelength is shown to not be a result of dispersion by plasma in the lensing galaxy (for reasonable electron densities). But for the analysis of the 6 cm and 4 cm data together, both the PRH and dispersion methods confirm the result for the $\mathcal{Y}_g$ alone. The PRH result is a compromise value between the 6 cm and 4 cm results, reflecting the similarity of the respective surfaces (Figures 5-6 and 5-18). In making this compromise, the χ^2 values for each wavelength increased only slightly, thus the compromise is a good fit for both. The dispersion result stayed at the value found for $\mathcal{Y}_4$ alone, since that surface was much steeper than the 6 cm surface (see Figures 5-12 and 5-19). When $\mathcal{Y}_g$ was added to the analysis, the results of both PRH and the dispersion methods shifted towards the optical value, and

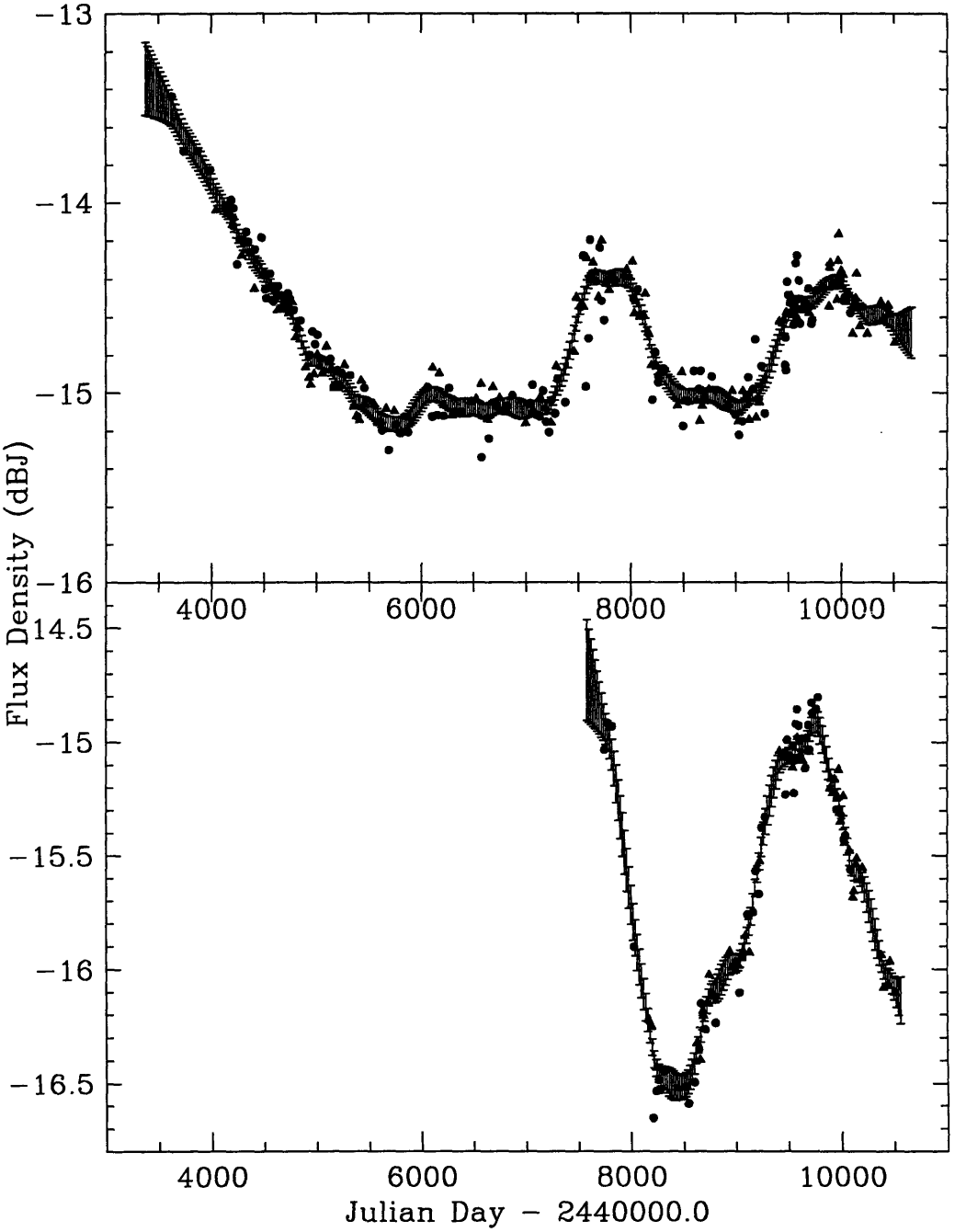

Figure 5-27: The $\mathcal{Y}_6'$ and $\mathcal{Y}_4$ curves aligned at a delay of $\tau_{AB} = 420$ days, $R_6 = 0.6996$, and $R_4 = 0.6968$, with PRH optimal reconstruction. The A image observations are marked by triangles, the B image by circles. The four Spring 1990 observations are plotted, but were not included in the optimal reconstruction.

again, the PRHχ^2 increased only slightly indicating the fit is still good. In all cases where both $\mathcal{Y}_6'$ and $\mathcal{Y}_6$ were considered, the time delay changed only slightly upon removal of the four Spring 1990 points, indicating that as more features enter the light curve these points have less of an impact on the result.

The time delay for a particular light curve may also depend on which statistical method is used. The PRH and dispersion results for $\mathcal{Y}_6'$ disagree by about one σ. Fortunately, the results for $\mathcal{Y}_4$ agree quite well for these two methods, perhaps because the 4 cm curves are more variable than the 6 cm curves. This consistency between statistical techniques is a significant improvement over past controversies (Table 1.1; Haarsma *et al.* 1997).

Chapter 6

Modeling and Cosmological Conclusions

With the time delay found from the 0957+561 light curves, it can be used with the mass model of the lens to determine the distance to the lens. The distance and the redshift can then be used to determine cosmological parameters. In §6.1, the observational constraints available for mass models are described and counted. Section 6.2.1 then does some basic calculations for the 0957+561 system based on the observed positions of the images and the lens. Three lens models in the literature are reviewed in §6.2.2, 6.2.3, and 6.2.4. In §6.3.1, the distance to the lens found from the most recent model is used to determine values of the Hubble parameter for various cosmologies. Sections 6.3.2 and 6.3.3 compares these results to the results from other lenses and from other distance measurement techniques.

6.1 Observational Constraints on 0957+561 Models

6.1.1 Observational Status

Table 6.1 lists some of the observational constraints available for modeling. The positions of the A image and the lensing galaxy are given relative to the position of the B image. The objects G and G1 are the lensing galaxy as detected at radio and optical wavelengths, respectively. The object G′ has been detected in VLBI images and might be either the

Constraint	Value	Reference
Position of A	RA $-1''.25271 \pm 0''.00004$ Dec $6''.04662 \pm 0''.00004$	Gorenstein *et al.* 1988a, Falco *et al.* 1991a
Position of G1 (optical)	RA $0''.19 \pm 0''.03$ Dec $1''.00 \pm 0''.03$	Stockton 1980
Position of G (VLA)	RA $0''.151 \pm 0''.001$ Dec $1''.051 \pm 0''.001$	Roberts *et al.* 1985
Position of G′ (VLBI)	RA $0''.181 \pm 0''.001$ Dec $1''.029 \pm 0''.001$	Gorenstein *et al.* 1983
Redshift of quasar	$z_s = 1.4136 \pm 0.0002$	Weymann *et al.* 1979
Redshift of G1	$z_l = 0.356 \pm 0.002$	Falco *et al.* 1997
Velocity dispersion of G1	$\sigma = 266 \pm 12$ km/s	Falco *et al.* 1997
Velocity dispersion of cluster	$\sigma_{cl} = 715 \pm 130$ km/s	Angonin-Willaime *et al.* 1994
Flux ratio of core	$R_{core} = 0.75 \pm 0.02$	Garrett *et al.* 1994
Flux ratio of jet	$R_{jet} = 0.63 \pm 0.03$	Garrett *et al.* 1994

Table 6.1: Some observational constraints relevant for modeling. Positions are given relative to the B image. Flux ratios are B/A in linear units.

lensing galaxy or the third image of the source. The large uncertainty in the optical position of the lensing galaxy has created ambiguity in modeling of the system (the difference in the results between the FGS91 and GN96 models is due largely to the use of the G1 position rather than the G′ position, see §6.2.4). The *Hubble Space Telescope* image has found a precise optical position for the galaxy that agrees with the position of G′ (Bernstein *et al.* 1997).

The redshifts of the quasar source and of G1 are given in the table. In addition, there is a cluster of galaxies at the redshift of G1 and a cluster at z=0.505 (Angonin-Willaime *et al.* 1994).

The line-of-sight velocity dispersion of G1 has recently been measured precisely by Falco *et al.* (1997) using the Keck telescope. They found that the velocity dispersion was much larger for the inner region of the galaxy (316 ± 14 km/s) than for regions further from the center (266 ± 12 km/s). If the increase towards the center is a systematic problem in the

data, then the value used for lens modeling should be the average of all the measurements, which is 279 ± 12 km/s. Falco *et al.* (1997) suggest, however, that the increase in σ is due to a black hole or other concentrated mass at the center, and since this mass would contribute little to the overall lensing effect, only the σ from the outer region of G1 should be used. Both values are used to find the cosmological results in §6.3.1.

The velocity dispersion of the cluster was found from the redshifts of 21 galaxies in the cluster (Angonin-Willaime *et al.* 1994).

The flux ratio between the two images is due to the different magnifications (see the discussion of lensing magnification in §2.1.2). The ratios reported in the table are the B image flux density divided by the A image flux density, both measured in linear units (such as mJy). If the flux ratio were determined from a single observation of the system, the time delays and source variability would corrupt the measurement, so the flux ratio must be found either from light curves shifted by the delay, or from two observations separated by roughly the delay. Both the A and B images have a core jet structure, with the brightest jet component about 50 milli-arcsec (mas) from the core (R_{jet} is the ratio between the brightest jet components). The magnification of the B image decreases rapidly along the jet in the direction of G (since the third image is faint, the magnification must be small near the lensing galaxy). At the resolution of the VLA, both the core and jet are in the beam, and the VLA flux ratio is a combination of the core and jet ratios (this caused confusion for some time, and was clarified by Conner *et al.* 1992; the results in Chapter 5 are VLA flux ratios). The core and jet flux ratios can be found in three ways: by VLBI observations which resolve the structure, by separating the constant (jet) and variable (core) contributions to the VLA light curves (Conner *et al.* 1992), and by optical observations (which detect only the core). Garrett *et al.* (1994) compiled all such observations from the literature, and averaged the measurements to determine the values reported in Table 6.1.

There are several other important constraints besides those shown in the table. The most important set of these is the mas structure of the A and B images. The best VLBI observations of this structure have been made by Garrett *et al.* (1994) at 18 cm. They found six distinct components in each jet, with the components for the A image mirrored in the B image (clearly demonstrating the opposite parity of the images). The authors model the

components as elliptical Gaussians. The position, flux density, ellipticity, and position angle of each component produce a wealth of constraints on the lens model. The authors used the component positions, and the core and jet flux ratios, to solve for the relative magnification matrix and its spatial variation, which are an alternative set of modeling constraints.

Another important constraint is the number of images. Smooth elliptical lenses can produce up to five images, yet only two bright images are seen in 0957+561. Models of the system must produce only two bright images of the source core, and only one image of the arcsec scale jets and lobes. There has been much discussion about the possibility of a third faint (demagnified) image near the position of the lensing galaxy. The third image would be completely demagnified if the lens mass density were singular at the center, but could be observable if the lens was non-singular (*e.g.* if it has a core radius). Such an image would be difficult to see at optical and radio wavelengths on arcsec scales, since it would be swamped by the lensing galaxy itself. At VLBI scales, the core of the lensing galaxy and the third image would be separated, and thus ambiguity in the lens position and VLBI flux density could lead to speculation about the third image. A VLBI source G′ has been detected at 18 cm (Garrett 1990; Patnaik & Porcas 1996), 13 cm (0.6 ± 0.1 mJy, Gorenstein *et al.* 1983), 6 cm (Bonometti 1985; Rogers 1988), and 3.6 cm (Rogers 1988). Gorenstein *et al.* (1984) did not detect G′ (in analysis of a different VLBI data set than the one discussed in their 1983 paper), and place a 5σ upper limit on the G′ flux density of 1/30 of the B image flux density (or 0.6 mJy, at the time of observation). Gorenstein *et al.* (1984) point out that the results for the two data sets are consistent. Different models make different assumptions about the nature of G′, and this can affect the results.

The observed structure of the lensing galaxy could also be useful information for modeling. G1 is a cD elliptical galaxy and the brightest member of the surrounding cluster. Attempts have been made to measure the ellipticity, core radius, and other structural properties of G1 (Young *et al.* 1980; Stockton 1980), but the measurements are difficult with ground-based instruments and the results have usually not been used as lens model constraints.

Deep optical images of the system have been made in order to find other lensing effects in the field, and hopefully improve the understanding of the cluster potential. Background

galaxies lensed into bright arc-like images were reported in the field (Bernstein *et al.* 1993), but were later found to be a coincidental alignment (Dahle *et al.* 1994). Background galaxies can also be elongated slightly perpendicular to the lens direction, an effect called weak lensing. Fischer *et al.* (1997) have made a deep image of the field with the Canada-France-Hawaii Telescope and have used weak lensing information to reconstruct the mass distribution of the cluster. They find the cluster center to be about 20″ east of G1, and model the surface mass density distribution as an isothermal sphere with a core radius, $\Sigma(b) = \Sigma_0[1 + (b/c_c)^2]^{-1/2}$, where the core radius of the cluster is $c_c = 17h^{-1}$ kpc, and the central surface mass density is $\Sigma_0 = 3600 \pm 1100h\,\mathrm{M}_\odot\ \mathrm{pc}^{-2}$. The authors show that the total mass using this model is consistent the the cluster velocity dispersion found by Angonin-Willaime *et al.* 1994 (see Table 6.1).

6.1.2 Counting Constraints and Model Parameters

The observational information described above is used to constrain the model in a few different ways. The number of images, the observed galaxy ellipticity and core radius, and the cluster center and structure are typically not used to constrain the model, but are used to select the parameterization of the model (King model, isothermal sphere, etc.) and to check the reasonableness of the resulting fit. The redshifts of the lens and the source are usually fixed during modeling, and are not counted as constraints or parameters. The galaxy position is used to reference the coordinate system and is not counted explicitly as a parameter or constraint. The time delay, the velocity dispersion of G1, and the velocity dispersion of the cluster are also not used to constrain the model, but rather are combined with the model results to determine cosmological quantities, as described in §2.3.3. The observables that do function as constraints during model fitting are the flux densities and positions of the images. (The flux density limit on the third image could be included either as a constraint or as a check on the fitted model.)

Exactly how many constraints do the image positions and flux densities provide for modeling? This is an important question, since there must be more constraints than model parameters (otherwise the fit is under-determined), and it is important to know the degrees of freedom to determine the goodness-of-fit. The larger the number of constraints, the

more parameters can be used in the model, allowing more sophisticated (and realistic) lens potentials can be explored. The constraints and parameters in this thesis are counted in this way:

- For a lens with n images of a single *point* source, there are $2(n-1)$ constraints from the relative positions of the images and $n-1$ constraints from the flux ratios between the images.

- For a lens with n images of a single *extended* source, there are again $2(n-1)$ constraints from the image positions, but now the relative magnification matrix M_{ij} can be measured (not just the flux ratios), giving $4(n-1)$ more constraints. A spatial change in the magnification can give two additional constraints (the direction and magnitude of the change in the image plane).

- Model parameters are all those parameters necessary to describe the mass distribution (galaxy position and core radius, cluster shear and position angle, etc.), and do not include the source positions or flux densities.

If the source positions and flux densities are counted in the model parameters, then the count of the constraints should be increased to $2n$ positions of the images and n flux densities (or $4n$ components of the magnification matrix, 4 for each image). Either way of counting results in the same number of degrees of freedom. The modeling papers are split between these two methods of counting, generating quite a bit of confusion when comparing papers.

If the 0957+561 system is viewed as two images of six point sources (the VLBI core and jet components), there are 3 constraints for each source (2 from the relative positions of the images and 1 from the flux ratio), giving a total of 18 constraints.

If the system is viewed as two images of a single extended source, there are 2 constraints from the relative image positions, 4 from the relative magnification matrix between the images, and 2 from the change in the matrix along the image, giving 8 constraints. There might be additional parameters describing the extended images, and additional constraints describing the extended source, but some of this information is already included in the

magnification matrix. It is more difficult to count parameters and constraints when viewing the 0957+561 system this way.

The actual modeling papers use the second view, or some combination of the two.

6.2 Mass Models of 0957+561

Since 0957+561 was the first gravitational lens discovered, many attempts have been at modeling the potential. Many of the early papers were aimed at finding a plausible lens model, not a unique or most likely model, in order to demonstrate that lensing was indeed taking place in this system. Early modeling work was done by: Young *et al.* 1980, Young *et al.* 1981, Borgeest & Refsdal 1984, Narasimha *et al.* 1984, Greenfield *et al.* 1985, and Falco *et al.* 1985. In §6.2.2, §6.2.3, and §6.2.4 three more recent models are discussed: Falco *et al.* 1991a (FGS91), Kochanek 1991, and Grogin & Narayan 1996a (GN96). The model of Bernstein *et al.* 1993 is not included since that work was based on an incorrect observation of an arc in the system. This section begins with some "back of the envelope" calculations for the 0957+561 system.

6.2.1 Basic Calculations

A few basic calculations and comments can be made regarding the 0957+561 system, even without sophisticated models and careful constraints.

If the lens is assumed to be a simple geometry, then the image positions can be used to make various calculations. The images positions relative to the lens galaxy are $\vec{\theta}_A \sim +5''$ and $\vec{\theta}_B \sim -1''$ when measured along a line between the images. First, assume that the lens is a point mass (described in §2.1.3). Equation 2.16 can be solved for the source position, finding $\vec{\beta} \sim +4''$ (in the same coordinates, *i.e.* the source is about $1''$ south of A), and for the Einstein ring radius, which is $\theta_E \sim 2.2''$. This model thus has the source *outside* the Einstein radius. Equation 2.15 can then be used to find the mass of the lens. For $H_0 = 70\,\mathrm{km\,s^{-1}Mpc^{-1}}$ and $\Omega_0 = 1$, the mass of the lens is about $9 \times 10^{11}\,\mathrm{M}_\odot$. The magnification of the images is found from eq. 2.17 to be $|\mathrm{M}|_A = 1.04$, $|\mathrm{M}|_B = 0.04$. In this model, then, the B image is demagnified to only 4% of the source flux density, and is

not inverted (its magnification is positive). This is very inconsistent with the observed flux ratio and parity of the images.

Next, consider a model of the lens as a singular isothermal sphere. This model is much closer to a galaxy mass distribution than a point mass, so the results are expected to be more realistic. Equations 2.22 can be solved for the source position and Einstein radius to find $\vec{\beta} \sim +2''$ and $\theta_E \sim 3''$. Thus, the source is *inside* the Einstein radius. Equation 2.23 can then be used to find the magnifications: $|\mathsf{M}|_A = 2.5$ and $|\mathsf{M}|_B = -0.5$. The parity of the images is now correct (the B image has negative magnification), and the flux ratio is closer to the observed value. Thus, sophisticated models are typically based on variations of a singular isothermal sphere.

Other important features of the lens modeling can be determined from the map of the source (see Figure 3-1). The images A and B and lens galaxy G do not fall along a line, but G is offset to the east. This indicates that the lens is not circularly symmetric, and either the lens galaxy has some ellipticity or the cluster is contributing a shear to the lens potential. Another important feature is that there is no bright third image near the lens; if the lens galaxy had infinite density at the center (singular), the third image would be completely demagnified, but if the galaxy had a smooth mass density in the central regions (large core radius) a third image would be detectable. Thus the observations indicate that G1 is either singular or has at most a small core radius.

If the galaxy is assumed to be a singular isothermal sphere and the cluster a constant density sheet, an estimate of the time delay for the system can be made (see eq. 2.47). Plugging in the image positions, lens redshift, and the effective distance (assuming $H_0 = 70\,\mathrm{km\,s^{-1}Mpc^{-1}}$ and $\Omega_0 = 1$), the result is about 0.8 years or 300 days. This is within a factor of 2 of the measurement made in Chapter 5.

The 0957+561 system can be understood in terms of the time delay surface discussed in §2.3.2. The image A is at the lowest point in the time delay surface, and has the smallest light travel time (light arrives in this image first). Since it is a minimum, the image is not inverted. The B image is at a saddle point in the time delay surface, and light arrives later in this image than in the A image. The B image is inverted.

6.2.2 Falco *et al.* 1991 Model

This section discusses the lens modeling work by Falco, Gorenstein, and Shapiro (1991a), hereafter FGS91.

The FGS91 model fit was based on earlier observations than those reported in §6.1. In particular, the model used as constraints the components of the relative magnification matrix M_{AB} found by Gorenstein *et al.* (1988a) from the 4 Gaussian components fitted to the VLBI core-jet structure. FGS91 assumed that the VLBI source G′ was the lensing galaxy, and used its position (with its small error) in the model. The third image was assumed to be very faint, with a flux density less than 3% of the B image. Model fits were checked to ensure that a bright third image or second images of the extended source structure were not created.

There were 6 constraints on the model: 2 from the relative position of images A and B, and 4 from the relative magnification matrix. A model of the mass distribution was chosen with 5 parameters, leaving 1 degree of freedom in the fit. The galaxy was assumed to be a King model sphere with a core mass added at the center. The cluster was modeled as a mass sheet with convergence and shear.

The King model (King 1966) was chosen because it it is a good description for other cD galaxies and brightest cluster members. It can fit observational data well with just two free parameters: the core radius θ_c and line of sight velocity dispersion σ. The King profile is similar to an isothermal sphere with core radius (described in §2.1.3), except the phase space distribution function[1] is modified so that the galaxy is less dense at large radii while still maintaining an isothermal profile at small radii (Binney & Tremaine 1987, p. 232). The resulting gravitational potential, density distribution, and lensing bending angle cannot be determined analytically for this phase space distribution function and must be found numerically. Young *et al.* (1981) introduced a functional approximation to the numerical result for the bending angle. As stated by Grogin & Narayan(1996a), the bending angle in radians is

$$\vec{\hat{\alpha}}_{\rm King}(\vec{\theta}) = \frac{\sigma^2}{c^2}\frac{\vec{\theta}}{\theta}\alpha_*(\theta) \tag{6.1}$$

[1] the phase space distribution function $f(\mathbf{x},\mathbf{v},t)d^3\mathbf{x}d^3\mathbf{v}$ is the number density of stars at time t in volume $d^3\mathbf{x}$ centered on $\mathbf{x}$ and in velocity range $d^3\mathbf{v}$ centered on $\mathbf{v}$

where

$$\alpha_*(\theta) = 53.2468 f\left(1.155\frac{\theta}{\theta_c}\right) - 44.0415 f\left(0.579\frac{\theta}{\theta_c}\right) \tag{6.2}$$

and

$$f(x) = \frac{\sqrt{1+x^2}-1}{x}. \tag{6.3}$$

FGS91 found that the King model alone could not produce the observed lensing geometry (regardless of the cluster contribution) since the density distribution was too flat at the galaxy center. They added a core mass M_c to the galaxy which contributes to the bending angle as

$$\vec{\alpha}_{M_c}(\vec{\theta}) = \frac{4GM_c}{c^2 D_{\rm eff}\theta^2}\vec{\theta} \tag{6.4}$$

The King model plus core mass is a circularly symmetric distribution and cannot produce the asymmetry of the images or account for the observed cluster. The cluster was modeled as a smooth sheet of dark matter, with convergence κ, and shear γ at position angle φ_γ. As explained in §2.3.1, the convergence is assumed to be $\kappa = 0$ during the modeling, and the other parameters are scaled appropriately. The scaled shear is $\gamma' = \gamma/(1-\kappa)$, and the resulting bending angle is

$$\vec{\alpha}_{cl}(\vec{\theta}) = \gamma' \begin{pmatrix} -\cos 2\varphi_\gamma & \sin 2\varphi_\gamma \\ \sin 2\varphi_\gamma & \cos 2\varphi_\gamma \end{pmatrix} \vec{\theta} \tag{6.5}$$

Thus there are 5 parameters in the model fit: $\sigma, \theta_c, M_c, \gamma$, and φ_γ.

The model fit was found using χ^2 minimization, and the best fit had $\bar{\chi}^2$=1.3 (this included the correlated errors in $\mathsf{M}_{\rm AB}$). The results for the model parameters are given in Table 6.2. FGS91 found that the size of the multiply imaged region depends strongly on the core radius θ_c and the core mass M_c. The value of the core mass is driven primarily by one of the eigenvalues of $\mathsf{M}_{\rm AB}$. The authors experimented with modeling the cluster as a point mass at a particular angle, rather than the mass sheet with shear; they found that this modification caused less than a 3% change in H_0 for cluster distances greater than $10''$. The paper contains a nice discussion of each of these fitted parameter values, comparing them to measurements of other galaxies and showing that they are reasonable.

Parameter	Value
σ	$390 \pm 4\,\mathrm{km/s}$
θ_c	$2''.9 \pm 0''.1$
M_c	$111 \pm 1 \times 10^9 h^{-1}\,\mathrm{M}_\odot$
γ	0.30 ± 0.01
φ_γ	$63°.3 \pm 0°.6$

Table 6.2: Parameter fits found by FGS91 for the King model.

To determine the cosmological result, the above model fit (assuming $\Omega_0 = 0.5$, $\lambda_0 = 0$) was used to determine the Hubble parameter,

$$H_0 = 90 \pm 10 \left(\frac{\sigma}{390\,\mathrm{km/s}}\right)^2 \left(\frac{1\,\mathrm{year}}{\tau_{AB}}\right) \mathrm{km\,s^{-1}Mpc^{-1}} \quad \text{(FGS91)}. \tag{6.6}$$

The value of 390 km/s is used in the equation because it is the velocity dispersion of the galaxy when the convergence $\kappa = 0$, *i.e.*, when all of the focusing effect is from the galaxy. In §2.3.3 it was shown that the fundamental quantity found from lens time delays is not the Hubble parameter, but the distance to the lens D_{OL}. The above expression can be converted to an equation for D_{OL} using the filled-beam angular diameter distance equation, eq. 2.33 (since that was assumed in deriving eq. 6.6) with their assumed values of $\Omega_0 = 0.5$ and $\lambda_0 = 0$. The distance is then

$$D_{OL}(\tau_{AB}, \sigma) = 729 \pm 81 \left(\frac{390\,\mathrm{km/s}}{\sigma}\right)^2 \left(\frac{\tau_{AB}}{1\,\mathrm{year}}\right) \mathrm{Mpc} \quad \text{(FGS91)}. \tag{6.7}$$

This distance measurement is independent of H_0, Ω_0, and λ_0. The authors noted that for the 0957+561 system, using the empty-beam distance (§2.2.2) rather than the filled-beam distance has less than 4% effect on H_0. The velocity dispersion σ to be used in eqs. 6.6 and 6.7 is the line of sight dispersion, presumably of the visible material, although this is not discussed explicitly in the paper. As explained in the end of §2.3.3, including the effect of the dark matter by substituting $3\sigma^2/2$ in the above equation can reduce D_{OL} by 50%, and thus increase the estimate of H_0 by 50% (*e.g.* Roberts *et al.* 1991).

In comparison with the other models, the FGS91 model used the data available at the

time, which were poorer than the data available to Grogin & Narayan (1996a). Their parameterization of the model, however, turned out to provide the best fit for the improved data (see §6.2.4). The FGS91 model is simple enough to be constrained by the then-available observations, but Kochanek (1991) showed that the 0957+561 system is too complex to be modeled in this simple fashion, and that assuming a simple model introduces systematic error. FGS91 used the relative magnification matrix as an observational constraint rather than the VLBI jet positions and flux densities directly, which would have provided several more constraints.

6.2.3 Kochanek 1991 Model

This section is based on the model of Kochanek (1991).

The observational data available to Kochanek were the same as those available to FGS91. Similar to FGS91, Kochanek used the VLBI data of Gorenstein *et al.* (1988a), and assumed the VLBI source G′ was the lensing galaxy. Kochanek assumed that there was no third image of the source core, and thus the density of the galaxy was singular at the center. Kochanek counted 5 observational constraints: 2 from the relative positions of the A and B cores, 2 from the brightest jet component in A and B, and 1 from the core flux ratio. These last three correspond to three components of the relative magnification matrix; the fourth component of M_{AB} was not used because it was less well-determined than the others.

Rather than using a model simple enough to be constrained by the observables, Kochanek explored a family of models appropriate to the system to determine how many parameters are needed to make an acceptable model. Both the galaxy and the cluster are modeled as elliptical systems with several free parameters, resulting in a total of 9 parameters in the model. This is 4 more than the number of constraints, thus the model is able to fit the observables exactly with a range allowed for each of the 4 free variables.

The galaxy is modeled as a singular elliptical, with ellipticity ϵ_g at a position angle $\varphi_{\epsilon g}$ (the notation here is polar coordinates r, φ). The potential has a general radial function, $\psi_0(r)$ and $\psi_2(r)$, and Kochanek experiments with two different radial functions. The galaxy

potential is expanded in φ, giving

$$\psi_g(r,\varphi) = g_{cr}\psi_0(r) + \epsilon_g\psi_2(r)\cos 2(\varphi - \varphi_{\epsilon g}), \tag{6.8}$$

where g_{cr} is the critical radius of the galaxy, and ϵ_g is the ellipticity of the galaxy with position angle $\varphi_{\epsilon g}$. For a singular isothermal radial potential, the radial functions are $\psi_0(r) = r$ and $\psi_2(r) = g_{cr}r/3$.

The cluster is modeled as an elliptical pseudo-isothermal potential with a core radius, expanded in φ as

$$\psi_{cl}(r,\varphi) = c_{cr}(c_c^2 + r^2)^{1/2} + \frac{\epsilon_{cl}}{3}r^2(c_c^2 + r^2)^{-1/2}\cos 2(\varphi - \varphi_{\epsilon c}), \tag{6.9}$$

where c_{cr} is the cluster critical radius, c_c cluster core radius, and ϵ_{cl} is the ellipticity of the cluster density distribution with position angle $\varphi_{\epsilon c}$. Kochanek also gives an expression for this potential that is expanded about the position of the primary lens galaxy but assumes zero ellipticity. That expression shows clearly the terms for the convergence and shear of the cluster, as well as higher order terms with give the position and core radius of the cluster.

Thus the model contains 9 free parameters: g_{cr}, ϵ_g, $\varphi_{\epsilon g}$, c_c, c_{cr}, ϵ_{cl}, and $\varphi_{\epsilon c}$, plus two parameters for the position of the cluster. These 9 parameters correspond to the galaxy mass, ellipticity, and orientation, and the cluster dipole (2), quadrupole(2), and octopole(2). This is in addition to the 2 free functions to express the radial structure of the galaxy.

When fitting this general model, Kochanek finds "a new problem – it is too easy to model the system." Model fits are given for several fixed values of four parameters: the critical radius of the galaxy, the distance to the cluster, the core radius of cluster, and the direction to cluster. For reasonable ranges of these parameters, keeping only fits with galaxy velocity dispersion $240 < \sigma < 320$ km/s, cluster velocity dispersion $500 < \sigma_{cl} < 1500$ km/s, and assuming $\Omega_0 = 1, \lambda_0 = 0$, Kochanek finds a range of models that fit the constraints exactly and predict time delays in the range $0.1h^{-1} < \tau_{AB} < 1.0h^{-1}$ years (where $h \equiv H_0/100\,\mathrm{km\,s^{-1}Mpc^{-1}}$). This is a clear demonstration that this lens model was underdetermined by the observations available at the time, and that choosing a simpler model introduces systematic errors much larger than the errors in the fit. Another important

result is that the cluster cannot be modeled by just a convergence κ and a shear γ, as was done by FGS91 and GN96. Modeling the cluster with shear requires the assumption that the expansion of the cluster potential can be cut off after the shear term, *i.e.* that the higher order terms are smaller than the shear. Kochanek finds that if the shear dominates over the higher order terms, the cluster becomes supercritical and generates extra images. Thus, the observations indicate that the higher order terms are significant and parameters such as the cluster core radius and position must be included in the model.

At the time this paper was written, Kochanek had not yet done worked on the problem of the dark matter velocity dispersion (Kochanek 1993), so the models were not corrected for the effects of dark matter, finite slit width, and galaxy anisotropy on the line of sight luminous matter dispersion, σ.

Since 1992, the FGS91 model has been cited continually to determine a value for H_0 from the 0957+561 time delay, but the systematic error in the model was probably mentioned too seldom. When there were only a few constraints available, no improvement could be made. Now, however, many more observational constraints are available and a general approach to modeling such as this work by Kochanek should be done.

6.2.4 Grogin & Narayan 1996 Model

This section describes the recent model of Grogin & Narayan (1996a, and the *erratum* 1996b). This work will be referred to as GN96.

More and better observational constraints were available to GN96 than to the authors of the earlier models described above. The VLBI observations of Garrett *et al.* (1994) detected more components in the mas structure than the observations of Gorenstein *et al.* (1988a), and found new constraints in the gradient in the relative magnification matrix along the jet (see §6.1 for a description of the Garrett *et al.* 1994 data). GN96 used the optical position of the galaxy, G1, rather than the VLBI position G′ (since they doubted whether the VLBI position is as good as the stated 1 mas errors). They used the flux density limit on the third image (Gorenstein *et al.* 1984) as an explicit constraint during modeling, rather than as a check on the model after it was found. Specifically, they set no penalty on χ^2 if the source was below the limit, but a steeply increasing χ^2 penalty if the third image is brighter than

the limit.

Unlike the two models above, GN96 included the positions of the sources in the count of both the constraints and the parameters (they list 15 constraints and 9 model parameters, with 6 degrees of freedom). If the source positions are not included, there are 11 constraints: 2 from the relative position of A and B, 2 from the relative positions of the brightest jet component in A and B, 4 from the relative magnification matrix M_{AB}, 2 from its gradient along the jet, and 1 from the flux density limit on the third image. There are 5 more constraints than FGS91. The new constraints are from the gradient of M_{AB}, the limit on the third image, and the positions of the jet components. Unfortunately, the jet position information was already used by Garrett *et al.* (1994) to find M_{AB}, so these may not be independent constraints. On the other hand, there are a large number of constraints in the positions and flux densities of the six jet components (for a count, see §6.1.2), so GN96 are not actually using a smaller number of constraints than are in the data. When the source positions are not counted with the model parameters, there are 5 parameters in the model. This leaves 6 degrees of freedom in the fit.

GN96 parameterized the lens mass distribution in two different ways. The first is a softened power-law sphere (SPLS) with core radius for the galaxy, and the second is the King model sphere with core mass (the same as FGS91, described in §6.2.2. In both cases, the cluster is modeled as a mass sheet with convergence and shear, just as described in §6.2.2.

The softened power-law sphere is a generalization of the isothermal sphere with core radius (described in §2.1.3). It has three parameters: a central density ρ_0, angular core radius θ_c, and radial index η. The mass density profile is

$$\rho(r) = \rho_0 \left(1 + \frac{r^2}{r_c^2}\right)^{(\eta-3)/2} \tag{6.10}$$

where $r_c = \theta_c D_{OL}$. For $r >> r_c$, the mass enclosed in r is $M(r) \propto r^\eta$. The radial index is $\eta = 1$ for an isothermal sphere, $\eta = 0$ for a modified Hubble profile, and $\eta = 2$ for a constance surface mass density sheet. Thus, this parameterization allows a wider range of models to be explored. There is no analytic expression for the potential, but there is for

the deflection angle:

$$\vec{\alpha}_g(\vec{\theta}) = \frac{\alpha_0^2}{\theta^2}\left[\frac{(\theta^2+\theta_c^2)^{\eta/2}-\theta_c^\eta}{\alpha_0^\eta}\right]\vec{\theta} \tag{6.11}$$

where

$$\alpha_0 = \left(\frac{4G\rho_0 r_c^3}{c^2 D_{\rm eff}}\frac{2\pi^{3/2}\theta_c^{-\eta}}{\eta}\frac{\Gamma(1-\eta/2)}{\Gamma(3/2-\eta/2)}\right)^{1/(2-\eta)}. \tag{6.12}$$

The parameters of the SPLS model then become α_0, θ_c, and η for the galaxy, plus γ' and φ_γ for the cluster.

Due to an error in the model fitting code, the results in the original paper (Grogin & Narayan 1996a) were incorrect; corrected results are given in the erratum (Grogin & Narayan 1996b). The results are supposedly reported with 2σ (or 95%) confidence intervals, which they define as a change by 4 in $\bar{\chi}^2$, saying that this is more conservative than a change of 4 in χ^2. Actually, for 6 degrees of freedom, the 95% confidence interval corresponds to a change of 2 in $\bar{\chi}^2$. The reported confidence intervals (change of 4 in $\bar{\chi}^2$) are actually 99.95% intervals.

The χ^2 minimization of the SPLS model resulted in a fit with $\bar{\chi}^2$=6.9, which has a probability of 0.00002%. The values of the fitted parameters are given in Table 6.3. The largest contributions to $\bar{\chi}^2$ came from the poor agreement with the position of G1, the components of M_{AB}, and the gradient of M_{AB}. The resulting galaxy position fell 62 mas from G1, 44 mas from G′, and 64 mas from G.[2] When they used the G′ position and error instead, they found $\bar{\chi}^2$=70. The authors also comment that (using the G1 position) the value of $\bar{\chi}^2$ is significantly reduced if the errors of the M_{AB} components are assumed to be uncorrelated. The fitted radial index η is slightly more than 1, indicating that the mass density increases slightly more than an isothermal distribution out to at least $15h^{-1}$ pc. The upper limit on the core radius θ_c corresponds to a distance of $330h^{-1}$ pc, constrained mostly by the third image flux density limit. The small ranges of η and θ_c keep the resulting range in H_0 small. GN96 experimented with adding additional parameters to the SPLS model, such as ellipticity or a core mass, but found that these changes improved $\bar{\chi}^2$ only slightly and caused little change in H_0. Making the cluster model more complicated by adding singular

[2]These position offsets are from Grogin & Narayan 1996a; the corrected model fit in the erratum (Grogin & Narayan 1996b) may have slightly different offsets.

Parameter	Value
α_0	$2''.40^{+0.28}_{-0.34}$
θ_c	$0''.058^{+0.053}_{-0.058}$
η	$1.08^{+0.09}_{-0.08}$
γ'	$0.298^{+0.095}_{-0.082}$
φ_γ	$-67°.4^{+4.1}_{-3.2}$

Table 6.3: Parameter fits found by GN96 for the SPLS model.

Parameter	Value
σ	$330 \pm 26\,\mathrm{km/s}$
θ_c	$0''.63^{+0.29}_{-0.15}$
M_c	$0 < M_c < 72 \times 10^9\,\mathrm{M}_\odot$
γ'	$0.377^{+0.069}_{-0.061}$
φ_γ	$-67°.8^{+2.7}_{-2.3}$

Table 6.4: Parameter fits found by GN96 for the King model.

isothermal spheres for the two nearest galaxies changed H_0 little and made $\bar{\chi}^2$ significantly worse.

The fit to the King model had a better $\bar{\chi}^2$ of 3.8, with probability of 0.19% (there is one less degree of freedom for the King model than the SPLS model because the constraint on the third image flux density is useless when the model is singular). The fitted parameters are given in Table 6.4. The parameter fits for the galaxy are significantly different than those found by FGS91 (see Table 6.2). GN96 state that if the position of G′ is used as the constraint rather than G1, the parameter fits become very similar to those of FGS91, but the value of $\bar{\chi}^2$ increases to 35. Thus the position chosen for the lens galaxy can make a large difference in the model results. The results of GN96 and FGS91 for the cluster are similar (the sign difference is probably due to the choice of coordinate system, but neither paper defines theirs).

Since the King model had a better fit, it will be used here to determine the cosmological

results. GN96 assumed $\Omega_0 = 1$, $\lambda_0 = 0$, and used a filled-beam distance to find a Hubble parameter of

$$H_0 = 98^{+12}_{-11} \left(\frac{\sigma}{330\,\mathrm{km/s}}\right)^2 \left(\frac{1.1\,\mathrm{year}}{\tau_{AB}}\right) \mathrm{km\,s^{-1}Mpc^{-1}} \quad \text{(GN96)}, \tag{6.13}$$

where 330 km/s is the model predicted galaxy velocity dispersion for $\kappa = 0$. The error includes modeling uncertainties and measurement effects of the velocity dispersion (see below). No error is included for large scale structure along the line of sight. The fundamental result, the distance to the lens, can be deconvolved from the cosmology using eq. 2.33 to find

$$D_{OL}(\tau_{AB}, \sigma) = 583^{+65}_{-71} \left(\frac{330\,\mathrm{km/s}}{\sigma}\right)^2 \left(\frac{\tau_{AB}}{1\,\mathrm{year}}\right) \mathrm{Mpc} \quad \text{(GN96)}. \tag{6.14}$$

This equation is difficult to compare to the distance equation for the FGS91 fit (eq. 6.7) due to the different normalization; eq. 6.7 is equivalent to $D_{OL}(\tau_{AB}, \sigma) = 1018 \pm 113\ (330\,\mathrm{km\,s^{-1}}/\sigma)^2$ $(\tau_{AB}/1\,\mathrm{year})\,\mathrm{Mpc}$, thus the fits in the two papers are very different.

The SPLS model gave a value of H_0 only 3% different than the King model for the same values of τ_{AB} and σ and the same constraints. GN96 give this as evidence that there is little systematic error due to how the model is parameterized. Yet, both models treated the galaxy cluster in the same way, and Kochanek showed in his model that much of the systematic uncertainty is due to how the cluster is treated. Also, both the SPLS and King model fits assumed G1 as the galaxy position, and the results change significantly if G′ is used.

As explained at the end of §2.3.3, there is the question of systematic errors in the velocity dispersion and what value should be used in the above equations. GN96 carefully discuss this. For their fitted lens model, they calculated the different distributions of luminous and dark matter in the lens, and found the bias and errors due to anisotropy in the galaxy and the finite slit width in the observation. These systematic corrections and errors are included in the above expressions for H_0 and D_{OL}. Thus, it is correct to plug in the line-of-sight velocity dispersion of the luminous matter, measured with a finite slit and under the assumption the galaxy is isotropic ($3\sigma^2/2$ should *not* be used instead of σ^2).

In comparison to the models described above, the GN96 model is based on better VLBI observations with more constraints. Thus, the results of this model will be used for cosmological tests below. However, there are several ways this modeling work could be improved. First, the authors did not make full use of the constraints available in the VLBI observations. They used the components of M_{AB} instead of the positions and flux densities of the jet features, which meant there were fewer constraints on the model. Also, the errors on the M_{AB} components are significantly correlated, which could have been avoided by using the positions directly. Second, the constraints were counted in a confusing way, including some position information for the jets in addition to M_{AB}, even though those positions were used to determine M_{AB}. Third, although more constraints were available (even in their counting scheme) the authors did not take the opportunity to explore more general models, and to model more carefully the contribution of the cluster in order to reduce the systematic error and perhaps improve the $\bar{\chi}^2$ of the fit. Finally, the confidence intervals on the reported result were incorrectly reported as 95% intervals; they are actually 99.95% intervals. A good feature of their work was the careful treatment of the velocity dispersion issues.

6.3 Cosmological Results

6.3.1 Results From 0957+561

Cosmological results are found here using the GN96 (Grogin & Narayan 1996a, 1996b) fit to the King model sphere with core mass model suggested by FGS91. GN96 used the best observational data of the available modeling papers, and of the models they tried, the King sphere model had the best $\bar{\chi}^2$. As explained in §2.3.3, the fundamental quantity determined in the time delay measurement is the distance to the lens D_{OL}. This distance measurement is independent of H_0, Ω_0, λ_0, the convergence κ, and the source redshift z_s. The measurement is dependent on whether a filled- or empty-beam angular diameter distance is used (see §2.2). The distance to the lens from the work of GN96 is

$$D_{OL}(\tau_{AB}, \sigma) = 583^{+65}_{-71} \left(\frac{330\,\mathrm{km/s}}{\sigma}\right)^2 \left(\frac{\tau_{AB}}{1\,\mathrm{year}}\right) \mathrm{Mpc}, \tag{6.15}$$

where the error includes the statistical error in the lens model, and the line-of-sight luminous matter velocity dispersion through a finite slit can be substituted for σ. The expression does not include the (significant) systematic error in the lens model, or the uncertainty due to large-scale structure along the line of sight. The error given by GN96 for H_0 is a 99.95% confidence interval, but the values of τ_{AB} and σ are reported with 1σ errors. To make the expression more consistent, the error reported by GN96 will be divided by two in the following calculations.

To find the distance, the velocity dispersion of $\sigma = 266 \pm 12$ km/s (measured for the outer part of the galaxy by Falco *et al.* (1997), assuming the behavior of σ towards the center is due to the core mass), and the time delay of 420 ± 13 days (see Chapter 5) are used in eq. 6.15. Adding 3.3% error for large scale structure (as calculated for 0957+561 by Bar-Kana (1996); see §2.3.3 for more about error due to large scale structure), the distance to the lens is

$$D_{OL} = 1032^{+119}_{-122}\,\mathrm{Mpc}. \tag{6.16}$$

If instead a velocity dispersion of $\sigma = 279 \pm 12$ km/s is used (averaged over the whole galaxy by Falco *et al.* (1997), assuming the behavior at the center is a measurement problem), the distance is

$$D_{OL} = 938^{+105}_{-108}\,\mathrm{Mpc}. \tag{6.17}$$

This distance can then be used with equations 2.32 and 2.35 to determine H_0 for various combinations of Ω_0 and λ_0. Some interesting combinations are reported in Table 6.5. The estimates for H_0 are all in the range of 61 to $82\,\mathrm{km\,s^{-1}Mpc^{-1}}$. The distance measurement of $D_{OL} = 1032^{+119}_{-122}$ Mpc and the corresponding H_0 results for several cosmologies are shown in Figure 6-1 (compare this to Figure 2-2).

The error budget on these estimates of H_0 is the following:

- 9% from velocity dispersion σ (double the 4.5% measurement error because it is squared in the formula)
- 6% from model (half of the reported 99.95% confidence interval of 12%)
- 3.3% from large scale structure
- 3.0% from the radio wavelength time delay τ_{AB}

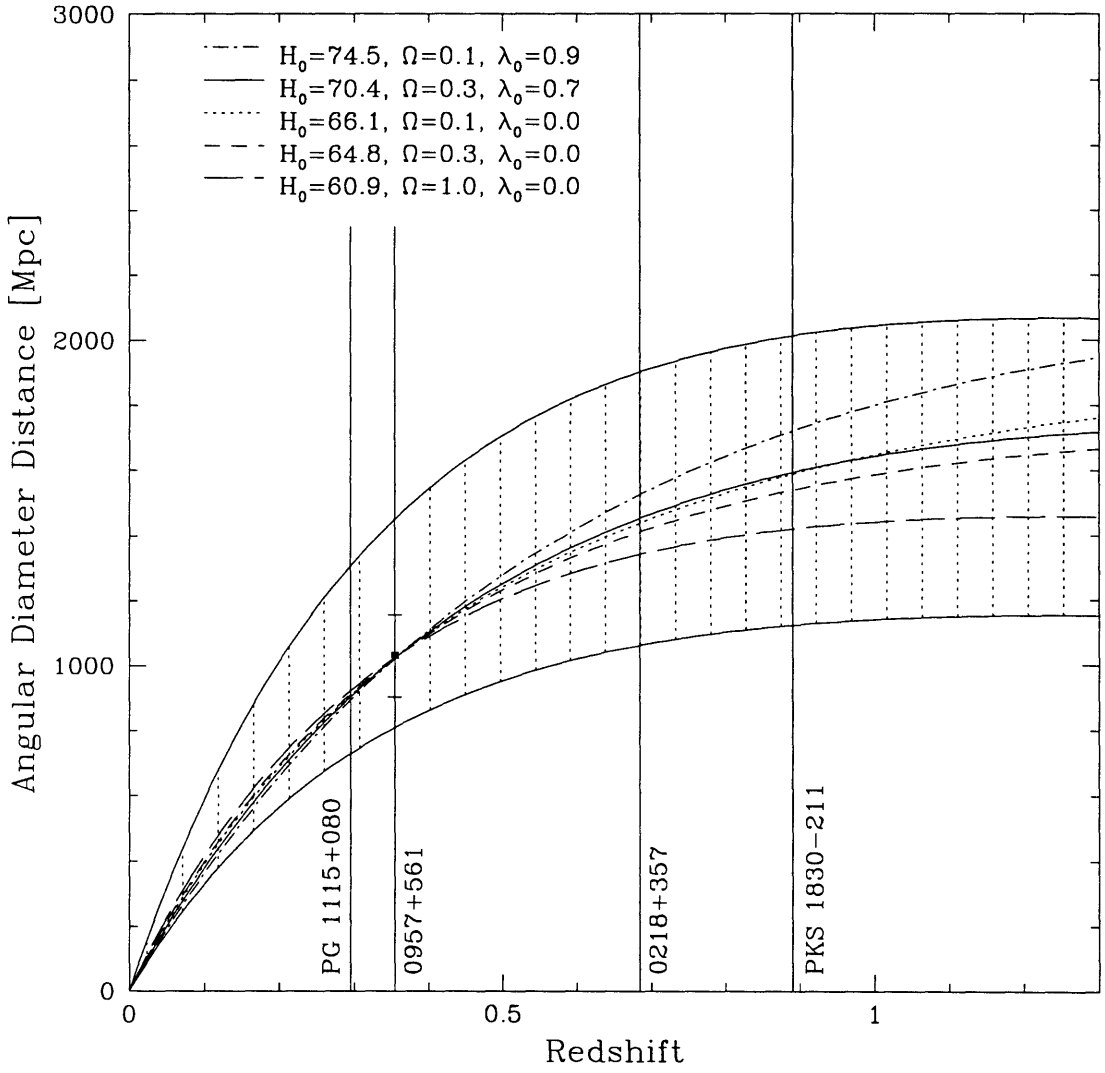

Figure 6-1: Cosmology as a function of angular diameter distance and redshift. A distance to the lens in 0957+561 of $D_{OL} = 1032^{+119}_{-122}$ Mpc and corresponding cosmologies are plotted. The shaded region indicates the result for gravitational lens PG 1115+080.

Assumed parameters	Result for $H_0(\mathrm{km\,s^{-1}Mpc^{-1}})$	
	$D_{OL} = 1032^{+119}_{-122}$ Mpc	$D_{OL} = 938^{+105}_{-108}$ Mpc
$\Omega_0 = 1.0,\ \lambda_0 = 0.0$	$60.9^{+7.2}_{-7.0}$	$67.0^{+8.1}_{-7.9}$
$\Omega_0 = 0.3,\ \lambda_0 = 0.0$	$64.8^{+7.6}_{-7.5}$	$71.3^{+8.6}_{-8.4}$
$\Omega_0 = 0.1,\ \lambda_0 = 0.0$	$66.1^{+7.8}_{-7.6}$	$72.7^{+8.8}_{-8.6}$
$\Omega_0 = 0.3,\ \lambda_0 = 0.7$	$70.4^{+8.3}_{-8.1}$	$77.5^{+9.4}_{-9.2}$
$\Omega_0 = 0.1,\ \lambda_0 = 0.9$	$74.5^{+8.3}_{-8.6}$	$81.9^{+9.9}_{-9.7}$

Table 6.5: Results for H_0 for several values of Ω_0 and λ_0.

The total uncertainty is about 12%. If instead the full 12% error quoted on the model is used, the total uncertainty is 16%. If instead the optical wavelength time delay is used (417 ± 3 days, Kundić *et al.* 1997), the uncertainty is 11%. The largest contribution to the error is from the velocity dispersion measurement and the model; the measurement is not limited by the time delay uncertainty or by the fundamental uncertainty due to large scale structure. Keep in mind that there may be significant systematic errors in the model (due to its simplistic treatment of the cluster and the choice of galaxy position) that are not included in these results for H_0.

Use of the empty beam distance instead of the filled beam distance makes very little difference in the calculations of D_{OL}. For $H_0 = 70\,\mathrm{km\,s^{-1}Mpc^{-1}}, \Omega_0 = 1, \lambda_0 = 0$, the filled-beam distance to the lens at $z_l = 0.36$ is 898 Mpc, and the empty-beam distance is 920 Mpc (the difference is just 2.4%). For higher redshift objects, however, the effect does become important: the filled-beam distance to the source at $z_s = 1.41$ is 1265 Mpc, while the empty-beam distance is 1524 Mpc, a difference of 18.5%.

In §2.3.3, it was mentioned that a lens model plus measurements of the source redshift z_s, galaxy velocity dispersion σ, and cluster convergence κ (but *not* the time delay τ_{AB}) could be used to find the ratio D_{OS}/D_{LS}, which is a function of Ω_0 and λ_0. Since this measurement is not based on the time delay, and involves information about the lens model that is unavailable in the papers described above, it is not discussed further here.

6.3.2 Status of Other Lens Time Delays

Many other gravitational lenses have been studied in hopes of making a similar measurement of H_0. To do this, the time delay must be found from monitoring the lensed images, a good lens model must be made, and the redshift of the lens must be measured. Variability has been detected in the following lenses, but no time delay has been measured: MG 1131+0456 (Hewitt *et al.* 1995), 2016+112 (Langston 1996), B 1422+231 (Hjorth *et al.* 1996), and CL 1600+434 (Jaunsen & Hjorth 1997).

Three lenses besides 0957+561 have measured time delays. The time delay of PKS 1830-211 has been estimated at 44 ± 9 days (van Ommen *et al.* 1995). Absorption lines, probably indicating the lens, have been seen at a redshift of 0.89 (Lovell *et al.* 1996). Some modeling work has been done (Kochanek & Narayan 1992), but the lack of an optical counterpart, redshift information, and its location near the galactic center have made modeling difficult.

The time delay for 0218+357 has been estimated as 12 ± 3 days based on the variability of polarized flux density (Corbett *et al.* 1996). The redshift of the lens is 0.6847. Some models have been explored (Nair 1996), but the time delay measurement needs to be confirmed and more careful modeling work must be done before cosmological measurements can be made with this lens.

Time delays were recently found for the lens PG 1115+080, which has a lens redshift of 0.295 and a source redshift of 1.722. Schechter *et al.* (1996) initially estimated the delay between the B and C images to be 23.7 ± 3.4 days (using the PRH statistical method described in §4.2). Bar-Kana (1997) later found the BC delay to be $25^{+3.3}_{-3.8}$ days using a new statistical technique (described briefly in §4.1), and found the ratio of AB and AC delays to be more consistent with models. Some modeling work was done by Schechter *et al.* (1996), but was improved by Keeton & Kochanek (1997), who explored a range of models. Unlike the 0957+561 system, there is not a large galaxy cluster accompanying the primary lens galaxy, thus there is no degeneracy with the cluster convergence (a few galaxies near the primary lens are included in the model individually). Keeton & Kochanek used a Bayesian weighting scheme with the ensemble of models to determine $H_0 = 60 \pm 17\,\mathrm{km\,s^{-1}Mpc^{-1}}$. This value assumes the Schechter *et al.* (1996) BC delay, $\Omega_0 = 1$, and $\lambda_0 = 0$. For a system with a measured time delay and redshifts, but no sheet of dark matter, the distance to the lens

can be measured, but is dependent on the assumptions for Ω_0 and λ_0. Figure 6-1 indicates the range of H_0 found from PG 1115+080 with shading. The result is completely consistent with the results from 0957+561, confirming the internal consistency of the gravitational lens distance measurement technique. The figure also demonstrates that measurements at different redshifts would begin to differentiate between cosmologies. Continued work on PKS 1830-211 and 0218+357 would be very useful.

6.3.3 Comparison with Other Techniques

How do the cosmological results found from gravitational lenses compare with the results of other distance measurement techniques? What are the advantages (and disadvantages) of the lens technique compared to others? This section discusses the distance techniques currently being used to measure the Hubble parameter H_0.

A good review of the many different techniques is given by Jacoby *et al.* (1992). The current observational status was reported at recent conferences: "The Extragalactic Distance Scale" at the Space Telescope Science Institute, May 1996 (Livio & Donahue 1997), and "Critical Dialogues in Cosmology" at Princeton, June 1996 (Turok 1997).

Freedman (1997) suggests four important criteria for a good distance indicator; the fifth is implicit in her discussion:

1. Based upon well-understood physics
2. Operates well out into the smooth Hubble flow (greater than 10,000 km/s)
3. Can be applied to a statistically significant sample of objects and can be empirically established to have high internal accuracy
4. Can be empirically demonstrated to be free of systematic errors
5. Independent of calibration to another distance indicator

Freedman points out that there is no technique that satisfies all of these criteria! Different techniques excel in different areas. All of the methods described here meet criterion #1; the Tully-Fisher method is an example of a technique based on an empirical observational law rather than a physical description. Ideally a single distance method would meet criteria #3

and #5, *i.e.* the method would work from nearby stars to distant galaxies and be independent of calibration with other techniques. Many techniques, however, only work for nearby galaxies (where the Hubble flow is distorted by the peculiar motion of nearby galaxies) but not for objects in the Galaxy (thus they require calibration with Cepheid variable stars). Despite these limitations, such methods can be useful in checking for systematic errors in methods that work out to larger distances. Methods that operate to large redshift can be used to determine not only H_0, but Ω_0 and λ_0 as well. Criterion #4 can only be met by comparing techniques with each other, for instance by comparing the distance each finds to a particular galaxy or cluster. Several techniques are discussed below in terms of how they meet the above criteria and their results for the Hubble parameter.

Gravitational Lenses. The gravitational lens time delay technique used above is based on well-understood physics, works to very high redshift (beyond the range of even SNIa), and is independent of calibration to Cepheids. Unfortunately, only two lenses have distance estimates, and while these agree, it is hardly a statistically significant sample. The values of the Hubble parameter found from this technique are listed in Table 6.5; for interesting values of Ω_0 and λ_0, the Hubble parameter is in the range 60 to 80 (although this estimate may still include significant systematic errors from the lens model).

Cepheid Variable Stars. Distance measurements using Cepheid variable stars have improved greatly with the use of the *Hubble Space Telescope* (for which observations of Cepheids in other galaxies was a major scientific goal). The Cepheid technique meets criteria #1, 3, 4, and 5, but only works for nearby galaxies (out to about 20 Mpc). Metallicity, reddening, and the distance to the Large Magellanic Cloud are the dominant sources of error. When the Cepheid data from HST are combined with the information from the SNIa, Tully-Fisher, SNII, and $D_N - \sigma$ methods, the result for the Hubble parameter is $H_0 = 73 \pm 10\,\mathrm{km\,s^{-1}Mpc^{-1}}$ (Freedman 1997). This value includes both systematic and random errors, and reflects distance measurements out to 150 Mpc. This is perhaps the most reliable measurement of H_0 currently available. The H_0 estimates from 0957+561 are completely consistent with this value for reasonable cosmologies.

Type Ia Supernovae. The distance to Type Ia supernovae (SNIa) can be found by assuming the peak luminosity is a standard candle. Riess, Press, & Kirshner (1996) improve

the standard candle technique by using the information in the light curve shape. The SNIa method is based on fairly well understood physics, and can be used out to redshifts of 0.65 and higher (with the limitation being the exposure times necessary to monitor faint objects and the seeing needed to resolve the SNIa emission from its host galaxy). Recent papers list 20 or more objects, enough to check the internal consistency of the method. The method must be calibrated with Cepheid variables. Riess *et al.* (1996) use 20 SNIa out to $z = 0.6$ and find $H_0 = 64 \pm 6\,\mathrm{km\,s^{-1}Mpc^{-1}}$. Kim *et al.* (1997) study 28 SNIa with $0.35 < z < 0.65$, compare them with nearby SNIa ($z < 0.1$), and find that for $\lambda_0 = 0$ the Hubble parameter is $H_0 < 70\,\mathrm{km\,s^{-1}Mpc^{-1}}$, and for $\Omega_0 + \lambda_0 = 1$, $H_0 < 82\,\mathrm{km\,s^{-1}Mpc^{-1}}$. These results are completely consistent with the results for gravitational lens 0957+561, which were found at comparable redshift.

Type II Supernovae. The distance to Type II supernovae (SNII) can be found by comparing its variation in total brightness and in spectral lines, and using a model of the the expanding photosphere of the explosion to determine the absolute luminosity. The physics of this is becoming better understood, the method works out to $z = 0.1$, and it is independent of Cepheid calibration. There are a small but growing number of SNII that have been monitored in this way, so studies of internal consistency are becoming possible. Schmidt *et al.* (1994) used 18 SNII and found $H_0 = 73 \pm 7$(systematic) ± 6(statistical) $\mathrm{km\,s^{-1}Mpc^{-1}}$. These results are consistent with the values from 0957+561.

Surface Brightness Fluctuations. This method is based on the fact that the surface brightness of a galaxy does not change with its distance, but variations in the surface brightness (due to stars, globular clusters, HII regions, etc.) become smoother with distance. The method is based on well understood physics, and hundreds of galaxies have been measured to demonstrate internal accuracy. With ground-based instruments, SBF can be measured only out to a redshift of 2000 km/s, and it requires Cepheid calibration. Tonry *et al.* (1997) used hundreds of galaxies to find $H_0 = 81 \pm 6\,\mathrm{km\,s^{-1}Mpc^{-1}}$, in agreement with the values from gravitational lensing.

Sunyaev-Zel'dovich Effect. The Sunyaev-Zel'dovich effect refers to the decrease of the Cosmic Microwave Background Radiation (CMBR) in the direction of galaxy clusters due to the inverse-Compton scattering with the hot gas in the cluster. The reduction in

the CMBR can be compared to the x-ray emission of the hot gas to infer the size of cluster along the line of sight. The method is based on good astrophysics, but requires significant assumptions in the modeling of the temperature and density profiles, and assumptions about the ellipticity of the cluster (to compare the apparent size with the physical size along the line of sight). The method can work for high redshift clusters and is independent of calibration to other methods. Recent measurements include $H_0 = 78^{+60}_{-40}\,\mathrm{km\,s^{-1}Mpc^{-1}}$ from Abell cluster 2163 at $z = 0.2$ (Holzapfel *et al.* 1997), where the uncertainty includes several systematic errors from the assumptions and measurements, and $H_0 = 54 \pm 14\,\mathrm{km\,s^{-1}Mpc^{-1}}$ from Abell clusters 478, 2142, and 2256 and Coma (all nearby) (Myers *et al.* 1997), where the uncertainty is much smaller since the X-ray measurements are better for nearby systems. It is currently difficult to achieve internal consistency in the method, given the large systematic and statistical errors for higher redshift clusters.

Do the above values of H_0 disagree with the age of the oldest stars in globular clusters? The age of the universe based on the cosmologies listed in Table 6.5 range from 10 Gyr ($\Omega_0 = 1.0$, $\lambda_0 = 0.0$, $H_0 = 67.0\,\mathrm{km\,s^{-1}Mpc^{-1}}$) to 17 Gyr ($\Omega_0 = 0.1$, $\lambda_0 = 0.9$, $H_0 = 74.5\,\mathrm{km\,s^{-1}Mpc^{-1}}$). The age of the oldest stars has often been quoted at around 16 Gyr, which is obviously inconsistent with the younger ages of the universe. Recent work on stellar evolution, however, has focused on the problems of metallicity, and current age estimates are in the range of 11 to 16 Gyr and older (Chaboyer 1995; Shi 1995; Jimenez & Padoan 1996).

Comparison of the gravitational lens technique to these methods shows that its merits are complementary to the other methods presented here: it works at high redshift like SNIa and the Sunyaev-Zel'dovich effect, it is independent of Cepheid calibration like SNII and the Sunyaev-Zel'dovich effect, but has a much smaller sample of measurements than Cepheid variables or surface brightness fluctuations. The results for H_0 from the lenses 0957+561 and PG 1115+080 are consistent with the results of other techniques given here. The gravitational lens technique can be best improved by finding the time delays for more lens systems, thus increasing the statistical sample size and allowing better checks against systematic errors.

Chapter 7

Physical Sources of Variability

The radio light curves of 0957+561 contain useful scientific information besides the gravitational lensing time delay. With the time delay and flux ratio found in Chapter 5, the curves for the two images can be combined to give a densely sampled light curve of the source. This combined light curve contains two important types of information. The first is information about the intrinsic variability of the source. In §7.2, models of the radio wavelength variability of Active Galactic Nuclei (AGN) are discussed and compared with the observed light curves. The second type of information is the differences between the curves for the two images. Since both curves have the same underlying source emission, differences between them above the noise level must be due to differences in the propagation path. Thus, gravitational lensing has provided a unique opportunity to study the effects of propagation on the same emission. In §7.3, the possibility of microlensing of the B image by stars in the lensing galaxy is described, and in §7.4 scattering by the interstellar medium is discussed, with an emphasis on extreme scattering events. Section 7.5 contains a discussion of the sharp fluctuation in the B image in Spring 1990. Finally, §7.6 discusses the possibility of ionized gas in the lens contributing to the time delay between the images.

Throughout this chapter, the calculations require the distances to the lens and the source. In Chapter 6, the angular diameter distance to the lens was found to be $D_{OL} =$ 1030 Mpc. In this chapter, a cosmology of $H_0 = 60\,\mathrm{km\,s^{-1}Mpc^{-1}}$, $\Omega_0 = 1$, and $\lambda_0 = 0$ will be used (this is one of the results from Chapter 6, see Table 6.5). In this cosmology, the angular diameter distance (eq. 2.33) to the source is $D_{OS} = 1475$ Mpc, and between the lens

and the source is $D_{LS} = 885$ Mpc.

7.1 Size of the Radio Emission Region

When discussing the variability of the radio source, the size of the emission region becomes important. This is the region emitting the variable emission, and probably contains several shock fronts moving out from the core (see the shock front model of variability, §7.2.3). In fact, the VLBI "core" is probably just a superposition of these shock fronts, not emission from the accretion disk or black hole at the center of the AGN. The variable emission seen in the light curves is too rapid to be coming from the VLBI jet components and knots, which are tens of pc and more from the core.

The emission region size can be estimated in a few ways. The intrinsic variability gives a size scale for the system, since the light travel time across the emission region cannot be larger than the variation time (in the absence of beaming). In 1988, the A image increased in flux density over about 345 days (between the 88Mar17 and 89Feb24 observations). This corresponds to a linear size of $L_s = 0.29$ pc at the source, or an angular size of $\theta_s = 40\,\mu$as.

The size can also be found by considering the emitted flux density at a particular frequency. It has been found that the emission region size depends on the frequency beyond just a resolution effect. Explanations have been suggested for this, such as a radial dependence for the magnetic field and electron energy distribution in the region (Kellermann & Pauliny-Toth 1981). These models find the source size to be

$$\theta_s \sim 2\frac{\sqrt{S}}{\nu}\,\text{mas} \tag{7.1}$$

where S is flux density in Jy, and ν is the observing frequency in GHz. In the A image 0957+561 light curves at 6 cm, the variable part is about 5 mJy, which gives an angular size of $\theta_s = 28\,\mu$as, or a linear size of $L_s = 0.20$ pc.

Observationally, the most recent results include a VLBA observation of the radio galaxy Centaurus A at 43 GHz (Kellermann *et al.* 1997) where the most compact component was found to be 0.5 ± 0.1 mas, or 0.01 pc at the source. This does not disagree with the above calculations, since if the above light travel time result is scaled up to 43 GHz, a linear size

of 0.03 pc is found.

The calculation above assumes that the gravitational lensing magnification of the A image does not significantly change the result. In §6.2.1, the magnification of the A image was found to be on order of a few.

The source size can also be related to brightness temperature. With a flux density of 5 mJy, a region of size $L_s = 0.3$ pc has a brightness temp of $T_B = 1.7 \times 10^{12}$ K. In Spring 1990, the B image at 6 cm changed in flux density by 4 mJy in just 20 days. If this variation were intrinsic, it would correspond to a light travel time size of 2.3 μas, and thus a brightness temperature of $T_B = 4.1 \times 10^{14}$ K. This is a strong indication that the Spring 1990 feature is not intrinsic to the source (an even better indication is the lack of a corresponding feature in the A image).

7.2 Models of Intrinsic AGN Variability

The combined light curves are a well-sampled data set of the radio galaxy variability, including monitoring at two wavelengths during the second half of the curves. This variability is described below, followed by discussion of two models for variation in Active Galactic Nuclei (AGN). These models describe radio wavelength variability on time scales of weeks and longer (models of x-ray variability, intra-day radio variability, or statistical properties of the population of variable radio sources are ignored).

7.2.1 Characteristics of Variability

The 0957+561 light curves show several typical characteristics of variable radio sources. The flux density at both wavelengths changes slowly over several months or years. At 6 cm the emission seems to have a constant component and a component that has occasional outbursts (two to three bursts in 17 years). The 4 cm light curves do not have a quiescent component, but the bursts happen on the same time scale. All of this behavior is typical of radio galaxies (Kellermann & Pauliny-Toth 1981; Aller *et al.* 1985), although some radio sources have several outbursts per year, or have frequent bursts overlapping one other so that there are few isolated events.

In Chapter 5, the structure function (defined in §4.2) was found for the light curves at each wavelength. The derived exponent of the structure function is $\alpha = 1.665$ at 6 cm and $\alpha = 1.702$ at 4 cm. The exponent indicates the how the variability changes with time scale in the light curve. Hughes, Aller, & Aller (1992) report that structure function exponents for the many radio sources in their data base are typically between 0.8 and 1.5. Sources that are dominated by a few large outbursts or have long linear trends have exponents between 1.5 and 2. Thus, the structure function of the 0957+561 light curves is consistent with the structure function of other extragalactic radio sources.

The 4 cm light curves have 40% variability (maximum to minimum divided by average), while the 6 cm curves have just 20%. This is also typical of other radio light curves (Aller *et al.* 1985) which typically have greater amplitude of variation at higher frequency.

The outbursts at the two radio wavelengths are definitely correlated. An event occurs first in the 4 cm curves, then appears with a delay in the 6 cm curves. This behavior is seen in other sources at cm wavelengths (Stevens *et al.* 1996). While 0957+561 has been monitored at optical and radio wavelengths for years, features at these two bands have not been coincident or correlated.

Besides these characteristics, the models below also predict and explain behavior that is not in the 0957+561 light curves, but has been seen in the monitoring of other radio sources. The polarization angle of some radio sources has been found to remain basically constant during an outburst, even a burst with a large change in the percentage of polarized flux density (Aller *et al.* 1985). The polarization was not measured for the 0957+561 light curves, so the polarization variability is unknown.

The variability also depends on wavelength. The variability models below predict the evolution of the spectrum of the source, *i.e.* the propagation of the burst through frequency over time. Stevens *et al.* (1996) report observations of a burst at 10 frequency bands from 375 GHz to 4.8 GHz taken over a few years. The burst appeared simultaneously in the high-frequency bands, then propagated to lower frequencies with the largest delay at the lowest frequency. The flux density of the burst peaked in the 37 GHz band. The measurement of the flux density at the peak and the time and frequency band in which the peak occurred are important parameters for both of the models below. The 0957+561 monitoring, however,

has only been done at 8 GHz and 5 GHz, thus the peak flux density was probably not observed for the outbursts and quantitative analysis of the variability cannot be done.

7.2.2 Expanding Synchrotron Source Model

An early model to explain these variability characteristics was put forth by Pauliny-Toth & Kellermann (1966) and van der Laan (1966), and reviewed in Kellermann & Pauliny-Toth (1981).

The variability is modeled as emission from an idealized expanding synchrotron region in the source. The relativistic electrons are injected into the region or accelerated in the region by an unknown process. The decrease in the emission is due to adiabatic expansion and radiation loss. The frequency dependence of the variability depends on the optical depth of the region. If the region is optically thin, the burst is seen in all frequencies at once, with the amplitude of the burst independent of frequency. If the region is opaque, the outburst occurs first at high frequencies with a large amplitude, than as the region expands adiabatically, the burst propagates to lower frequencies with decreasing amplitude.

The model is idealized in that the region is spherically symmetric and uniformly expanding, and that there is a single emitting region rather than multiple ones. The model explains single, isolated bursts with a clear increase and decrease, but not the more typical behavior of bursts overlapping one another. The model does not address the source of the energetic electrons. It explains the general features of the variability spectrum and was a good initial model of the process. More recent work, however, has shown that the model cannot describe the observed increase and decrease of bursts (Aller *et al.* 1985), unless artificial variations are made in the injection of energetic electrons (Marscher & Gear 1985).

7.2.3 Jet Shock Front Model

More recent modeling work is better able to describe observed variability. A general version of the model was initially used to explain superluminal motion (Blandford & Konigl 1979), and was later developed and applied to radio light curves (Marscher & Gear 1985; Hughes *et al.* 1985). A more sophisticated version has been given (Hughes *et al.* 1989) and applied recently to observations (Stevens *et al.* 1996).

The variability is modeled as synchrotron emission from a shock wave traveling along the jet. As the bulk flow of the material propagates outward along the collimated jet, high pressure regions and shock fronts are formed. These shock fronts are probably the source of the relativistic electrons. The electron energy loss is due to a combination of inverse-Compton scattering, synchrotron emission, and adiabatic expansion. If the collimated jet is aligned with the observer, then superluminal motion is observed. If the region initially has a random magnetic field, it becomes compressed in the shock front, leading to an ordered magnetic field (this explains the observed constant polarization angle during outbursts, Aller *et al.* 1985). The frequency dependence of the variability from 10 to 10^5 GHz is also explained by the model: at low frequencies, the shocks are optically thick and the combination of shocks leads to a flat spectrum source at cm wavelengths. At high frequency, the shock is optically thin, leading to the observed steep spectrum at optical and near-infrared wavelengths. Stevens *et al.* (1996) observed a burst decay faster than predicted by the Marscher & Gear (1985) model, and explored modifications to that model, such as curving the jet, or making the expansion non-adiabatic.

This model is an improvement over the expanding synchrotron model in that the emission region is more realistic, the superluminal motion and polarization variability are explained, the source of the relativistic particles is known, and the model can be used to describe multiple bursts. Again, however, the important parameter of the model is the peak flux density as a function of time and frequency, which is unavailable for the 0957+561 light curves. The 0957+561 light curves are, however, qualitatively consistent with this model.

7.3 Microlensing

In this section and the next, the differences between the light curves of the A and B images are explored. Since the emission of the source is the same, the differences are due to the effects of the propagation path. The B image passes much closer to the lensing galaxy G than the A image, so its much more likely to be microlensed by stars in G. In particular, an explanation of the Spring 1990 fluctuation in the B image at 6 cm is sought.

7.3.1 Theory

This discussion of microlensing variability is based on Blandford & Narayan 1992, Chang & Refsdal 1979, Kayser *et al.* 1986, Schneider *et al.* 1992, and Stabell 1993.

Consider an isolated star located within a few Einstein radii of the line of sight between the observer and the source. Assume also that the star is not part of a larger mass distribution and that the source is a point. The gravitational magnification of the source by the star will change as the lens, source, and observer move with respect to each other, causing a change in the observed flux density of the source. The time scale for this variability is just the time for the source to move past the Einstein radius of the star (the microlens),

$$t_{pt} \sim \frac{D_{OS}\theta_E}{v} = 13.4\sqrt{\frac{M}{\mathrm{M}_\odot}}\sqrt{\frac{D_{LS}D_{OL}}{D_{OS}}}\left(\frac{10^3\,\mathrm{km/s}}{v}\right)\ \mathrm{years} \tag{7.2}$$

where the distances are in units of Gpc. The velocity v is the velocity of the source relative to the line of sight between the observer and the lens, corrected for time dilation,

$$\vec{v} = \frac{\vec{v}_s}{(1+z_s)} - \frac{\vec{v}_l}{(1+z_l)}\frac{D_{OS}}{D_{OL}} + \frac{\vec{v}_o}{(1+z_l)}\frac{D_{LS}}{D_{OL}}, \tag{7.3}$$

where $\vec{v}_s$ is the velocity of the source, $\vec{v}_l$ is the velocity of the lens, and $\vec{v}_o$ is the velocity of the observer, all two-dimensional transverse velocities to the optical axis (the line from observer to lens) (Schneider *et al.* 1992, p. 421; Kayser *et al.* 1986). Equation 7.2 shows that microlensing events are more rapid for lower mass stars and for larger relative velocities.

A realistic source, however, is extended rather than a point. For a source larger than the Einstein radius of the microlens in the source plane, the time scale for the observed flux density variation increases with source size, since only parts of the source are being magnified at any one time and the effect is averaged over the source. For an extended source of linear size L_s, the time scale for variability becomes

$$t_{ext} \gtrsim \frac{t_{pt}L_s}{\theta_E D_{OS}} = \frac{L_s}{v}. \tag{7.4}$$

Thus, the shortest time scale for microlensing of an extended source becomes the time for the source to move the length of its own diameter (Chang & Refsdal 1979; Schneider

et al. 1992, pp. 422-23). Other papers characterize this dependence on source size differently, and find that significant microlensing flux density variations occur only if the source is of comparable size to the Einstein radius of the lens, θ_E. Chang & Refsdal (1979) show that to create microlensing events of a similar shape to the Spring 1990 event, the source must be approximately $\theta_s \lesssim 2\theta_E$. Stabell (1993), in a numerical analysis of the effects of large sources on microlensing, found a limit of

$$\theta_s < 5\theta_E \tag{7.5}$$

for significant magnification by the microlens. The dependence of microlensing on source size has been used to set an upper limit on the size of the optical emission region in the gravitational lens Q 2237+031 (the "Einstein cross") by simulation of the lensing galaxy and stellar density using the model of the macrolens in the system (Wambsganss *et al.* 1990; Rauch & Blandford 1991).

For the 0957+561 system, the microlensing effect is not due to an isolated star. The microlensing of the ensemble of stars in the lensing galaxy G must be taken into account, as well as the effects of the dark matter in G and in the cluster. Recall that the convergence, κ, is the surface mass density divided by the critical surface mass density Σ_{cr} (eqs. 2.8, 2.26). Then the combined surface mass density of the stars (the microlenses) is κ_s, whereas the surface mass density of the continuum dark matter is κ_c. The shear of the continuum, γ is also important. The values of κ_s, κ_c, and γ affect the shape of microlensing light curve and the frequency of events.

If the microlenses are sparse ($\kappa_s \ll 1$), microlensing events would be only be seen occasionally, and then as clear, isolated events. As the density of stars increases, the events begin to overlap, and as the critical density is approached ($\kappa_s \sim 1$), a complicated network of magnified and demagnified regions develops in the source plane (a mirage).

If the continuum mass density is small ($\kappa_c \ll 1$), the microlenses will magnify background sources, producing characteristic spikes in the light curve when the source passes near a star. If, however, the underlying continuum density is supercritical ($\kappa_c > 1$), then the source will be sharply *de*magnified when the source passes near a microlens (Kayser

et al. 1986; Chang & Refsdal 1979). If the continuum mass distribution has shear, the number of events will depend on the direction of the relative velocity between the source and the mirage.

It is difficult to predict the shape of microlensing flux density variations analytically, particularly when there are a large number of microlenses. A numerical method such as ray-tracing must be used to find the magnification at each location in the source plane, and from that produce the light curves for a given relative motion. Simulations must be used to answer questions regarding the time scale of events when there are many microlenses in a large smooth mass distribution acting on a large source.

7.3.2 Describing the Spring 1990 Event as Microlensing

The 0957+561 light curves for the A and B images are surprisingly similar to each other, at both wavelengths. This means that, in general, microlensing does not cause flux density changes (above the noise level) on time scales of up to 17 years. It is possible, however, that microlensing could cause variations at the 2% level on any time scale, or some of the differences between the curves that occur at the 3-4% level. The general lack of microlensing effects is important for determining the time delay, and is an advantage of the radio wavelength monitoring over optical monitoring, since microlensing is much more prevalent at optical wavelengths (the optical emission region is much smaller than the radio emission region). The exception to all of this is the Spring 1990 feature in the B image which is well above the noise and does not occur in the A image.

Using the distances found at the beginning of this Chapter in eq. 7.2, the time scale for variability of a point source in the 0957+561 system due to an isolated star is

$$t_{pt} = 15.1\sqrt{\frac{M}{\mathrm{M}_\odot}}\left(\frac{10^3\,\mathrm{km/s}}{v}\right)\ \text{years} \tag{7.6}$$

The relative velocity of the source can be estimated using eq. 7.3 with the distances for the 0957+561 system to find

$$\vec{v} = 0.41\vec{v}_s - 1.05\vec{v}_l + 0.63\vec{v}_o. \tag{7.7}$$

If a transverse velocity of 300 km/s is assumed for each field, the relative velocity is in the

range $0 < |\vec{v}| < 600\,\mathrm{km/s}$.

For $M = 1\,\mathrm{M}_\odot$, the variability time scale t_{pt} is 25 years for the maximum velocity, and longer for smaller velocities. For $M = 0.1\,\mathrm{M}_\odot$, velocities of $|\vec{v}| > 300$ km/s correspond to time ranges of 8 to 16 years. Thus, a solar mass microlens would cause variations on time scales longer than the observed light curves, so only a large change in magnification could be detected. A lower mass star would cause variations on time scales that would have been detected in the current light curves if the magnification had caused flux density changes greater than the noise level.

The case of an isolated star, however, is unrealistic for the 0957+561 system. The B image is close enough to the lensing galaxy to be affected by a large ensemble of microlenses, as well as a significant continuum mass distribution (dark matter in both the cluster and the galaxy) and shear. Since the continuum mass is significantly greater than the stellar mass (for a typical mass to light ratio of the galaxy), the convergence of the continuum must be supercritical. Thus, any microlensing events in the 0957+561 light curves are most likely to be demagnifications, *i.e.* dips in the light curve away from the emission due to the source and the macrolens. The Spring 1990 event is in fact such a decrease, as shown in Figure 7-1. The figure shows the B image points superimposed on the PRH optimal reconstruction of the combined A and B curves with the Spring 1990 points removed. The deviant points rise slightly above the reconstruction on either side of a significant dip below the reconstruction. This shape is typical of lens demagnification events (see for example, the light curves of Bennett & Rhie 1996, who show the demagnification caused by planets orbiting stars which are lensing background stars).

Thus, the shape of the Spring 1990 event is consistent with microlensing. If this event were indeed microlensing, what would this imply for the size of the emission region? Using the limit of the time for the source to travel the distance of its diameter (eq. 7.4), the limit on the source size is $L_s < 100\,\mu\mathrm{pc} = 20\,\mathrm{AU}$, or $\theta_s < 0.014\,\mu\mathrm{as}$. To use the limit of the source size less than about five Einstein radii (7.5), the Einstein radius of a 1 $\mathrm{M}_\odot$ star is first found from eq. 2.15 to be $\theta_E = 2.2\,\mu\mathrm{as}$. Then the limit is $\theta_s < 11\,\mu\mathrm{as}$, or $L_s < 0.08$ pc. These estimates are very different. The second set of limits, however, is within an order of magnitude of the emission region size found in §7.1 from the light travel time of this

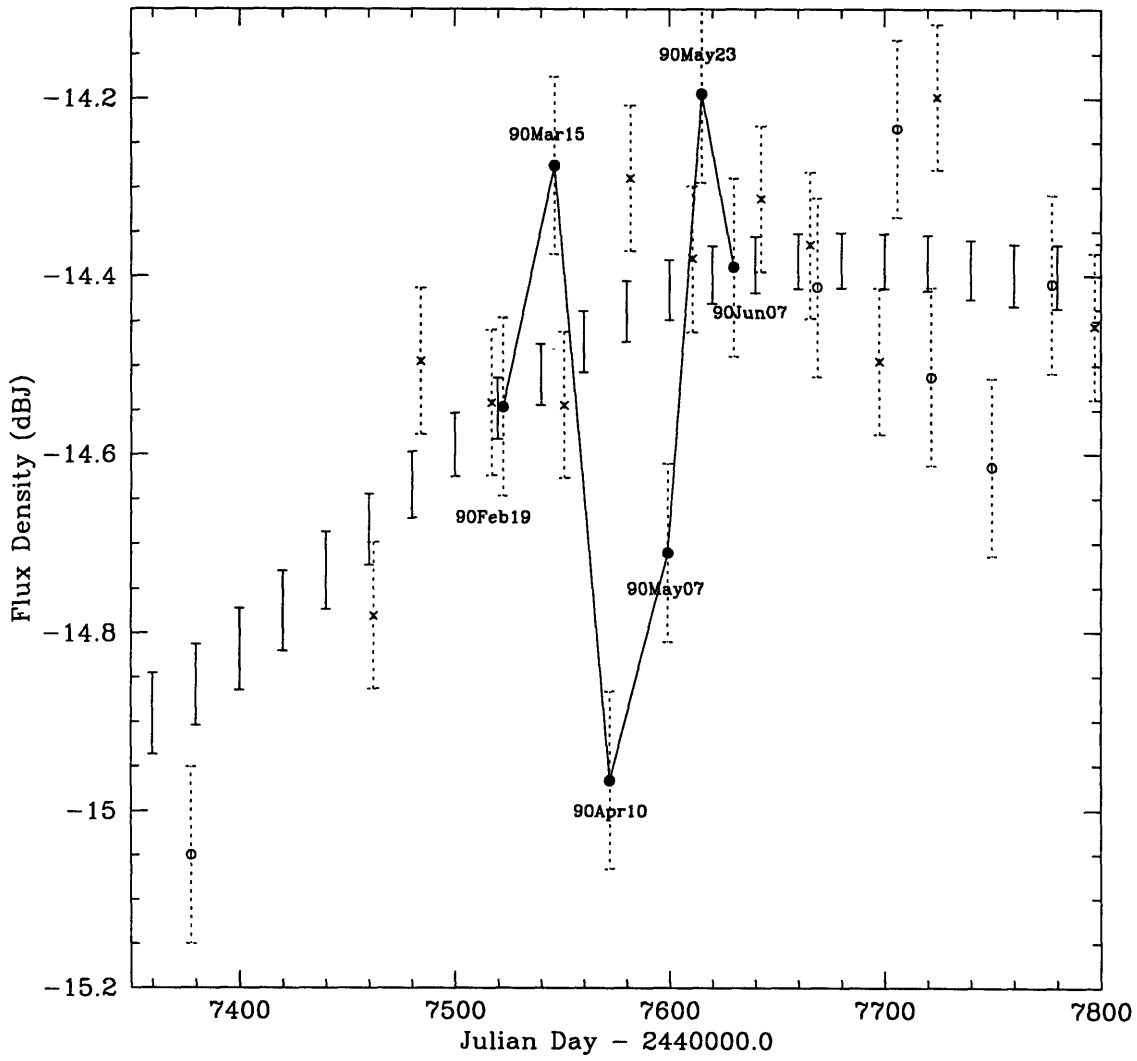

Figure 7-1: Spring 1990 event in B image at 6 cm. The crosses are the A image observations, and the circles are the B image observations (shifted by the delay and ratio). The six observations making up the event are marked. The one sigma error bars of the optimal reconstruction are shown, where the reconstruction was made with the four inner points of the event removed.

feature. A much more detailed analysis (including simulated light curves) is needed in order to determine a more accurate upper limit on the emission region size. If such a limit were found, it would be a significant aid in understanding the nature of radio jets.

7.4 Interstellar Scintillation

Besides microlensing of the B image, there are other physical processes that may affect one image and not the other. In this section, scintillation (scattering) by plasma in the interstellar medium is discussed. The several types of interstellar scintillation (ISS) are described, then the mostly likely type is used as an explanation for the Spring 1990 event. Rickett (1990) provides a general review of propagation of radio waves through the interstellar medium, and was used heavily in the following sections.

7.4.1 Weak ISS

Rickett 1990 describes several regimes of interstellar scattering. Weak interstellar scattering is a type of ISS that affects observations at frequencies $\gtrsim 10$ GHz. It is distinguished from the various types of strong ISS by the linear mathematical solutions used to describe the phenomenon. The amplitude of weak ISS will be reduced if the source size θ_s is less than the characteristic angle for weak ISS,

$$\theta_{wk} \sim 8\sqrt{\frac{s_{ism}}{\mathrm{kpc}}}\sqrt{\frac{\mathrm{GHz}}{\nu}}\,\mu\mathrm{as}, \tag{7.8}$$

where s_{ism} is the distance through scattering medium and ν is the observing frequency. For $s_{ism} = 0.2$ kpc and $\nu = 5$ GHz, the limiting value is $\theta_{wk} = 1.6\,\mu$as. Considering the size estimates found in §7.1 and §7.3.2, the emission region in the source is most likely several times θ_{wk}; thus, this type of scattering is not expected in the light curves.

7.4.2 Diffractive ISS

Diffractive ISS is a type of strong interstellar scattering. For strong ISS, the mathematical description of the phenomenon requires non-linear solutions. Strong ISS is typical for ob-

servations at frequencies of less than a few GHz. There are two main types of strong ISS: diffractive and refractive.

To describe diffractive and refractive ISS, first define the field coherence scale, d_0. This is the lateral separation at the observing plane across which there is a 1 radian difference in the phase of the arriving emission. The corresponding scattering angle is defined as

$$\theta_{sc} \sim 15 \sqrt{\frac{\mathrm{kpc}}{s_{ism}}} \sqrt{\frac{\lambda}{\mathrm{cm}}} \, \mu\mathrm{as}, \tag{7.9}$$

where λ is the observing wavelength. Diffractive ISS is caused by the summing and interference of waves from locations θ_{sc} or less apart. Diffractive ISS only affects sources with sizes $\theta_s \lesssim \theta_{sc}/100$. For $s_{ism} = 0.2$ kpc and $\lambda = 6$ cm, the scattering angle is $\theta_{sc} = 82\,\mu$as. Thus, the source must be smaller than about $0.8\,\mu$as to display diffractive ISS, but the size estimates found in §7.1 and §7.3.2 are much larger than this. Thus, 0957+561 is unlikely to show diffractive ISS.

7.4.3 Refractive ISS

Refractive interstellar scintillation (RISS) is the other major type of strong ISS. First define the radius of the scattering disk, $s_{ism}\theta_{sc}$, to be the longest transverse scale that influences the signal arriving at a single point. Large phase differences across the disk cause partial focusing or defocusing of the source, *i.e.* refractive amplitude variations, analogous to refraction by a wavy piece of glass. Displacement of the observer by $s_{ism}\theta_{sc}$ corresponds to a new scattering volume. RISS does not cause significant variability in polarization, except if two regions in the source of different polarization (amplitude or angle) are affected differently by the scattering. Only sources with $\theta_s < \theta_{sc}$ will be affected by RISS, where θ_{sc} was estimated above to be $82\,\mu$as. The size estimates in §7.1 and §7.3.2 are somewhat less than θ_{sc}, thus, the variable emission region in 0957+561 would probably be susceptible to RISS.

RISS manifests itself in several ways. One is "low frequency variables." These sources have variations of up to 30% over a time scale of months at frequencies less than 1 GHz, and tend to be located in the galactic plane. This type of variability has also been seen on time scales of tens of days at cm wavelengths. Another manifestation of RISS is "flickering"

sources. These have variations of a few percent on a time scale of about 10 days at cm wavelengths (Heeschen & Rickett 1987; Heeschen 1984; Simonetti *et al.* 1985). Both the flickering sources and low frequency variables would have brightness temperatures exceeding 10^{12} K if refractive ISS could not be used to explain the variability.

It is possible that these two versions of RISS are happening in the 0957+561 light curves. The variability in both cases is too rapid for detection in the current monitoring, so it would appear as deviations of individual observations from the light curves. Since the measurement error in the light curves is of order 2%, the flickering phenomenon would appear mainly as an addition to the noise.

7.4.4 Extreme Scattering Events

A third type of refractive interstellar scintillation is an extreme scattering event (ESE). Fiedler *et al.* (1987) first detected an extreme scattering event in the light curve of an extragalactic radio source and suggested a basic theoretical description. The theory was developed by others as well (Romani *et al.* 1987), and the events to date and theory were recently reviewed (Fiedler *et al.* 1994). ESEs continue to be detected (Clegg *et al.* 1996), occasionally at several wavelengths (Pohl *et al.* 1995). VLBI observations were recently made of several sources exhibiting ESEs (Fey *et al.* 1996).

Extreme scattering events are the discrete version of refractive interstellar scattering. The event occurs when a dense plasma cloud (or scatterer) moves past the source (see Figure 7-2), scattering emission away from the line of sight to create a dip in the observed flux density. Before and after the cloud is in front of the source, the emission is scattered *into* the line of sight, producing a slight increase in flux density on either side of the dip. The scattering is caused by the dispersion of electromagnetic waves in the plasma cloud. The inhomogeneities in the cloud redistribute the radiation from a point source into a Gaussian distribution of angles, thus the ray bundle from the source undergoes broadening, or defocusing. There are four important parameters in modeling an extreme scattering event: the angular size of the source, the angular size of the cloud, the broadening angle, and the velocity of the cloud. An ESE is different from other types of RISS. Other types persist over many years, are more erratic, and are created by the proper motion of small-

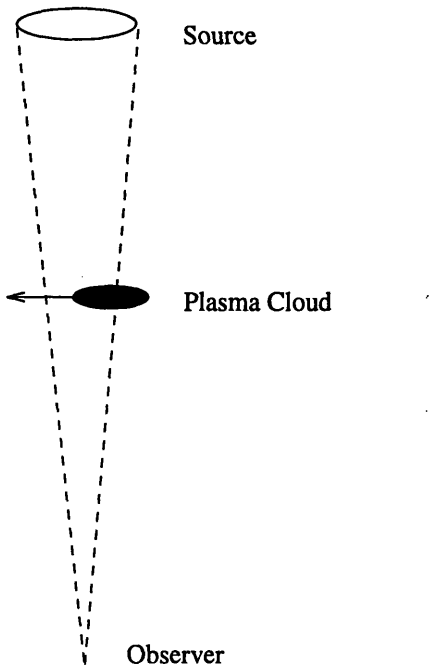

Figure 7-2: Plasma cloud moving in front of source in an extreme scattering event.

scale electron density turbulence in a large region of the interstellar medium. An ESE is caused by the proper motion of a smaller cloud with larger electron density variations and much large peak densities. The resulting event is more clearly defined in the light curve.

The light curve of an ESE typically has a slight increase followed by a large decrease to a round or flat minimum, then an increase back to above the quiescent level before returning to quiescent. When the source and the scatterer are of comparable angular size, the minimum is rounded, but when the cloud is larger than the source, the minimum is flat. The angular size of the cloud must be comparable to the angular size of the source in order for the event to occur: if the cloud is much smaller than the source, the scattered flux will be negligible compared to the intrinsic flux; if cloud is much larger, then as much flux will be scattered towards the observer as away and no variation will be seen. Events typically last 90 to 450 days, and the decrease in flux density is typically 6% to 100%, at 2.7 GHz (Fiedler *et al.* 1994). The events are frequency dependent, lasting longer and having larger flux density decreases at lower frequencies. One particular event lasted a few days at 10.6 GHz, a week at 5 GHz, and 4 weeks at 2.7 GHz (Pohl *et al.* 1995). Fiedler *et al.* (1994)

have also found that many of the ESEs are seen within 10° of loops of galactic continuum emission, a correlation that is statistically significant. This is evidence that the events are due to plasma in the interstellar medium of the Galaxy.

7.4.5 Describing Spring 1990 Event as an ESE

The Spring 1990 variation in the B image (see Figure 7-1) could be an extreme scattering event. Since the intrinsic source emission is recorded in both the A and B images, gravitational lensing provides a unique opportunity to measure the light curve both with and without the extreme scattering event. The deviations of the observations from the optimal reconstruction have the characteristic shape of simple ESEs. The event at 5 GHz is at least 69 days long (between the 90Mar15 and 90May23 observations), with the length of the minimum t_{min} roughly 30 days, and the rise time from the minimum to the second peak, t_{rise}, is between 16 and 43 days. These are typical time scales for ESEs at this frequency. The event has a 10% decrease in flux density from quiescent, which is also typical. The Spring 1990 event could be round or flat bottomed, since there are not enough data points to distinguish the shape at the minimum. It is interesting that the event occurs just at the beginning of an outburst in the intrinsic emission of the source (this was also seen by Pohl *et al.* 1995). Fiedler *et al.* (1994) point out that if the source is flaring, then the evolving compact emission region could be a significant fraction of the flux density and would increase the likelihood of an extreme scattering event.

The quantitative analysis here of the Spring 1990 event as an ESE will be very simple. Current papers on ESEs (Fey *et al.* 1996, Pohl *et al.* 1995) have a difficult time finding unique models for the events, and usually only attempt to find plausible models. Fey *et al.* (1996) only attempt a basic model if the event has a simple shape and the source does not have complicated VLBI structure (at least 80% of the flux density in the core). The 0957+561 event shape is simple, and the source structure at 6 cm is dominated by the core (Campbell *et al.* 1994), but with just four data points a detailed description cannot be made.

First, could the plasma cloud be known interstellar material? Since Fiedler *et al.* (1994) found most ESEs to be near the loops of galactic continuum emission, it is worth exploring

this possibility. The galactic coordinates of 0957+561 are $l = 157.6°$, $b = 48.7°$. This location is about 10° from one of the loops (Fiedler *et al.* 1994; Berkhuijsen *et al.* 1971). This adds to the plausibility of an ESE as an explanation for the Spring 1990 event.

The angular speed of the plasma cloud can be estimated from the time needed for the back edge of cloud to move past the whole source,

$$v_{cld} = \frac{\theta_s}{t_{rise}}, \tag{7.10}$$

where θ_s is the angular size of the source, t_{rise} is the rise time from the minimum to the second peak, and v_{cld} is the angular speed of the plasma cloud. If $\theta_s = 1$ mas and $t_{rise} = 20$ days, then the angular speed of the cloud is $v_{cld} = 50\,\mu$as/day. For the source size found from light travel time (§7.1), $\theta_s = 40\,\mu$as, the angular speed is $v_{cld} = 2\,\mu$as/day. In the papers describing ESEs, the source size is usually assumed to be a few tenths of a mas (from VLBI observations, although this is really only an upper limit on the true source size), and thus those papers usually report angular speeds of a few tens of μas/day.

The angular speed of the cloud is helpful in estimating its distance. An angular speed of $v_{cld} = 50\,\mu$as/day implies a speed of $415c$ at the source, $290c$ at the lens, and 84 km/s in the Galaxy (at a distance of 1 kpc; at these low relative speeds the motion of the earth and sun would have to be incorporated into the model). Of these three possible locations for the scatterer, the interstellar medium of the Galaxy is the most likely, given the highly superluminal speeds at the other locations. If, however, the angular speed of the cloud is just $2\,\mu$as/day, the speed at the source is $17c$, at the lens is $11c$, and at 1 kpc away is just a few km/s. Superluminal motion on the order of $10c$ has been seen in extragalactic sources, so with $v_{cld} = 2\,\mu$as/day the possibility of the scatterer at the source or the lens cannot be ruled out. The simplicity of the event and the nearness of the source to known interstellar plasma clouds support the argument for a galactic scatterer. If the cloud is at a known distance or has a known linear velocity, the calculation can be reversed to find a (highly assumption dependent) estimate of the source size.

The shape of the event can also be used to relate the angular sizes of the scatterer and the source. The size of the scatterer is found from the time the front edge of the cloud

covers the whole source until the back edge of the cloud just starts to uncover the source,

$$\theta_{cld} = v_{cld} t_{min} = \theta_s \frac{t_{min}}{t_{rise}} \tag{7.11}$$

where θ_{cld} is the angular size of the plasma cloud and t_{min} is the length of the minimum. For $v_{cld} = 50\,\mu$as/day, and $t_{min} = 40$ days, the angular size is $\theta_{cld} = 2$ mas. At a distance of 1 kpc, that corresponds to a linear size of 2 AU. For $v_{cld} = 2\,\mu$as/day, the angular size is $\theta_{cld} = 80\,\mu$as, or a linear size of 0.08 AU at a distance of 1 kpc. The larger angular velocity and its results are similar to the numbers found in ESE papers (Fiedler *et al.* 1987; Fey *et al.* 1996). As the second part of the equation shows, this is not a calculation of the absolute size of the scatterer or the source, but rather a way of using the timing of the event to find the relative sizes. The fact that an ESE occurred shows that the cloud and the source are of comparable size. Although the A and B images are just 6″ apart, the cloud size is comparable to the size of the B image core, thus it is not expected to affect the A image in any way, or even the jets of the B image.

The electron density of the cloud could presumably be found from the depth of the event, the sizes of the cloud and the source, and the observing frequency, but this would require a closer reading of the ESE literature.

7.5 Discussion of Spring 1990 Event in B Image

In Spring 1990, the B image changed sharply in flux density at 6 cm (see the 6 cm light curves in Figure 3-5). In §3.3 the event was shown to be of physical origin (rather than poor or corrupted data). In §5.1.1, the PRH analysis showed that the event has different statistical properties than the rest of the curve. Figure 7-1 plots the event with the optimal reconstruction of the rest of the 6 cm light curves, showing that (for the delays found in Chapter 5), the event is a sharp dip in flux density. Sections 7.3.2 and 7.4.5 found that the event could be a microlensing event due to the stars in the lensing galaxy G, or an Extreme Scattering Event (ESE) due to the interstellar medium in the Galaxy.

The event is unique in the light curves. Why do similar events not occur elsewhere in the monitoring? Both the ESE and microlensing effects become less probable as the source

size increases, and are therefore not likely to affect the quiescent emission region (which is much larger than the variable emission region). Thus the most likely time for these events is at the beginning of an outburst when the size of the shock front or hot spot is small. Microlensing is expected to affect only the B image, but the A image could be just as likely as the B image to experience an ESE at the beginning of an outburst.

Is there any observational way to distinguish these two explanations of the Spring 1990 event? The event was only observed at one frequency and there are only a few data points, so the current data do not distinguish between the explanations. If an event were well sampled, the shape could be modeled as each of the two events to see which gave a more reasonable fit. If an event were observed at several frequencies, the frequencies dependence could distinguish clearly between the two. Extreme scattering events last longer and have larger amplitudes at lower frequencies. Microlensing is independent of frequency for a given emission region size, but the emission region is smaller at high frequency (see eq. 7.1), so the microlensing event will be shorter and of larger amplitude at higher frequency.

Both effects are dependent on the emission region size. As shown in §7.3.2, the appearance of a microlensing event can be used to set an upper limit on the source size. If the event is an ESE, the angular size of the source must be comparable to the angular size of the plasma cloud causing the ESE. Since the current observations cannot distinguish between the microlensing and ESE theories, no definitive statement about the source size can be made from the Spring 1990 event.

7.6 Plasma Delay

In Chapter 5, all of the statistical techniques found somewhat longer time delays for the 6 cm light curves than for the 4 cm light curves (see Table 5.1). Could there be a physical process causing this frequency dependence? One possible explanation is the plasma dispersion of the B image. The delay due to the electron gas in the galaxy cluster and in the interstellar medium of the Galaxy are ignored, since they are the same for the A and B images, but the plasma in the lensing galaxy would affect primarily the B image. The plasma delay is larger at longer wavelengths, so it would cause the B image to have a longer delay at

6 cm than 4 cm. In this section, the plasma delay is calculated. Note, however, that if the plasma is dense enough to cause a delay of several days, a significant delay would be seen at both radio bands (with respect to the optical light curves), yet in Chapter 5 the radio delay was found to be consistent with the optical result. The plasma delay is unlikely, but for reference the amount of the delay is calculated below.

The plasma frequency, below which an electromagnetic wave will not propagate, is

$$\nu_p^2 = \frac{n_e q_e^2}{\pi m_e}, \tag{7.12}$$

where n_e is the electron density of the plasma, q_e is the electron charge, and m_e is the electron mass. The increased travel time for a radio wave in a plasma (relative to the travel time in vacuum) is

$$t_{pl}(\nu_i) = \frac{q_e^2}{2\pi c m_e \nu_i^2} \int n_e ds, \tag{7.13}$$

where the integral is known as the dispersion measure and is taken along the light travel path. This equation assumes the observing frequency is much greater than the plasma frequency (Rybicki & Lightman 1979).

The integral can be roughly approximated by $\langle n_e \rangle \cdot s_g$, where s_g is the distance the B image passes through the lens galaxy G, and $\langle n_e \rangle$ is the mean electron density over s_g. The delay of the signal between two wavebands due to the plasma in the lens is then

$$t_{pl}(\nu_i) - t_{pl}(\nu_j) = \left(\frac{\langle n_e \rangle}{\mathrm{cm}^{-3}}\right)\left(\frac{s_g}{\mathrm{kpc}}\right)\left(\frac{1}{\nu_i^2} - \frac{1}{\nu_j^2}\right) 4.1\,\mathrm{sec} \tag{7.14}$$

where ν_i, ν_j are measured in GHz. If $\nu_i = 5$ GHz and $\nu_j = 8$ GHz, then

$$\Delta t_{pl} = \left(\frac{\langle n_e \rangle}{\mathrm{cm}^{-3}}\right)\left(\frac{s_g}{\mathrm{kpc}}\right) 0.10\,\mathrm{sec}. \tag{7.15}$$

The average electron density $\langle n_e \rangle$ is roughly $0.03\,\mathrm{cm}^{-3}$ for a spiral galaxy, and would be less in an elliptical galaxy. The distance s_g through G can be approximated as 10 kpc, which corresponds to $2''$ at the lens redshift. The relative delay would then be $\Delta t_{pl} \sim 1$ second, which would be completely undetectable in the monitoring. To achieve a delay of 40 days between 6 cm and 4 cm, the average electron density would have to be on order of $10^4\,\mathrm{cm}^{-3}$,

even when assuming the largest reasonable galaxy size of 25 kpc or 5″ (the largest size before the A image would also be affected). This average electron density is completely unrealistic. For reasonable values of electron density and distance ($\langle n_e \rangle = 0.03\,\mathrm{cm}^{-3}$ and $s_g = 10\ kpc$), a much larger frequency difference is needed to achieve a 40 day delay (for example, 22 GHz to 590 kHz).

Thus the plasma delay could not cause the difference in the time delay between 6 cm and 4 cm. Note that the value of PRHχ^2 did not increase significantly for the joint analysis of the two wavelengths, thus the light curves at both wavelengths are consistent with a delay of 420 days.

Chapter 8

Conclusion

8.1 Summary of Results

A strong gravitational lens can create multiple images of a background source. If the source varies, the time delay between the images can be measured through careful monitoring. The time delay, along with a measurement of the velocity dispersion of the lensing galaxy and a model of the lens mass distribution, determines the angular diameter distance to the lens, as explained in Chapter 2. The redshift and the distance of the lens determine the Hubble parameter for a given cosmology. The main scientific goal of this thesis has been to monitor the gravitational lens 0957+561 in order to measure the time delay and set limits on cosmological parameters.

Chapter 3 describes the monitoring program. Observations of 0957+561 have been made approximately monthly with the VLA radio telescope at 6 cm and 4 cm. There are 140 observations of good quality at 6 cm between 1979 and February 1997, and 52 observations at 4 cm since 1990. The data were analyzed with AIPS software, using the same data analysis techniques that were used on the early sections of the 6 cm light curves (Lehár *et al.* 1992). Maps of the lens system are given in Figure 3-1 and 3-3. The resulting light curves are shown in Figures 3-5 and 3-6. The time delay between the images is slightly more than one year, as can be seen by inspection of the light curves. At 4 cm, the events occur earlier and are twice as variable compared to the 6 cm curves.

In order to determine the time delay from the light curves, three statistical techniques

were used, as described in Chapter 4: χ^2 structure function analysis (Press, Rybicki, & Hewitt 1992b, 1992c), dispersion analysis (Pelt *et al.* 1994, 1996), and discrete correlation function analysis (Lehár *et al.* 1992). Gaussian process Monte Carlo light curves were made to determine the confidence interval of the result for the observed light curves, and a pseudo-jackknife technique was used to check the confidence interval and determine the dependence of the result on the removal of points. The results of applying these analyses to the light curves are described in Chapter 5 and summarized in Table 5.1. The PRHχ^2 result for the time delay was found to depend only slightly on the structure function or the removal of points, although the confidence interval and the smoothness of the χ^2 surface depends on the structure function. The dispersion result for the time delay of the full 6 cm light curve was found by the pseudo-jackknife analysis to be very dependent on the removal of points. The discrete correlation result for the time delay was dependent on the range used to fit the peak of the binned correlation. The analysis of the 6 cm and 4 cm data together resulted in delays consistent with optical monitoring, using either the dispersion or PRH techniques. The PRH result of $\tau_{AB} = 420 \pm 13$ days had a smaller confidence interval and was used for the determination of the cosmological results.

In Chapter 6, the models of the mass distribution and the cosmological results were discussed. Three lens models in the literature were reviewed. Falco, Gorenstein, & Shapiro (1991a) modeled the galaxy as a King model sphere plus a core mass, and the cluster as a sheet of matter with shear and convergence. The model of Kochanek (1991) was very general, and demonstrated that the lens is too complicated to be described by a model of 5 or 6 parameters. Kochanek found that modeling the galaxy cluster as a matter sheet with shear and convergence introduced significant systematic error into the result. Grogin & Narayan (1996a, 1996b) had access to more and better quality observational constraints, yet continued to use the simple model of Falco *et al.* (1991a). They also used the magnification matrix (with its correlated errors) rather than the positions of the jet components (which is much more direct). Grogin & Narayan found that the results depended significantly on the position used for the lensing galaxy. Thus, the Grogin & Narayan result probably contains large systematic errors, yet since it is based on better observational data, it is used here. The distance to the lens found using this model and the velocity dispersion of Falco *et al.*

(1997) is $D_{OL} = 1032^{+119}_{-122}$ Mpc.

When this distance is compared with the redshift of the lens for several combinations of Ω_0 and λ_0, the Hubble parameter H_0 is found to be in the range of 60 to 75 $\mathrm{km\,s^{-1}Mpc^{-1}}$ (see Table 6.5 and Figure 6-1). The systematic errors in the modeling could significantly enlarge this range. The recent measurement of the time delay in the lens PG 1115+080 by Schechter *et al.* (1996), when combined with a lens model (Keeton & Kochanek 1997), yields values of H_0 consistent with this. Compared with other distance measurement techniques, gravitational lensing has the advantage of working at high redshift, beyond the proper motion of local galaxies, and giving information about Ω_0 and λ_0 as well as H_0. It is also independent of calibration to other distance indicators. There are very few lenses with measured time delay thus far, so it is difficult to test the internal consistency of the method. Yet the results for H_0 are consistent with recent results from Cepheid variable stars, type Ia supernovae, type II supernovae, and surface brightness fluctuations.

Besides these cosmological results, there is other scientific information in the light curves, as discussed in Chapter 7. The combined light curve can be used to study the intrinsic variability of the source. The intrinsic variability at the two wavelengths is consistent with the expanding shock front model of AGN outbursts. Differences between the light curves for the two images give information about the propagation path of the two ray bundles. In particular, the B image underwent a large fluctuation in Spring 1990 which is not seen in the shifted A image (the event is plotted in Figure 7-1). This event is consistent with microlensing by a star in the lensing galaxy which would cause a significant demagnification. If the event were microlensing, simulations could be used to set an upper limit on the emission region size. The event is also consistent with scattering by a plasma cloud in the Galaxy moving past the B image, an "extreme scattering event." If the event is an ESE, the angular size of the source must be comparable to the angular size of the plasma cloud. Multi-wavelength observations of the event would distinguish between the microlensing and ESE possibilities. Finally, the difference in delay found between the 6 cm and 4 cm light curves could not be due to dispersion by plasma in the lensing galaxy.

8.2 Future Work

This thesis work has answered several scientific questions, but other questions have been raised. This section gives recommendations for work that could be done to address these questions.

Could the systematic and random error of the light curve data points be reduced? In the discussion of the VLA data reduction (§3.2) several possible improvements were mentioned. These include amplitude calibration to a model of the calibrator 3C286, rather than calibration to 3C286 as a point or calibration to the phase calibrator 1031+567 (which may have varied in flux density over the 17 years). At 6 cm, self-calibration should be done after the cross-calibration step, since this is known to introduce a small bias in the measured flux density of the points. Use of modern AIPS procedures in the analysis of the 6 cm data would allow for more precise CLEAN boxes and other improvements. During a reanalysis of all the VLA data, the polarization angle and fractional flux density could be measured to check for polarized variability (either intrinsic to the source or due to propagation effects). Polarization analysis would require accurate polarization calibration and careful accounting for Faraday effects before the polarized variability could be used to determine the time delay. Finally, the Monte Carlo techniques developed by Moore (Moore 1996) could be used to find and remove the deconvolution and self-calibration bias from the flux density measurements.

Would reduction of errors in the light curve measurements aid in answering the scientific questions? These improvements would probably not reduce the uncertainty in the measurements to less than 1% (the lowest value obtained by Moore). The difference between 2% and 1% random error will not make a significant difference in the time delay analysis. It is possible that reanalysis of the data may change the measurement of a few individual points by several percent which could affect the delay somewhat; the pseudo-jackknife analysis suggests, however, that for the PRH and dispersion methods, a change in an individual point alters the time delay only by roughly the confidence interval found from Gaussian Monte Carlo data. New, well-sampled events in the light curves are much more likely to improve the resulting time delay than reanalysis of the old data. Reanalysis could, how-

ever, improve the understanding of the interstellar scattering and microlensing effects in the curves. If 1% errors were achieved, then differences of a few percent between the A and B images become significant and could be evidence of one of these effects.

Could the the precision or accuracy of the 0957+561 time delay analysis be improved? With this thesis work, the radio and optical results for the time delay have been found to be consistent with each other to within 3%, with several statistical analyses agreeing for each. It would be difficult to confirm the optical result and its 1% confidence interval with the radio light curves, since this would require a rapid change in the flux density of the source (the optical result is based on a 10% change over 10 days, which is unlikely to occur at radio wavelengths). Thus the radio monitoring of this lens could be discontinued now that the time delay is known. Since events are currently taking place in the radio light curves, it would be nice to include the expected decrease in both images at 6 cm before ending the monitoring.

Yet, the question of how to improve the statistical time delay analysis is still interesting in itself, and will be important for analysis of light curves from other lenses. The question becomes: what is the most accurate way to find the time delay between two irregularly sampled signals with some non-Gaussian and non-stationary characteristics? With the delay known, the 0957+561 radio light curves become an ideal data set for such studies. Methods could be tested for the effects of sampling by dividing the curves into subsections in time, or removing observations to simulate less frequent sampling. Another area to explore is that of inhomogeneous errors, particularly the dependence of the measurement error on VLA array, length of the observation, weather conditions, or the observed random and systematic error in the map. The analysis method of Bar-Kana (1997) allows for correlated errors, and could be used to better understand the errors in the flux density measurements. Other statistical techniques in the literature or in the list in Table 1.1 could also be tried on the current 0957+561 light curves to better understand the advantages and disadvantages of each technique. In particular, a rigorous technique that allows for non-Gaussian or non-stationary properties in the light curves is needed, and some work has begun on this (Press & Rybicki 1997). Such a technique would be useful both for analysis of the real light curves, and for making synthetic Monte Carlo data that has all the properties of the real curves.

Given the time delay, could the determination of the distance to the lens be improved through better modeling? Even with the observational constraints currently available, the recent lens modeling work of Grogin & Narayan (1996a, 1996b) could be improved upon, as described above. Mass models of 0957+561 could also be improved by the use of better observational constraints. Current observational work includes observations by the author using the Very Long Baseline Array (VLBA), the Green Bank 140 Foot Telescope, and the VLA. These observations will be more sensitive than the those of Garrett *et al.* (1994) to the faint milli-arcsec scale jet structure in the A and B images, and will also be better able to study the spectrum and structure of the object G′. Observations of the system have been made with Hubble Space Telescope (HST) and have found the optical position of the lensing galaxy G1 with more precision (Bernstein *et al.* 1997). Future work should include a confirmation of the precise measurement of the galaxy velocity dispersion (Falco *et al.* 1997), since its value and error are squared in the calculation of the distance to the lens. Future work could also include a more careful calculation of the core and jet flux ratios, through comparison of coincident VLBI and VLA observations (made by the author and collaborators in 1995 September), or through fitting four parameters in the time delay analysis: time delay, quiescent (jet) flux ratio, variable (core) flux ratio, and the difference between the core and jet flux densities in one of the images. Finally, a full synthesis (several hour) observation of 0957+561 at 4 cm in the VLA A-array would allow analysis of emission in the region between the core of the B image and the lensing galaxy G, and of the structure of G at radio wavelengths.

How could the cosmological results from gravitational lenses be improved? The precision of the Hubble parameter estimate from 0957+561 is currently limited by systematic error in the model and systematic and random error in the velocity dispersion measurement. The method in general could be most improved by finding time delays for more lenses. The author is collaborating with J. Hewitt, C. Moore, and C. Trotter to monitor several radio bright lenses with the VLA and VLBA telescopes in order to determine their time delays. Most of these lens systems have delays on the order of days or weeks, thus the monitoring project can be shorter than the years needed to determine the 0957+561 time delay. Other areas of future work are measuring the redshifts of each lens and source, and modeling the

lens mass distributions with small systematic and random errors. It has been difficult to find lens systems that have all the necessary components for cosmological tests: a variable source, measurable lens and source redshifts, and an easily modeled mass distribution. More lenses will ultimately be needed, and these are being sought in several survey projects at optical and radio wavelengths.

In Chapter 7 a variety of interesting science in the light curves (besides the time delay) was discussed. Future work in this area can include further study of the current observations, new observational work, and consideration of yet other science in the curves. Further study of the current observations should perhaps begin with a reanalysis of the light curve data to reduce the measurement error on each point, so that differences between the curves at the few percent level become significant. The models of intrinsic variability could be tested by measurement of the spectral index of the variable component in the light curves, but would ultimately require monitoring at several wavelengths (which would go beyond the needs of the time delay monitoring and be a poor use of VLA time). To improve the analysis of microlensing in the curves, simulations should be done which take into account the stellar density in the lensing galaxy, the shear and continuum matter of the cluster and galaxy dark matter, the size of the emission region at various times in the light curve, and the structure function of the intrinsic source variability.

If an event such as the Spring 1990 fluctuation in the B image were to occur again in the light curves, how could the observing strategy be improved to better understand it? First, the observations could be made more frequently in order to track the shape of the variation (this is important, even if the length of each observation must be reduced). Second, observing should be done in at least two frequencies, since the frequency dependence of the event could be used to differentiate between microlensing and extreme scattering events. Polarization variability, or changes in the position or size of the image during the event, would also give clues about the physical process (although the position and size changes would most likely be overwhelmed by the VLA beam size).

Is there any other scientific information that could be determined from the light curves? As the longest monitoring sequence of any gravitational lens (by far), this is a unique data set. One remaining question is the cause of the slightly longer delays at 6 cm compared

to 4 cm. Another is the longer delays in early sections of the 6 cm curves compared to later sections. Are these phenomena caused by a physical process, some exotic cosmological effect, or are they just a fluke of these light curves? Other questions may exist that could also be addressed with these light curves. Monitoring should not be discontinued without careful consideration of these questions.

Appendix A

List of Symbols

Symbols used in the thesis are listed below. They are grouped by topic with the relevant chapters indicated, and are roughly in alphabetical order. In some cases the same symbol is used for more than one quantity, but the context and chapter topic should make it clear which quantity is meant.

Radio Astronomy (Chapter 1)

A_e	effective antenna area
A	amplitude of signal
$\tilde{A}_{ij}$	observed amplitude
A_{ij}	true amplitude
a_i	amplitude of gain of antenna i
$\vec{B}$	baseline
$D(l,m)$	dirty beam
g_i	complex gain of antenna i
$I_\nu(\vec{s})$	intensity of source at frequency ν and position $\vec{s}$
I_ν^{dirty}	dirty image
l,m,n	coordinates for the sky
N_a	number of antennas
$\mathcal{S}(u,v)$	sampling function
S	known amplitude of source
$\vec{s}$	position of source
$\vec{s}_0$	phase tracking center
$\vec{s}'$	2-dimensional vector between $\vec{s}$ and $\vec{s}_0$.
t	time
t_G	geometric delay between arrival of a plane wave at two antennas

t_{obs}	total observing time
T_{sys}	system temperature
u, v, w	coordinates for the baselines on the ground
V_1, V_2	voltage at antenna 1, 2
η_c	correlator efficiency
ν	observing frequency
$\Delta\nu$	total bandwidth
$\Gamma(u,v)$	visibility
$\tilde{\Gamma}_{ij}$	observed visibility
Γ_{ij}	true visibility
ϕ_i	phase gain of antenna i
$\tilde{\vartheta}_{ij}$	observed phase
ϑ_{ij}	true phase

Cosmology, Lenses, and Modeling (Chapters 2, 6)

A	north image
B	south image
$\vec{b}$	impact parameter of an image with the lens, linear distance from center of lens in lens plane (in cylindrical coordinates)
c_c	cluster core radius
c_{cr}	cluster critical radius
D^A	angular diameter distance
D^L	luminosity distance
D_{OS}	distance from the observer to the source
D_{OL}	distance from the observer to the lens
D_{LS}	distance from the lens to the source
$D_{\rm eff}$	effective distance of the lens system
$f(x)$	function in King lens model
g_{cr}	galaxy critical radius
G	lensing galaxy at radio wavelengths
G1	lensing galaxy at optical wavelengths
G′	VLBI object near lensing galaxy
H_0	Hubble parameter
M_i	magnification matrix of image i with respect to the unlensed source
M_{ij}	relative magnification matrix between images i and j
$\mathsf{M}_{\rm AB}$	relative magnification matrix between images A and B
M	mass of point mass lens
M_c	core mass of lensing galaxy
$M(r)$	mass included in radius r
n_r	index of refraction

n	number of images
q	used in expression for magnification of images by point mass lens
$\vec{r}$	linear distance from center of lens in spherical coordinates
r_c	linear core radius of galaxy
R	flux ratio, B/A in linear units
R_{jet}	flux ratio of brightest jet component
R_{core}	flux ratio of core
s	distance along line of sight or ray path
z_i	redshift of object i
z_s	source redshift
z_l	lens redshift
$\hat{\vec{\alpha}}_i$	bending angle for image i
$\vec{\alpha}_i$	effective bending angle for image i
$\alpha_*(\theta)$	function in FGS91 King model
α_0	coefficient in GS96 SPLS model
$\vec{\alpha}_g$	bending angle due to galaxy
$\vec{\alpha}_{M_c}$	bending angle due to core mass
$\vec{\alpha}_{cl}$	bending angle due to cluster
$\vec{\beta}$	position of source
χ^2	indicator of goodness of fit
$\bar{\chi}^2$	χ^2 per degree of freedom, reduced χ^2
ϵ_g	ellipticity of galaxy
ϵ_{cl}	ellipticity of cluster
η	radial index of mass increase
$\Gamma(x)$	Gamma function
γ	shear
γ'	scaled shear
κ	convergence
Λ_0	cosmological constant
λ_0	cosmological constant in units of Ω_0
Ω_0	scaled mass density of universe
φ	polar angle
φ_ϵ	position angle of ellipticity ϵ
$\varphi_{\epsilon c}$	position angle of cluster ellipticity
$\varphi_{\epsilon g}$	position angle of galaxy ellipticity
φ_γ	position angle of shear γ
Φ	conventional Newtonian 3-dimensional gravitational potential
ψ	scaled 2-dimensional (projected, surface) gravitational potential
ψ_0	spherical part of radial galaxy potential, Kochanek model
ψ_2	quadrapole of radial galaxy potential, Kochanek model

ψ_{cl}	cluster potential
ψ_g	galaxy potential
$\rho(r)$	mass density as a function of radius r
ρ_0	central mass density
$\Sigma(b)$	surface mass density
Σ_{cr}	critical surface mass density necessary to make multiple images
Σ_0	central surface mass density
σ	confidence interval
σ	line of sight velocity dispersion of luminous matter in galaxy
σ_{dark}	velocity dispersion of dark matter in galaxy
σ_{3D}	three-dimensional velocity dispersion of galaxy
σ_{cl}	velocity dispersion of cluster
τ_{geom}	lensing geometric time delay
τ_{grav}	gravitational time delay
τ_i	time delay of one image relative to no-lens case
τ_{ij}	time delay between two images
τ_{AB}	time delay between the A and B images
$\vec{\theta}$	position of an image on sky, 2-dimensional angle
θ_c	angular core radius
θ_E	Einstein radius
θ_x, θ_y	components of $\vec{\theta}$ along the major and minor axes of an elliptical galaxy
$\theta_{xcl}, \theta_{ycl}$	components of $\vec{\theta}$ along the major and minor axes of a cluster with shear
ζ	function of cluster convergence κ and galaxy velocity dispersion σ found from modeling

Time Delay Analysis (Chapters 4, 5)

A	inverse of B
a_i	observation from A light curves
$\bar{a}_*$	mean of a_i in discrete correlation delay bin
b_i	observation from B light curve
$\bar{b}_*$	mean of b_i in discrete correlation delay bin
b'_i	observation from B light curve, shifted by flux ratio
B_{ij}	covariance model associated with $y(t)$
C_{ij}	covariance matrix associated with $s(t)$
$\mathcal{D}(\tau, R)$	dispersion
$e(t)$	measurement error in $y(t)$
e_i	measurement error for y_i
e_a	measurement error for a_i
g	optical g wavelength band (green)
$\mathcal{I}$	Pelt *et al.* (1994) statistic for removal of points
$\mathcal{L}(\tau)$	locally normalized discrete correlation function

l	location in list where point removed in $\mathcal{I}$
m	number of points in list removed in $\mathcal{I}$
N	number of points in light curve
n_*	number of pairs in discrete correlation delay bin
$P(y)$	joint probability distribution of the data vector y
PRHQ	Press, Rybicki, & Hewitt Q statistic
R	flux ratio, B/A in linear units
R_6	VLA flux ratio at 6 cm
R_4	VLA flux ratio at 4 cm
R_g	flux ratio at optical g band, includes emission from lensing galaxy
$s(t)$	signal from source
$\langle s^2 \rangle$	variance of the signal
$\hat{s}(t)$	optimal reconstruction of the signal
t_i	time of the observation y_i
T	lag between two points on a light curve
$V(T)$	structure function of a light curve
V_0	coefficient of the structure function
v_{ij}	point estimates of the structure function
W_i	weight of data point i
W_{ij}	weight of pair of data points ij
$y(t)$	measured light curve, data vector
$\bar{y}$	estimate of the mean of y_i
$\mathcal{Y}_6$	data vector of full 6 cm light curves
$\mathcal{Y}_6'$	data vector of 6 cm light curves minus four Spring 1990 points
$\mathcal{Y}_4$	data vector of 4 cm light curves
$\mathcal{Y}_g$	data vector of optical light curves at g band
Z_{ij}	to downweight pairs with larger separation in the dispersion statistic
α	exponent of structure function
PRHχ^2	Press, Rybicki, & Hewitt χ^2 statistic
Δ	separation with zero weight in the dispersion statistic
δ_{ij}	delta function (equals 1 for $i = j$, equals 0 otherwise)
σ^2_{a*}	standard deviation of observations a_i in delay bin
τ_{AB}	time delay between the A and B images
$\Delta\tau_{AB}$	size of delay bin around τ_{AB}

Physical Sources of Variability (Chapter 7)

b	galactic latitude coordinate
d_0	field coherence scale for strong ISS
l	galactic longitude coordinate
L_s	linear size of the source, projected along the line of sight

n_e	electron density of the plasma
$\langle n_e \rangle$	mean electron density of the plasma
s	line of sight to source
s_g	length of ray path through lensing galaxy
s_{cld}	distance to plasma cloud causing an extreme scattering event
s_{ism}	distance through the interstellar medium causing ISS
S	flux density of source
T_B	brightness temperature
t_{pt}	microlensing time scale for a point source
t_{ext}	microlensing time scale for extended source
t_{rise}	extreme scattering event rise time
t_{min}	extreme scattering event length of minimum
$t_{pl}(\nu_i)$	plasma delay at frequency ν_i
Δt_{pl}	plasma delay between two frequencies
v_{cld}	extreme scattering event angular velocity of plasma cloud
$\vec{v}$	relative transverse velocity of source for microlensing
$\vec{v}_s$	transverse velocity of source
$\vec{v}_l$	transverse velocity of lens
$\vec{v}_o$	transverse velocity of observer
γ	shear of the continuum mass distribution
κ_s	convergence due to stars (microlenses) in the lensing galaxy
κ_c	convergence due to the continuum mass distribution
λ	observing wavelength
ν	observing frequency
ν_p	plasma frequency
θ_s	angular source size
θ_{wk}	angular source size limit for weak interstellar scattering
θ_{sc}	scattering angle for strong interstellar scattering
θ_{cld}	angular size of plasma cloud in extreme scattering event

Abbreviations

AGN	active galactic nuclei
AIPS	Astronomical Image Processing System
ESE	extreme scattering event
FGS91	Falco *et al.* 1991a
FITS	flexible image transport system (a standard format for storing images)
GN96	Grogin & Narayan 1996a, 1996b
HST	Hubble Space Telescope
ISS	interstellar scattering
L92	Lehár *et al.* 1992

LST	local sidereal time
P94	Pelt *et al.* 1994
P96	Pelt *et al.* 1996
PRH1, PRH2	Press *et al.* 1992b, Press *et al.* 1992c
S90	Schild 1990
SPLS	softened power law sphere lens model
ST95	Schild & Thomson 1995
V89	Vanderriest *et al.* 1989
VLA	Very Large Array
VLBA	Very Long Baseline Array
VLBI	Very Long Baseline Interferometry

Physical Constants

c	speed of light
G	gravitational constant
k_B	Boltzmann constant
π	3.14159
e	2.71828
q_e	electron charge
m_e	electron mass

Units

$''$, mas, μas	arcsecond, milli-arcsecond, micro-arcsecond
AU	astronomical unit
dBJ	decibels relative to 1 Jy
$^\circ$	degree
kHz, MHz, GHz	Hertz
mJy, Jy	Jansky
K	Kelvin
mag	optical magnitude
$M_\odot$	solar mass
cm, km	meter
pc, kpc, Mpc, Gpc	parsec
s, day, year	time

Appendix B

VLA Observations of 0957+561

Table B.1 lists all the observations of 0957+561 made at the Very Large Array which are known to the author. The calendar date is given in the first column. The second column records the "Snap" number (an inherited designation of the data used in old records, from "snapshot" observation) for the 6 cm data sets used in the light curve. The VLA array for the observation is reported in the third column, with the arrow indicating a transitional array.

The fourth column gives the VLA Program code for each. In the early years of the VLA, the codes were based on the observers name: "GREEN" indicates the observer was P. Greenfield, "BURKE" indicates B. Burke, and "ROBE" indicates D. Roberts. In later years, numbers were assigned to observing proposals: the program codes AB129, AB456, AB705, and AH604 refer to the series of proposals made by the MIT Radio Astronomy group to monitor the source. The comments indicate the proposer associated with other program codes (the data were included in the light curve if the proposer has collaborated with the MIT Radio Astronomy group). Codes starting with V, W, or B generally indicate VLBI observations.

The fifth column gives the frequency band(s) used in the observation: the bands are L $\sim$ 1.5 GHz, C $\sim$ 5 GHz, X $\sim$ 8 GHz, U $\sim$ 15 GHz, and K $\sim$ 22 GHz. The sixth column gives the tape and file numbers for the data set. The raw VLA data has been archived on six tapes, with a data set sometimes being saved on more than one tape or file. The data on tapes 1, 2, and 3 are recorded in VLA export format, and must be read by the task

"FILLM" within AIPS. Tapes 4, 5, and 6 contain FITS format files written to tape with the unix command "tar."

The seventh column gives the length of the observation in hours. This is time allocated, and includes moves and calibrator observations. The eighth column gives the Local Sidereal Time (LST) at the middle of the observation. Finally, comments are given in the last column, such as which data sets were used as references. A question mark indicates the quantity is unknown. In particular, a question mark in the Tape; File column indicates the data set is not on any of the six tapes, while question marks in other columns indicate the information that could be found from the data files on tape. Dots indicate the quantity is not applicable.

Table B.1: VLA observations of 0957+561

Date	Snap	Array	Program	Bands	Tape; File	Length	LST	Comments
79Jun23	45	P	?	?	?	?	?	
79Oct13	46	P	GREEN	C	2;36-37	12h	10:00	
				L,U	2;35			
80Feb23	47	P	GREEN	C	2;33-34	12h	10:00	
80Feb26	?	P	GREEN	L	2;31-32	12h	10:00	
80May26	?	P	BURKE	C	2;30	0.3h	11:30	
80May31	?	P	BURKE	C	2;29	0.3h	10:15	
80Jun20	48	P	GREEN	C,L	2;28	5h	6:00	
80Jul12	?	?	ROBE	U	1;108-109 2;25-27	12h	10:00	
80Jul26	01	C	ROBE	C	1;107, 2;24	?	?	
80Aug20	02	C	ROBE	C	1;106, 2;23	1h	6:30	
80Sep17	03	C	ROBE	C	1;105	1h	6:30	
80Oct03	04	C	ROBE	C	1;104	1h	10:30	
80Nov24	05	A	ROBE	C	1;103	1h	7:20	
80Dec16	49	A	GREEN	C,L	1;100-102	11.5h	9:00	
81Jan06	06	A	ROBE	C	1;99	1h	11:30	
81Jan23	6X	A	ROBE	C	1;97-98 2;45-46	?	?	
81Jan24	6A	A	ROBE	C	2;47	0.5h	9:45	

Date	Snap	Array	Program	Bands	Tape; File	Length	LST	Comments
81Jan26	6B	A	ROBE	C	1;96	0.5h	10:20	
81Feb13	?	A	ROBE	C	?	1.5h	8:45	
81Mar03	07	A	ROBE	C	1;95	0:30	8:30	
81Mar27	08	A	BURK	C,L	1;94	1h	9:45	
81Apr13	09	A	ROBE	C	1;93	1h	11:30	
81May14	10	B	ROBE	C	1;92	1h	11:00	
81May28	11	B	ROBE	C	1;91	1h	13:30	
81Jun14	12	B	ROBE	C	1;90	1h	11:30	
81Jul16	13	B	ROBE	C	1;89	?	?	
81Aug15	14	B	ROBE	C	?	1h	9:30	
81Sep17	15	D	ROBE	C	?	1h	7:30	
81Oct20	16	C	ROBE	C	1;88, 2;44	1h	10:30	
81Nov21	17	C	ROBE	C	1;87	1.5h	10:45	
81Nov25	18	C	ROBE	C	1;86	1h	9:00	
81Dec05	19	C	ROBE	C	1;85	0.75h	11:10	
82Jan09	20	C	ROBE	C	1;83-84	1h	11:15	
82Feb09	21	C→A	ROBE	C	1;82	1h	10:30	
82Mar03	22	A	ROBE	C	1;81	1h	9:30	
82Mar27	23	A	ROBE	C	1;80	1h	8:20	
82May08	24	A	ROBE	C	1;79	5h	10:20	6 cm A-array reference
82Jun02	25	A	ROBE	C	1;78	2h	10:00	
82Jun27	26	A	ROBE	C	1;72	2h	?	
82Jul16	27	B	ROBE	C	2;42-43	2h	8:00	
82Aug21	44	B	ROBE	C	1;70-71	2h	10:00	
82Sep23	28	B	ROBE	C	1;69	2h	8:00	
82Oct25	29	B→D	AB129 ROBE	C	?	2h	10:30	
82Dec04	?	D	AB129	C	?	?	?	
82Dec19	30	D	ROBE	C	1;67-68	2h	9:00	6 cm D-array reference
83Jan20	31	C	ROBE	C	1;66	2h	10:00	
83Feb16	32	C	ROBE	C	1;65	2h	10:00	
83Mar15	33	C	ROBE	C	1;64	2h	12:00	
83Apr03	34	C	ROBE	C	2;41	3h	9:30	6 cm C-array reference

Date	Snap	Array	Program	Bands	Tape; File	Length	LST	Comments
83May05	35	C	ROBE	C	1;63	2h	10:30	
83Jun13	...	D	VG032	C	...	...	...	
83Jul22	...	...	VG32	C	...	...	...	
83Aug04	36	D→A	ROBERT	C	1;33	2h	11:30	
83Aug13	...	A	AR98	L,U	...	0.3h	9:00	Proposer is L. Rudnick
83Sep06	37	A	AL60	C,U	1;61-62	2h	11:00	Proposer is J.Hewitt
83Sep19	...	A	W97	C	...	0.3h	8:30	
83Oct08	38	A	AB129	C,U	1;60	3h	10:30	
83Nov01	...	A	AB263	C,U	1;73-77 1;56-59 2;48-49	15.5h	9:00	Proposer is D. Roberts
83Nov26	39	A	AB129	C,U	1;54-55	3h	10:30	
84Feb11	40	B	AB129	C,U	1;32	3h	?	
84Apr22	41	C	AB129	C,U	1;30-31	3h	?	
84Jun22	42	C	AB129	C,U	1;28-29	3.25h	?	
84Aug02	43	D	AB129	L,C	2;39-40	?	?	
84Nov16	?	D→A	AB129	C	?	?	?	
84Dec12	50	A	AB129	C	1;53	2h	?	
85Feb12	51	A	AB129	C	1;27	2h	?	
85Apr20	52	B	AB129	C	1;51-52	2h	?	
85Jun02	53	B	AB129	C	1;25	2.5h	10:50	6 cm B-array reference
85Aug17	54	C	AB129	C	1;24	2h	?	
86Feb19	55	A	AB129	C	1;23	2h	?	
86Apr03	56	A	AB129	C	1;49-50	2h	?	
86May21	57	A	AB129	C	1;47-48	2h	?	
86Jul20	58	B	AB129	C	1;22	2h	7:30	
86Sep11	59	B	AB129	C	1;20-21	2h	7:10	
86Nov12	60	C	AB129	C	1;19	2h	11:00	
87Jan11	61	C	AB129	C	1;18	3h	9:25	
87Jul20	62	A	AB129	C	1;45-46	2h	9:00	
87Sep27	63	A	AB456	C	1;43-44	3h	11:45	
87Dec09	64	B	AB456	C	1;16-17	2.25h	9:45	
88Jan26	65	B	AB456	C	1;15	2h	9:10	

Date	Snap	Array	Program	Bands	Tape; File	Length	LST	Comments
88Mar17	66	C&D	AB456	C	1;42	2h	9:30	
88May08	67	C&D	AB456	C	1;41	2h	10:00	
88Oct27	68	A	AB456	C	2;38-39	2.5h	10:20	
88Nov18	69	A	AB456	C	1;39	2h	11:40	
88Dec21	70	A	AB456	C	1;38	2h	10:00	
89Jan24	71	A	AB456	C	1;37	2.25h	11:30	
89Feb24	72	AnB	AB456	C	1;14	2h	9:00	
89Mar25	73	B	AB456	C	1;13	2h	10:00	
89Apr26	74	B	AB456	C	1;12	2.3h	10:50	
89May19	75	BnC	AB456	C	1;11	2h	10:00	
89Jun20	76	C	AB456	C	1;36	2.25h	12:45	
89Jul16	77	C	AB456	C	1;10	1.67h	10:00	
89Sep27	78	C	AB456	C	1;34-35	2h	12:00	
89Nov11	...	D	VG61	C	...	...	...	
90Jan12	79	D	AB46(sic)	C	1;9	1.5h	14:15	
90Jan23	80	D	AB456	C	1;8	1.5h	9:30	
90Feb01	81	D→A	AB456	C	1;7	1.5h	11:00	
90Feb19	82	A	AB456	C	1;6	2h	11:00	
90Mar15	83	A	AB456	C	4;29	2h	12:00	
90Apr10	84	A	AB456	C	1;5	2h	9:30	
90May07	85	A→AnB	AB456	L,C,U,K	1;4	1h	13:20	
90May23	86	A→AnB	AB456	C	1;3	1.5h	9:50	
90Jun07	87	A→AnB	AB456	C	1;2	2h	11:30	
90Jul15	88	AnB	AB456	C	2;22	2h	9:15	
90Aug21	89	B	AB456	C	2;21	2h	10:30	
90Sep06	90	B	AB456	C	2;20	2h	9:00	
90Oct04	91	BnC	AB456	C,X	2;19	2h	11:00	
90Nov01	92	C	AB456	C,X	2;18	2.75h	9:00	
90Dec13	93	C	AB456	C,X	2;17	1.75h	7:15	
91Jan17	94	C	AB456	C,X	2;16	1.75h	7:20	
91Jul10	95	A	AB456	C,X	2;15	0.5h	9:30	
91Aug18	96	A	AR247	C,U	2;13-14	3h?	10:00	Proposer is D. Roberts
91Oct17	...	AnB	AP0001	L	...	3h	8:45	Proposer is R. Porcas

Date	Snap	Array	Program	Bands	Tape; File	Length	LST	Comments
92Jan06	97	B	AB456	C,X	2;12	2h	11:00	
92Feb04	98	BnC	AB456	C,X	2;9	2h	9:00	
92Feb29	99	C	AB456	C,X	2;8	2h	8:50	
92Mar07	100	C	AB456	C,X	2;7	2h	7:50	
92Apr18	101	C	AH437	C,X	2;6	2h	9:00	Proposer is J. Hewitt
92May03	102	C	AB456	C,X	2;5	2h	11:20	
92May20	···	C	AO107	L,C	···	0.3h	13:45	Proposer is A. Oren
92Jul28	···	D	AB456	C,X	2;4	1.5h	10:30	
92Oct23	103	A	AB456	C,X	2;3	2h	9:00	
92Nov11	104	A	AB456	C,X	2;2	2.3h	10:15	
92Dec10	105	A	AB456	C,X	3;13	2h	9:40	4 cm A-array reference
93Jan19	···	A→AnB	AB456	C,X	3;2	···	···	Data lost due to snow
93Feb05	106	AnB	AB456	C,X	3;1	2h	8:30	
93Mar21	107	B	AB456	C,X	3;3	2h	8:00	
93Apr09	108	B	AB456	C,X	3;4,5	2h	10:00	4 cm B-array reference
93May18	108A	B→C	AB456	C,X	4;27,28	1.5h	8:00	
93Jul25	109	C	AB456	C,X	3;6	2h	6:00	
93Aug26	110	C	AB456	C,X	3;7	2h	9:30	
93Nov12	···	D	AB456	X	3;8	2h	10:00	4 cm D-array reference
93Nov22	···	D	AB456	C,X	4;26	0.5h	9:15	
94Jan15	···	D	AB456	X	3;9	2.5h	8:45	
94Feb14	111	D&B&A	AB705	C,X	3;10	2.5h	9:15	
94Mar04	112	A	AB705	C,X	3;11	1h	9:00	
94Apr11	113	A	AB705	C,X	4;24,25	1h	10:30	
94May07	114	A→AnB	AB705	L,C,X	4;21-23	2h	11:00	
94Jun25	115	B	AB705	C,X	4;19,20	2h	11:00	
94Jul06	116	B	AB705	C,X	5:1	2h	10:00	
94Aug18	117	B	AB705	C,X	4;17,18	1.5h	9:15	
94Sep08	118	B	AB705	C,X	4;15,16	2h	10:30	
94Oct10	119	BnC	AB705	C,X	4;13,14	2h	10:30	
94Nov07	120	C	AB705	C,X	4;11,12	2h	10:00	4 cm C-array reference
94Dec08	121	C	AB705	C,X	4;9,10	2h	8:00	
95Jan12	···	CnD	AB705	X	4;8	2h	11:30	

Date	Snap	Array	Program	Bands	Tape; File	Length	LST	Comments
95Jan25	···	CnD	AB705	X	4;7	2h	11:30	
95Feb20	···	D	AB705	X	4;6	2h	8:30	
95Mar08	···	D	AB705	X	4;5	1.5h	8:45	
95Apr18	···	D	AB705	X	4;4	2h	8:30	
95May06	···	D	AB705	X	4;3	2h	9:00	
95May21	···	D→A	AB705	X	4;2	1h	9:30	
95May28	···	D→A	AB705	X	4;1	2h	10:00	
95Jun18	122	D→A	AB761	C,X	5;2	1h	12:00	Time from A. Fletcher
95Jun23	123	A	AB705	C,X	5;3	2h	11:00	
95Jun28	124	A	AB705	C,X	5;4	1h	12:00	Some time from P. Hicks
95Jul08	125	A	AB705	C,X	5;5	2h	5:30	
95Jul20	126	A	AB705	C,X	5;6	2h	13:00	
95Jul30	127	A	AB705	C,X	5;7	2h	11:30	
95Aug07	128	A	AB705	C,X	5;8	2h	10:00	
95Aug10	129	A	software	C,X	5;9	0.5h	12:15	Time from K. Sowinski
95Aug14	130	A	AM484	C,X	5;10	0.5h	?	Time from S. Myers
95Aug17	131	A	?	C,X	5;11	0.5h	4:45	Time from S. Conner
95Aug18	132	A	AB705	C,X	5;12	0.5h	14:15	Some time to S. Myers
95Aug18	133	A	AL357	C,X	5;13	0.5h	?	Time from J. Lehár
95Aug28	134	A	AH552	C	4;30	0.25h	8:00	Time from C. Trotter
95Sep01	135	A	AB705	C,X	6;1	1h	11:30	
95Sep09	136	A→AnB	AB705	C,X	6;2	2.5h	7:15	
95Sep15	137	AnB	AB705	C,X	6;3	2h	7:00	
95Sep23	138	AnB	AB705	C,X	6;4	2h	9:00	
95Sep30	139	AnB	AB705	C,X	6;5	2h	9:30	
95Oct10	140	B	AB705	C,X	6;6	2h	10:00	
95Oct27	141	B	AB705	C,X	6;7	2h	12:00	
95Nov09	142	B	AB705	C,X	6;8	2h	9:30	
95Dec26	143	B	AB705	C,X	6;9	2h	10:00	
96Jan26	144	BnC	AB705	C,X	6;10	2h	9:00	
96Feb05	145	BnC	AB705	C,X	6;11	2.5h	8:15	
96Feb26	146	C	AB705	C,X	6;12	2.5h	7:15	
96Mar04	147	C	AB705	C,X	6;13	2h	8:00	

Date	Snap	Array	Program	Bands	Tape; File	Length	LST	Comments
96Apr05	148	C	AB705	C,X	6;14	2h	7:00	
96Apr25	149	C	AB705	C,X	6;15	2h	11:00	
96May27	...	CnD	AB705	X	6;16	2h	9:00	
96Jun11	150	CnD	AB705	C,X	6;17	2.5h	9:45	
96Jul07	...	D	AB705	X	6;18	2h	11:00	
96Aug19	...	D	AB705	X	?	2h	9:00	
96Sep16	...	D	AB705	X	?	3h	10:00	
96Oct19	151	A	AB705	C,X	6;19	2h	8:00	
96Nov10	152	A	AB705	C,X	6;20	2h	7:00	
96Dec26	153	A	AB705	C,X	6;21	1.5h	10:45	
97Jan10	154	A	AH604	C,X	6;22	1h	9:30	
97Feb26	155	B	AH604	C,X	6;23	1.5h	10:45	

Appendix C

AIPS Run Files

This appendix contains the AIPS "Run" Files used for the automated VLA data reduction.

UTILITY contains basic procedures used in the other run files.

CFLAG contains the necessary procedures and variable settings for flagging and calibrating 6 cm data in preparation for the run files of Joseph Lehár (DQPROC, DQALL). DQPROC contains the basic procedures and definitions used in DQALL. DQALL contains higher level procedures for the major steps of the reduction. DQDO runs these higher level procedures on the chosen data set. The file "crecipe" is not an AIPS run file, but a description of the manual steps used to process a 6 cm observation from beginning to end.

XPROC contains low level procedures and definitions for use in XFLAG and XCALGRND. XFLAG contains those procedures necessary for flagging and calibrating the 4 cm data. XCALGRND defines the "grand" procedure which does all the major steps of data reduction on the 4 cm data. XACT runs "grand" on the chosen data set. "xrecipe" is a description of the manual steps used to process a 4 cm observation from beginning to end.

```
$****************************************************************
$ UTILITY: several basic procedures and definitions
$ some elements inspired by or copied from J.Lehar and C.Moore

restore 0
docrt 1

$ **** Declare temporary variables ****

PROC TDECLARE
STRING*50 title
STRING*15 tempname, tempclass
STRING*2 temptype
SCALAR tempseq, tempdisk
SCALAR clsz, mpsz, rs, ds, off
FIN

$ ******* miscellaneous procedures *******

PROC GOWT(TASK)
go; wait
RET;FIN

PROC CLRZAP
type 'DELETING:',inna,incl,inse
clrstat; zap
RET;FIN

PROC DELETE
type 'DELETING:',inna, incl, inseq
zap
RET;FIN

PROC MESSAGE
priority 0; prnumber -1; prtask ''; prtime 0
docrt -1; outprint 'curdir:messages'
prtmsg; clrmsg
docrt 1; outprint ' '
FIN

PROC CLR2O
in2name ''; in2seq 0; in2class ''; in2disk 0
FIN

PROC HEAD(TITLE)
type '########################################'
type '#', title
type '########################################'
RET;FIN

$ ****** file moving procedures *******

PROC SETUVCOP
$moves data between aips disks
$ like Conner's MOVEDATA for 'uv'
$ getn file, set outname, outclass, outseq, outdisk
selband -1; selfreq -1; freqid -1; bchan 1; echan 0;
bif 1; eif 0; sources ''; qual -1; uvrange 0 0;
timeran 0; antennas 0; baseline 0; uvcopprm 0 0 0 1
FIN

PROC SETSUBIM
$moves data between aips disks
$ like Conner's MOVEDATA for 'ma'
$ getn file, set outnam, outclass, outseq, outdisk
blc 0; trc 0; xinc 0; yinc 0; opcode ''
FIN

PROC SETIMLOD
$loads file from unix disk to aips disk
$ like Conner's RSTRDATA for 'ma' --
$ set infile, outname, outclass, outseq, outdisk
intape 1; ncount 1; dotable 1; nfiles 0; nmaps 0
FIN

PROC SETUVLOD
$loads file from unix disk to aips disk
$ like Conner's RSTRDATA for 'uv'
$ set infile, outname, outclass, outseq, outdisk
doall -1; object ''; qual -1; band ' '; bcount 1; ncount 0
doconcat -1; npoints 0
intape 0; nfiles 0; douvcomp -1
FIN

PROC SETFITTP
$ like Conner's SAVEDATA: writes file from aips disk to unix disk
$ getn file (include intype), set outfile
doall -1; doeot -1; dostokes -1; outtape 1; dotwo -1
$ dotwo +1 gives greater precision, but only for UV data
donewtab -1
$ if donewtab +1, then data can only be read by jul94 aips,
$       not apr92
format 0
blocking 0
$ blocking is ignored when writing to disk.  For writing to tape,
$    blocked data may not be able to be read by other FITS
$    readers, but will make reads & writes more efficient
FIN

$ ******* catalog procedures ********

PROC SAVENAME(inname, inclass, inseq, indisk, intype)
tempname = inname; tempclass = inclass; tempseq = inseq;
tempdisk = indisk; temptype = intype
FIN

PROC RESTNAME(tempname, tempclass, tempseq, tempdisk, temptype)
inname = tempname; inclass = tempclass; inseq = tempseq;
indisk = tempdisk; intype = temptype
FIN

PROC ACAT
savename(inname, inclass, inseq, indisk, intype)
clrname; catalog
restname(tempname, tempclass, tempseq, tempdisk, temptype)
FIN

PROC CAT1
savename(inname, inclass, inseq, indisk, intype)
clrname; indi 1; catalog
restname(tempname, tempclass, tempseq, tempdisk, temptype)
FIN

PROC CAT2
savename(inname, inclass, inseq, indisk, intype)
clrname; indi 2; catalog
restname(tempname, tempclass, tempseq, tempdisk, temptype)
FIN

PROC CAT3
savename(inname, inclass, inseq, indisk, intype)
clrname; indi 3; catalog
restname(tempname, tempclass, tempseq, tempdisk, temptype)
FIN

PROC CAT4
savename(inname, inclass, inseq, indisk, intype)
clrname; indi 4; catalog
restname(tempname, tempclass, tempseq, tempdisk, temptype)
FIN

PROC CAT5
savename(inname, inclass, inseq, indisk, intype)
clrname; indi 5; catalog
restname(tempname, tempclass, tempseq, tempdisk, temptype)
FIN

PROC CAT6
savename(inname, inclass, inseq, indisk, intype)
clrname; indi 6; catalog
restname(tempname, tempclass, tempseq, tempdisk, temptype)
FIN

PROC CAT7
savename(inname, inclass, inseq, indisk, intype)
clrname; indi 7; catalog
restname(tempname, tempclass, tempseq, tempdisk, temptype)
FIN

save utility
clrmsg
```

```
$****************************************************************
$ CFLAG: all settings and procedures needed to flag and calibrate
$ data before running through Lehar's DQ stuff.

get utility

PROC DECLARE
string*12 dataname
string*2 dataarray
scalar  dataant, workdisk
scalar  newname, inttime, whichif
FIN

$ *** Explanations of variables ***
$ dataname is the SNAP name of the dataset, eg "SNAP152"
$ dataarray is the VLA array used to take the data
$     'A', 'B', or 'C' (whatever's closest)
$ dataant is the reference antenna for the dataset
$ workdisk is the aips scratch disk
$ newname is a variable for what source names to use for the
$   current dataset. sets B1950 names or J2000 names, and
$   indicates a second phase calibrator
$            +1 means '1331+305','1035+564','0957+561'
$            -1 means '3C286','1031+567','0957+561'
$            -2 means '3C286','1031+567','0955+476','0957+561'
$ inttime is the integration time for the current dataset, for use
$      in tvflag.  Usually 10 or 30 seconds.
$ whichif indicates which if we're on, 1 or 2


PROC SETFILLM
$sets all but intap, nfiles, band, vlaobs, refdate, outdisk
qual -1; vlamode ''; bchan 1; echan 0; clro
douvcomp 1; doall -1; doconcat -1; dparm 0
cparm 10 0 0 0 0 0 2000 2 0 0
timeran -1 0 0 0 2 0 0 0
calcode ''
FIN

PROC SETTVFLG
$ set diskbad, workdisk before using
$ does all but getn file, and set sources, calcode,
$                                  docalib, gainuse, dparm
dohist 1; sources ' '
selband -1; selfreq -1; freqid -1
bif 1; eif 0; bchan 0; echan 0; antennas 0; baseline 0;
uvrange 0 0; subarray 0; blver -1; doband -1; bpver -1
$ docat -1 means that it deletes its own workfile afterwards
docat -1; smooth 0;  timeran 0; stokes 'rrll'; flagver 1
baddisk = diskbad; in2disk=workdisk; in2seq 0
FIN

PROC SETSETJY
$ sets all but getn file, sources, optype.  Check zerosp, bif, eif
qual -1; zerosp 0; sysvel 0; restfreq 0; freqid 1; calcode ''
veltyp ''; veldef ''; aparm 0; bif 1; eif 0
FIN

PROC SETCALIB
$ set diskbad, dataant, inttime and dataarray before using
$ setcalib, plus commented sections below, sets all inputs except
$    infile
$ may wish to adjust timerang, uvrange, snver, docalib

$*multisource, using setjy:  set calsour
$  solmode 'A&P'; solint 2; cmethod 'grid'; clr2n; invers 0;
$  ncomp 0; clro; cparm 0 0 10 10 1 0; cmodel ''
$*multisource, using 3C286 model:
$  set in2file, invers, ncomp, calsour
$  solmode 'A&P'; solint 2; cmethod 'dft'; clro;
$  cparm 0 0 10 10 1 0; cmodel 'COMP'
$*self-calibration: set in2file, invers, ncomp, outfile, cparm
$  solmode 'P'; solint=inttime; cmethod 'grid';
$  calsour '0957+561',''; cmodel 'COMP'
$*cross-calibration to a reference map:
$  set in2file, invers, ncomp,
$  outfile, cparm, cmodel 'COMP'
$  solmode 'P'; solint=inttime; cmethod 'dft';
$  calsour '0957+561',''

type 'setcalib'
qual -1; calcode ''; selband -1; selfreq -1; freqid -1;
bchan 1; echan 0; doband -1; bpver 0; smooth 0;
timeran 0; antennas 0; subarray 0; uvrang 0 0; wtuv 0
docalib -1; gainuse 0; flagver 1;
nmaps 1; smodel 0; aparm 0
if dataarray = 'C' then nmaps = 4; end
if dataarray = 'B' then nmaps = 4; end
soltype ''; solcon 0
snver 0; antwt 0; gainerr 0
baddisk = diskbad; refant=dataant
FIN

PROC SETGETJY
$ sets all but infile, sources, calsour, snver (snver 0 -> all)
$     may want to reset bif and eif to whichif
soucode ''; qual -1; calcode ''; bif 1; eif 0; subarray 0;
selband -1; selfreq -1; freqid -1; timeran 0; antennas 0
FIN

PROC SETCLCAL
$ sets all but infile, sources, calsour, calcode, timeran,
$              opcode, interpol, smotype, snver, gainver, gainuse
soucode ''; qual -1; subarray 0; antennas 0;
selband -1; selfreq -1; freqid -1 ;
intparm 0; baddisk = diskbad; refant=dataant
FIN

PROC SETSNPLT
$ sets all but getn file, newname
$ grchan 3; gron
if newname = -2 then sources '3C286','1031+567','0955+476',''; end
if newname = -1 then sources '3C286','1031+567',''; end
if newname = 1 then sources '1331+305','1035+564',''; end
qual -1; timeran 0; stokes 'diff'; selband -1; selfreq -1
freqid -1; bif whichif; eif whichif; antennas 0; pixrang 0;
ncount 5; xinc 1; optype ''; opcode ''; xaxis 0; doebar 0;
cutoff 0;
$ cparm 0 in SNPLX
inext 'cl'; invers 2; dotv 1
FIN

PROC SETLISTR
$ setup for LISTR matx output, to check goodness of solutions
$ set newname before using
$ sets all inputs for listr except getn file
optype 'matx'; inext 'cl'; invers 2; docalib 1; gainuse 2
if newname = -1 then sources '3C286','1031+567',''; end
if newname = -2 then sources '3C286','1031+567','0955+476',''; end
if newname = 1 then sources '1331+305','1035+564',''; end
dparm 5 1 0; calcode ''; timeran 0; stokes ''; antennas 0;
baseline 0; selband -1; selfreq -1; freqid 0; bchan 1; echan 0
bif whichif; eif whichif; uvrange 0 0; subarray 0;
dopol -1; blver -1; flagver 1; doband -1; bpver 0; smooth 0;
factor 0; docrt 132; outprint ''; baddisk = diskbad
FIN

PROC RESET
$ getn file
$ deletes all SN tables, and vers 2 of CL table, also
$  resets all source fluxes to zero
inext 'sn'; invers -1; EXTDEST
inext 'cl'; invers 2; EXTDEST
setsetjy
source ''; zerosp 0; optype 'rese'
gowt('setjy')
FIN

PROC SETSPLIT
$ sets all inputs except infile, docalib, gainuse, flagver,
$ outfile
type 'setsplit'
selband -1; selfreq -1; freqid -1; bchan 1; echan 0; chansel 0
qual -1; subarray 0; smooth 0; douvcomp -1; aparm 0
dopol -1; blver -1; doband -1; bpver -1; chansel 0
sources '0957+561',''; calcode ''; timeran 0; stokes 'full';
bif 1; eif 0; baddisk = diskbad
FIN


$****************************************************************
PROC FLAG1
$ for first round of flagging just with calibrators
$ before using: getn file
$               set dataant, diskbad, workdisk, inttime, newname

settvflg
dparm 0; dparm(6)=inttime
docalib 0; gainuse 0; flagver 1
if newname = -1 then sources '3C286','1031+567',''; end
if newname = -2 then sources '3C286','1031+567','0955+476',''; end
if newname = 1 then sources '1331+305','1035+564',''; end

go TVFLG
```

```
FIN

$****************************************************************
PROC RECAL1
$ Finds flux and phase solutions for antennas using calibrators
$ Use on a multisource dataset, just IF1
$ This doesn't split the data
$
$ before using: getn file to calibrate
$               set dataant, newname
$                   diskbad, workdisk,
$     dataname = 'SNAP??'

RESET

$ set flux of 1031 in source table.  Same for all arrays
setsetjy
if newname < 0 then source '1031+567',''; end
if newname > 0 then source '1035+564',''; end
optype ''
zerosp 1.241 0
gowt('SETJY')

$ make SN table for 1031
setcalib
clr2n; clro
solmode 'A&P'; solint 2; cmethod 'grid'; cparm 0 0 10 10 1 0
if newname < 0 then calsour '1031+567',''; gowt('CALIB'); end
if newname > 0 then calsour '1035+564',''; gowt('CALIB'); end

$ Make CL table for 1031
setclcal
calcode ''
timeran 0; antennas 0; opcode 'cali'; interp '2pt'; smotype ' '
snver 1; gainver 1; gainuse 2
if newname < 0 then
     sourc '1031+567',''; calsour '1031+567',''; end
if newname > 0 then
     sourc '1035+564',''; calsour '1035+564',''; end
gowt('CLCAL')

$ actually interpolate phas calibrations:
if newname < 0 then
     sourc '0957+561',''; calsour '1031+567',''; end
if newname > 0 then
     sourc '0957+561',''; calsour '1035+564',''; end
gowt('CLCAL')

RET; FIN


$****************************************************************
PROC FLAG2
$ for second round of flagging, including 0957
$ before using: getn file
$               set diskbad, workdisk, inttime, newname

settvflg
dparm 0; dparm(6) = inttime
docalib 1; gainuse 2; calcode ''
if newname = -1 then
       sources '3C286','1031+567','0957+561',''; end
if newname = -2 then
       sources '3C286','1031+567','0955+476','0957+561',''; end
if newname = 1 then
       sources '1331+305','1035+564','0957+561',''; end

go TVFLG

FIN


$****************************************************************
PROC RECAL2
$ to split the data and rename it correctly.
$ see above for things to set.

$ Split the data
setsplit
docalib 1; gainuse 2; flagver 1; clro; outdisk = workdisk
bif 1; eif 1
gowt('SPLIT')

inname '0957+561'; inclass 'split'; indisk = workdisk; inseq 1
clro; outname = dataname; outcl 'uvdata'
RENAME

RET;FIN

save cflag
clrmsg
```

```
$****************************************************************
$ DQPROC:  defines procedures to be used in reduction of 0957+561
$ snapshot maps
$ Originally written by Joseph Lehar, comments added by D. Haarsma
$ Modified so that *all* parameters for procedures are set for
$ current versions of AIPS.

RESTORE 0
docrt 1

$define: some definitions
PROC DEFINE
SCALAR DSK1,DSK2,DSKO,SEQ1,SEQ2,SEQO,XLEV,POPT, workdisk
STRING*12 NAM1,NAM2,NAMO
STRING*6 CLA1,CLA2,CLAO,XTASK
ARRAY CNTBOX(4)
array diskbad(10)
FIN

$gwt: executes & waits for a task
PROC GWT(XTASK)
TASK=XTASK;TYP'TASK',XTASK,'BEGINS';GO;WAIT
RET;FIN

$xzap: zaps a file but notifies first
PROC XZAP
TYP'ZAP=',INNA,INCL,INSE;ZAP
RET;FIN

$file1: loads filename 1
PROC FILE1(INDI,INNA,INCL,INSE)
DSK1=INDI;NAM1=INNA;CLA1=INCL;SEQ1=INSE
RET;FIN

$file2: loads filename 2
PROC FILE2(INDI,INNA,INCL,INSE)
DSK2=INDI;NAM2=INNA;CLA2=INCL;SEQ2=INSE
RET;FIN

$fileo: loads output filename
PROC FILEO(INDI,INNA,INCL,INSE)
DSKO=INDI;NAMO=INNA;CLAO=INCL;SEQO=INSE
RET;FIN

$get1: loads filename 1 from cat=1
PROC GET1(I)
GETN 1;FILE1(INDI,INNA,INCL,INSE)
RET;FIN

$uvplot: makes a (amp/uv) plot of uvdata
$ parameters:
$  FILE1()     input UV file
$  POPT        plot option (0=hist,1=QMS,2=both)
PROC UVPLOT(POPT)
  $ before using: do FILE1, set POPT, diskbad
  $ may wish to adjust xinc
  TYP'--->UVPLOT:'
  TYP'...IN=',DSK1,NAM1,CLA1,SEQ1
  INDI=DSK1;INNA=NAM1;INCL=CLA1;INSE=SEQ1;INTY='UV'
  UVRA=0;APA=0;BPA=0;source ''; qual -1; calcode ''; stokes ''
  selband -1; selfreq -1; freqid -1; timeran 0; antenna 0;
  baseline 0; subarray 0;
  bchan 0; echan 0; chinc 1; bif 0; docalib 1; gainuse 0
  dopol -1; blver -1; flagver 1; doband -1; bpver -1; smooth 0
  xinc 20; bparm 0; factor 0; baddisk = diskbad; dotv -1; grchan 0
  GWT('UVPLT')
  plver 0; aspmm 0; lpen 1; functype ''; dparm 0; outfile ''
  IF(POPT>0)THEN GWT('LWPLA');END
  plver 0; aspmm 0
  IF(POPT<>1)THEN DOCRT=2;GWT('TXPL');END
  $INVER=0;INEXT='PL';EXTD
RET;FIN

$gaplot: makes a gainplot of uvdata
$ parameters:
$  FILE1()     input UV file
$  POPT        plot option (0=hist,1=QMS,2=both)
PROC GAPLOT(POPT)
  $ before using, do FILE1, set POPT
  $ may wish to adjust cparm
  TYP'--->GAPLOT:'
  TYP'...IN=',DSK1,NAM1,CLA1,SEQ1
  INDI=DSK1;INNA=NAM1;INCL=CLA1;INSE=SEQ1;INTY='UV'
  cparm 0; dotv -1 grchan 0
  GWT('GNPL')
  plver 0; aspmm 0; lpen 1; functype ''; dparm 0; outfile ''
  IF(POPT>0)THEN GWT('LWPLA');END
  IF(POPT<>1)THEN DOCRT=2;GWT('TXPL');END
  $INVER=0;INEXT='PL';EXTD
RET;FIN

$maplot: makes a plot of a map, levs are pwrs of 2
$ parameters:
$  FILE1()    input map file
$  POPT       plot option (0=hist,1=QMS,2=both)
$  XLEV       start contour level (0=largest negative)
$  CLEV       contour scale (LEV(I)=CLEV*2^I) 0=>%levs
$  CNTBOX(4) specifies the plotted region; blc,trc
$  other CNTR parms:
PROC MAPLOT(POPT)
  $ before using do FILE1, set CNTBOX, XLEV, CLEV, POPT
  $ I _think_ I got DOINVERS correct, but may need to adjust
  TYP'--->MAPLOT:'
  TYP'...IN=',DSK1,NAM1,CLA1,SEQ1
  INDI=DSK1;INNA=NAM1;INCL=CLA1;INSE=SEQ1;INTY='MA'
  BLC=CNTBOX(1),CNTBOX(2);TRC=CNTBOX(3),CNTBOX(4)
  X=XLEV;LEVS=0
  IF(CLEV=0)THEN
    doinvers -1
    IF(X=0)THEN IMSTAT;X=100*ABS(PIX2V)/PIXV;END
    Y=64;PLEV=1;PIXR=PIXV*X/100,0.8*PIXV
  ELSE
    IF(X=0)THEN IMSTAT;X=ABS(PIX2V)/CLEV;END
    Y=PIXV/CLEV;PLEV=0;PIXR=XLEV,0.8*PIXV
  END
  IF(POPT>0)THEN
    X=CEIL(LOG(X)/.30103-.5);Y=CEIL(LOG(Y)/.30103-.5)
    I=2;FOR J=X:Y;LEVS(I)=2**J;I=I+1;END
    LEVS(1)=-LEVS(2);IF(CLEV=0)THEN LEVS(I)=95;END
    xyratio 0; ltype 3; docircle -1; invers 0; stfactor 0;
    dotv -1; grchan 0; tvcorn 0
    GWT('CNTR')
    plver 0; aspmm 0; lpen 1; functype ''; dparm 0; outfile ''
    GWT('LWPLA')
  END
  IF(POPT<>1)THEN
    DOCONT=-1;
    xyratio 0; pixrang 0; ltype 3; doalign 1; dowedge 1;
    docircle -1; invers 0; stfactor 0; in2vers 0; in3vers 0;
    nboxes 0; box 0; dotv -1; grchan 0; tvchan 1; tvcorn 0
    GWT('GREYS')
    DOCRT=2
    plver 0; aspmm 0
    GWT('TXPL')
  END
  $INVER=0;INEXT='PL';EXTD
  $IF(POPT>1)THEN EXTD;END
RET;FIN

$uvscale: rescales uv data
$ parameters:
$  FILE1()     input UV data
$  FILEO()     output rescaled UV data
$  X       scaling factor (resets to 0)
$PROC UVSCALE(X)
$ TYP'--->UVSCALE:'
$ TYP'...IN=',DSK1,NAM1,CLA1,SEQ1
$ INDI=DSK1;INNA=NAM1;INCL=CLA1;INSE=SEQ1;INTY='UV'
$ OUTD=DSKO;OUTN=NAMO;OUTC=CLAO;OUTS=SEQO
$ FACTOR=X;GWT('SCALE');FACTOR=0
$RET;FIN
$ ** Needed to replace, because SCALE didn't compile now.
$ Can use uvmod:
PROC UVSCALE(X)
 TYP'--->UVSCALE:'
 TYP'...IN=',DSK1,NAM1,CLA1,SEQ1
 INDI=DSK1;INNA=NAM1;INCL=CLA1;INSE=SEQ1;INTY='UV'
 OUTD=DSKO;OUTN=NAMO;OUTC=CLAO;OUTS=SEQO
 FACTOR=X; zerosp 0;
 shift 0; bmaj 0; bmin 0; bpa 0; opcode ''; flux 0; qual -1
 GWT('UVMOD');FACTOR=0
RET;FIN


$clnap: makes a cleaned map of the snapshot using APCLN.
$ parameters:
$  FILE1()     input UV file, in 'TB' order
$  FILEO()     output clean map
$  other UVMAP & APCLN parms: GAIN,NITER,CELLS,IMSIZ,...
$  *NOTE*      sets BLC,TRC=0
PROC CLNAP
 $ before using, do FILE1, FILEO, diskbad, cntbox
 $ imsize, cellsize, gain(using xg), niter(using xnc,rnc,or snc)
 TYP'--->CLNAP:'
```

```
 TYP'...IN=',DSK1,NAM1,CLA1,SEQ1
 TYP'..OUT=',DSKO,NAMO,CLAO,SEQO
 INDI=DSK1;INNA=NAM1;INCL=CLA1;INSE=SEQ1;INTY='UV'
 OUTD=DSK1;OUTN=NAM1;OUTC='UVSRT';OUTS=1
 SORT='XY'; baddisk = diskbad; rotate 0
 GWT('UVSRT')
 indi=dsk1;inna=nam1;INCL='UVSRT';INSE=1
 OUTD=DSKO;OUTN=NAMO;OUTC='';OUTS=1
 $ cellsize and imsize set in ?_ARRAY
 $ shift set at top level -- non-zero for some data sets
 channel 0; nmaps 0; stokes 'I'; uvtape 0 0;
 uvrang 0 0; uvwtfn 'UN'; uvbox 0; dogridcr 1; dotv -1; zerosp 0;
 xtype 0; ytype 0; xparm 0; yparm 0; guard 0 0; baddisk = diskbad
 GWT('UVMAP')
 XZAP
 INDI=DSKO;INNA=NAMO;INCL='IMAP';INTY='MA'
 IN2D=DSKO;IN2N=NAMO;IN2C='IBEAM';IN2S=1;IN2T='MA'
 outd=dsko;outna=namo;OUTC=CLAO;OUTS=SEQO;
 $ gain set using xg, niter set using xnc in scmap
 $ gain and niter set in ?_ARRAY in xcsub
 $ cntbox set in ?_ARRAY
 BLC=0;TRC=0; invers 0; flux 0; phat 0; biter 0; bmaj 0; bmin 0;
 bpa 0; nboxes 1; box = cntbox; factor 0; minpatch 51;
 maxpixel 0; dotv -1; baddisk = diskbad
 GWT('APCLN')
 XZAP;INCL='IBEAM';XZAP
 TYP'--->CLNAP DONE'
RET;FIN

$xcal: crosscals FILE1 using a model from FILE2
$ parameters:
$  FILE1()    input UV file specifiers
$  FILE2()    input map model file specifiers
$  FILEO()    output UV file specifiers
$  APARM(1)   min. baseline
$  APARM(7)   calibr. type: 1=phase, 2=amp+phase
$  APARM(9)   integration time
$  other ASCAL parms: NCOMP,APARM,BPARM,...
PROC XCAL
 $ before using, do FILE1, FILE2, and FILEO,
 $                 set ncomp, aparm, bparm
 TYP'--->XCAL:'
 TYP'...IN=',DSK1,NAM1,CLA1,SEQ1
 TYP'.MODL=',DSK2,NAM2,CLA2,SEQ2
 TYP'..OUT=',DSKO,NAMO,CLAO,SEQO
 INDI=DSK1;INNA=NAM1;INCL=CLA1;INSE=SEQ1;INTY='UV'
 IN2D=DSK2;IN2N=NAM2;IN2C=CLA2;IN2S=SEQ2;IN2T='MA'
 OUTD=DSKO;OUTN=NAMO;OUTC=CLAO;OUTS=SEQO
 $ ncomp and aparm set in xcsub using RNC/SNC and XCP
 invers 0; nmaps 1; docat 1; baddisk diskbad
 GWT('ASCAL')
 TYP'--->XCAL DONE'
RET;FIN

$modsub: Subtracts a model in FILE2 from UV data in FILE1
$ parameters:
$  FILE1()     input UV file specifiers
$  FILE2()     input map model file specifiers (if SMOD(1)=0)
$  FILEO()     output UV file specifiers
$  SMODEL(1-7) ellipsoid model to subtract
$  other UVSUB parms: NCOMP,BCOMP,FACT,...
PROC MODSUB
  $ before using, do FILE1, FILE2, FILEO, set smodel, ncomp
  TYP'--->MODSUB:'
  TYP'...IN=',DSK1,NAM1,CLA1,SEQ1
  INDI=DSK1;INNA=NAM1;INCL=CLA1;INSE=SEQ1;INTY='UV'
  IF(SMODEL(1)=0)THEN
    TYP'.MODL=',DSK2,NAM2,CLA2,SEQ2
    IN2D=DSK2;IN2N=NAM2;IN2C=CLA2;IN2S=SEQ2;IN2T='MA'
  ELSE
    TYP'.MODL=',SMODEL
    CLR2N
  END
  TYP'..OUT=',DSKO,NAMO,CLAO,SEQO
  OUTD=DSKO;OUTN=NAMO;OUTC=CLAO;OUTS=SEQO
  OPCOD='SUB';CMOD='COMP'
  $ ncomp and smodel set in XCSUB
  $ opcode and cmodel set a few lines above
  nmaps 1; channel 0; bif 0; eif 0; invers 0
  $ old history file says dft was used
  bcomp 0; cmethod ''; factor 1; baddisk=diskbad
  GWT('UVSUB')
  TYP'--->MODSUB DONE'
RET;FIN

SAVE DQPROC
PRNU 0;PRTA '';CLRMSG
```

```
$*****************************************************************
$ DQALL
$ Joseph Lehar wrote the run files DQSCMAP, DQXCSUB, and DQFITS,
$ here I combined them together for easier handling.
$
$ Had to change a few definitions (see below), and a few
$   procedure names (A_ARRAY, etc.)

get dqproc

PROC DEFALL
$ to define all variables for the three run files

SCALAR MDISK,UDISK,
scalar KITER,LITER,DOMAP,DOSC
SCALAR XDISK,XSEQ,RDISK,RSEQ,RNC,SDISK,SNC,SSEQ
scalar XFACT
SCALAR MFACTOR
$ had to change XFACTOR in DQFITS to MFACTOR (for "multiplcation
$   factor") so as not to conflict with XFACT in DQXCSUB

ARRAY XG(4),XNC(4)
ARRAY XCP(10),XMP(10),OPT(6)
$ had to change OPT in DQSCMAP to be a 6 term array, so as not
$    to conflict with OPT in XCSUB.   The last two terms won't be
$    used in SCMAP

STRING*12 XNAME,RNAME,SNAME
STRING*6 XCLASS,RCLAS,SCLAS,LCLAS
STRING*6 MCLAS,UCLAS
FIN


************************** DQSCMAP ******************************

$ DQSCMAP, written by J Lehar, modified slightly for readability
$   and to make sure all parameters are set.
$ Also commented out references to AIPS versions, and clarified
$ popt and opt

$ Before using, data must be flagged, calibrated, split, and in
$ an aips data area.
$ Is the message file saved? -- no. Added a prtmsg at end of DQDO.

$scmap: the standard snapshot data reduction
$ parameters:
$  XNAME        INNAME part of files to be mapped
$  UDISK,UCLAS  other parts of files, for UV data
$  MDISK,MCLAS  other parts of files, for maps
$  XG(1-4)      Gains for each of the sc/map iterations
$  XNC(1-4)     #CCs for each sc/map iteration
$  OPT(1-4)     option code for each sc/map iteration
$               0=don't, 1=do, 2=do&plot.,
$               <0=delete the last sc or map iteration
$               tens=selfcal, units=map
$               Note: OPT(1) must be 0, 1, or 2;
$                   _can't_ be 10, 11, 12, 20, 21, 22
$  POPT         plot  option (0=hist,1=ps,2=hist+ps)
$   hist writes a plot to the history file
$   ps sends a postscript file to the printer
$   except I disabled lwpla, so it only makes plot
$   extension file
$  XVER         determines AIPS version to be used
$  other APCLN & ASCAL parms:
$               CELLS,IMSIZ,BLC,TRC,APARM,BPARM,...
PROC SCMAP
  $set XNAME, UDISK, UCLAS, MDISK, MCLAS
  $set OPT, XNC, POPT, DOMAP, XG, XNC, XVER, CNTBOX
  $ set APARM, BPARM for xcal, CELLSIZE and IMSIZE for clnap
  $ set diskbad
  FOR KITER=1:4
    TYP'===>START SC/MAP ITER=',KITER
    X=ABS(OPT(KITER))
    DOSC=FLOOR(X/10)
    DOMAP=MOD(X,10)
    LITER=KITER-1
    IF(DOSC>0)THEN
      FILE1(UDISK,XNAME,UCLAS,LITER)
      FILE2(MDISK,XNAME,MCLAS,LITER)
      FILEO(UDISK,XNAME,UCLAS,KITER)
      APARM(7)=0;IF(KITER=4)THEN APARM(7)=1;END
      NCOMP=-XNC(KITER);
      XCAL
      IF(DOSC>1)THEN
        FILE1(UDISK,XNAME,UCLAS,KITER);GAPLOT(POPT)
      END
    END
    IF(OPT(KITER)<0)THEN
      INDI=UDISK;INNA=XNAME;INCL=UCLAS;INSE=LITER;INTY='UV';XZAP
      INDI=MDISK;INNA=XNAME;INCL=MCLAS;INSE=LITER;INTY='MA';XZAP
    END
    IF(DOMAP>0)THEN
      FILE1(UDISK,XNAME,UCLAS,KITER)
      FILEO(MDISK,XNAME,MCLAS,KITER)
      GAIN=XG(KITER);NITER=XNC(KITER)
      CLNAP
      IF(DOMAP>1)THEN
        FILE1(MDISK,XNAME,MCLAS,KITER);MAPLOT(POPT)
      END
    END
    TYP'===>END SC/MAP ITER=',KITER
  END
RET;FIN

$ set in ?_ARRAY:  aparm, bparm, cellsize, imsize, cntbox, xg, xnc

PROC SA_ARRAY
 TYP'--->A_ARRAY'
 APARM=0;BPARM=0;APARM(1)=50;APARM(9)=2
 CELLS=.075;IMSIZ=512;CNTBOX=129,129,384,384
 XG=.2,.1,.1,.1;XNC=1000,2000,8000,8000
RET;FIN

PROC SB_ARRAY
 TYP'--->B_ARRAY'
 APARM=0;BPARM=0;APARM(1)=30;APARM(9)=2
 CELLS=.3;IMSIZ=128;CNTBOX=33,33,96,96
 XG=.2,.1,.1,.1;XNC=1000,2000,10000,10000
RET;FIN

PROC SC_ARRAY
 TYP'--->C_ARRAY'
 APARM=0;BPARM=0;APARM(1)=0;APARM(9)=2
 CELLS=.6;IMSIZ=128;CNTBOX=33,33,96,96
 XG=.2,.1,.1,.1;XNC=500,1000,5000,5000
RET;FIN

PROC SD_ARRAY
 TYP'--->D_ARRAY'
 APARM=0;BPARM=0;APARM(1)=0;APARM(9)=2
 CELLS=2.4;IMSIZ=128;CNTBOX=33,33,96,96
 XG=.2,.1,.1,.1;XNC=250,500,2000,2000
RET;FIN


************************** DQXCSUB ******************************

$ Lehar's procedure, modified slightly for readability, and to
$ make sure all parameters are set.
$ Use this on data that has already been through SCMAP

$ DQXCSUB
$ defines the crosscal/UVSUB mapping procedure for 0957+561


$xcsub: the crosscal/UVSUB method of 0957+561 snapshot reduction
$ parameters:
$  XDISK,XNAME,XCLAS,XSEQ  input UV data file specifiers
$  RDISK,RNAME,RCLAS,RSEQ  ref. model file specifiers
$  SDISK,SNAME,SCLAS,SSEQ  subtr. model file specifiers
$  RNC,SNC       #CCs for ref. and subtr. models
$  XFACT         scale factor for UV data
$  XCP(1-10)     crosscal APARMs for XCAL
$  XMP(1-10)     model APARMs for DQFIT
$  OPT(1-7)      option codes for each step
$                0=don't,1=do,2=do&plot,<0=delete [class]
$                (1)=rescale.by.XFACT =>  'SCALE' [XCLAS]
$                (2)=phase.xcal to ref => 'PXCAL' [last]
$                (3)=subtr.model =>       'UVSUB' [last]
$                (4)=final map =>         'MASUB' ['UVSUB']
$                (5)=dqfit data =>        'DQFIT' ['DQFIT']
$                (6)=check.model =>       'UCHEK' ['UCHEK']
$  POPT          plot  option (0=hist,1=qms,2=hist+qms)
$  XVER          determines AIPS version to be used
$ other APCLN & ASCAL parms:
$                CELLS,IMSIZ,GAIN,NITER,TRC,BLC,APARM,BPARM,...
PROC XCSUB
 typ'===>START XCSUB'
 LCLAS=XCLAS
 $ Rescale by xfact:
 IF(OPT(1)<>0)THEN
   FILE1(XDISK,XNAME,LCLAS,XSEQ)
   FILEO(XDISK,XNAME,'SCALE',XSEQ)
   UVSCALE(XFACT)
```

```
  IF(ABS(OPT(1))>1)THEN
    FILE1(XDISK,XNAME,'SCALE',XSEQ);UVPLOT(POPT)
  END
  IF(OPT(1)<0)THEN INCL=LCLAS;INTY='UV';XZAP;END
  LCLAS='SCALE'
 END
 $ Phase crosscal to reference
 IF(OPT(2)<>0)THEN
  FILE1(XDISK,XNAME,LCLAS,XSEQ)
  FILE2(RDISK,RNAME,RCLAS,RSEQ)
  FILEO(XDISK,XNAME,'PXCAL',XSEQ)
  NCOMP=RNC;APARM=XCP
  XCAL
  IF(ABS(OPT(2))>1)THEN
    FILE1(XDISK,XNAME,'PXCAL',XSEQ);GAPLOT(POPT)
  END
  IF(OPT(2)<0)THEN INCL=LCLAS;INTY='UV';XZAP;END
  LCLAS='PXCAL'
 END
 $ Check model, by subtracting it from itself (I think . .)
 IF(OPT(6)<>0)THEN
  FILE1(XDISK,XNAME,LCLAS,XSEQ)
  FILE2(RDISK,RNAME,RCLAS,RSEQ)
  FILEO(XDISK,XNAME,'UCHEK',XSEQ)
  NCOMP=0; smodel = 0
  MODSUB
  IF(ABS(OPT(6))>1)THEN
    FILE1(XDISK,XNAME,'UCHEK',XSEQ);UVPLOT(POPT)
  END
  IF(OPT(6)<0)THEN INCL='UCHEK';INTY='UV';XZAP;END
 END
 $ Subtract model of extended structure from the data
 IF(OPT(3)<>0)THEN
  FILE1(XDISK,XNAME,LCLAS,XSEQ)
  FILE2(SDISK,SNAME,SCLAS,SSEQ)
  FILEO(XDISK,XNAME,'UVSUB',XSEQ)
  NCOMP=SNC; smodel = 0
  MODSUB
  IF(ABS(OPT(3))>1)THEN
    FILE1(XDISK,XNAME,'UVSUB',XSEQ)
    UVPLOT(POPT)
  END
  IF(OPT(3)<0)THEN INCL=LCLAS;INTY='UV';XZAP;END
  LCLAS='UVSUB'
 END
$ The DQFIT subroutine is not implemented yet
$ $ Fit the data using the DQFIT procedure on uvdata
$ IF(OPT(5)<>0)THEN
$   INDI=XDISK;INNA=XNAME;INCL=LCLAS;INSE=XSEQ
$   OUTD=XDISK;OUTN=XNAME;OUTC='DQFIT';OUTS=XSEQ
$   APARM=XMP;DOMODEL=-1
$   GWT('DQFIT')
$   IF(ABS(OPT(5))>1)THEN
$     FILE1(XDISK,XNAME,'DQFIT',XSEQ);UVPLOT(POPT)
$   END
$   DOCRT=-1;PRTA=' ';INCL='DQFIT';PRTHI
$   INCL=LCLAS;OUTC=LCLAS;DOMODEL=0;APARM=XMP
$   GWT('DQFIT');
$   IF(OPT(5)<0)THEN INCL='DQFIT';INTY='UV';XZAP;END
$ END
 $ Make final map:
 IF(OPT(4)<>0)THEN
  FILE1(XDISK,XNAME,LCLAS,XSEQ)
  FILEO(XDISK,XNAME,'MASUB',XSEQ)
  CLNAP
  IF(ABS(OPT(4))>1)THEN
    FILE1(XDISK,XNAME,'MASUB',XSEQ);MAPLOT(POPT)
  END
  IF(OPT(4)<0)THEN
    INDI=XDISK;INCL=LCLAS;INTY='UV';XZAP
  END
 END
 typ'===>END XCSUB'
RET;FIN


$ My check of all the necessary parameters:
$Set in DQDO file:
$  xname; xfact,
$  also xlev, clev, popt, opt, shift, uclas, snc, calls ?_ARRAY
$    xdisk, xclas, xseq, rdisk, rclas, rseq, sdisk, sclas, sseq
$Set inside XCSUB:
$  ncomp, factor
$Set in A_ARRAY:
$  imsize; cellsize; gain; niter; xfact; rname; sname; rnc
$  aparm; bparm; xcp; xmp; cntbox;
$Set in DQPROC:
$   opcode; cmodel
$I confirmed that all other parameters are now set in DQPROC
$   (usually the ones that don't matter)


PROC XA_ARRAY
 type'--->A_ARRAY'
 APARM=0;BPARM=0;XCP=50,0,0,0,0,0,0,0,2,0
 XMP=-.234,2.451,1.0155,-3.591,50,0,.02,0
 CELLS=.075;IMSIZ=512;GAIN=.1;NITER=8000
 CNTBOX=129,129,384,384;XFACT=1
 RNAME='SNAP24';SNAME=RNAME;RNC=-8000
RET;FIN

PROC XB_ARRAY
 type'--->B_ARRAY'
 APARM=0;BPARM=0;XCP=30,0,0,0,0,0,0,0,2,0
 XMP=-.222,2.451,1.017,-3.582,30,0,.02,0
 CELLS=.3;IMSIZ=128;GAIN=.1;NITER=10000
 CNTBOX=33,33,96,96;XFACT=1
 RNAME='SNAP53';SNAME=RNAME;RNC=-10000
RET;FIN

PROC XC_ARRAY
 type'--->C_ARRAY'
 APARM=0;BPARM=0;XCP=0,0,0,0,0,0,0,0,2,0
 XMP=-.204,2.466,1.038,-3.558,0,0,.02,0
 CELLS=.6;IMSIZ=128;GAIN=.1;NITER=5000
 CNTBOX=33,33,96,96;XFACT=1
 RNAME='SNAP34';SNAME=RNAME;RNC=-5000
RET;FIN

PROC XD_ARRAY
 type'--->D_ARRAY'
 APARM=0;BPARM=0;XCP=0,0,0,0,0,0,0,0,2,0
 XMP=-.204,2.466,1.038,-3.558,0,0,.02,0
 CELLS=2.4;IMSIZ=128;GAIN=.1;NITER=2000
 CNTBOX=33,33,96,96;XFACT=1
 RNAME='SNAP30';SNAME=RNAME;RNC=-2000
RET;FIN


**************************  DQFITS ******************************

$DQFITS  contains routines to JMFIT to A&B components of 0957+561

***********Fit the A,B components***A-array**********
PROC ABFIT_A
 type'===>START ABFIT_A'
 INDI=XDISK;INNA=XNAME;INCL=XCLASS;INSE=XSEQ;INTY='MA'
 clro
 NITER=100;CTYPE=0;NGAUSS=1;BLC=245,281;TRC=266,311
 GMAX=.03*MFACTOR,0
 GPOS=259.12,289.68,0
 GWIDTH=0,0,0
 DOMAX=1;DOPOS=1;DOWIDTH=1,1,1,0
 DOOUTPUT=-1;DOMODEL=-1;OFFSET=0; docrt 1; outprint ''
 gwt('JMFIT')
 BLC=230,198;TRC=251,234
 GMAX=.02*MFACTOR,0; GPOS=242.47,209.11,0
 gwt('JMFIT')
RET;FIN

***********Fit the A,B components***B-array**********
PROC ABFIT_B
 type'===>START ABFIT_B'
 INDI=XDISK;INNA=XNAME;INCL=XCLASS;INSE=XSEQ;INTY='MA'
 clro
 NITER=100;CTYPE=0;NGAUSS=2;BLC=56,47;TRC=68,76
 GMAX=.03*MFACTOR,.02*MFACTOR
 GPOS=64.77,73.15,60.,53.,0
 GWIDTH=0,0,0,0,0,0
 DOMAX=1;DOPOS=1;DOWIDTH=1,1,1,1,1,1,0
 DOOUTPUT=-1;DOMODEL=-1;OFFSET=.1; docrt 1; outprint ''
 $ why does this one have no-zero OFFSET?
 gwt('JMFIT')
 OFFSET=0
RET;FIN

***********Fit the A,B components***C-array**********
PROC ABFIT_C
 type'===>START ABFIT_C'
 INDI=XDISK;INNA=XNAME;INCL=XCLASS;INSE=XSEQ;INTY='MA'
 NITER=100;CTYPE=0;NGAUSS=2;BLC=60,55;TRC=68,73
 GMAX=.03*MFACTOR,.02*MFACTOR
 GPOS=64,69,62.5,59,0
 GWIDTH=0,0,0,0,0,0
```

```
 $ why is dowidth negative here?
 DOMAX=1;DOPOS=1;DOWIDTH=-1,-1,-1,-1,-1,-1,0
 DOOUTPUT=-1;DOMODEL=-1; docrt 1; outprint ''; offset 0
 OUTCL='JMFIT'
 gwt('JMFIT')
RET;FIN

MFACTOR=1;DOCRT=1

save dqall
clrmsg
```

```
$*****************************************************************
$ DQDO
$ This is a combination of Joseph's Z_DO routines, to do scmap as
$     well as xcsub and dqfits.
$ This calls dqall for each data set.  Data sets and a few
$ parameters are listed at the end, these should be changed and
$ uncommented when you want to process a data set.  )

get dqall

PROC DODEFINE
string*2  dataarray
string*5  writedisk, readdisk
string*12 doname
scalar    refdisk, subdisk, workdisk, namesize
array     diskbad(10)
FIN

PROC DQDOIT
$ Before using,
$       prepare data using recal, put on readdisk
$    set:
$ doname = snap name of dataset
$       namesize = 2 or 3, depending on # of digits in snap number
$  dataarray = array of dataset
$
$ refdisk = aips disk where reference map is
$ subdisk = aips disk where subtracted (jet) map is
$ workdisk = aips disk to do work (usually scratch disk)
$ diskbad = baddisk, don't put scratch files on these disks
$       readdisk = unix disk where uvdata is. Must have name in
$     form SNAP??.UVDATA.1.UVFITS
$ writedisk = unix disk to write the reduced data & maps

clrmsg

type'===>BEGIN REDUCTION OF', doname

*****************************************************************
$ load disk from writedisk (unix) to workdisk (aips)

doall -1; object ''; qual -1; band ' '; bcount 1; ncount 0
doconcat -1; npoints 0
intape 0; nfiles 0; douvcomp -1
if namesize = 2 then
   infile '     :       .uvdata.1.uvfits'
   $       scrat snap7i
   substr (infile, 7, 12) = doname
end
if namesize = 3 then
   infile '     :       .uvdata.1.uvfits'
   $       scrat snap101
   substr (infile, 7, 13) = doname
end
substr (infile, 1, 5) = readdisk
outname = doname; outclass 'uvdata'; outseq 1; outdi = workdisk

gwt('UVLOD')


*****************************************************************
$ do SCMAP

udisk = workdisk; mdisk = workdisk
uclas 'uvdata'; mclas 'icln'
popt 1; opt 1, 11, 11, 0
XLEV=1; CLEV=0

if dataarray = ' A' then SA_ARRAY; end
if dataarray = ' B' then SB_ARRAY; end
if dataarray = ' C' then SC_ARRAY; end

xname = doname

SCMAP

indisk = workdisk; recat


*****************************************************************
$ do XCSUB

XDISK=workdisk; XCLAS='UVDATA';XSEQ=0
rdisk = refdisk; RCLAS='REFCLN';RSEQ=1
sdisk = subdisk; SCLAS='SUBCLN';SSEQ=1;SNC=0
XLEV=1;CLEV=0
$POPT=2;OPT=-2,-2,-2,2,-2,0
popt 1; opt 0 1 1 1 0 0

if dataarray = ' A' then XA_ARRAY; end
if dataarray = ' B' then XB_ARRAY; end
if dataarray = ' C' then XC_ARRAY; end

shift 0 0
if xname = 'SNAP6X' then shift = 0, -10; end
if xname = 'SNAP6A' then shift = 0, -10; end
if xname = 'SNAP6B' then shift = 0, -10; end

xname = doname

XCSUB

indisk = workdisk; recat

*****************************************************************
$ do JMFIT

XDISK=workdisk;XCLASS='MASUB';XSEQ=0;INTY='MA'

xname = doname

if dataarray = ' A' then ABFIT_A; end
if dataarray = ' B' then ABFIT_B; end
if dataarray = ' C' then ABFIT_C; end


$*****************************************************************
$ Write files to unix disk, save messages to a file

doall -1; doeot -1; dostokes -1; dotwo -1; donewtab -1;
format 0; blocking 0; outtape 1

inname = doname; indisk workdisk

inclas 'uvdata'; inseq 3; intyp 'uv'
if namesize = 2 then
   outfile '     :       .uvdata.3.uvfits'
   $        scrat snap71
   substr (outfile, 7, 12) = doname
end
if namesize = 3 then
   outfile '     :       .uvdata.3.uvfits'
   $        scrat snap101
   substr (outfile, 7, 13) = doname
end
substr (outfile, 1, 5) = writedisk
GWT('FITTP'); ZAP

inclas 'pxcal'; inseq 1; intype 'uv'
if namesize = 2 then
   outfile '     :       .pxcal.1.uvfits'
   $        scrat snap71
   substr (outfile, 7, 12) = doname
end
if namesize = 3 then
   outfile '     :       .pxcal.1.uvfits'
   $        scrat snap101
   substr (outfile, 7, 13) = doname
end
substr (outfile, 1, 5) = writedisk
GWT('FITTP'); ZAP

inclas 'uvsub'; inseq 1; intype 'uv'
if namesize = 2 then
   outfile '     :       .uvsub.1.uvfits'
   $        scrat snap71
   substr (outfile, 7, 12) = doname
end
if namesize = 3 then
   outfile '     :       .uvsub.1.uvfits'
   $        scrat snap101
   substr (outfile, 7, 13) = doname
end
substr (outfile, 1, 5) = writedisk
GWT('FITTP'); ZAP

inclas 'icln'; inseq 3; intype 'ma'
outfile 'scrat:snap71.icln.3.mafits'
if namesize = 2 then
   outfile '     :       .icln.3.mafits'
   $        scrat snap71
   substr (outfile, 7, 12) = doname
end
if namesize = 3 then
```

```
   outfile '     :       .icln.3.mafits'
   $        scrat snap101
   substr (outfile, 7, 13) = doname
end
substr (outfile, 1, 5) = writedisk
GWT('FITTP'); ZAP

inclas 'masub'; inseq 1; intype 'ma'
if namesize = 2 then
   outfile '     :       .masub.1.mafits'
   $        scrat snap71
   substr (outfile, 7, 12) = doname
end
if namesize = 3 then
   outfile '     :       .masub.1.mafits'
   $        scrat snap101
   substr (outfile, 7, 13) = doname
end
substr (outfile, 1, 5) = writedisk
GWT('FITTP'); ZAP

inclas 'icln'; inseq 1; intype 'ma'; zap
inseq 2; zap
inclas 'uvdata'; inseq 1; intype 'uv'; zap
inseq 2; zap

type '===>END REDUCTION OF' doname

prnum 0; docrt -1; prtask ''; prtim 0; prior 0
if namesize = 2 then
   outprint '     :       .messages'
   $         scrat snap71
   substr (outprint, 7, 12) = doname
end
if namesize = 3 then
   outprint '     :       .messages'
   $         scrat snap101
   substr (outprint, 7, 13) = doname
end
substr (outprint, 1, 5) = writedisk
PRTMSG
clrmsg
docrt 1; outprint ''


FIN

*****************************************************************

$ on Alphas:
refdisk 4; subdisk 4
workdisk 5; diskbad 1 2 3 4

$ on Suns:
$refdisk 4; subdisk 4
$workdisk 8; diskbad 1 2 3 4 5 6 7

writedisk 'vig3c'; readdisk 'vig3c'

$doname 'snap45'; namesize 2; dataarray ' P'; dqdoit
$doname 'snap46'; namesize 2; dataarray ' P'; dqdoit
$doname 'snap48'; namesize 2; dataarray ' P'; dqdoit

$doname 'snap01'; namesize 2; dataarray ' C'; dqdoit
$doname 'snap02'; namesize 2; dataarray ' C'; dqdoit
$doname 'snap03'; namesize 2; dataarray ' C'; dqdoit
$doname 'snap04'; namesize 2; dataarray ' C'; dqdoit

$doname 'snap05'; namesize 2; dataarray ' A'; dqdoit
$doname 'snap49'; namesize 2; dataarray ' A'; dqdoit
$doname 'snap06'; namesize 2; dataarray ' A'; dqdoit
$doname 'snap6I'; namesize 2; dataarray ' A'; dqdoit
$doname 'snap6A'; namesize 2; dataarray ' A'; dqdoit
$doname 'snap6B'; namesize 2; dataarray ' A'; dqdoit
$doname 'snap07'; namesize 2; dataarray ' A'; dqdoit
$doname 'snap08'; namesize 2; dataarray ' A'; dqdoit
$doname 'snap09'; namesize 2; dataarray ' A'; dqdoit
$doname 'snap10'; namesize 2; dataarray ' B'; dqdoit
$doname 'snap11'; namesize 2; dataarray ' B'; dqdoit
$doname 'snap12'; namesize 2; dataarray ' B'; dqdoit
$doname 'snap13'; namesize 2; dataarray ' B'; dqdoit
$doname 'snap14'; namesize 2; dataarray ' B'; dqdoit
$doname 'snap16'; namesize 2; dataarray ' C'; dqdoit
$doname 'snap17'; namesize 2; dataarray ' C'; dqdoit
$doname 'snap18'; namesize 2; dataarray ' C'; dqdoit
$doname 'snap19'; namesize 2; dataarray ' C'; dqdoit
$doname 'snap20'; namesize 2; dataarray ' C'; dqdoit

$doname 'snap21'; namesize 2; dataarray ' A'; dqdoit
$doname 'snap22'; namesize 2; dataarray ' A'; dqdoit
$doname 'snap23'; namesize 2; dataarray ' A'; dqdoit
$doname 'snap24'; namesize 2; dataarray ' A'; dqdoit
$doname 'snap25'; namesize 2; dataarray ' A'; dqdoit
$doname 'snap26'; namesize 2; dataarray ' A'; dqdoit
$doname 'snap27'; namesize 2; dataarray ' B'; dqdoit
$doname 'snap44'; namesize 2; dataarray ' B'; dqdoit
$doname 'snap28'; namesize 2; dataarray ' B'; dqdoit
$doname 'snap29'; namesize 2; dataarray 'BD'; dqdoit
$doname 'snap31'; namesize 2; dataarray ' C'; dqdoit
$doname 'snap32'; namesize 2; dataarray ' C'; dqdoit
$doname 'snap33'; namesize 2; dataarray ' C'; dqdoit
$doname 'snap34'; namesize 2; dataarray ' C'; dqdoit
$doname 'snap35'; namesize 2; dataarray ' C'; dqdoit

$doname 'snap36'; namesize 2; dataarray ' A'; dqdoit
$doname 'snap37'; namesize 2; dataarray ' A'; dqdoit
$doname 'snap38'; namesize 2; dataarray ' A'; dqdoit
$doname 'snap38A'; namesize 3; dataarray ' A'; dqdoit
$doname 'snap39'; namesize 2; dataarray ' A'; dqdoit
$doname 'snap40'; namesize 2; dataarray ' B'; dqdoit
$doname 'snap41'; namesize 2; dataarray ' C'; dqdoit
$doname 'snap42'; namesize 2; dataarray ' C'; dqdoit

$doname 'snap50'; namesize 2; dataarray ' A'; dqdoit
$doname 'snap51'; namesize 2; dataarray ' A'; dqdoit
$doname 'snap52'; namesize 2; dataarray ' B'; dqdoit
$doname 'snap53'; namesize 2; dataarray ' B'; dqdoit
$doname 'snap54'; namesize 2; dataarray ' C'; dqdoit

$doname 'snap55'; namesize 2; dataarray ' A'; dqdoit
$doname 'snap56'; namesize 2; dataarray ' A'; dqdoit
$doname 'snap57'; namesize 2; dataarray ' A'; dqdoit
$doname 'snap58'; namesize 2; dataarray ' B'; dqdoit
$doname 'snap59'; namesize 2; dataarray ' B'; dqdoit
$doname 'snap60'; namesize 2; dataarray ' C'; dqdoit
$doname 'snap61'; namesize 2; dataarray ' C'; dqdoit

$doname 'snap62'; namesize 2; dataarray ' A'; dqdoit
$doname 'snap63'; namesize 2; dataarray ' A'; dqdoit
$doname 'snap64'; namesize 2; dataarray ' B'; dqdoit
$doname 'snap65'; namesize 2; dataarray ' B'; dqdoit
$ snap 65 and 75 are marked  'BC' array -- but
$   in Z_DO files its not clear what was used for final
$   data.  I know B array can work well, so I'll do that.
$doname 'snap66'; namesize 2; dataarray 'CD'; dqdoit
$doname 'snap67'; namesize 2; dataarray 'CD'; dqdoit

$doname 'snap68'; namesize 2; dataarray ' A'; dqdoit
$doname 'snap69'; namesize 2; dataarray ' A'; dqdoit
$doname 'snap70'; namesize 2; dataarray ' A'; dqdoit
$doname 'snap71'; namesize 2; dataarray ' A'; dqdoit
$doname 'snap72'; namesize 2; dataarray ' A'; dqdoit
$doname 'snap73'; namesize 2; dataarray ' B'; dqdoit
$doname 'snap74'; namesize 2; dataarray ' B'; dqdoit
$doname 'snap75'; namesize 2; dataarray ' B'; dqdoit
$doname 'snap76'; namesize 2; dataarray ' C'; dqdoit
$doname 'snap77'; namesize 2; dataarray ' C'; dqdoit
$doname 'snap78'; namesize 2; dataarray ' C'; dqdoit

$doname 'snap82'; namesize 2; dataarray ' A'; dqdoit
$doname 'snap83'; namesize 2; dataarray ' A'; dqdoit
$doname 'snap84'; namesize 2; dataarray ' A'; dqdoit
$doname 'snap85'; namesize 2; dataarray ' A'; dqdoit
$doname 'snap86'; namesize 2; dataarray ' A'; dqdoit
$doname 'snap87'; namesize 2; dataarray ' A'; dqdoit
$doname 'snap88'; namesize 2; dataarray ' A'; dqdoit
$doname 'snap89'; namesize 2; dataarray ' B'; dqdoit
$doname 'snap90'; namesize 2; dataarray ' B'; dqdoit
$doname 'snap91'; namesize 2; dataarray ' B'; dqdoit
$doname 'snap92'; namesize 2; dataarray ' C'; dqdoit
$doname 'snap93'; namesize 2; dataarray ' C'; dqdoit
$doname 'snap94'; namesize 2; dataarray ' C'; dqdoit

$doname 'snap95'; namesize 2; dataarray ' A'; dqdoit
$doname 'snap96'; namesize 2; dataarray ' A'; dqdoit
$doname 'snap96E'; namesize 3; dataarray ' A'; dqdoit
$doname 'snap96L'; namesize 3; dataarray ' A'; dqdoit
$doname 'snap97'; namesize 2; dataarray ' B'; dqdoit
$doname 'snap98'; namesize 2; dataarray ' B'; dqdoit
$doname 'snap99'; namesize 2; dataarray ' C'; dqdoit
$doname 'snap100'; namesize 3; dataarray ' C'; dqdoit
$doname 'snap101'; namesize 3; dataarray ' C'; dqdoit
$doname 'snap102'; namesize 3; dataarray ' C'; dqdoit
```

```
$doname 'snap103'; namesize 3; dataarray ' A'; dqdoit
$doname 'snap104'; namesize 3; dataarray ' A'; dqdoit
$doname 'snap105'; namesize 3; dataarray ' A'; dqdoit
$doname 'snap106'; namesize 3; dataarray ' A'; dqdoit
$doname 'snap107'; namesize 3; dataarray ' B'; dqdoit
$doname 'snap108'; namesize 3; dataarray ' B'; dqdoit
$doname 'snp108A'; namesize 3; dataarray ' B'; dqdoit
$doname 'snap109'; namesize 3; dataarray ' C'; dqdoit
$doname 'snap110'; namesize 3; dataarray ' C'; dqdoit

$doname 'snap111'; namesize 3; dataarray ' B'; dqdoit
$doname 'snap111'; namesize 3; dataarray ' A'; dqdoit
$doname 'snap112'; namesize 3; dataarray ' A'; dqdoit
$doname 'snap113'; namesize 3; dataarray ' A'; dqdoit
$doname 'snap114'; namesize 3; dataarray ' A'; dqdoit
$doname 'snap115'; namesize 3; dataarray ' B'; dqdoit
$doname 'snap116'; namesize 3; dataarray ' B'; dqdoit
$doname 'snap117'; namesize 3; dataarray ' B'; dqdoit
$doname 'snap118'; namesize 3; dataarray ' B'; dqdoit
$doname 'snap119'; namesize 3; dataarray ' B'; dqdoit
$doname 'snap120'; namesize 3; dataarray ' C'; dqdoit
$doname 'snap121'; namesize 3; dataarray ' C'; dqdoit

$doname 'snap122'; namesize 3; dataarray ' A'; dqdoit
$doname 'snap123'; namesize 3; dataarray ' A'; dqdoit
$doname 'snap124'; namesize 3; dataarray ' A'; dqdoit
$doname 'snap125'; namesize 3; dataarray ' A'; dqdoit
$doname 'snap126'; namesize 3; dataarray ' A'; dqdoit
$doname 'snap127'; namesize 3; dataarray ' A'; dqdoit
$doname 'snap128'; namesize 3; dataarray ' A'; dqdoit
$doname 'snap129'; namesize 3; dataarray ' A'; dqdoit
$doname 'snap130'; namesize 3; dataarray ' A'; dqdoit
$doname 'snap131'; namesize 3; dataarray ' A'; dqdoit
$doname 'snap132'; namesize 3; dataarray ' A'; dqdoit
$doname 'snap133'; namesize 3; dataarray ' A'; dqdoit
$doname 'snap134'; namesize 3; dataarray ' A'; dqdoit
$doname 'snap135'; namesize 3; dataarray ' A'; dqdoit
$doname 'snap136'; namesize 3; dataarray ' A'; dqdoit
$doname 'snap137'; namesize 3; dataarray ' A'; dqdoit
$doname 'snap138'; namesize 3; dataarray ' A'; dqdoit
$doname 'snap139'; namesize 3; dataarray ' A'; dqdoit
$doname 'snap140'; namesize 3; dataarray ' B'; dqdoit
$doname 'snap141'; namesize 3; dataarray ' B'; dqdoit
$doname 'snap142'; namesize 3; dataarray ' B'; dqdoit
$doname 'snap143'; namesize 3; dataarray ' B'; dqdoit
$doname 'snap144'; namesize 3; dataarray ' B'; dqdoit
$doname 'snap145'; namesize 3; dataarray ' B'; dqdoit
$doname 'snap146'; namesize 3; dataarray ' C'; dqdoit
$doname 'snap147'; namesize 3; dataarray ' C'; dqdoit
$doname 'snap148'; namesize 3; dataarray ' C'; dqdoit
$doname 'snap149'; namesize 3; dataarray ' C'; dqdoit
$doname 'snap150'; namesize 3; dataarray ' C'; dqdoit

$doname 'snap151'; namesize 3; dataarray ' A'; dqdoit
$doname 'snap152'; namesize 3; dataarray ' A'; dqdoit
$doname 'snap153'; namesize 3; dataarray ' A'; dqdoit
$doname 'snap154'; namesize 3; dataarray ' A'; dqdoit
$doname 'snap155'; namesize 3; dataarray ' B'; dqdoit
```

```
$*****************************************************************
Recipe to follow when reducing 6cm, cband data.  This includes
what actually was done with the data sets, not other things I
tried along the way.

Start up aips, and
> get cproc

*****************************************************************
READ THE DATA SET OFF OF TAPE.

If AIPS archive format, use:
> remhost 'vigdis'
> intap 1; gowt('MOUNT')
> setfillm
> set refdate in format 'dd/mm/yy',  vlaobs, nfiles, clro, outdi
> band 'c'; outdi 5
> gout('FILLM')
> ewind; dismount

If FITS format recorded with unix tar, use tar to extract from
tape, and UVLOD to read into AIPS.  FITS files of raw data in unix
typically have names in the form 90MAY27.CBAND.FITS.

Copy data, taking only if1, and renaming
getn file
> inname '07/05/90'; inclass 'c band'; inseq 1; indisk 6
or any variety of innames when I ftp data from VLA
> outdi=workdisk; outna '90May07if1'; outcl 'multi'
> setuvcop; eif 1; go UVCOP

*****************************************************************
FIND IMPORTANT PARAMETERS

Do scan in listr to get a look at data
> optype 'scan'; go listr
make sure OK, set variables newname, inttime, caltime1, caltime2

newname indicates source names used
  if newname = -1 then
sources '3C286','1031+567','0957+561',''; end
  if newname = -2 then
sources '3C286','1031+567','0955+476','0957+561',''; end
  if newname = 1 then
sources '1331+305','1035+564','0957+561',''; end

caltime indicates time range used for getjy.  It is the time range
enclosing 1031 and 3C286.  If there are two observations of 3C286,

caltime1 is the first and caltime2 is the second.  If there is
only one observation of 3C286, then caltime1 is zero, and
caltime2 is time enclosing just 1031 and 3C286.  I never actually
used this variable, but I recorded it for all the data sets.

inttime is the length of integration scans, usually 10 or 30
seconds

Do prtan to see antenna table and set initial value for refant,
and set dataarray

dataant is the reference antenna for the data set, usually
the first one on the north arm, unless that has problems

Put all this information in a file like '89Apr26.notes'

Example of top of notes file:

89Apr26: dataarray 'B'; dataant 28; inttime 10; newname -2
         caltime1 0 2 25 0 0 2 43 0; caltime2 0 4 41 50 0 4 55 0
dataname = 'SNAP74'
-----------------------------------------------------------------

Check operator log for problems and record significant ones in
notes file.  Watch for these problems when flagging.


*****************************************************************
FIRST ITERATION OF FLAGGING

getn file
set dataant, diskbad, workdisk, inttime, newname
FLAG1

Enter Stokes Flag 1111
Get rid of jagged edges at beginning of scans (handdone quack)

Select type of display, then select LOAD

Look at amplitude:
IF 1 RR
IF 1 LL
(IF 2 LL, IF 2 RR if necessary)
  get rid of any data from other observations
  remove other dubious looking data, such as whole antenna growing
fainter or brighter in time, an antenna dim for a short
time, etc.
  antennas occasionally "blink", this is online flagging.
Probably no need to flag around it; but if a large
fraction of an antennas has been flagged online, probably
should flag whole antenna
  if a whole antenna is much fainter than others, usually don't
flag it here, but wait to see if it calibrates OK in next
section, can flag if necessary in FLAG2

*****************************************************************
CALIBRATE ANTENNA GAINS
calibration is to a constant 1031, doesn't include
calibrating 3c286

getn file
set dataant, newname, diskbad, workdisk, and dataname = 'SNAP??'
RECAL1
copy to log the summary from CALIB (number of solutions, errors)

*****************************************************************
EVALUATE RESULTS

getn file, set newname
> setlistr
> go listr
Check that phase calibrators have good amplitudes and phases near
zero, not any antenna or time based problems for later.
(expect flux cal 3c286 will not be calibrated)

getn file, set newname
> setsnplt
> tvcl; grcl
> go snplt
Look at left minus right differences in gains of CL table to
check for phase jumps in one polarization that aren't in the
other.
Check if refant well chosen (if bad refant, all antennas will
have same large variations)
Check for bad phasejumps between RR and LL which indicate
mechanical problems.  Jump will be between two 1031 scans,
flag 0957 data in between these (where jump occured)

*****************************************************************
SECOND ROUND OF FLAGGING

get file, set diskbad, workdisk, inttime, newname
FLAG2

Compare with notes from flag1 to see if weak antennas
calibrated OK

Enter Stokes Flag 1111

Check operator log for problems happening when observing 0957

Look at amplitude -- same as above, plus
IF 1  RR
IF 1  LL
  get rid of jagged edges at beginning of scans (handdone quack)
  check that 1031 calibration applied: all baselines and times
same flux
  remove 0957 data that is surrounded by calibrators that are
flagged
  check to make sure that _too_ much data was not deletied during
1031 quacking and 0957 was snagged.
  remove other dubious looking data

Look at phase:
IF 1  RR
IF 1  LL
  make sure 1031 calibrated well.  Look for phase jumps remaining
in the data.

Look at rms:
   set smooth time to a multiple of minimum time unit for rms or
      rms/mean
IF 1  RR
IF 1  LL
   get rid of times or baselines with high noise
```

```
Actually, what is "high noise" is deceptive, because the image is
scaled to show the full range of RMS.  Look for regions of time
or antenna that are consistently much stronger than the typcial
RMS variations.  MSG window reports the range loaded, and
0 to 7E-03 is typical and OK for uncalibrated data (I think).
(less than 9E-02 is fine for calibrated data, I think)

*****************************************************************

If any flagging done during FLAG2, repeat RECAL1.  Sometimes a few
iterations between RECAL, flagging, and evalutaing the results are
necessary.

set dataname 'SNAP??', run RECAL2.

On ~1993-94 data (newname > 0), use eposwtch to change the header
coordinates from J2000 to B1950 for the cross calibration
(newname is only used in pre-Grand processing, so don't worry that
using eposwtch means you have to change to newname -1).

save flagged multi-source data to disk using FITTP

save split SNAP uv data to disk using FITTP

Date notes file

*****************************************************************
RUN THROUGH AIPS

Start AIPS with appropriate user number (contains REFCLN and
  SUBCLN maps, has run files linked in)
Edit DQDO in the middle to specify disks, and uncomment lines for
  data files to run.

Inside aips,
> run dqdo

This will load the flagged, split, uv data into AIPS, run the
lehar procedures on it, and put the results back on the unix disk.

*****************************************************************

After it has finished, go to directory where data was put, and
extract crucial lines from the SNAP151.MESSAGES file into
snap151.notes (I use a perl script for this).  Look at extracted
messages to make sure there were no problems.

Inside aips, load in maps and look at them:
> setimlod; clro; outdi 5
> infile 'vigd3:snap151.icln.3.mafits'; go imlod
> infile 'vigd3:snap151.masub.1.mafits'; go imlod

Write in the snap151.notes file how maps look, particularly if
there was high noise, artifacts, or if the subtraction didn't
work.

Enter the integral JMFIT flux for each image in the lightcurve
file.

Write reduced data to tape.

Ideally,
        print copies of ICLN and MASUB maps
        print out the 89Apr26.notes and snap75.notes files
```

```
$****************************************************************
$ XPROC:
$ settings, procedures, and declarations used later by
$   XFLAG and XCALGRND
$ for reducing 0957 xband time-delay data

get utility

$ Declare variables needed in procedures below, XFLAG, XCALGRND,
$     and XACT
PROC DECLARE
string*2 dataarray
string*12 dataname, refname, jetname
string*5 readdisk, writedisk
string*6 refclass, jetclass
scalar  dataant, workdisk
scalar  refdisk, refseq, refvers, refcomp
scalar  jetdisk, jetseq, jetvers, jetcomp
scalar  newname, inttime
scalar  mapnoise
scalar  numrow, tabnum, a, b
scalar  major, minor
scalar  peak, drange
scalar  if1flux, if2flux, if1angle, if2angle
array diskbad(10)
array xaltime1(8), xaltime2(8)
array Aant(9), Bant(6), ABant(27)
FIN

$ *** Explanations of variables ***
$ datarray is the VLA array used to take the data, also the array
$     used for crosscalibrating.  'A', 'B', 'C', or 'D'
$     (whatever's closest)
$ dataname is the inname of the dataset, i.e. '89Jun20x'
$     (8 letters long)
$ refname is the inname of the reference map, i.e. 'aref'
$ refclass is the inclass of the referene map, i.e. 'icln'
$ jetname is the inname of the jet map, i.e. 'ajet'
$ jetclass is the inclass of the jet map, i.e.'icln'
$ readdisk and writedisk are unix disk aliases (5 letters long)
$  for use during GRAND, such as 'vigd3' and 'boad1'
$ dataant is the reference antenna for the dataset
$ workdisk is usually the aips scratch disk, where data is during
$  grand
$ refdisk and refseq are the aips disk and sequence number of the
$     reference map, similarly for the jet map
$ refvers is the version number of reference clean component table
$ refcomp is the number of reference map clean components to use
$ jetvers and jetcomp are same as refvers and refcomp, but for the
$     jet model map
$ newname is a variable for what source names to use. Sets B1950
$   names or J2000 names, and indicates a second phase
$ calibrator
$            +1 means '1331+305','1035+564','0957+561'
$            -1 means '3C286','1031+567','0957+561'
$            -2 means '3C286','1031+567','0955+476','0957+561'
$ inttime is the integration time for the current dataset, for use
$      in tvflag.  Usually 10 or 30 seconds.
$ mapnoise is the RMS noise in the map.
$ numrow, tabnum, a, b are used in boxflux
$ major, minor are the major and minor axis of the beam
$ peak and drange are the peak and dynamic range of the map
$ if1flux, if2flux, are the fluxes found for 3C286 using
$ optype 'CALC' in setjy
$ if1angle, if2angle, are the phaseoffsets found between the
$    observed polarization angle of 3C286 and the expected angle
$ diskbad is used to set baddisk.  usually includes all disks
$    except the workdisk
$ xaltime is the time enclosing a 3C286 scan and the nearest 1031
$ scan (for finding the flux of 1031 accurately).  xaltime1
$  and xaltime2 are for the first and second occurences of
$ 3C286.  See xrecipe
$ aant is an array with the antenna numbers of the 3 inner
$  antennas on each arm.  For A-array Xband cookbook 3C286
$ calibration
$ bant is an array with the antenna numbers of the 2 outermost
$  antennas on each arm, each with a negative number (saying
$ NOT to use these, so that the inner 7 on each arm are
$ used). For B-array Xband cookbook 3C286 calibration
$ ABant is an array of up to 27 antennas, for combination arrays
$ where neither aant or bant works

PROC MSG0957
$ writes messages to file with dataname in the filename
$ set dataname before using
priority 0; prnumber -1; prtask ''; prtime 0
docrt -1; outprint '     :        .MESSAGES'
$                  ZEN01 89apr26x
substr (outprint, 1, 5) = writedisk
substr (outprint, 7, 14) = dataname
PRTMSG; CLRMSG
docrt 1; outprint ''
FIN

PROC SAVE5
$ getn file, set writedisk
$ works for data names of length 89Apr26x, i.e. 8 characters
$    with inclass of 5 characters, like 'multi' . with inseq 1
setfittp
outfile '     :        .     .1.  FITS'
$        ZEN01 89apr26x multi   uv
$        12345678901234567890123456789012345
substr (outfile, 1, 5) = writedisk
substr (outfile, 7, 14) = inname
substr (outfile, 16, 20) = inclass
substr (outfile, 24, 25) = intype
type '# outfile for fittp is', outfile
gowt('FITTP')
FIN

PROC SAVE6
$ getn file, set writedisk
$ works for data names of length 89Apr26x, i.e. 8 characters
$    with inclass of 6 characters, like 'iclnsc', with inseq 1
setfittp
outfile '     :        .      .1.  FITS'
$        ZEN01 89apr26x iclnsc   uv
substr (outfile, 1, 5) = writedisk
substr (outfile, 7, 14) = inname
substr (outfile, 16, 21) = inclass
substr (outfile, 25, 26) = intype
type '# outfile for fittp is', outfile
gowt('FITTP')
FIN

PROC ZAPIMAGR
inname=dataname; inclass 'imagr'; inseq 0; indisk=workdisk;
intype 'uv'
delete
FIN

PROC ZAPIBEAM
$ set inseq before running
inname dataname; inclass 'ibeam'; inseq 0;
indisk=workdisk; intype 'ma'; delete
RET; FIN

PROC SETSETJY
$ sets all but getn file, sources, optype.  Check zerosp, bif, eif
qual -1; zerosp 0; sysvel 0; restfreq 0; freqid 1; calcode ''
veltyp ''; veldef ''; aparm 0; bif 1; eif 0
FIN

PROC SETCLCAL
$ sets all but infile, sources, calsour, calcode, timeran,
$              opcode, interpol, smotype, snver, gainver, gainuse
soucode ''; qual -1; subarray 0; antennas 0;
selband -1; selfreq -1; freqid -1 ;
intparm 0; baddisk = diskbad; refant=dataant
FIN

PROC SETSPLIT
$ sets all inputs except infile, docalib, gainuse, flagver,
$    outfile
type 'setsplit'
qual -1; selband -1; selfreq -1; freqid -1; bchan 1; echan 0;
chansel 0; subarray 1; smooth 0; douvcomp -1; aparm 0
dopol -1; blver -1; doband -1; bpver -1; chansel 0
sources '0957+561',''; calcode ''; timeran 0; stokes 'full';
bif 1; eif 0; baddisk = diskbad
FIN

PROC SETCALIB
$ set diskbad, dataant, inttime and dataarray before using
$ setcalib, plus commented sections below, sets all inputs except
$  infile
$ may wish to adjust timerang, uvrange, snver, docalib
$*multisource, using setjy:  set calsour
$  solmode 'A&P'; solint 2; cmethod 'grid'; clr2n; invers 0;
$  ncomp 0; clro; cparm 0 0 10 10 1 0; cmodel ''
$*multisource, using 3C286 model: set in2file, invers, ncomp,
$                                    calsour
$ solmode 'A&P'; solint 2; cmethod 'dft'; clro;
$  cparm 0 0 10 10 1 0; cmodel 'COMP'
```

```
$*self-calibration: set in2file, invers, ncomp, outfile, cparm
$  solmode 'P'; solint=inttime; cmethod 'grid';
$  calsour '0957+561','''; cmodel 'COMP'
$*cross-calibration to a reference map: set in2file, invers,
$  ncomp, outfile, cparm,
$  cmodel 'COMP'; solmode 'P'; solint=inttime; cmethod 'dft';
$  calsour '0957+561',''
type 'setcalib'
qual -1; calcode ''; selband -1; selfreq -1; freqid -1;
bchan 1; echan 0; doband -1; bpver 0; smooth 0;
timeran 0; antennas 0; subarray 1; uvrang 0 0; wtuv 0
docalib -1; gainuse 0; flagver 1;
nmaps 1; smodel 0; aparm 0
$if dataarray = 'C' then nmaps = 4; end
$if dataarray = 'B' then nmaps = 4; end
soltype ''; solcon 0
snver 0; antwt 0; gainerr 0
baddisk = diskbad; refant=dataant
FIN

PROC SETSCMAP
$ need set before using: diskbad, dataant, inttime, dataarray,
$ need to also set: infile, in2file, outfile, out2file
$ setscmap DOESN'T set what's in setARRAYscmap:
$    cellsize, imsize, nbox, clbox, flux, niter
$ this also sets several parameters that may be set in
$       setARRAYscmap
type 'setscmap'
$$ ------for mapping $$
shift 0 0;
uvtaper 0 0; uvrange 0 0; uvwtfn ''; uvsize 0; robust 0; uvbxfn 1;
rotate 0; zerosp 0; xtype 5; ytype 5; xparm 0; yparm 0; guard 0;
$$ ------for cleaning $$
gain 0.05; minpatch 51; bmaj 0; bmin 0; bpa 0; factor -0.1;
maxpixel 0; cmethod '';
$$ ------for self-calibration $$
nmaps 2;     $ number of selfcalibration loops
smodel 0; refant=dataant; solint=inttime;
aparm 0; soltype ''; solmode 'P'; solcon 0; antwt 0; gainerr 0;
wtuv 0; docalib 0; gainuse 0;
$$ ------other $$
flagver 0; dotv 0; baddisk=diskbad; bparm 0; cparm 0;
FIN

PROC SETASCMAP
type 'setascmap'
$ scmap settings specific for Aarray maps
$ stop cleaning when clean flux changes by less than 2% or niter
$  reaches 10000, whichever comes first. flux -2000; niter 20000;
flux 0; niter 20000; uvwtfn 'un'
cellsize 0.0279365 0.0279365; imsize 512 512
$ for careful cleaning of extended structure:
factor -0.3
$ five boxes (B, A, C, east, west )
nboxes 5
clbox  214 120 232 138  258 337 276 355  204 138 230 179
clbox(1,4) 55;  clbox(2,4) 355; clbox(3,4) 273; clbox(4,4) 456
clbox(1,5) 379; clbox(2,5) 209; clbox(3,5) 444; clbox(4,5) 299
$ shift to center point images on pixels
shift -0.0084088, 0.003531654
FIN

PROC SETBSCMAP
type 'setbscmap'
$ things specific for Barray maps
flux 0; niter 7000; uvwtfn 'un'
cellsize 0.100671 0.100672; imsize 256 256
$ three boxes (B&C, east + A, west)
nboxes 3; clbox 111 85 127 111  68 145 139 188  147 113 183 152
$ shift to center point sources on pixels
shift -0.0100671, 0.055066912
$ could include boxes for confusing sources
FIN

PROC SETCSCMAP
type 'setcscmap'
$ things specific for Carray maps
niter 5000; flux 0; uvwtfn 'un'
cellsize 0.304495 0.304495; imsize 128 128
$ 3 boxes: center, southlobe, northlobe
nbox 3; clbox  39 44 85 91  41 8 67 44  62 98 83 125
$ no shift necessary to center on pixels
$ could also clean at locations of confusing sources
FIN

PROC SETDSCMAP
type 'setdscmap'
$ things specific for Darray models
niter 3000; flux 0; uvwtfn 'un'
cellsize 0.608990 0.608990; imsize 128 128
$ slow down clean!
factor -0.3
$ one box for everything
nbox 1; clbox 39 28 89 104
$ shift to center A and B on pixels:
shift -0.3045, 0
$ this weighting gives a beam size of 6.426 x 5.152 = 33.11 asec^2
$ and an increase in noise above natural weighting of 1.848
uvtaper 0; uvrange 0; guard 0; uvwtfn 'un';
robust -4; uvsize 128; uvbox 2; uvbxfn 3;
$ could also clean at locations of confusing sources
FIN

PROC GETGAIN
type '## getgain:'
$ uses LISTR to report maximum antennas gains.  Important info
$  goes to message file, rest to 'SNTABLE'
$ getn file before using, set invers
optype 'gain'; inext 'sn'; sources ''; calcode ''
timerang 0; stokes 'half';
selband -1; selfreq -1; freqid -1; bchan 1; echan 0
bif 1; eif 0; antennas 0; baseline 0; uvrange 0; subarray 1
docalib 1; gainuse 2; dopol -1; blver -1; flagver 1; doband -1
bpver -1; smooth 0; dparm 5 1 0; factor 0
docrt -1; outprint 'VIG3X:SNTABLE'; baddisk diskbad
gowt('LISTR')
docrt 1; outprint ''
RET; FIN

PROC GETMAPNOIS
$ Uses imstat to measure peak of map, and noise away from sources
$  in map
$ before using, getn file, set dataarray
if dataarray = 'A' then blc 10 10; trc 150 250; end
if dataarray = 'B' then blc 10 10; trc 50 120; end
if dataarray = 'C' then blc 10 10; trc 30 100; end
if dataarray = 'D' then blc 10 10; trc 20 110; end
doinvers -1; IMSTAT
mapnoise = pixstd
type '## mapnoise is ', mapnoise
doinvers 1; IMSTAT
peak = pixval
drange = peak/mapnois
type '## dynamic range is ', drange
RET;FIN

PROC GETBEAMSIZ
$ Getn map
$ gets major and minor axis and does ROUGH conversion to arcsec
$    (get errors on order of a few tenths of arcsec)
keyword 'BMAJ'; gethead; major = keyvalue(1) * 3500
type 'Major axis is', major
keyword 'BMIN'; gethead; minor = keyvalue(1) * 3500
type 'Minor axis is', minor
keyword 'BPA'; gethead; type 'Position angle is', keyvalue(1)
RET;FIN

PROC SETIMAGR
type 'setimagr'
$ Sets inputs for IMAGR.  Needed for polarization maps, and if I
$  want to map confusing sources (using nfields)
$ Need set before using: diskbad, dataant, inttime, dataarray,
$ Need to also set: infile, outfile, in2file, stokes
$ setimagr DOESN'T set what's in setARRAYimagr:
$    cellsize, imsize, nbox, clbox, flux, niter
$ This also sets several parameters that may be set in
$       setARRAYimagr
$ Set up for mapping of split data, so don't need to apply
$ calibration
$$ -----for data selection and calibration $$
source '0957+561','''; qual -1; calcode ''; timerang 0;
selband -1; selfreq -1; freqid -1; subarray 1
docalib -1; gainuse 0; dopol -1; blver -1; flagver 0;
doband -1; bpver -1; smooth 0; stokes '';
bchan 1; echan 0; channel 0; npoints 1; chinc 1
bif 1; eif 0
$$ ------for mapping $$
nfield 1; fldsize 0; rashift 0 0; decshift 0
uvtaper 0 0; uvrange 0 0; guard 0; rotate 0; zerosp 0;
uvwtfn ''; uvsize 0; robust 0; uvbox 0; uvbxfn 1;
xtype 5; ytype 5; xparm 0; yparm 0;
$$ ------for cleaning $$
bcomp 0; boxfile ''; gain 0.1; flux 0; minpatch 51;
bmaj 0; bmin 0; bpa 0;
```

```
phat 0; factor -0.1; cmethod ''; cparm 0; maxpixel 0;
$$ ------other $$
dotv -1; baddisk=diskbad;
FIN

PROC SETAIMAGR
type 'setaimagr'
$ imagr settings specific for Aarray maps
flux 0; niter 10000; uvwtfn 'un'
cellsize 0.0279365 0.0279365; imsize 512 512
$ for careful cleaning of extended structure:
factor -0.3
$ five boxes (B, A, G, east, west )
nboxes 5
clbox  214 120 232 138  258 337 276 355  204 138 230 179
clbox(1,4) 55;  clbox(2,4) 355; clbox(3,4) 273; clbox(4,4) 456
clbox(1,5) 379; clbox(2,5) 209; clbox(3,5) 444; clbox(4,5) 299
$ shift to center point images on pixels
rashift -0.0084088; decshift 0.003631654
FIN

PROC SETBIMAGR
type 'setbimagr'
$ things specific for Barray maps
flux 0; niter 7000; uvwtfn 'un'
cellsize 0.100671 0.100671; imsize 256 256
$ three boxes (B&G, east + A, west)
nboxes 3; clbox 111 85 127 111  68 145 139 188  147 113 183 152
$ three boxes (G, east, west), for cleaning jet map
$ nboxes 3; clbox 111 98 124 111  68 160 129 188  147 113 183 152
$ shift to center point sources on pixels
rashift -0.0100671; decshift 0.055066912
$ could include boxes for confusing sources
FIN

PROC SETCIMAGR
type 'setcimagr'
$ things specific for Carray maps
niter 5000; flux 0; uvwtfn 'un'
cellsize 0.304495 0.304495; imsize 128 128
$ 3 boxes: center, southlobe, northlobe
nbox 3; clbox  39 44 85 91  41 8 67 44  62 98 83 125
rashift 0; decshift 0;
$ could also clean at locations of confusing sources
FIN

PROC SETDIMAGR
type 'setdimagr'
$ things specific for Darray models
niter 3000; flux 0; uvwtfn 'un'
cellsize 0.608990 0.608990; imsize 128 128
$ slow down clean!
factor -0.3
$ one box for everything
nbox 1; clbox 39 28 89 104
$ shift to center A and B on pixels:
rashift -0.3045; decshift 0
$ could also clean at locations of confusing sources
uvtaper 0; uvrange 0; guard 0; uvwtfn 'un';
robust -4; uvsize 128; uvbox 2; uvbxfn 3;
$ this gives a beam size of 6.426 x 5.152 = 33.11 asec^2
$ and an increase in noise above natural weighting of 1.848
FIN

PROC SETUVSUB
type 'setuvsub'
$ these default settings are for use in subtracting a CC model
$    from a data set
$ sets all but infile, in2file, invers, and outfile
$ use cmethod 'dft' because 'grid' doesn't work for LR, RL data
nmaps 1; channel 0; bif 1; eif 0
bcomp 1 0; ncomp 0; cmethod 'dft'; cmodel 'comp'; factor 1
opcode ''; smodel 0; baddisk = diskbad
FIN

PROC SETJMFIT
type 'setjmfit'
$ when used with setARRAYjmfit, sets all but infile info.
$ setARRAYjmfit sets blc, trc, ngauss, ctype, gmax, gpos
clro; outdi = workdisk;
gwidth 0; domax 1 0; dopos 1 1 0; dowidth 1 1 0
ngauss 1; ctype 1 0; niter 100; offset 0
docrt 1; outprint ''; dooutput -1; domodel -1; docat 1
FIN

PROC SETAJMFITA
type 'setajmfita'
gmax 0.025 0; blc 258 337; trc 276 355; gpos 267 346
FIN

PROC SETAJMFITB
type 'setajmfitb'
gmax 0.015 0; blc 214 120; trc 232 138; gpos 223 129
FIN

PROC SETBJMFITA
type 'setbjmfita'
gmax 0.025 0; blc 123 145; trc 139 161; gpos 131 153
FIN

PROC SETBJMFITB
type 'setbjmfitb'
gmax 0.015 0; blc 111 85; trc 127 101; gpos 119 93
FIN

PROC SETCJMFITA
type 'setcjmfita'
gmax 0.025 0; blc 60 68; trc 70 78; gpos 65 73
FIN

PROC SETCJMFITB
type 'setcjmfitb'
gmax 0.015 0; blc 56 48; trc 66 58;  gpos 61 53
FIN

PROC SETDJMFITA
type 'setdjmfita'
gmax 0.025, 0; blc 61 66; trc 67 72; gpos 64 69
FIN

PROC SETDJMFITB
type 'setdjmfitb'
gmax 0.015, 0; blc 59 56; trc 65 62; gpos 62 59
FIN

PROC SETDJMFTAB
type 'setdjmfitab'
$ to fit for both at once
ngauss 2; ctype 1 1
gmax 0.025, 0.015; blc 57 54; trc 69 74;
gpos 64 69  62 59
domax 1 1 0 0; dopos 1 1 1 1 0; dowidth 1 1 1 1 0
FIN

PROC BOXFLUX
type 'boxflux'
$ originally from CMoore, but revised heavily to use CCEDT
$ Adds up clean components in clean boxes for each image
$ Before using: getn file, set dataarray
$ *** First, seperate out the A and B CC into seperate CC tables
inver 1; outver 0; bcount 1; ecount 0; cutoff -100; cparm 0
nccbox -2
$ CCBOX is in arcsec relative to reference position, with cosdec
$   included in RA term.  Shift from ref. to position of A:
$   shift -0.316, 2.48;  to position of B: shift 0.910, -3.58
if dataarray = 'A' then
$ Make sides of box 4pix*0.027 = 0.1 asec from center
     ccbox -0.216, 2.38, -0.416, 2.58,  1.010, -3.68, 0.810, -3.38
end
if dataarray = 'B' then
$ Make sides of box 3pix*0.101 = 0.3 asec from center
     ccbox -0.016, 2.18, -0.616, 2.78,  1.210, -3.88, 0.610, -3.28
end
if dataarray = 'C' then
$ Make sides of box 2pix*0.304 = 0.6 asec from center
     ccbox  0.284, 1.88, -0.916, 3.08,  1.510, -4.18, 0.310, -2.98
end
if dataarray = 'D' then
$ Make sides of box 2pix*0.609 = 1.2 asec from center
     ccbox  0.884, 1.28, -1.516, 3.68, 2.110, -4.78, -0.290, -2.38
end
gowt('CCEDT')
a=0; b=0; inext 'cc';
$ Find number of highest-numbered CC table
keyword 'extver2'; gethead; tabnum = keyval(1)
$ **** Add up flux in tables 3 and 4
if tabnum = 4 then
   $ Get number of rows in CC table 3
   invers 3; keyword 'num row'; getthead; numrow=keyval(1)
   $ For each row in CC table get flux and add it to current flux
   for i = 1 to numrow
      pixxy=i,1; tabget; flux=keyval(1)*1000 + keyval(2)*1000
      a = a + flux; flux = 0
   end
```

```
   type 'CC flux in box A is', a
   $ Get number of rows in CC table 4
   invers 4; keyword 'num row'; getthead; numrow=keyval(1)
   $ For each row in CC table get flux and add it to current flux
   for i= 1 to numrow
      pixxy=i,1; tabget; flux=keyval(1)*1000 + keyval(2)*1000
      b = b + flux; flux = 0
   end
   type 'CC flux in box B is', b
end
$ **** Add up flux in tables 2 and 3
if tabnum = 3 then
   $ Get number of rows in CC table 2
   invers 2; keyword 'num row'; getthead; numrow=keyval(1)
   $ For each row in CC table get flux and add it to current flux
   for i = 1 to numrow
      pixxy=i,1; tabget; flux=keyval(1)*1000 + keyval(2)*1000
      a = a + flux; flux = 0
   end
   type 'CC flux in box A is', a
   $ Get number of rows in CC table 3
   invers 3; keyword 'num row'; getthead; numrow=keyval(1)
   $ For each row in CC table get flux and add it to current flux
   for i= 1 to numrow
      pixxy=i,1; tabget; flux=keyval(1)*1000 + keyval(2)*1000
      b = b + flux; flux = 0
   end
   type 'CC flux in box B is', b
end
RET;FIN

PROC RESET
$ getn file
$ deletes all SN tables, and vers 2 of CL table, also
$  resets all source fluxes to zero
inext 'sn'; invers -1; EXTDEST
inext 'cl'; invers 2; EXTDEST
inext 'cl'; invers 3; EXTDEST
setsetjy
source ''; zerosp 0; optype 'rese'
gowt('SETJY')
FIN

PROC GOSPLIT
$ splits data, WITHOUT applying polarization info
$ before using: getn file
$               set workdisk, dataname
type 'Gosplit:'
setsplit
dopol -1; docalib 1; gainuse 0; flagver 1; clro; outdisk=workdisk
gowt('SPLIT')
inname '0957+561'; inclass 'split'; indisk = workdisk; inseq 1
clro; outname = dataname
RENAME
FIN

save xproc
clrmsg
```

```
$*****************************************************************
$ XFLAG:  procedures I need in addition to XPROC to
$    do flagging and calibration of Xband 0957 time-delay data

get XPROC

PROC SETFILLM
$sets all but intap, nfiles, band, vlaobs, refdate, outdisk
qual -1; vlamode ''; bchan 1; echan 0; clro
douvcomp 1; doall -1; doconcat -1; dparm 0
cparm 10 0 0 0 0 0 2000 2 0 0
timeran -1 0 0 0 2 0 0 0
calcode ''
FIN

PROC SETTVFLG
$ set diskbad, workdisk before using
$ does all but getn file, and set sources, calcode,
$                                  docalib, gainuse, dparm
dohist 1; sources ' '
selband -1; selfreq -1; freqid -1
bif 1; eif 0; bchan 0; echan 0; antennas 0; baseline 0;
uvrange 0 0; subarray 0; blver -1; doband -1; bpver -1
$ docat -1 means that it deletes its own workfile afterwards
docat -1; smooth 0;  timeran 0; stokes 'rrll'; flagver 1
baddisk = diskbad; in2disk=workdisk; in2seq 0
FIN

PROC SETGETJY
$ sets all but infile, sources, calsour, snver (snver 0 -> all)
soucode ''; qual -1; calcode ''; bif 1; eif 0; subarray 0;
selband -1; selfreq -1; freqid -1; timeran 0; antennas 0
FIN

PROC SETSNPLT
$ sets all but getn file, newname
$ grchan 3; gron
if newname = -2 then sources '3C286','1031+567','0955+476',''; end
if newname = -1 then sources '3C286','1031+567',''; end
if newname = 1 then sources '1331+305','1035+564',''; end
qual -1; timeran 0; stokes 'diff'; selband -1; selfreq -1
freqid -1; bif 1; antennas 0; pixrang 0; ncount 5;
xinc 1; optype ''; opcode ''; xaxis 0; doebar 0; cutoff 0;
$ cparm 0 in SNPLX
inext 'cl'; invers 2; dotv 1
FIN

PROC SETLISTR
$ setup for LISTR matx output, to check goodness of solutions
$ set newname before using
$ sets all inputs for listr except getn file
optype 'matx'; inext 'cl'; invers 2; docalib 1; gainuse 2
if newname = -1 then sources '3C286','1031+567',''; end
if newname = -2 then sources '3C286','1031+567','0955+476',''; end
if newname = 1 then sources '1331+305','1035+564',''; end
dparm 5 1 0;
calcode ''; timeran 0; stokes ''; antennas 0; baseline 0
selband -1; selfreq -1; freqid 0; bchan 1; echan 0
bif 1; eif 0; uvrange 0 0; subarray 0;
dopol -1; blver -1; flagver 1; doband -1; bpver 0; smooth 0;
factor 0; docrt 132; outprint ''; baddisk = diskbad
FIN

PROC SETPCAL
$ getn file, and set dataant before using
$ sets all inputs to pcal but infile and calsour
$ may want to change timerang, bif/eif, antennas, gainuse
timerang 0; selband -1; selfreq -1; freqid -1; bif 0; eif 0;
antennas 0; uvrange 0; flagver 0; docalib 1; gainuse 2;
clr2n; invers 0; ncomp 0; nmaps 0; pmodel 0; solint 2;
soltype 'appr'; prtlev 1; refant = dataant; bparm 0;
cparm 0; baddisk = diskbad
FIN

PROC SETCLCOR
$ need to getn file, set clcorprm, gainver
sources ''; stokes ''; selband -1; selfreq -1; freqid -1;
bif 0; eif 0; timerang 0; antenna 0; subarray 0
opcode 'polr'
baddisk = diskbad;
FIN


*****************************************************************
PROC FLAG1
$ for first round of flagging just with calibrators
$ before using: getn file
$               set dataant, diskbad, workdisk, inttime, newname

settvflg
dparm 0; dparm(6)=inttime
docalib 0; gainuse 0; flagver 1
if newname = -1 then sources '3C286','1031+567',''; end
if newname = -2 then sources '3C286','1031+567','0955+476',''; end
if newname = 1 then sources '1331+305','1035+564',''; end

go TVFLG

FIN


$*****************************************************************
PROC XCAL
$ Procedure to do basic flux and phase calibration of xband data.
$ Follows cookbook 96Aug08.
$ before using: getn file to calibrate
$               set dataant, newname, dataarray
$                   diskbad, workdisk, aant, bant
$     if1flux, if2flux
$ (for details, see 0957/Notes/xflagcal.recipe)

$ Set the flux of 3C286:
$ ** Modify SU table
setsetjy
optype '';  bif 1; eif 1;
if newname < 0 then source '3C286',''; end
if newname > 0 then source '1331+305',''; end
if dataarray = 'A' then zerosp if1flux*.99, 0; end
if dataarray = 'AB' then zerosp if1flux*.99, 0; end
if dataarray = 'B' then zerosp if1flux*.99, 0; end
if dataarray = 'C' then zerosp if1flux*.99, 0; end
if dataarray = 'D' then zerosp if1flux, 0; end
gowt('SETJY')
bif 2; eif 2
if dataarray = 'A' then zerosp if2flux*.99, 0; end
if dataarray = 'AB' then zerosp if2flux*.99, 0; end
if dataarray = 'B' then zerosp if2flux*.99, 0; end
if dataarray = 'C' then zerosp if2flux*.99, 0; end
if dataarray = 'D' then zerosp if2flux, 0; end
gowt('SETJY')

$ Find antenna gains for the inner antennas using the appropriate
$ baselines and the flux of 3C286
$ ** Create SN table 1
setcalib
bif 1; eif 2
solmode 'A&P'; solint 2; cmethod 'grid'; clr2n;
invers 0; ncomp 0; clro; cparm 0 0 10 10 1 0; cmodel ''
clro; outdi = workdisk;
snver 1
if dataarray = 'A' then uvrange 50 300; antennas Aant; end
if dataarray = 'AB' then uvrange 50 300; antennas ABant; end
if dataarray = 'B' then uvrange 50 300; antennas Bant; end
if dataarray = 'C' then uvrange 50 300; end
if dataarray = 'D' then uvrange 0 15; end
if newname < 0 then calsour '3C286',''; end
if newname > 0 then calsour '1331+305',''; end
gowt('CALIB')

$ Find antenna gains for all antennas,
$ assuming a flux of 1 Jy for 1031
$ and for baselines less than 400 klambda.
$ ** Create SN table 2
if newname < 0 then calsour '1031+567',''; end
if newname > 0 then calsour '1035+564',''; end
uvrange 0 400; antennas 0
snver 2
gowt('CALIB')

$ Find flux of 1031 from SN tables 1 & 2 and flux of 3C286
$ Eventually modify this to use xaltime1 and xaltime2
$ ** Modify SU table, SN tables
setgetjy; snver 0
if newname < 0 then
       source '1031+567',''; calsour '3C286',''; end
if newname > 0 then
       source '1035+564',''; calsour '1331+305',''; end
gowt('GETJY')

$ Apply gain solutions found for 1031 to 0957 and to itself
$ ** Create CL table 2
setclcal; calcode ''
timeran 0; antennas 0; opcode 'cali'; interp '2pt'; smotype ' '
snver 2; gainver 1; gainuse 2
```

```
if newname < 0 then sourc '1031+567','0957+561',''; end
if newname < 0 then calsour '1031+567',''; end
if newname > 0 then sourc '1035+564','0957+561',''; end
if newname > 0 then calsour '1035+564',''; end
gowt('CLCAL')

$ Apply gain solutions found for 3C286 to itself (need this
$ for polarization calibration later, and its a check that all is
$ well, and it lets you flag 3C286 intelligently after a good
$ calibration). The phase gains for 3C286 are often different
$ than the gains for 1031, which is not unreasonable since they
$ can be in very different parts of the sky.
snver 1; gainver 1; gainuse 2
if newname < 0 then sourc '3C286',''; end
if newname < 0 then calsour '3C286',''; end
if newname > 0 then sourc '1331+305',''; end
if newname > 0 then calsour '1331+305',''; end
gowt('CLCAL')

RET; FIN

$************************************************************
PROC FLAG2
$ for second round of flagging, including 0957
$ before using: getn file
$               set diskbad, workdisk, inttime, newname

settvflg
dparm 0; dparm(6) = inttime
docalib 1; gainuse 2; calcode ''
if newname = -1 then
        sources '3C286','1031+567','0957+561',''; end
if newname = -2 then
        sources '3C286','1031+567','0955+476','0957+561',''; end
if newname = 1 then
        sources '1331+305','1035+564','0957+561',''; end

go TVFLG

RET; FIN

$************************************************************
PROC LOADMAP
$ loads in the three maps I want to look at of each processed
$    data set

$ before using: set writedisk, workdisk, dataname

setimlod
clro; outdi = workdisk

infile  '     :        .ICLNSC.1.MAFITS'
$        ZEN01 89apr26x
$        123456789012345678
substr (infile, 1, 5) = writedisk
substr (infile, 7, 14) = dataname
type '## filename for imlod is', infile
gowt('IMLOD')

infile  '     :        .ICLNXC.1.MAFITS'
substr (infile, 1, 5) = writedisk
substr (infile, 7, 14) = dataname
type '## filename for imlod is', infile
gowt('IMLOD')

$infile  '     :        .POLIXC.1.MAFITS'
$substr (infile, 1, 5) = writedisk
$substr (infile, 7, 14) = dataname
$type '## filename for imlod is', infile
$gowt('IMLOD')

infile  '     :        .ICLNPT.1.MAFITS'
substr (infile, 1, 5) = writedisk
substr (infile, 7, 14) = dataname
type '## filename for imlod is', infile
gowt('IMLOD')

FIN

save xflag
clrmsg
```

```
$***************************************************************
$ XCALGRND:
$ Grand procedure to push each data set through, start with
$ multi-source xband data.  Does flux calibration at beginning of
$ each to constant 1031 flux.  No polarization maps.
$
$ Keeps track of names of files as they go through procedures.
$ Variables used here are declared in XPROC.
$ *** This will bomb if any maps are already made ****
$ Set up for when multi-source data is on non-aips disk.
$ Necessary Set up before using:
$
$ type RUN UTILITY
$ type RUN XPROC
$ type RUN XFLAG
$ follow xrecipe
$ save multi source data to unix disk
$ type RUN XCALGRND
$ adjust parameters in XACT script, and type RUN XACT

get xproc
clrmsg

$***************************************************************
PROC GRAND
$ before running, set dataname, dataant, dataarray, inttime,
$ workdisk, diskbad, readdisk, writedisk, newname
$ Dataname must be 8 characters long
$ readdisk and writedisk must be 5 char long

type '################################################'
type '## Begin reduction of data set', dataname
type '## Array is', dataarray
type '## Reference antenna is', dataant
type '## Integration time is', inttime
type '## Newname is set to', newname
type '## Reading from disk', readdisk
type '## Writing to disk', writedisk
type '################################################'
type '  '

type '## LOAD IN FILE FROM UNIX DISK ## '$$$$$$$$$$$$$$$$$$$$$$$$$
setuvlod
infile '     :         .FLAGD.1.UVFITS'
$       VIG3X 90Nov01x
substr (infile, 1, 5) = readdisk
substr (infile, 7, 14) = dataname
outname = dataname; outclass 'multi'; outseq 1; outdi = workdisk
gowt('UVLOD')

$type '## DO FLUX CALIBRATION ##'
$ Remove all SN tables, version 2 of CL table, reset all source
$  fluxes to 0
inname = dataname; inclass 'multi'; inseq 1; intype 'uv';
indi = workdisk
RESET

$ Set the flux of 1031:     ** Modify SU table
setsetjy; optype '';  bif 1; eif 1;
if newname < 0 then source '1031+567','1035+564','1035+564','';
if newname > 0 then source '1035+564','1035+564','1035+564','';
zerosp = 0.776, 0;  gowt('SETJY')
bif 2; eif 2; zerosp = 0.771, 0;  gowt('SETJY')

$ Find antenna gains for all antennas for 1031
$ and for baselines less than 400 klambda.  ** Create SN table 1
setcalib; bif 1; eif 2
solmode 'A&P'; solint 2; cmethod 'grid'; clr2n;
invers 0; ncomp 0; clro; cparm 0 0 10 10 1 0; cmodel ''
clro; outdi = workdisk;
snver 1; uvrange 0 400; antennas 0
if newname < 0 then calsour '1031+567','1035+564','1035+564','';
if newname > 0 then calsour '1035+564','1035+564','1035+564','';
gowt('CALIB')

$ Apply gain solutions found from 1031 to 0957 and to itself
$ ** Create CL table 2
setclcal; calcode ''; snver 1; gainver 1; gainuse 2
timeran 0; antennas 0; opcode 'cali'; interp '2pt'; smotype ' '
if newname < 0 then sourc '1031+567','0957+561','1035+564','';
if newname < 0 then calsour '1031+567','1035+564','1035+564','';
if newname > 0 then sourc '1035+564','0957+561','1035+564','';
if newname > 0 then calsour '1035+564','1035+564','1035+564','';
gowt('CLCAL')

type '## SPLIT MULTISOURCE DATA ##'
$ assumes highest version of CL table, assumes no pol cal
inname = dataname; inclass 'multi'; inseq 1; indi = workdisk;
GOSPLIT
inname = dataname; inclass 'multi'; inseq 1; indi = workdisk;
intype 'uv'
delete; recat

$ Do eposwtch, if necessary
inclass 'split'; inseq 1; inname=dataname; indisk=workdisk
keyword 'epoch'; GETHEAD; type 'Epoch is', keyvalue(1)
if keyvalue(1) = 1950 then
    type 'Changing epochs to J2000'; EPOSWTCH;
end

$Sort UV data, if necessary
inclass 'split'; inseq 1; inname=dataname; indisk=workdisk
keyword 'sortord'; GETHEAD; type 'Sort Order is', keystrng
if keystrng <> 'TB' then
    type '## SORT THE DATA TO TB ORDER ##'
    outclass 'uvsrt'; inseq 1; inname=dataname; indisk=workdisk
    sort 'TB'; baddisk = diskbad; rotate 0; gowt('UVSRT')
    inclass 'split'; inseq 1; inname=dataname; indisk=workdisk;
intype 'uv'
    DELETE;
    inclass 'uvsrt'; inseq 1; inname=dataname; indisk=workdisk
    clro; outcl 'split'; RENAME
end

$ Check epoch and sort order
inclass 'split'; inseq 1; inname=dataname; indisk=workdisk;
    intype 'uv'
keyword 'epoch'; GETHEAD; type 'Epoch is', keyvalue(1)
keyword 'sortord'; GETHEAD; type 'Sort Order is', keystrng

type '## DO FIRST MAP & SELF-CAL CYCLE ##' $$$$$$$$$$$$$$$$$$$$$$$$
setscmap
if dataarray = 'A' then setascmap; end
if dataarray = 'B' then setbscmap; end
if dataarray = 'C' then setcscmap; end
if dataarray = 'D' then setdscmap; end
$ Clean cautiously;  set number of self-cal loops
factor = -0.3; nmaps 2
inclass 'split'; inseq 1; inname=dataname; indisk=workdisk
clr2n; in2disk=workdisk; clro; outdisk=workdisk; clr2o;
out2disk=workdisk
gowt('SCMAP'); msg0957

$remove stuff, get stats, rename image
inname = dataname; inclass 'split'; inseq 1; indi = workdisk;
intype 'uv'
invers 1; getgain; invers 2; getgain; delete
inseq 1; zapibeam; recat
inclass 'icln'; inseq 1; indisk=workdisk; inname = dataname
getmapnois; clro; outclass 'iclnsc'; RENAME

$rename uv data coming out of loop
inclass 'scmap'; inseq 1; inname=dataname; indisk=workdisk
outclass 's-cal'; outseq 0; outname=dataname; outdisk=workdisk
RENAME

type '## PRELIMINARY FIT FOR FLUX OF POINTS ##' $$$$$$$$$$$$$$$$$$
$ Fit to see what fluxes are before doing crosscal (out of
$ curiousity).  Don't do C or D array.  Assume positions close
$ enough to use box positions
setjmfit;
inclass 'iclnsc'; inseq 1; indisk=workdisk; inname=dataname
clro; outdisk=workdisk
if dataarray = 'B' then
    type '## JMFIT on image a, VLA array B ##'; setbjmfita;
    gowt('JMFIT')
    type '## JMFIT om image b, VLA array B ##'; setbjmfitb;
    gowt('JMFIT')
end
if dataarray = 'A' then
    type '## jmfit on image a, VLA array A ##'; setajmfita;
    gowt('JMFIT')
    type '## jmfit on image b, VLA array A ##'; setajmfitb;
    gowt('JMFIT')
end
BOXFLUX; msg0957

type '# WRITE SELF-CALIBRATED MAPS TO UNIX DISK ##'
inclass 'iclnsc'; inseq 1; indisk=workdisk; inname=dataname;
intype 'ma'
save6; delete; recat

head('CROSS CALIBRATE DATA TO REFERENCE') $$$$$$$$$$$$$$$$$$$$$$$$
inclass 's-cal'; inseq 1; indisk=workdisk; inname=dataname
```

```
keyword 'epoch'; GETHEAD; type 'Epoch is', keyvalue(1)
keyword 'sortord'; GETHEAD; type 'Sort Order is', keystrng
in2name = refname; in2class = refclass; in2seq = refseq;
in2disk = refdisk; invers = refvers; ncomp = refcomp;
clro; outclass 'x-cal'; outdisk=workdisk
setcalib; cmodel 'comp'
$ use grid for speed, dft for accuracy
solmode 'P'; solint=inttime; cmethod 'dft'; calsour '0957+561',''
$cparm 3 and 4 limit reports of closure errors. negative means
$    no report
cparm 0, 0, -1, -1, 1, 0
gowt('CALIB');  $$ Hope it doesn't die of a forrtl!!!!

$ get gain applied to self-cal'd data, write to disk, and delete
inclass 's-cal'; inseq 1; indisk=workdisk; inname=dataname;
intype 'uv'
invers 1; getgain; save5; delete; recat; msg0957

head('SECOND MAP & SELF-CAL CYCLE') $$$$$$$$$$$$$$$$$$$$$$$$$$$$$$$$
setscmap
if dataarray = 'A' then setascmap; end
if dataarray = 'B' then setbscmap; end
if dataarray = 'C' then setcscmap; end
if dataarray = 'D' then setdscmap; end
$ Clean cautiously; set number of self-cal loops
factor = -0.3; nmaps 2;
inclass 'x-cal'; inseq 1; inname=dataname; indisk=workdisk
clr2n; in2disk=workdisk; clro; outdisk=workdisk; clr2o;
out2disk=workdisk
gowt('SCMAP'); msg0957

$remove stuff, get stats  (don't write x-cal uvdata to disk)
inclass 'x-cal'; inseq 1; inname=dataname; indisk=workdisk
invers 1; getgain; invers 2; getgain; delete
inseq 1; zapibeam; recat
inclass 'icln'; inseq 1; indisk=workdisk; inname = dataname
getmapnois; getbeamsiz

$rename data coming out of loop
inclass 'icln'; inseq 1; inname=dataname; indisk=workdisk
clro; outclass 'iclnxc'; RENAME
inclass 'scmap'; inseq 1; inname=dataname; indisk=workdisk
outclass 'xscal'; outseq 0; outname=dataname; outdisk=workdisk
RENAME

type '## FIT FOR POINTS BEFORE SUBTRACTION, IN A AND B ARRAYS' $$
setjmfit;
inclass 'iclnxc'; inseq 1; indisk=workdisk; inname=dataname
clro; outdisk=workdisk
if dataarray = 'B' then
    type '## jmfit on image a, vla array B ##'; setbjmfita;
    gowt('JMFIT')
    type '## jmfit on image b, vla array B ##'; setbjmfitb;
    gowt('JMFIT')
end
if dataarray = 'A' then
    type '## jmfit on image a, vla array a ##'; setajmfita;
    gowt('JMFIT')
    type '## jmfit on image b, vla array a ##'; setajmfitb;
    gowt('JMFIT')
end
BOXFLUX; msg0957

type '# WRITE CROSS-SELF-CALIBRATED MAP TO DISK ##'
inclass 'iclnxc'; inseq 1; indisk=workdisk; inname=dataname;
intype 'ma'
save6; delete

head('SUBTRACT JET MODEL') $$$$$$$$$$$$$$$$$$$$$$$$$$$$$$$$$$$$$$$$
$ Subtract jet model from cross-self-cal'd data
setuvsub
inclass 'xscal'; inseq 1; indisk=workdisk; inname=dataname
in2name = jetname; in2class = jetclass; in2seq = jetseq
in2disk = jetdisk; invers = jetvers; ncomp = jetcomp
clro; outdisk=workdisk
$need 'DFT' to make accurate for RL and LR, but its slow,
$     so skip it
cmethod 'GRID';
gowt('UVSUB'); msg0957

type '# WRITE CROSS-SELF-CALIBRATED UVDATA TO DISK ##'
inclass 'xscal'; inseq 1; indisk=workdisk; inname=dataname;
intype 'uv'
save5; delete; recat

type '## MAKE FINAL MAP ##' $$$$$$$$$$$$$$$$$$$$$$$$$$$$$$$$$$$$$$$$
inclass 'uvsub'; inseq 1; indisk=workdisk; inname=dataname
clr2n; in2disk=workdisk;   clro; outdisk=workdisk
setimagr
$ just clean points, and don't need to clean as deep:
if dataarray = 'A' then
    setaimagr; niter 3000; factor 0
    nbox 2; clbox 214 120 232 138  258 337 276 355
end
if dataarray = 'B' then
    setbimagr; niter 2000; factor 0
    nbox 2; clbox 123 145 139 161  111 85 127 101
end
if dataarray = 'C' then
    setcimagr; niter 1000; factor 0
    nbox 2; clbox 60 68 70 78  56 48 66 58
end
if dataarray = 'D' then
    setdimagr; niter 1000; factor 0
    nbox 1; clbox 57 54 69 74;
end
gowt('IMAGR')

$ Delete stuff, get stats, rename map
zapimagr; inseq 1; zapibeam; recat
inclass 'icln'; inseq 1; inname=dataname; indisk=workdisk
getmapnois; getbeamsiz
clro; outclass 'iclnpt'; RENAME; msg0957

type '# WRITE FINAL UVDATA TO UNIX DISK ##'
inclass 'uvsub'; inseq 1; indisk=workdisk; inname=dataname;
intype 'uv'
save5; delete; recat

head('FIT FOR FLUXES OF POINTS') $$$$$$$$$$$$$$$$$$$$$$$$$$$$$$$$$$
$ Fit for the points
setjmfit;
inclass 'iclnpt'; inseq 1; indisk=workdisk; inname=dataname
clro; outdisk=workdisk
if dataarray = 'D' then
   type '## JMFIT on images a and b, vla array d ##'; setdjmftab;
   gowt('JMFIT')
end
if dataarray = 'C' then
    type '## JMFIT on image a, vla array c ##'; setcjmfita;
    gowt('JMFIT')
    type '## jmfit on image b, vla array c ##'; setcjmfitb;
    gowt('JMFIT')
end
if dataarray = 'B' then
    type '## JMFIT on image a, vla array b ##'; setbjmfita;
    gowt('JMFIT')
    type '## jmfit on image b, vla array b ##'; setbjmfitb;
    gowt('JMFIT')
end
if dataarray = 'A' then
    type '## jmfit on image a, vla array a ##'; setajmfita;
    gowt('JMFIT')
    type '## jmfit on image b, vla array a ##'; setajmfitb;
    gowt('JMFIT')
end
$Get flux in clean boxes and write final list of CC components
BOXFLUX; msg0957

type '# WRITE FINAL MAP TO DISK ##'
inclass 'iclnpt'; inseq 1; indisk=workdisk; inname=dataname;
intype 'ma'
save6; delete
type '################################################'
type '## Finished with reduction of data set', dataname
type '################################################'
scrdest; msg0957
FIN
save xcalgrnd; clrmsg
```

```
$*****************************************************************
$ XACT: run file to run grand on any XBAND data set

$ do setup as described in XCALGRND first.
$ please delete MESSAGE file on unix disk before starting

clrmsg
get XCALGRND
workdisk 5
diskbad 1 2 3 4
readdisk 'V3XFG'
writedisk 'VIG3X'
refdisk 4
jetdisk 4

$readdisk is unix location of uvdata, and writedisk is where all
$   the processed data should go.
$ refdisk & jetdisk are aips disk location of jet and reference
$    maps
$ file name on unix disk must be in format:
$    dataname.FLAGD.1.UVFITS
$  where dataname is the 8 character name, like 85AUG17X.
$ required for xcalgrnd:
$ dataarray, dataant, inttime in minutes, newname

$*************** REDUCE A-ARRAY DATA: *********************

refname = 'arefx'; refclass = 'icln'
refseq = 1; refvers = 0; refcomp = 0
jetname 'ajetx' ; jetclass 'icln';
jetseq = 1; jetvers 0; jetcomp 0
$ jetvers 0 defaults to highest, jetcomp 0 defaults to all CC

newname -1
$dataname '91Jul10x'; dataarray 'A'; dataant  9; inttime 1/3;grand
$dataname '91Aug18x'; dataarray 'A'; dataant 25; inttime 1/6;grand
$dataname '92Oct23x'; dataarray 'A'; dataant  2; inttime 1/6;grand
$dataname '92Nov11x'; dataarray 'A'; dataant  9; inttime 1/6;grand
$dataname '92Dec10x'; dataarray 'A'; dataant 27; inttime 1/6;grand
newname 1
$dataname '94Mar04x'; dataarray 'A'; dataant 27; inttime 1/6;grand
$dataname '94Apr11x'; dataarray 'A'; dataant 27; inttime 1/6;grand
newname -1
$dataname '95Jun23x'; dataarray 'A'; dataant 27; inttime 1/6;grand
$dataname '95Jun28x'; dataarray 'A'; dataant 27; inttime 1/6;grand
$dataname '95Jul08x'; dataarray 'A'; dataant 27; inttime 1/6;grand
$dataname '95Jul20x'; dataarray 'A'; dataant  8; inttime 1/6;grand
$dataname '95Jul30x'; dataarray 'A'; dataant 27; inttime 1/6;grand
$dataname '95Aug07x'; dataarray 'A'; dataant 27; inttime 1/6;grand
$dataname '95Sep01x'; dataarray 'A'; dataant 27; inttime 1/6;grand
$dataname '95Sep09x'; dataarray 'A'; dataant  8; inttime 1/6;grand
$dataname '95Sep15x'; dataarray 'A'; dataant  8; inttime 1/6;grand
$dataname '95Sep30x'; dataarray 'A'; dataant 27; inttime 1/6;grand
$dataname '96Oct19x'; dataarray 'A'; dataant  8; inttime 1/6;grand
$dataname '96Nov10x'; dataarray 'A'; dataant 27; inttime 1/6;grand
$dataname '96Dec26x'; dataarray 'A'; dataant 27; inttime 1/6;grand
$dataname '97Jan10x'; dataarray 'A'; dataant 27; inttime 1/6;grand

$AnB datasets:
$dataname '93Feb05x'; dataarray 'A'; dataant 27; inttime 1/6;grand
newname 1
$dataname '94May07x'; dataarray 'A'; dataant 12; inttime 1/6;grand
newname -1
$dataname '95Sep23x'; dataarray 'A'; dataant 27; inttime 1/6;grand

$A&B&D dataset:
newname 1
$dataname '94Feb14x'; dataarray 'A'; dataant 11; inttime 1/6;grand

$A&D dataset:
newname -1
$ 95Jun17 is newname -1 for 1031 (but is 1331 not 3c286)
$dataname '95Jun17x'; dataarray 'A'; dataant 13; inttime 1/6;grand

$*************** REDUCE B-ARRAY DATA: *********************

refname = 'brefx'; refclass = 'icln'
refseq = 1; refvers = 0; refcomp = 0
jetname 'bjetx' ; jetclass 'icln';
jetseq = 1; jetvers 0; jetcomp 0

newname -1
$dataname '92Jan06x'; dataarray 'B'; dataant  3; inttime 1/6;grand
$dataname '93Mar21x'; dataarray 'B'; dataant 12; inttime 1/6;grand
$dataname '93Apr09x'; dataarray 'B'; dataant 12; inttime 1/6;grand
newname 1
$dataname '94Jul06x'; dataarray 'B'; dataant 14; inttime 1/6;grand
$dataname '94Jun24x'; dataarray 'B'; dataant 14; inttime 1/6;grand
$dataname '94Aug18x'; dataarray 'B'; dataant 14; inttime 1/6;grand
$dataname '94Sep08x'; dataarray 'B'; dataant 12; inttime 1/6;grand
newname -1
$dataname '95Oct10x'; dataarray 'B'; dataant 25; inttime 1/6;grand
$dataname '95Oct27x'; dataarray 'B'; dataant 25; inttime 1/6;grand
$dataname '95Nov09x'; dataarray 'B'; dataant 25; inttime 1/6;grand
$dataname '95Dec26x'; dataarray 'B'; dataant 13; inttime 1/6;grand
$dataname '97Feb26x'; dataarray 'B'; dataant 20; inttime 1/6;grand

$BnC datasets:
$dataname '90Oct04x'; dataarray 'B'; dataant 17; inttime 1/3;grand
$dataname '92Feb04x'; dataarray 'B'; dataant 17; inttime 1/6;grand
$dataname '93May18x'; dataarray 'B'; dataant 23; inttime 1/6;grand
newname 1
$dataname '94Oct10x'; dataarray 'B'; dataant  3; inttime 1/6;grand
newname -1
$dataname '96Jan26x'; dataarray 'B'; dataant  3; inttime 1/6;grand
$dataname '96Feb05x'; dataarray 'B'; dataant  6; inttime 1/6;grand

$A&B&D dataset:
newname 1
$dataname '94Feb14x'; dataarray 'B'; dataant 11; inttime 1/6;grand


$******** REDUCE C-ARRAY DATA: ****************************

refname = 'crefx'; refclass = 'icln'
refseq = 1; refvers = 0; refcomp = 0
jetname 'cjetx' ; jetclass 'icln';
jetseq = 1; jetvers 0; jetcomp 0

newname -1;
$dataname '90Nov01x'; dataarray 'C'; dataant 26; inttime 1/3;grand
$dataname '90Dec13x'; dataarray 'C'; dataant 26; inttime 1/3;grand
$dataname '91Jan17x'; dataarray 'C'; dataant  5; inttime 1/3;grand
$dataname '92Feb29x'; dataarray 'C'; dataant  2; inttime 1/2;grand
$dataname '92Mar07x'; dataarray 'C'; dataant  2; inttime 1/2;grand
$dataname '92Apr18x'; dataarray 'C'; dataant  2; inttime 1/6;grand
$dataname '92May03x'; dataarray 'C'; dataant  2; inttime 1/6;grand
$dataname '93Jul25x'; dataarray 'C'; dataant 25; inttime 1/6;grand
$dataname '93Aug26x'; dataarray 'C'; dataant 25; inttime 1/6;grand
$dataname '94Nov07x'; dataarray 'C'; dataant 22; inttime 1/6;grand
$dataname '94Dec08x'; dataarray 'C'; dataant 13; inttime 1/6;grand
$dataname '96Feb26x'; dataarray 'C'; dataant  6; inttime 1/6;grand
$dataname '96Mar04x'; dataarray 'C'; dataant 16; inttime 1/6;grand
$dataname '96Apr05x'; dataarray 'C'; dataant  6; inttime 1/6;grand
$dataname '96Apr25x'; dataarray 'C'; dataant 13; inttime 1/6;grand

$CnD datasets:
$dataname '96Jun11x'; dataarray 'C'; dataant 24; inttime 1/6;grand

$A&B&D dataset:
newname 1
$dataname '94Feb14x'; dataarray 'C'; dataant 11; inttime 1/6;grand


$******** REDUCE D-ARRAY DATA: ****************************

refname = 'drefx'; refclass = 'icln'
refseq = 1; refvers = 0; refcomp = 0
jetname 'djetx' ; jetclass 'icln';
jetseq = 1; jetvers 0; jetcomp 0

newname -1
$dataname '92Jul28x'; dataarray 'D'; dataant  8; inttime 1/3;grand
newname 1
$dataname '93Nov12x'; dataarray 'D'; dataant 11; inttime 1/6;grand
$dataname '94Jan15x'; dataarray 'D'; dataant 11; inttime 1/6;grand
newname -1
$dataname '95Jan12x'; dataarray 'D'
$dataname '95Jan25x'; dataarray 'D'
$dataname '95Feb20x'; dataarray 'D'
$dataname '95Mar09x'; dataarray 'D'; dataant 15; inttime 1/6;grand
$dataname '95Apr18x'; dataarray 'D'
$dataname '95May06x'; dataarray 'D'; dataant 23; inttime 1/6;grand
$dataname '95May21x'; dataarray 'D'
$dataname '95May28x'; dataarray 'D'
$dataname '96Jul07x'; dataarray 'D'; dataant 24; inttime 1/6;grand
```

```
$****************************************************************
Recipe to follow when reducing 4cm, xband data.  This includes
what actually was done with the data sets, not other things I
tried along the way.

Start up aips, and
> get xflag

*************************************************************
READ THE DATA SET OFF OF TAPE.

XBAND data usually in FITS format.  FITS files of raw data in unix
have names in the form 90MAY27.XBAND.FITS.

Use tar to extract from tape, and UVLOD to read into AIPS.

Rename to outname '90May27X'; outclass 'xband'

*************************************************************
FIND IMPORTANT PARAMETERS

Do scan in listr to get a look at data
> optype 'scan'; go listr
make sure OK, set variables newname, inttime, caltime1, caltime2

newname indicates source names used
  if newname = -1 then
        sources '3C286','1031+567','0957+561',''; end
  if newname = -2 then
        sources '3C286','1031+567','0955+476','0957+561',''; end
  if newname = 1 then
        sources '1331+305','1035+564','0957+561','';
   end

caltime indicates time range used for getjy.  It is the time range
enclosing 1031 and 3C286.  If there are two observations of 3C286,
caltime1 is the first and caltime2 is the second.  If there is
only one observation of 3C286, then caltime1 is zero, and
caltime2 is time enclosing just 1031 and 3C286.  I never actually
used this variable, but I recorded it for all the data sets.

inttime is the length of integration scans, usually 10 or 30
seconds

Do prtan to see antenna table and set initial value for refant,
and set dataarray

dataant is the reference antenna for the data set, usually
the first one on the north arm, unless that has problems

Put all this information in a file like '89Apr26.notes'

Example of top of notes file:

89Apr26: dataarray 'B'; dataant 28; inttime 10; newname -2
         caltime1 0 2 25 0 0 2 43 0; caltime2 0 4 41 50 0 4 55 0
 xaltime1 0 2 21 0 0 2 39 0; xaltime2 0 4 39 0 0 4 50 0
        mid-observation is at _____LST
--------------------------------------------------------------

Check operator log for problems and record significant ones in
notes file.  Watch for these problems when flagging.



*************************************************************
FIRST ITERATION OF FLAGGING

same as in "crecipe"

*************************************************************
CALIBRATE ANTENNA GAINS
For now calibrate to 3c286 (in xcalgrnd, the data is recalibrated
to constant 1031 before splitting)

getn file
set dataant, dataarray, newname, xaltime1, xaltime2,
    diskbad, workdisk, aant, bant, ififlux, if2flux

If A-array, set aant (numbers of first three antennas on each arm)
If B-array, set bant (negative of numbers of last two antennas on
each arm, seperated by commas)
If combo array, set ABant, up to 27 numbers, of whatever antennas
should be included  (also set dataarray 'AB')

Check that there are no SN tables on dataset

Find 3C286 flux:
> setsetjy; optype 'calc'; go setjy
This will calculate the Perley-corrected Baars et al fluxes for
the band used.  Set these values in ififlux and if2flux.

Do calibration:
> xcal
Record: fluxes set by setjy,
calib results (which SN table, number of solutions,
closure errors)
getjy fluxes for 1031

*************************************************************
EVALUATE RESULTS

For various ways to use LISTR, see end of this document.
The way I already use LISTR and SNPLT are the most useful:

getn file, set newname
> setlistr
> bif 1; go listr
> bif 2; go listr
Check that phase calibrators have good amplitudes and phases
near zero, not any antenna or time based problems for later.

getn file, set newname
> grcl; tvcl
> setsnplt; bif 1; go snplt
> bif 2; go snplt
Look at left minus right differences in gains of CL table to
check for phase jumps in one polarization that aren't in the other
Check if refant well chosen (if bad refant, all antennas will
have same large variations)
Check for bad phasejumps between RR and LL which indicate
mechanical problems.  Jump will be between two 1031 scans,
flag 0957 data in between these (where jump occured)

*************************************************************
SECOND ROUND OF FLAGGING

same as in "crecipe"

*************************************************************

If any flagging done on calibrators during FLAG2, do RESET
and XCAL

******* POLARIZATION CALIBRATION *************************
I ended up not making polarization maps, but on most data sets I
did attempt pol cal.

Check parallactic angle of 1031, to see if enough to do good
   polarization calibration.
if newname < 0 then source '1031+567',''; end
if newname > 0 then source '1035+564',''; end
> optype 'gain'; inext 'cl'; dparm 9 0; inver 1; stokes 'half'
> go listr

Use 1031 to solve for the problems in the telescope feed AND
 the polarization (% polarized flux) for 1031
** Modifies SU and AN tables (overwrite previous stuff in
AN table)
if newname < 0 then calsour '1031+567',''; end
if newname > 0 then calsour '1035+564',''; end
> setpcal; gainuse 2
> gowt('PCAL')
Record results for IF1 and If2 (not for each antenna, just few
lines at the end)

Find the observed right minus left phase angle of 3C286
if newname < 0 then sour '3C286',''; end
if newname > 0 then sour '1331+305',''; end
if dataarray = 'A ' then uvrange 50 300; antennas Aant; end
if dataarray = 'AB' then uvrange 50 300; antennas ABant; end
if dataarray = 'B ' then uvrange 50 300; antennas Bant; end
if dataarray = 'C ' then uvrange 50 300; end
if dataarray = 'D ' then uvrange 0 15; end
> optype 'matx'; stokes 'polc'; dparm 1 0
> docalib 1; dopol 1; gainuse 2
> bif 1; eif 1
> go listr
> bif 2; eif 2
> go listr
The matrix average is the observed value.
Set ifiangle and if2angle equal to +66 degrees minus the observed
value.  If this value is not (-180 < value < +180), then fix
it so it is (add or subtract 360)
```

```
Check that the observed right-minus-left angle is well-determined.
If necessary, redo calib with just phases and short baselines
(see cookbook)

Copy the extension files to higher numbers, so next step can be
redone if necessary
> inext 'cl'; inver 2; ncount 1; outver 3; go tacop
> inext 'an'; inver 1; ncount 1; outver 2; go tacop

Correct for difference between known and observed
right-minus-left angle
** Modifies CL table 3 and AN table 1
> setclcor; gainver 3; clcorprm if1angle, if2angle
> gowt('CLCOR')

Check that everything worked OK.
> tget listr; uvrange 0; antennas 0; gainuse 3
> bif 1; go listr;
> bif 2; go listr
Phases should be consistent, about 66 degrees
Record mean and sigma of matrix

If it doesn't work, or you make a mistake, remove CL table 3, and
copy AN table 2 back to AN table 1, then start over by recopying
tables, then running CLCOR.  If it just looks bad and I can't
fix it, I usually don't both removing the bad tables.

************************************************************

On older xband data (usually newname < 0, but check header and
listr scan to see what system it uses), use eposwtch to change the
header coordinates from B1950 to J2000 for the cross calibration.
(newname is only used in pre-Grand processing, so don't worry that
using eposwtch means you have to change to newname -1).

If not in TB sort order, sort it to that.

Rename outclass 'FLAGD', and outna 'YYMMMDDX' , and move
multi-source uv data back to unix disk

Check that info in XACT script is there and is correct

Date the notes file


************************************************************

To run data:

Start AIPS with appropriate user number (contains REF and
JET maps, has run files linked in)
Edit XACT to specify disks, and uncomment lines for data
  files to run.

In aips, type
> run xact

This will load the flagged uv into AIPS, run the xcalgrnd
procedure, and put the results back on the unix disk.


************************************************************

After it finishes:

After it has finished, go to directory where data was put, and
extract crucial lines from the 960CT19X.MESSAGES file into
960ct19.xrun (I use a perl script for this).  Look at extracted
messages to make sure there were no problems.

Inside aips, look at maps
> get xflag
set writedisk, workdisk, and dataname = 96oct19x
> loadmap
> pixran -0.0005 0.02
> go tvlod

Write in the .xrun file how the maps look.

Write comments in the xlightcurve file
("Subtraction tolerable" was at some point defined as peaks and
valleys less than 1 mJy in amplitude and not too close to point
sources.  Worse than that is labled "bad subtraction")

Enter the Integral JMFIT flux for each image in the xlightcurve
file.

Write reduced data to tape.

Ideally,
        print copies of ICLNXC and ICLNPT maps
        print out the 960ct19.xrun and 960ct19.notes files
```

Afterword: Astrophysics in Context

A modern Ph.D. education is incredibly specialized, in both thesis and course work. Yet this work is done in the larger contexts of the scientific community, the anti-intellectualism in American society, government funding for scientific research (or lack thereof), and one's personal relationships and beliefs. At various times in my graduate school years I have considered these topics. This *Afterword* is a brief statement of my thoughts, with a focus on my reasons for doing research in astrophysics. I also discuss governmental funding, scientific education, the relationship between science and religion, the limitations of science, and finally my thoughts on the relationship of the Christian faith to astrophysical research.

Why do scientists pursue research in astrophysics? There are several reasons that most of us share. Scientists do research because they are able to, and because they enjoy describing and understanding the physical world in a mathematical way. To a scientist, the intrinsic beauty and elegance of these descriptions are very captivating. In astrophysics we have the chance to use the physical principles learned from phenomena on earth to describe events in distance places – events which may have far greater extremes of temperature, density, and radiation than can be recreated on earth. Scientists are drawn by their curiosity to seek answers to the many remaining questions about our universe and how it functions. I share all of these motivations as I pursue my own work.

Currently, nearly all funding for astrophysical research in the United States comes from the federal government. Why should society support astrophysics and other basic science research? The question is particularly important if the research doesn't obviously lead to a cure for disease or a faster computer chip. In the case of astrophysics, the study of stars, galaxies, and the universe helps answer some of the big questions of humanity: how did we get here? how old is the universe? are we alone? The government should also provide funding because of the public interest in this field – astronomy and planetary science are probably second only to dinosaurs in exciting children and adults about scientific study. The technical needs of astrophysical research do help drive computing and other technology, with spin-offs into medical imaging, image processing, and radio communications. But beyond these reasons, we need to remind the public of the intrinsic value of basic scientific knowledge

as an important part of our culture, similar to the arts.

Educating children and the public about science is important for several reasons (besides encouraging continued governmental support). It gives people the critical thinking skills and scientific literacy necessary to operate in our technology-based culture. Many people don't feel they have skills or interest in science, yet an enthusiastic presentation of real science results and insight into the scientific process might pique their interest. Scientific education, in schools and in the general public, will help people interpret the scientific and medical results in the media; since the media tend to report only the latest and most controversial results, an understanding of the scientific method will help people put reports in context. Scientific literacy will also help the public be less susceptible to the abundance of pseudo-science in our culture; alien abductions, conspiracy theories, astrology, new-age thought, and a general tone of anti-intellectualism seem to be everywhere in the media. Pseudo-science can be defined as ideas which are clothed in the language of science and claim to be scientific, yet lack backing by repeatable experiment, theoretical explanation, and the consensus of the scientific community. Despite occasional reports to the contrary, the scientific community is *not* in a great conspiracy to withhold information from the public. While it may be slow to come to a consensus, rejection of an idea by a vast majority of the scientific community is a good sign that the idea does not have scientific merit.

But what do the ideas of the new-age movement, or religion in general, have to do with science? As a believer in the historic Christian faith, I have thought about, read about, and discussed this issue a great deal. Some of my colleagues would argue, along with Karl Marx, that religion is simply "the opiate of the masses," disprovable by science, and anyone who holds religious beliefs is not thinking logically or clearly. Yet what can science actually disprove? Certainly it can disprove false scientific claims (for instance, by showing that a phenomenon is not repeatable). But I would argue that science cannot disprove many other claims, or answer other types of questions, such as: is this a good painting? how can I rebuild my marriage? is the defendant guilty? which college should I attend? Occasionally, scientific tests can provide information useful in these decisions (do the materials in the painting indicate it is a fraud? does the defendant's DNA match blood found at the crime site?), yet science is not equipped to answer many types of questions we face every day.

Questions of religious belief generally fall in this category. Religion addresses questions such as: is there a God? what is the value of human life? what is the right way to live? Although science may sometimes provide useful information or perspective, it cannot answer questions of religion or philosophy and provides no more support for atheism than it does for any other religious viewpoint. (Any *scientific* claims made by a religion should, however, be considered with the scientific method.) Thus, the claim that science can "disprove" religion reflects a misunderstanding of the realistic limits of science.

The scientific method and scientific results are generally independent of the religious beliefs of the scientist. Unfortunately, popularizers of science often intermingle the results of science with their own personal religious viewpoint. For example, Carl Sagan opened his television program Cosmos by stating "The Cosmos is all there is, and all there ever will be," implying that there is no reality beyond the physical universe. Steven Weinberg closes his book *The First Three Minutes* with these remarks:

> It is very hard to realize that [the earth] is just a tiny part of an overwhelmingly hostile universe. ... The more the universe seems comprehensible, the more it also seems pointless.
> But if there is no solace in the fruits of our research, there is at least some consolation in the research itself. ... The effort to understand the universe is one of the very few things that lifts human life a little above the level of farce, and gives it some of the grace of tragedy.

Thus, Weinberg adds a bit of nihilism, atheism, humanism, and anthropomorphism of the universe to his excellent book on the Big Bang. As an astrophysicist, I know exactly where he makes the transition from science to his personal beliefs, yet that would not be clear for the intended audience of non-experts. Since the philosophical questions outside science are important, I do not begrudge him for addressing them in his own way, yet I (and other scientists, including many atheists) wish that such comments would be clearly labeled as his own opinion and beyond scientific inquiry. To the average Christian, the implication that science has disproved the existence of God causes a rejection of science as a whole, not just a rejection of the atheistic overtone. Given the present climate of science and religion debates, it is important for me to state (in the rest of this *Afterword*) my own beliefs on the integration of the Christian faith with scientific study, and the motivation it gives me to pursue scientific work.

I am motivated by many of the same reasons that contributed to the beginnings of science itself. There were a variety of socio-economic factors that caused science to arise in European culture rather than in many older civilizations, but the Christian worldview had an important influence. First, Christians believe that the physical world is a direct result of God's activity; thus, there is spiritual merit in studying it, even if nothing "practical" is learned. Second, the Christian view of time is linear with beginning and end (rather than a cycle), giving us the scientific concepts of time and cause & effect. Third, Christians believe that human beings are sinful by nature, so that our arbitrary ideas about how the world "ought" to function are bound to be wrong (*i.e.* different than God's) in some ways; thus, experimentation must be done to test every theory. Finally, Christians believe that God is sustaining and controlling the creative world and that he works in consistent (faithful) ways; thus, the functioning of the physical world can be described by repeatably testable physical laws.

I have given a lot thought to the various tensions between science and Christian faith. For the Christian, the tensions can often be lessened by remembering a few key concepts. First, all truth is God's truth. No matter how or why we come to discover a true fact or idea, that fact is part of God's ordering of the world. There is just one set of what is true and it cannot conflict with itself, regardless of whether it is learned through a scientific experiment, studying a piece of art, or reading an historical account. Second, the Christian must remember that the created world and the Bible are both direct revelations from God and cannot conflict with each other. Science and theology are both human endeavors (to study the creation and the Bible, respectively) and thus prone to error. So when there are conflicts between science and theology, neither the scientific evidence or the written word should be ignored, but the human interpretation of both should be questioned until the truth is found. Third, we must remember the limitations of science. The physical sciences would interpret a Shakespeare sonnet as nothing but ink on paper, a medical patient as nothing but an illness to be cured, and human relationships as nothing but the desire to survive and reproduce. If you remove the words "nothing but" from the above phrases, you may have a true scientific statement, yet the statement is not a *complete* description of the situation. There is truth beyond what science can study; if God's work can be described

scientifically, it is no less his work.

As a Christian studying an old universe, I have given a great deal of thought to the Young Earth Creationist movement currently in conservative churches in America. Since this is my own religious background, I feel a particular motivation to discuss the interpretation of the early chapters of Genesis in the Bible. As I stated above, scientific claims made by a religion must be in agreement with scientific research. Thus, if the Bible claims the earth was literally formed in six days 10,000 years ago, then there is a huge conflict between the Bible and science. There are, however, many other ways to interpret Genesis besides the literal reading. The Biblical creation story is typical of origins stories in other ancient near-East cultures, with one striking difference. In Genesis 1, there is one God over the whole creation, while in the other stories there is a pantheon of gods, each of whom indwell an aspect of the world and are at war with one another. Thus, the original audience would have heard the story as primarily a religious statement: that God is the Creator of the entire physical world. Genesis was certainly not intended as a detailed scientific description (the author would have had no concept of science). The Christian may ask, What then is to prevent you from interpreting the resurrection story as just a parable? The answer lies in understanding the author, audience, and literary style of each section of the Bible and taking the meaning that the original audience would have heard. In contrast with the ancient near-East audience of Genesis, citizens of Roman culture around 60 A.D. would have heard the Gospel stories as historical accounts of the crucifixion and resurrection of a Jesus, not as a parable or other literary form. Most of the people in the Young Earth Creationist movement have good motives (they believe a "literal" reading of Genesis is the only way to uphold the integrity of the whole Bible), but their scientific work, unfortunately, often falls in the category of pseudo-science.

To help diffuse these and other tensions between science and Christian faith, I think an important task for scientists of faith is to make presentations to Christian groups of interesting scientific results in a Christian context. I have already given such talks at my church and campus Christian group. The goal is to fight the anti-intellectualism trend in the church and to remind Christians that science can be done in a Christian way.

A Christian may ask, however, Are you not being a "practical atheist" when you do your

research? Do you not perform experiments in exactly the same way as your colleagues, and only think about God on Sundays? Admittedly, I have learned nearly all of my scientific knowledge and skills in a secular environment. One of the nice things about science is that people with very diverse beliefs can work together using the scientific method to obtain the same results. Yet as a Christian, I need to remember the Creator in the midst of studying the creation, and to praise God for his faithfulness, beauty, and power when (through the eyes of faith) I see these attributes laid out in the universe. A poet looked at the night sky three thousand years ago and wrote:

> *The heavens declare the glory of God;*
> *the skies proclaim the work of his hands.*
> *Day after day they pour forth speech;*
> *night after night they display knowledge.*
> *There is no speech or language*
> *where their voice is not heard.*
> *Their voice goes out into all the earth,*
> *their words to the ends of the world.*
>
> Psalm 19

I feel the same awe that people of all nations and cultures (and especially astronomers) feel when they look at the starry sky, but as a Christian I can redirect this emotion into praise of the Artist who made it. This provides a meaningful context and strong personal motivation for my astrophysical research.

Even more impressive to me is the magnitude of the sizes and distances we see in the universe. The distance to the galaxies so beautifully displayed in the Hubble Deep Field image, and the knowledge of the immense number of galaxies out there, is enough to make a human being feel very small and insignificant. If God is truly making all those galaxies dance and spin, would the same God care about humans? After all, with all the planets in all the galaxies, there are most likely other planets that have developed intelligent life to whom God could relate. The Psalmist also considered this question:

> *When I consider your heavens,*
> *the work of your fingers,*
> *the moon and the stars*
> *which you have set in place,*
> *what is man that you are mindful of him,*

the son of man that you care for him?
You made us a little lower than the heavenly beings
and crowned us with glory and honor.
You made us rulers over the works of your hands;
you put everything under our feet.

Psalm 8, modified

The Psalmist answers his own question by recalling God's first words to human beings, wherein God placed us in stewardship over the earth and its creatures. Yet the answer for the Christian wondering about our significance today resounds even louder: we have been honored by the presence of God himself among us in the person of Jesus Christ, and by his sacrificial death for us. As the hymn writer puts it,

O Lord my God, when I in awesome wonder
consider all the worlds Thy hands have made,
I see the stars, I hear the rolling thunder,
Thy power throughout the universe displayed.

And when I think that God, His Son not sparing,
Sent Him to die, I scarce can take it in,
That on the cross, my burden gladly bearing,
He bled and died to take away my sin.

Then sings my soul, my Savior God, to Thee:
How great Thou art, how great Thou art!

Carl Boberg, 1885

When I study the universe and remember that its Creator is also the Savior of my soul, I am continually moved to worship. Thus, as I do my neutral scientific experiments, I also live out my faith. God has challenged me to communicate these truths about the created world to the church, and communicate his great salvation to my fellow academics.

You are King of creation and King of my life,
King of the land and the sea.
You were Lord of creation before there was time,
and Lord of all lords you will be!

from a modern hymn

Bibliography

Aller, H. D., Aller, M. F., Latimer, G. E., & Hodge, P. E. 1985, *ApJS* **59**, 513
Angonin-Willaime, M. C., Soucail, G., & Vanderriest, C. 1994, *A&A* **291**, 411
Bar-Kana, R. 1996, *ApJ* **468**, 17
Bar-Kana, R. 1997, preprint astro-ph/9701068
Bennett, D. P. & Rhie, S. H. 1996, *ApJ* **472**, 660
Berkhuijsen, E. M., Haslam, C. G. T., & Salter, C. J. 1971, *A&A* **14**, 252
Bernstein, G., Fischer, P., Tyson, J. A., & Rhee, G. 1997, preprint astro-ph/9705024
Bernstein, G. M., Tyson, J. A., & Kochanek, C. S. 1993, *AJ* **105**, 816
Beskin, G. M. & Oknyanskij, V. L. 1995, *A&A* **304**, 341
Binney, J. & Tremaine, S. 1987, *Galactic Dynamics*, Princeton University Press
Blandford, R. D. & Konigl, A. 1979, *ApJ* **232**, 34
Blandford, R. D. & Kundić, T. 1996, preprint astro-ph/9611229
Blandford, R. D. & Narayan, R. 1986, *ApJ* **310**, 568
Blandford, R. D. & Narayan, R. 1992, *ARA&A* **30**, 311
Bonometti, R. J. 1985, *Ph.D. thesis*, Massachusetts Institute of Technology
Borgeest, U. & Refsdal, S. 1984, *A&A* **141**, 318
Bourassa, R. R. & Kantowski, R. 1975, *ApJ* **195**, 13
Bourassa, R. R., Kantowski, R., & Norton, T. D. 1973, *ApJ* **185**, 747
Briggs, D. S. 1995, *Ph.D. thesis*, New Mexico Institute of Mining and Technology
Campbell, R. M., Corey, B. E., Falco, E. E., Shapiro, I. I., Gorenstein, M. V., Elósegui, P., Marcaide, J. M., & Alvi, K. 1994, *ApJ* **426**, 486
Campbell, R. M., Lehár, J., Corey, B. E., Shapiro, I. I., & Falco, E. E. 1995, *AJ* **110**, 2566
Carlstein, E. 1986, *The Annals of Statistics* **14**, 1171
Chaboyer, B. 1995, *ApJ* **444**, L9
Chang, K. & Refsdal, S. 1979, *Nature* **282**, 561
Clark, B. G. 1980, *A&A* **89**, 377
Clegg, A. W., Fey, A. L., & Fiedler, R. L. 1996, *ApJ* **457**, L23
Conner, S. R., Lehár, J., & Burke, B. F. 1992, *ApJ* **387**, L61
Cooke, J. H. & Kantowski, R. 1975, *ApJ* **195**, L11
Corbett, E. A., Browne, I. W. A., Wilkinson, P. N., & Patnaik, A. R. 1996, in C. S. Kochanek & J. N. Hewitt (eds.), *Astrophysical Applications of Gravitational Lensing: Proceedings of 173rd Symposium of the IAU*, p. 37, Kluwer
Crane, P. C. & Napier, P. J. 1989, in R. A. Perley, F. R. Schwab, & A. H. Bridle (eds.), *Synthesis Imaging in Radio Astronomy*, No. 6 in Conference Series, pp 139–165, Astronomical Society of the Pacific

Dahle, H., Maddox, S. J., & Lilje, P. B. 1994, *ApJ* **435**, L79
Dyer, C. C. & Roeder, R. C. 1972, *ApJ* **174**, L115
Edelson, R. A. & Krolik, J. H. 1988, *ApJ* **333**, 646
Efron, B. & Tibshirani, R. 1986, *Statistical Science* **1**, 54
Efron, B. & Tibshirani, R. 1993, *An Introduction to Bootstrap*, Chapman & Hall
Einstein, A. 1915, *Sitzungber. Preuss. Akad. Wissensch., erster Halbband* p. 831
Einstein, A. 1936, *Science* **84**, 506
Falco, E. E., Gorenstein, M. V., & Shapiro, I. I. 1985, *ApJ* **289**, L1
Falco, E. E., Gorenstein, M. V., & Shapiro, I. I. 1991a, *ApJ* **372**, 364
Falco, E. E., Shapiro, I. I., Moustakas, L. A., & Davis, M. 1997, preprint astro-ph/9702152
Falco, E. E., Wambsganss, J., & Schneider, P. 1991b, *MNRAS* **251**, 698
Fey, A. L., Clegg, A. W., & Fiedler, R. L. 1996, *ApJ* **468**, 543
Fiedler, R., Dennison, B., Johnston, K. J., Waltman, E. B., & Simon, R. S. 1994, *ApJ* **430**, 581
Fiedler, R. L., Dennison, B., Johnston, K. J., & Hewish, A. 1987, *Nature* **326**, 675
Fischer, P., Bernstein, G., Rhee, G., & Tyson, J. A. 1997, *AJ* **113**, 521
Florentin-Nielsen, R. 1984, *AJ* **138**, L19
Freedman, W. L. 1997, preprint astro-ph/9612024. To appear in conference proceedings "Critical Dialogues in Cosmology"
Fukugita, M., Futamase, T., Kasai, M., & Turner, E. L. 1992, *ApJ* **393**, 3
Garrett, M. A. 1990, *Ph.D. thesis*
Garrett, M. A., Calder, R. J., Porcas, R. W., King, L. J., Walsh, D., & Wilkinson, P. N. 1994, *MNRAS* **270**, 457
Gaskell, C. M. & Sparke, L. S. 1986, *ApJ* **305**, 175
Gondhalekar, P. M., Wilson, R., Dupree, A. K., & Burke, B. F. 1986, in *New Insights in Astrophysics: 8 years of UV Astronomy with IUE*, p. 715, European Space Agency, SP-63
Gorenstein, M. V., Cohen, N. L., Shapiro, I. I., Rogers, A. E. E., Bonometti, R. J., Falco, E. E., Bartel, N., & Marcaide, J. M. 1988a, *ApJ* **334**, 42
Gorenstein, M. V., Falco, E. E., & Shapiro, I. I. 1988b, *ApJ* **327**, 693
Gorenstein, M. V., Shapiro, I. I., Cohen, N. L., Corey, B. E., Falco, E. E., Marcaide, J. M., Rogers, A. E. E., Whitney, A. R., Porcas, R. W., Preston, R. A., & Ruis, A. 1983, *Science* **219**, 54
Gorenstein, M. V., Shapiro, I. I., Rogers, A. E. E., Cohen, N. L., Corey, B. E., Porcas, R. W., Falco, E. E., Bonometti, R. J., Preston, R. A., Rius, A., & Whitney, A. R. 1984, *ApJ* **287**, 538
Gott III, J. R. 1977, *ARA&A* **15**, 235
Greenfield, P. E., Roberts, D. H., & Burke, B. F. 1985, *ApJ* **293**, 370
Grogin, N. A. & Narayan, R. 1996a, *ApJ* **464**, 92
Grogin, N. A. & Narayan, R. 1996b, *ApJ* **473**, 570
Haarsma, D. B., Hewitt, J. N., Lehár, J., & Burke, B. F. 1997, *ApJ* **479**, 102
Heeschen, D. S. 1984, *AJ* **89**, 1111
Heeschen, D. S. & Rickett, B. J. 1987, *AJ* **93**, 587
Hewitt, J. N., Chen, G. H., & Messier, M. 1995, *AJ* **109**, 1956
Hjorth, J., Jaunsen, A. O., Patnaik, A. R., & Kneib, J. P. 1996, in C. S. Kochanek & J. N.

Hewitt (eds.), *Astrophysical Applications of Gravitational Lensing: Proceedings of 173rd Symposium of the IAU*, p. 343, Dodrecht: Kluwer
Hjorth, P. G., Villemoes, L. F., Teuber, J., & Florentin-Nielsen, R. 1992, *A&A* **255**, L20
Högbom, J. 1974, *ApJS* **15**, 417
Holzapfel, W. L., Arnaud, M., Ade, P. A. R., Church, S. E., Fischer, M. L., Mauskopf, P. D., Rephaeli, Y., & Wilbanks, T. M. 1997, *ApJ* **481**, 35
Hughes, P. A., Aller, H. D., & Aller, M. F. 1985, *ApJ* **298**, 301
Hughes, P. A., Aller, H. D., & Aller, M. F. 1989, *ApJ* **341**, 54
Hughes, P. A., Aller, H. D., & Aller, M. F. 1992, *ApJ* **396**, 469
Jacoby, G. H., Branch, D., Clardullo, R., Davies, R. L., Harris, W. E., Pierce, M. J., Pritchet, C. J., Tonry, J. L., & Welch, D. L. 1992, *PASP* **104**, 599
Jaunsen, A. O. & Hjorth, J. 1997, *A&A* **317**, L39
Jimenez, R. & Padoan, P. 1996, *ApJ* **463**, L17
Kayser, R. 1993, in J. Surdej *et al.* (eds.), *Gravitational Lenses in the Universe: Proceedings of the 31st Liége International Astrophysical Colloquium*, p. 5, Liége, Belgium: Universiteé de Liége, Institut d'Astrophysique
Kayser, R., Refsdal, S., & Stabell, R. 1986, *A&A* **166**, 36
Keel, W. C. 1982, *ApJ* **255**, 20
Keeton, C. R. & Kochanek, C. S. 1997, preprint astro-ph/9611216
Kellermann, K. I. & Pauliny-Toth, I. I. K. 1981, *ARA&A* **19**, 373
Kellermann, K. I., Zensus, J. A., & Cohen, M. H. 1997, *ApJ* **475**, L93
Kim, A. G. *et al.* 1997, *ApJ* **476**, L63
King, I. R. 1966, *AJ* **71**, 64
Kochanek, C. S. 1991, *ApJ* **382**, 58
Kochanek, C. S. 1993, *ApJ* **419**, 12
Kochanek, C. S. & Hewitt, J. N. (eds.) 1996, *Astrophysical Applications of Gravitational Lensing: Proceedings of 173rd Symposium of the IAU*, Kluwer
Kochanek, C. S. & Narayan, R. 1992, *ApJ* **401**, 461
Kundić, T., Colley, W. N., Gott III, J. R., Malhotra, S., Pen, U.-L., Rhoads, J. E., Stanek, K. Z., & Turner, E. L. 1995, *ApJ* **455**, L5
Kundić, T., Turner, E. L., Colley, W. N., Gott III, J. R., Rhoads, J. E., Wang, Y., Bergeron, L. E., Gloria, K. A., Long, D. C., Malhotra, S., & Wambsganss, J. 1997, preprint astro-ph/9610162
Kunsch, H. R. 1989, *The Annals of Statistics* **17**, 1217
Lahiri, S. N. 1992, in R. LePage & L. Billard (eds.), *Exploring the Limits of Bootstrap*, p. 183, Wiley
Langston, G. I. 1996, private communication
Lehár, J., Hewitt, J. N., & Roberts, D. H. 1988, in J. M. Moran, J. N. Hewitt, & K. Y. Lo (eds.), *Gravitational Lenses: Proceedings, Cambridge, Massachusetts, 1988*, No. 330 in Lecture Notes in Physics, p. 84, Springer-Verlag
Lehár, J., Hewitt, J. N., Roberts, D. H., & Burke, B. F. 1992, *ApJ* **384**, 453
Liebes, S. 1964, *Phys. Rev.* **133**, B835
Litchfield, S. J., Robson, E. I., & Hughes, D. H. 1995, *A&A* **300**, L385
Liu, R. Y. & Singh, K. 1992, in R. LePage & L. Billard (eds.), *Exploring the Limits of Bootstrap*, p. 225, Wiley

Livio, M. & Donahue, M. (eds.) 1997, *The Extragalactic Distance Scale: Proceedings of a Conference at the Space Telescope Science Institute, May 1996*

Lloyd, C. 1981, *Nature* **294**, 727

Lovell, J. E. J. *et al.* 1996, *ApJ* **472**, L5

Marscher, A. P. & Gear, W. K. 1985, *ApJ* **298**, 114

Moore, C. B. 1996, *Ph.D. thesis*, MIT

Myers, S. T., Baker, J. E., Readhead, A. C. S., Leitch, E. M., & Herbig, T. 1997, preprint astro-ph/9703123

Nair, S. 1996, in C. S. Kochanek & J. N. Hewitt (eds.), *Astrophysical Applications of Gravitational Lensing: Proceedings of 173rd Symposium of the IAU*, Kluwer

Narasimha, D., Subramanian, K., & Chitre, S. M. 1984, *MNRAS* **210**, 79

Narayan, R. 1991, *ApJ* **378**, L5

Narayan, R. & Bartelmann, M. 1996, preprint astro-ph/9606001

Oknyanskij, V. L. & Beskin, G. M. 1993, in J. Surdej *et al.* (eds.), *Gravitational Lenses in the Universe: Proceedings of the 31st Liége International Astrophysical Colloquium*, p. 65, Liége, Belgium: Universiteé de Liége, Institut d'Astrophysique

Oscoz, A., Mediavilla, E., Goicoechea, L. J., Serra-Ricart, M., & Buitrago, J. 1997, *ApJ* **479**, L89

Oscoz, A., Serra-Ricart, M., Goicoechea, L. J., Buitrago, J., & Mediavilla, E. 1996, *ApJ* **470**, L19

Patnaik, A. R. & Porcas, R. W. 1996, in C. S. Kochanek & J. N. Hewitt (eds.), *Astrophysical Applications of Gravitational Lensing: Proceedings of 173rd Symposium of the IAU*, p. 305, Kluwer

Pauliny-Toth, I. I. K. & Kellermann, K. I. 1966, *ApJ* **146**, 634

Pelt, J., Hoff, W., Kayser, R., Refsdal, S., & Schramm, T. 1994, *A&A* **286**, 775

Pelt, J., Kayser, R., Refsdal, S., & Schramm, T. 1996, *A&A* **305**, 97

Perley, R. A., Schwab, F. R., & Bridle, A. H. (eds.) 1989, *Synthesis Imaging in Radio Astronomy*, Astronomical Society of the Pacific

Pijpers, F. P. 1997, preprint astro-ph/9607082

Pohl, M., Reich, W., Krichbaum, T. P., Standke, K., Britzen, S., Reuter, H. P., Reich, P., Schlickeiser, R., Fiedler, R. L., Waltman, E. B., Ghigo, F. D., & Johnston, K. J. 1995, *A&A* **303**, 383

Politis, D. N. & Romano, J. P. 1992, in R. LePage & L. Billard (eds.), *Exploring the Limits of Bootstrap*, p. 263, Wiley

Press, W. H., Flannery, B. P., Teukolsky, S. A., & Vetterling, W. T. 1992a, *Numerical Recipes*, Cambridge University Press, 2nd edition

Press, W. H. & Gunn, J. E. 1973, *ApJ* **185**, 397

Press, W. H. & Rybicki, G. B. 1997, in D. Maoz (ed.), *Astronomical Time Series: Proceedings of the Wise Observatory 25th Anniversary Symposium*, Kluwer, Dordrecht

Press, W. H., Rybicki, G. B., & Hewitt, J. N. 1992b, *ApJ* **385**, 404

Press, W. H., Rybicki, G. B., & Hewitt, J. N. 1992c, *ApJ* **385**, 416

Rauch, K. P. & Blandford, R. D. 1991, *ApJ* **381**, L39

Refsdal, S. 1964a, *MNRAS* **128**, 295

Refsdal, S. 1964b, *MNRAS* **128**, 307

Refsdal, S. 1966, *MNRAS* **132**, 101

Rickett, B. J. 1990, *ARA&A* **28**, 561
Riess, A. G., Press, W. H., & Kirshner, R. P. 1996, *ApJ* **473**, 88
Roberts, D. H., Greenfield, P. E., Hewitt, J. N., Burke, B. F., & Dupree, A. K. 1985, *ApJ* **293**, 356
Roberts, D. H., Lehár, J., Hewitt, J. N., & Burke, B. F. 1991, *Nature* **352**, 43
Rogers, A. E. E. 1988, in J. M. Moran, J. N. Hewitt, & K. Y. Lo (eds.), *Gravitational Lenses: Proceedings, Cambridge, Massachusetts, 1988*, No. 330 in Lecture Notes in Physics, p. 77, Springer-Verlag
Romani, R. W., Blandford, R. D., & Cordes, J. M. 1987, *Nature* **328**, 324
Rybicki, G. B. & Kleyna, J. T. 1994, in P. M. Gondhalekar, K. Horne, & B. M. Peterson (eds.), *Reverberation Mapping of the Broad-Line Region in Active Galactic Nuclei*, No. 69 in Conference Series, p. 85, Astronomical Society of the Pacific
Rybicki, G. B. & Lightman, A. P. 1979, *Radiative Processes in Astrophysics*, Wiley-Interscience
Rybicki, G. B. & Press, W. H. 1992, *ApJ* **398**, 169
Schechter, P. L. *et al.* 1996, *ApJ* **475**, L85
Schild, R. & Thomson, D. J. 1995, *AJ* **109**, 1970
Schild, R. & Thomson, D. J. 1997, *AJ* **113**, 130
Schild, R. E. 1990, *AJ* **100**, 1771
Schild, R. E. & Cholfin, B. 1986, *ApJ* **300**, 209
Schild, R. E. & Smith, R. C. 1991, *AJ* **101**, 813
Schmidt, B. P., Kirshner, R. P., Eastman, R. G., Phillips, M. M., Suntzeff, N. B., Hamuy, M., Maza, J., & Aviles, R. 1994, *ApJ* **432**, 42
Schneider, P. 1996, preprint astro-ph/9512047
Schneider, P., Ehlers, J., & Falco, E. E. 1992, *Gravitational Lenses*, Springer-Verlag
Schwab, F. R. 1984, *AJ* **89**, 1076
Shi, X. 1995, *ApJ* **446**, 637
Simonetti, J. H., Cordes, J. M., & Heeschen, D. S. 1985, *ApJ* **296**, 46
Sopata, L. 1996, *Undergraduate thesis*, Massachusetts Institute of Technology
Stabell, R. 1993, in J. Surdej *et al.* (eds.), *Gravitational Lenses in the Universe: Proceedings of the 31st Liége International Astrophysical Colloquium*, p. 407, Liége, Belgium: Universiteé de Liége, Institut d'Astrophysique
Stevens, J. A., Litchfield, S. J., Robson, E. I., Cawthorne, T. V., Aller, M. F., Aller, H. D., Hughes, P. A., & Wright, M. C. H. 1996, *ApJ* **466**, 158
Stockton, A. 1980, *ApJ* **242**, L141
Thompson, A. R., Moran, J. M., & Swenson, Jr., G. W. 1994, *Interferometry and Synthesis in Radio Astronomy*, Krieger Publishing Company
Tonry, J. L., Blakeslee, J. P., Ajhar, E. A., & Dressler, A. 1997, *ApJ* **475**, 399
Turok, N. (ed.) 1997, *Cricital Dialogues in Cosmology: Proceedings of a Conference at Princeton, June 1996*
van der Laan, H. 1966, *Nature* **211**, 1131
van Ommen, T. D., Jones, D. L., Preston, R. A., & Jauncey, D. L. 1995, *ApJ* **444**, 561
Vanderriest, C., Schneider, J., Herpe, G., Chevreton, M., Moles, M., & Wlérick, G. 1989, *A&A* **215**, 1
Walker, R. C. 1995, in J. A. Zensus, P. J. Diamond, & P. J. Napier (eds.), *Very long basline*

interferometry and the VLBA, No. 82 in Conference Series, p. 133, Astronomical Society of the Pacific

Walsh, D., Carswell, R. F., & Weymann, R. J. 1979, *Nature* **279**, 381

Wambsganss, J., Schneider, P., & Paczynski, B. 1990, *ApJ* **358**, L33

Weymann, R. J., Jr., F. H. C., Carleton, N. P., Walsh, D., Carswell, R. F., & Davis, M. 1979, *ApJ* **233**, L43

White, R. J. & Peterson, B. M. 1994, *PASP* **106**, 879

Young, P., Gunn, J. E., Kristian, J., Oke, J. B., & Westphal, J. A. 1980, *ApJ* **241**, 507

Young, P., Gunn, J. E., Kristian, J., Oke, J. B., & Westphal, J. A. 1981, *ApJ* **244**, 736

Zwicky 1937, *Phys. Rev* **51**, 290